Studies of Ultracold Collisions of Ground-state ^{23}Na^{87}Rb Polar Molecules

基態^{23}Na^{87}Rb極性分子的超冷碰撞的研究

YE, Xin

葉鑫

A Thesis Submitted in Partial Fulfilment
of the Requirements for the Degree of
Doctor of Philosophy
in
Physics

The Chinese University of Hong Kong
January 2019

Thesis Assessment Committee

Professor LAW, Chi Kwong (Chair)

Professor WANG, Dajun (Thesis Supervisor)

Professor YANG, Sen (Committee Member)

Professor WU, Saijun (External Examiner)

Abstract of thesis entitled:

Studies of Ultracold Collisions of Ground-state ^{23}Na^{87}Rb Polar Molecules

Submitted by YE, Xin

for the degree of Doctor of Philosophy

at The Chinese University of Hong Kong in January 2019

This thesis mainly describes studies on the ultracold collisions with the ground-state ^{23}Na^{87}Rb molecules. The molecules are produced from a ultracold mixture of Na and Rb atoms via the magnetoassociation near an interspecies Feshbach resonance and are further transferred to the ground state via a Raman process. The precise internal state control of the molecule is achieved with Raman beams and microwaves. Based on the precise internal state control, a series of experimental studies including collisions with controlled chemical reactivities, collisions of molecules with induce electric dipoles, collisions in a molecular mixture and collisions between molecules and atoms are carried out. These experiments yield precise collision rate constant values. The comparison between the experimental results and the theoretical models shed new lights to the underlying interactions of the complicated molecular collisions. Besides, this thesis also presents an investigation on the molecular coherence to probe the intermolecular interaction and the recent progress on the optical lattice in our lab.

摘要

本論文主要敘述了有關基態^{23}鈉^{87}銣分子的超冷碰撞的研究。該分子由鈉和銣原子的超冷混合物，通過在種間費甚巴赫共振附近進行磁締合產生，並通過拉曼過程進一步地轉移到基態。通過使用拉曼光束和微波實現了分子精確的內態控制。基於精確的內態控制，我們開展了一系列實驗研究，包括受控化學反應性的碰撞，具有誘導電偶極子的分子的碰撞，分子混合物中的碰撞以及分子與原子之間的碰撞。這些實驗給出了精確的碰撞率常數值。實驗結果與理論模型的比較，幫助闡明了複雜的分子碰撞背後的相互作用。此外，本論文還敘述了以探究分子間相互作用的分子相干性的研究，並報告了本實驗室在光晶格上的最新進展。

Acknowledgements

During my 4-year stay in CUHK, I got support from many people. I would like to use this page to thank and acknowledge all the people who help to make this thesis possible.

First of all, I would like to express my gratitude to Prof. Dajun Wang for giving me the opportunity to join the CUHK group and his guidance in the group over the years. He is a very experienced researcher in AMO physics and I am always amazed by his physical insights, and his passion and hard-work. I learnt a lot from him of how to be a qualified researcher, from technical skills to scientific methodologies.

I would like to thank Dr. Fudong Wang. I worked with him for the first two years. Working with him, I got comprehensive understandings on the AMO physics. He is a person of great power of execution, who made the construction of most parts of our experimental systems. All other members of our group are benefited from his excellent works.

I would like to thank Dr. Mingyang Guo. For the last two years, I worked with him on the NaRb molecule projects. He is an expert on molecules and can give me answers whenever I encounter with a problem about molecules. He is hard-working and has a high criterion on everything. I am glad and thankful that we had a fruitful time working together.

Besides the few people mentioned above, I would also like to thank other past and present members of the group. I would like to thank Dr. Bo Lu who has a very nice personality and taught me a lot basics about optics and lasers in the first two years. Besides, I like his jokes and his Chinese medicine theory shared with us on the way to canteens. I would like to thank Dr. Xiaoke Li and Dr. Bing Zhu. They answered me a lot questions about AMO physics (as well as Cantonese) when I just entered the lab. I would like to thank Lintao Li for bringing his brilliance in electronics to our lab. I would like to thank Dr. Xiaodong He, Dr. Shi Yu, Junyu He, Zhichao Guo, Junyu Lin, Fan Jia for their kind assistance from time to time. Junyu He and Junyu Lin will continue to work on the molecule and I wish they could push the molecule experiment to a new level in the future.

I owe special gratitude to our theoretical collaborator from France, the Theomol team of Laboratoire Aimé Cotton in Orsay. We couldn't have gone so far if without them. In particular, I want to thank Prof. Goulven Quéméner and Dr. Maykel L. González-Martínez for their contributions in collision theories and calculations. A large part of the molecular collision knowledge I learnt comes from the correspondence with them.

I would also like to acknowledge the supporting staffs of the physics department, especially Ms. Florence, Mrs. Wong Lee Yeuk Lan, Ms. Pui Yee Ho, Ms. Mandy Tang and Mr. Edward W. K. Chao for their silent support of all aspects.

I thank my friends in Hong Kong. They shared all the memorable moments here with me, especially Mr. Xunze Zheng, Dr. Ning Wang, Dr. Chaojie Wang, Dr. Xiaotian Yu and Dr. Zhiyuan Yang.

I also want to thank several people outside Hong Kong, who are very influential in my academic career. My high school physics teacher Mr. Lexiao He, my undergraduate supervisor in Zhejiang University Prof. Zhaoying

Wang, other professors in Zhejiang University who taught me important things about doing research: Prof. Xin Wan, Prof. Dinghui Lu, Prof. David P. Landau, Prof. Shining Bao, Prof. Ping Zhu, and my mentors during my summer intern in Rice University, Prof. Qianfan Xu and Prof. Ciyuan Qiu.

Finally, I owe my deepest thanks to my family for their love and care, and their constant understanding and support.

Dedicated to my family.

Contents

Abstract i

摘要 ii

Acknowledgements iii

1 Introduction 1

- 1.1 Ultracold polar molecule: dipole-dipole interaction (DDI) . . . 2
- 1.2 Ultracold polar molecule: applications 4
  - 1.2.1 Ultracold chemistry 4
  - 1.2.2 Quantum simulation 4
  - 1.2.3 Quantum computation 5
  - 1.2.4 Precision measurements 5
- 1.3 Thesis outline 6

2 Theoretical backgrounds 8

- 2.1 Quantum scattering theory 8
  - 2.1.1 Basics 9
  - 2.1.2 Partial wave expansion 11
  - 2.1.3 Scattering length 12
  - 2.1.4 Unitarity limit 12
  - 2.1.5 Wigner threshold law 13

2.2 Ultracold collisions of molecules 14
2.2.1 Scattering in highly resonant regime 14
2.2.2 Universal model for bimolecular reaction 15
2.2.3 Coupled equations 16
2.2.4 Close-coupling calculation 18

3 Experimental setups 20
3.1 Overview 20
3.2 Vacuum 22
3.3 Stages in MOT cell 22
3.4 Magnetic transport 24
3.5 MW evaporative cooling in hybrid trap 25
3.6 Crossed ODT 25
3.7 B-field 26
3.8 LabVIEW control 27

4 Production of ground-state NaRb molecule and its internal state control 30
4.1 Feshbach resonance 30
4.1.1 Basics 31
4.1.2 Production of NaRb Feshbach molecule 32
4.1.3 Residual atom removal 33
4.2 Stimulated Raman Adiabatic Passage (STIRAP) 36
4.2.1 Basics 36
4.2.2 Ground-state NaRb molecule production and internal state control via STIRAP 39
4.3 One-photon MW transition 41
4.4 Two-photon MW transition 42

5 Technical issues 46

5.1 Number calibration 47

5.2 Temperature calibration 50

5.3 Suppression of molecular motion 53

5.4 Trap frequency 55

5.5 Image denoising 56

6 Collisions with controlled chemical reactivities 61

6.1 Overview 61

6.2 Chemical reactivity of Na and Rb system 62

6.3 Procedures 64

6.4 Exclusion of dependencies on several factors 65

6.4.1 Exclusion of dependency on STIRAP efficiency 67

6.4.2 Exclusion of dependency on ODT wavelength 67

6.4.3 Exclusion of dependency on B-field 70

6.5 Loss comparison and loss model 70

6.6 Segment fit 74

6.7 Temperature dependence 75

6.8 Comparison with close-coupling quantum calculations 77

6.9 Post-complex formation dynamics 79

6.9.1 Rice-Ramsperger-Kassel-Marcus (RRKM) theory . . . 79

6.9.2 The complex-mediated collision model 80

6.10 Conclusion 84

7 Collisions with induced electric dipoles in E-fields 86

7.1 Overview 86

7.2 Induction of electric dipole moment 87

7.3 Modification to molecule-molecule interaction potentials . . . 90

7.4 E-field dependence and temperature dependence of dipolar collision . . . 92
7.5 Characteristic energy scales . . . 96
7.6 Conclusion . . . 100

8 Collisions in molecular mixtures 101

8.1 Overview . . . 101
8.2 Molecular Hamiltonian . . . 102
8.3 State-dependent DDI . . . 106
8.4 Procedures . . . 107
8.5 DDI-dependent loss and temperature dependence . . . 113
8.6 Mixture collision without DDI . . . 117

9 Atom-molecule collisions 120

9.1 Overview . . . 120
9.2 Tuning collisional threshold . . . 121
9.3 Density of trimer states . . . 122
9.4 Measuring atom-molecule loss . . . 124
9.5 B-field dependence . . . 129

10 Molecular coherence 131

10.1 Overview . . . 131
10.2 Anisotropic polarizability . . . 132
10.3 Magic angle . . . 134
10.4 Spin echo method . . . 137
10.5 Moving average cluster expansion (MACE) calculation . . . 140
10.6 Density dependence and state dependence of decoherence . . . 146

11 Towards molecules in optical lattices 152

11.1 Overview . . . 152

11.2 Plug trap . . . 153

11.3 Optical lattice optics . . . 160

11.4 ODT optics . . . 162

11.5 Laser intensity noise . . . 164

11.6 Band structure . . . 166

11.7 Kapitza-Dirac scattering . . . 169

11.8 BEC phase correlation among 1D lattice layers . . . 172

11.9 Outlook . . . 176

12 Conclusions 178

Bibliography 182

List of Figures

1.1 The DDI depends on the orientation of the two dipoles. The interaction is positive (repulsive) with a parallel configuration and negative (attractive) with a head-to-tail configuration. . . 3

2.1 An illustration of the quantum scattering. The incoming wave is a plane wave with momentum $\vec{k}$. The orange target scatters the incoming wave, generating outgoing waves with momentum $\vec{k}'$. The outgoing flux is measured at an angle of θ. 9

2.2 Origin of high density of four-body bound states. The number of collision channels is large due to the rich internal structures of a molecule. Channels in different colors corresponds to different vibrational quantum numbers. Within each bunch of states of the same color, the splitting is due to rotational structures and hyperfine structures. Each potential curve is deep due to the large C_6 between a pair of UPMs. Molecular collisions take place in a highly resonant regime with the large density of four-body bound states at the short range. 15

3.1 The experimemtal system. (A) An overview of the system. (B) The translation stage for magnetic transport of atoms. (C) Science cell and coils. (D) MOT cell and MOT optics. . . 21

3.2 Trap lifetime in the science cell. The remaining Rb atom number is measurement with different holding times in the magnetic trap. The first-order exponential decay fitting gives $\tau =$ 212 s. 23

3.3 MW evaporative cooling in a hybrid trap. (A) Typical MW sweeps for the evaporation. (B) Hybrid trap potential after the magnetic trap decompression for Na (black) and Rb (red). 24

3.4 The ultracold mixture of Na and Rb atoms. Pictures are taken after a time-of-flight of 5 ms for Na and 10 ms for Rb. On the left-hand side plot the optical density distributions along vertical lines slicing through the centers of the clouds. The Na atoms are partially in BEC state shown clearly by the bimodal distribution. The Rb atoms are thermal gas but close to the quantum degeneracy. 28

3.5 Measure the B-field magnitude and the stability. Rb atom transition from the $|F, m_F\rangle = |1, -1\rangle$ state to the $|2, 0\rangle$ state is used. (A) Measured B field = 335.23 G with a standard deviation of 10 mG. (B) Plot the red points with respect to time. The data show an oscillation with a period of 10.3 min. 29

3.6 (A) The overall architecture of the LabVIEW control. (B) The state flow of Host.vi. (C) The state flow of FPGA.vi. . . . 29

4.1 Basic two-channel picture of a Feshbach resonance. (A) Feshbach resonance happens when one bound state in the closed channel gets energetically close to the collisional threshold. (B) Avoided crossing of a magnetically tuned Feshbach resonance and adiabatic B-field ramping for molecule association. . 31

4.2 The NaRb Feshbach molecule near the 347.6 G Feshbach resonance. (A) Creation of NaRb Feshbach molecule confirmed by the atomic signal revival after the dissociation. (B) The B-field dependent magnetic dipole of the Feshbach molecule extracted from measurements of the binding energy. 33

4.3 MW Rabi frequencies for the residual atom removal. MW transition from $|1,1\rangle$ to $|2,2\rangle$. (A) The Rabi frequency for Na is $\Omega = 2\pi\times 45$ kHz. (B) The Rabi frequency for Rb is $\Omega = 2\pi\times 39$ kHz 36

4.4 (A) A sketch of a three level system. (B) The STIRAP scheme for ground-state NaRb molecule production. The initial state is $a^3\Sigma^+\,|v=21, J=1\rangle$, the intermediate state is the coupled $2^1\Sigma^+/1^3\Pi\,|v'=55, J'=1\rangle$. The target state is $X^1\Sigma^+\,|v=0, J=0\rangle$. (C) Feshbach molecule number evolution during a double STIRAP process together with the STIRAP pulse shape. 37

4.5 Internal state control via STIRAP. (A), (B) STIRAP spectra of the ($v=0$,$J=0$), ($v=1$,$J=0$) with dump beam of mixed polarization. (C) STIRAP spectra of ($v=0$,$J=2$) with dump beam of π polarization (black) and σ^+/σ^- polarization (red). Spectra are obtained by tuning the wavelength of the dump beam. The vertical colored bars indicate the quantum number M_F with $M_F=3$ in red, $M_F=2$ in blue, and $M_F=1$ in green 41

4.6 Internal state control via one-photon MW transition. (A) MW transitions to the $J = 1$ rotational state from the absolute ground state. The colored vertical bars indicate the calculated positions of the relevant hyperfine levels of $J = 1$. Note some transitions are not observable due to the weak transition dipole. (B) Coherent population transfer between the hyperfine levels of the $J = 0$ and $J = 1$ states with MW pulses. $J = 1$ states possess considerable mixing between different nuclear spins due to the rotation-nuclear coupling 43

4.7 Internal state control via two-photon MW transition. The two-photon transition starts from the absolute ground state $|J, m_J, m_{Na}, m_{Rb}\rangle = |0, 0, 3/2, 3/2\rangle$ to the third lowest state $|0, 0, 3/2, 1/2\rangle$. The intermediate state is the lowest state in the $J = 1$ manifold. The one-photon detuning Δ is -$2\pi\times200$ kHz, the Rabi frequency of the two MWs are $2\pi\times12$ kHz and $2\pi\times19$ kHz. The pulse duration is 500 μs in (A). The two red point are only with either one MW source and confirm the observed transition is a two-photon transition. (B). The two-photon Rabi oscillation, the measured effective two-photon Rabi frequency is 530 Hz 44

5.1 Number calibration, extraction of number correction parameter α (A) The calculated peak optical depth of absorption images according to Eq. 5.2 with different given value of α under different probe intensities ranging from 0.136 to 5.29 times saturation intensity (B) The standard deviation of the six optical depths with respect to α value. A minimum fit to the standard deviations gives the optimal $\alpha = 1.21$. 49

5.2 Temperature calibration. (A)The extracted temperature correction parameter α' within a range from 350 nK to 1.3 μK by comparing the results from the single-shot measurement and the standard TOF method. (B)Relation between the temperature of the ground-state molecule and the temperature of the product Rb atoms from dissociation. Dots with different colors are with different ODT depths. The x coordinate and y coordinate of each point are from successive two experimental shots. A linear fit gives a slope of 1.15 and an intercept of -0.11. 52

5.3 Suppress the molecular motion by tuning the ODT control DAC voltage immediately after STIRAP. The Feshbach state is initially in an ODT with DAC voltage = 0.3V. When the final DAC to initial DAC ratio is close to the polarizability ratio of the Feshbach state and the ground state, both the slosh and the breathing motion can be greatly suppressed. The weighted average of the minimum fit results of the four figures gives a target DAC of 0.409 V for an initial DAC = 0.3 V. 54

5.4 Time scale of the emergence of significant breathing motions. The resultant amplitude of the breathing motion is measured with respect to the delay time of the rise of the ODT power after STIRAP. There is no recognizable difference for delays shorter than 500 μs while for delay times larger than 1 ms, the amplitudes of the breathing motion are significantly larger. . . 55

5.5 Determination of trap frequency of molecules in ODT. The ODT power rise after STIRAP is deliberately delayed to induce motions. The molecules are held in trap with various holding times, dissociated into Rb atoms and immediately released from the trap. The position of the Rb atom cloud is measured after typical TOF of 2 ms. The oscillation of the position is fit with a damped oscillator model. 57

5.6 A sketch of the image denoising process. A bunch of basis images are constructed from a same number of raw images with only the background fringe via the Gram-Schmidt process. To denoise a image with the atom signal, the region contains the atom signal is masked and the rest of the image takes the inner products with the basis images. The inner products give the components of the image that fall into the fringe subspace. Subtracting these components, the image gets denoised. The image on the right hand side is denoised with 59 basis images. 60

6.1 The schematic reaction coordinates for the NaRb + NaRb → Na_2 + Rb_2 process are shown. (A) In the lowest rovibrational level ($v = 0$, $J = 0$), the reaction is endothermic by 47 cm^{-1} and thus forbidden at ultracold temperatures. (B) In the first excited rovibrational level ($v = 1$, $J = 0$), the same reaction is already exothermic by 164 cm^{-1} and thus allowed. Molecules can also relax from $v = 1$ to $v = 0$ following the collision, but experimentally, this cannot be distinguished from chemical reactions. The ground Na_2Rb_2 tetramer level, which has much lower energy than both the reactant and product molecule pairs, is also shown. Near the NaRb + NaRb collision threshold, the density of Na_2Rb_2* states is estimated to be too large to be resolved. As a result, the collision is in the highly resonant regime. 63
6.2 The experimental time sequence for collision experiments. The sequence is mainly divided into seven phases, i.e. the pre-association, the association, the atom removal, the ground-state molecule (GSM) holding, the dissociation, the low-field holding and the probe. B-field, ODT power control voltage and other relevant pulses that involves molecular state transfer and residual atom removal are shown. 66

6.3 The effect of STIRAP efficiency on the resulting loss rate constant β. STIRAP efficiency are controlled by varying the power of the Raman beams. STIRAP efficiencies from 63% to 91% is achieved with pump/dump Rabi frequencies from $2\pi\times0.3$ MHz to $2\pi\times1.2$ MHz. A linear fit shows an 1.8% increase of β per 10% decrease of STIRAP efficiency. The result indicates the molecule population not in the ground state is not the major cause of the loss of the ground-state molecules. Besides, the result shows we can neglect the effect from the non-100% STIRAP efficiency given our STIRAP efficiency higher than 90% 68

6.4 The effect of ODT wavelength on the ground-state NaRb molecule's loss. The number of remaining molecules in trap after a certain holding time is measured under different ODT wavelengths. (A) No loss resonance is observed at the vicinity of 1064.4 nm, which is the ODT wavelength used in collision experiments. (B and C)Two of the broad loss features due to resonances of the Feshbach molecule but not the ground-state molecule. . . . 69

6.5 The effect of B-field on the ground-state NaRb molecule's loss. The remaining molecule number are measured after a certain fixed holding time under different B-field. Below 16 G, the "ground state" is no longer the ground one. The loss of the ground-state molecule show no dependence on the B-field from 5.6 G to 339.2 G. 71

6.6 Inelastic collisions with different chemical reactivities. (A and B) Time evolutions of (A) molecule numbers and (B) temperatures for both nonreactive ($v = 0$, $J = 0$) (filled circles) and reactive ($v = 1$, $J = 0$) (filled squares) samples. The temperature measurement, which stops at 0.1 s because of reduced signal-to-noise ratio following the time-of-flight expansion, is obtained separately from the number evolution with samples of essentially identical conditions. Error bars represent 1 standard deviation. The blue dashed and red solid curves are fitting results using Eq. 6.3 with temperature-dependent loss rate constants obtained from Fig. 6.8. The measured trap oscillation frequencies are $[\omega_x, \omega_y, \omega_z] = 2\pi \times [217(3), 208(3), 38(2)]$ Hz for the ($v = 0$, $J = 0$) molecules and $2\pi \times [219(3), 205(2), 40(2)]$ Hz for the ($v = 1$, $J = 0$) molecules. The calculated initial peak densities can reach 6×10^{11} cm^{-3}. 72

6.7 Extraction of β with segment fit. The number evolution (A) and the temperature evolution (B) are measured from holding time = 4 ms to holding time = 100 ms. The each whole curve, it is divided into four segments, coded with different color. In each segment, the temperature evolution doesn't exceed 20%, so that we can neglect the temperature dependence of β and treat β as a constant parameter in the fitting model Eq. 6.3. The number and the temperature in each segment are fitted together by minimizing a joint χ^2. 75

6.8 Temperature dependence of β for different chemical reactivities. Each β is obtained from a fit to Eq. 6.3 to a segment of one full loss and heating measurement. The solid lines are from fits of β to power-law functions of T. Theoretical results based on the CC calculation are also shown. The dashed vertical line marks the position of T_{vdW}. The error bars represent 1 standard deviation. 77

6.9 Fit the nonreactive collisions with the full loss model including the post-complex formation dynamics. (A)The N evolution and (B)the T evolution are fitted simultaneously with Eq. 6.19. The fitting extracts a complex lifetime $\tau = 1/\gamma = 0.038(6)$ s and a non-physical complex-molecule loss rate constant $\beta_{cm} = 4.4(6)\times10^{-9}$ cm^{3}s^{-1} 84

7.1 dc Stark shift of NaRb molecules in the lowest three rotational levels ($J = 0, 1, 2$). Energy levels are calculated by solving the eigenvalues of Eq. 7.1 with J truncated at $J_{\max} = 9$. . . . 89

7.2 Induced electric dipole of NaRb molecule in the lowest three rotational levels ($J = 0, 1, 2$). Dipoles are calculated according to Eq. 7.2 based on the results in Fig. 7.1. 90

7.3 DDI's modification to molecule-molecular interaction potentials. (A)The modification of the s-wave potential. The dashed curve is for $\mu = 0$ D and the solid curve is for $\mu = 0.5$ D. The potential becomes more attractive with the DDI. (B)The modification of the d-wave potentials. The blue dashed curve is for $\mu = 0$ D. Without the induced dipole, the different M_L channels are degenerate. The d-wave barrier with a height of 17.2 μK is located at 600 a_0. For $\mu = 0.5$ D, the DDI breaks the degeneracy of different $|M_L|$ and results in substantially modified heights and locations of the barriers. 93

7.4 β's dependence on induced dipole moment under different temperatures. The induce dipole moment ranges from 0 to 0.7 D with E-field less than 1 kV/cm. The data points in black squares, red circles, and blue triangles are measured with sample temperatures of about 400 nK, 700 nK and 1400 nK, respectively. The solid curves of the same colors are close-coupling calculations with the corresponding sample temperatures. The horizontal belts indicate the unitarity limit of the s-wave scattering with temperature ranges of 400 ± 50 nK, 700 ± 50 nK and 1400 ± 100 nK. β increases step-wisely with a plateau occurs at the unitarity limit of the s-wave scattering. The overall magnitude of β is smaller and the plateau is vaguer for higher sample temperature. 94

7.5 (A)The generalized characteristic energy E_α for s-wave potential, E_{s-wave} with respect to μ. (B)β attributed to the s-wave scattering with respect to μ. The data points are from the black squares in Fig. 7.4 with μ ¡ 0.5 D. The vertical line at $\mu = 0.21$ D marks the position where the DDI starts to be comparable with the van der Waals interaction. The vertical line at $\mu = 0.44$ D represents the point when E_α is lowered to about T. The grey horizontal belt represents the inelastic s-wave unitarity limit for $T = 400 \pm 50$ nK. The black solid curve gives the prediction of the s-wave contribution of β from the close-coupling calculation. 98

7.6 (A)The d-wave barrier heights E_{d-wave} for different $|M_L|$ channels. (B)β_{d-wave} attributed to all five different M_L channels. The $|M_L| = 1$ channels with the lowest barriers dominate the contribution. The vertical line at 0.55 D marks the position where $E_{d-wave} = 5T$ for $|M_L| = 1$. The black solid curve gives the prediction of the d-wave contribution of β from the close-coupling calculation, in which more than 99% is attributed to the $|M_L| = 1$ channels. 99

8.1 $J = 0$ molecular levels with respect to B-field. The red dots mark the states we use in the mixture collision experiments at B = 335.2 G. 104

8.2 $J = 1$ molecular levels with respect to B-field. The red dots mark the states we use in the mixture collision experiments at B = 335.2 G. The other four black dots mark the other states that are available via MW transition from the absolute ground state $|0, 0, 3/2, 3/2\rangle$. 105

8.3 An example of measuring the mixture collision. The 50/50 mixture of the ground state and the rotational excited state is initialized with a 6-μs $\pi/2$ MW pulse. The starting point of the measurement is 3 ms after the initialization for the coherence to die out. Population in the rotational excited state (A) and the ground state (B) is measured at holding time = 0 ms and 4 ms. The solid curves are the fitting results according to Eq. 8.3. (C)The temperature is determined by measuring the cloud size after TOF for holding times start from 0 ms to 4 ms with an interval of 0.5 ms. The size is oscillating because of the breathing motion of molecules and the sinusoidal function is used to fit out the mean size. 109

8.4 Rabi oscillation decay between the rotational excited state $|1,1\rangle$(A), $|1,0\rangle$(B) and the ground state $|0,0\rangle$. The decay time constant is 590 μs for (A) and 360 μs for (B). The decay time constant of the Rabi oscillation sets an upper limit for the decay time constant of the 50/50 molecular mixture. The result confirms that there is no coherence in the ensemble for measurements start from 3 ms after the MW initialization. . . 111

8.5 Comparison between β_{gg} of a pure $|0,0\rangle$ sample (grey) and β_{ee} of a pure $|1,1\rangle$ sample (black) and a pure $|1,0\rangle$ sample (red). Similar magnitudes and T-dependence are found. It indicates that as a good approximation, we can take β_{ee} the same value as β_{gg} of the ground state in the data analysis of mixture collisions. 112

8.6 Summary of β_{eg} for $|0,0\rangle$+$|1,0\rangle$ mixture and $|0,0\rangle$+$|1,1\rangle$ mixture and their temperature dependence. The $|0,0\rangle$+$|1,0\rangle$ data are shown in black and the $|0,0\rangle$+$|1,1\rangle$ data are shown in red. The dashed curves are resuls from close-coupling calculation. The orange dashed curve is the calculation for $|0,0\rangle$+$|1,1\rangle$ with only the complex formation but without the hyperfine changing collision. 114

8.7 Rate constants for the mixture collision grouped by partial wave projection m_l and inversion symmetry ϵ_I. (A) is the complex formation rate constant for $|0,0\rangle$+$|1,0\rangle$. (B) and (C) are the complex formation and the hyperfine changing collision rate constant for $|0,0\rangle$+$|1,1\rangle$, respectively. 115

8.8 β_{eg} for hyperfine mixture of $|m_{\rm Na} = 3/2, m_{\rm Rb} = 3/2\rangle$ and $|3/2, 1/2\rangle$. The dashed curve represents the prediction from the universal model. 119

9.1 (A) ^{23}Na 3^2S$_{1/2}$ (ground) level hyperfine structure in an external B-field. The Zeeman shift at B-field = 335.2 G is -0.048, -0.657 and 1.074 MHz per Gauss for $|F, m_F\rangle = |1,-1\rangle$, $|1,0\rangle$ and $|1,1\rangle$ respectively. (B) ^{87}Rb 5^2S$_{1/2}$ (ground) level hyperfine structure in an external B-field. The Zeeman shift at B-field = 335.2 G is 0.543, -0.191 and 0.833 MHz per Gauss for $|F, m_F\rangle = |1,-1\rangle$, $|1,0\rangle$ and $|1,1\rangle$ respectively. 123

9.2 Ground-state NaRb molecule loss with Na atoms in $|1,1\rangle$ state. (A) shows the number evolution of the molecules and (B) shows the number evolution of Na atoms. 125

9.3 Ground-state NaRb molecule loss with Rb atoms in $|1,1\rangle$ state. (A) shows the number evolution of the molecules and (B) shows the number evolution of Rb atoms. 125

9.4 Summary of atom-molecule collisions at 335.2 G. The black dashed line represent the universal model prediction. The two vertical grey dashed lines mark the case for Rb+NaRb and Na+NaRb at $m_r^{-3/4}C_6^{1/4} = 0.496$ and $m_r^{-3/4}C_6^{1/4} = 0.871$. Within the uncertainties, the two cases both agree with the universal model. 128

9.5 The B-field dependence of the ground-state molecule loss with Rb atoms in $|1,1\rangle$ state. The remaining molecule number is measured after a fixed holding time of 4 ms after the target B-field is reached with a ramp in 0.5 ms from 335.2 G. The Rb atom number is 3.5×10^4. Despite an overall decline due to the condition drift and no structure is observed. 130

10.1 Spherical harmonic wave functions of different rotational states. Plotted in the 3D spherical coordinates, the radial distance represents the probability amplitude and the color represents the phase of the wave function. 133

10.2 The transition frequency of from $|0,0\rangle$ to $|1,0\rangle$ (A) and from $|0,0\rangle$ to $|1,1\rangle$ (B) with respect to the angle θ between the quantization axis and the linear polarization of the trapping beams at B-field = 335.2 G. The red curve in (A) is a fitting result from the molecular Hamiltonian with the trapping beam intensity set as a free parameter. The fitted trapping beam intensity is 10.5 kW/cm^2. (B) shows the comparison of the transition frequency from the theoretical calculation with 10.5 kW/cm^2 trapping beam intensity and the experimental result. 135

10.3 Calculated relative polarizability difference between the the $|1,-1\rangle/|1,0\rangle/|1,1\rangle$ state and the $|0,0\rangle$ state. The polarizability $\tilde{\alpha}$ is defined as $-\partial E/\partial I$. The vertical axis is $(\tilde{\alpha}-\alpha_{00})/\alpha_{00}$ where α_{00} is the polarizability of the $|0,0\rangle$ state. 136

10.4 The magic angle measurement of the $|1,0\rangle$ state (A) and the $|1,1\rangle$ state (B). The coherence are measured with spin echo method with respect to different linear polarization of the ODT beams. The contrast shows a peak at $\theta = 68°$ for both case, which is consistent with the theoretical calculation. The overall contrast of the $|1,0\rangle$ state appear to be less, because the MW switch leaks some MW power and kills the coherence of the ensemble. For the $|1,1\rangle$ case, this problem is fixed. . . . 137

10.5 A schematics of the spin echo method in the Bloch sphere representation. In a Bloch sphere, the south pole represent the $|\downarrow\rangle$ state, the north pole represent the $|\uparrow\rangle$ state, and other points represent the superposition states of $|\downarrow\rangle$ and $|\uparrow\rangle$. The system is initialized by a $\pi/2$-pulse, the red arrows rotate 90 degrees with respect to $\hat{y}$ axis from the $|\downarrow\rangle$ state. During the first $T/2$ evolution time, the single-particle dephasing introduces different angular displacements of the red arrows. A π-pulse flips the red arrows. During the second $T/2$ evolution time, the accumulated angular displacements are the same but has an opposite sign than the previous ones. The angular displacements cancel out each other during the two $T/2$ evolution times. A third $\pi/2$-pulse further rotates the arrows and the population projects back to $|\downarrow\rangle$ will be measured. A phase shift ϕ can be introduced in the third MW pulse to change the rotation angle to $\hat{n}$ other than $\hat{y}$ axis. 139

10.6 A schematics of the MACE calculation. Solving an ensemble of N molecules are broken down to solving N independent clusters of size n. A cluster is constructed with a central molecule and its $n-1$ neighbors with the most interaction strengths. The dynamics of the central molecule of each cluster are picked and added up for the ensemble dynamics. 141

10.7 Convergence of the MACE calculation. (A) The cluster size n is tuned with molecule number $N = 1000$. (B) N is tuned with $n = 5$. Other conditions are, $|\downarrow\rangle = |0, 0\rangle$, $|\uparrow\rangle = |1, 0\rangle$, lattice constant = 0.532 nm, uniform lattice filling = 2.8%, molecular mass = 127 a.u., permanent dipole = 0.57 D, quantization axis direction = (1,1,0). Apart from some detailed differences, the MACE calculation converges well with $n \sim 5$ and $N \sim 1000$ and gives very reliable calculation result semi-quantitatively. . 143

10.8 MACE calculation of the coherence evolution and its Fourier transform. (A) The evolution in Ref. [1] is reproduced up to 500 ms with a time interval of 0.1 ms. Only the dynamics of the first 100 ms is shown. (B) The discrete Fourier transform of the calculated coherence evolution. Peaks appear at 56 Hz, 78 Hz and 114 Hz with a relative ratio about $1 : \sqrt{2} : 2$, indicating the underlying DDI between the weak and the strong neighbors. 144

10.9 Simulating the coherence decay for a bulk sample of NaRb molecules. (A) A realization of 4000 molecules distribution under the typical experimental condition of 700 nK, (200,190,30) Hz trap frequencies and the quantization axis on the vertical direction. (B) An example coherence decay of the bulk sample with the first-order exponential fitting in red curve. (C) The density dependence of the coherence decay rate. The decay rate is extracted from the time when the coherence decays down to 37%. The decay rate shows linear dependency on the peak density with a slope of $0.024(1)\times10^{-10}$ cm^3/ms. The red points are for $|\uparrow\rangle = |1,1\rangle$ with the density rescaled to 0.55 times. The scaled red points fall on the same line with the black points. 145

10.10 Measure the coherence with the spin echo method. The two first pulses of the spin echo method are in phase and the phase of the third pulse is tuned with a shift of ϕ. The molecule population in the $|\downarrow\rangle$ state are measured after the three-pulse sequence. The data are fit with the sinusoidal function with the period fixed to 360°. The contrast of the curve $(N_{max} - N_{min})/(N_{max} + N_{min})$ reflects the coherence of the system. With the longer evolution time, the blue data show less coherence than the red data. 147

10.11 The coherence decay of the NaRb bulk sample. The contrast is measured under different total evolution time T by tuning the interval length between the pulses. The red points represent the case with $|\uparrow\rangle = |1, 1\rangle$ and the black points represent the case with $|\uparrow\rangle = |1, 0\rangle$. The contrast decay are fitted with the first-order exponential decay with a fixed unity contrast at zero evolution time. The decay rates appear to be similar for the two cases. 148

10.12 The density dependence of the coherence decay rate. The red points represent the case with $|\uparrow\rangle = |1, 1\rangle$ and the black points represent the case with $|\uparrow\rangle = |1, 0\rangle$. The peak density ranges from 3×10^{10} cm^{-3} to 29×10^{10} cm^{-3}. The coherence decay rate of the two states are similar, depends approximately linearly on the sample density. A linear fit to all eight data points gives a slope of $0.037(2)\times10^{-10}$ cm^3/ms. The MACE calculation for the $|1, 0\rangle$ case is shown in blue triangles which gives a slope of $0.024(1)\times10^{-10}$ cm^3/ms. 150

11.1 The plug trap potentials for Na and Rb atoms generated by a 532 nm laser with a beam waist of 35 μm and a power of 1 W. The B-field gradient is 62 G/cm. The potentials shown are along the vertical direction. 155

11.2 The lifetime determined by Majorana loss for Na and Rb, with or without the plug potential. The plug potential is as shown in Fig. 11.1. Without the plug potential, the lifetime drops monotonically as the temperature drops and the lifetime is too short for efficient evaporative cooling under 5 μK. With the plug potential, the lifetime rises again on the low temperature side and gives a minimum lifetime longer than 100 s. The low loss rates promise efficient evaporative cooling. 156

11.3 The trajectories of MW evaporative cooling with or without the plug. Without the plug (black), the efficiency of cooling gradually decreases as the majorana loss becomes severe with lower temperatures. There is no PSD gain anymore from cooling stages below N = 10^7. With the plug (red), the cooling efficiency maintains the same throughout the stages. The overall efficiency is $\Delta \log(\text{PSD})/\Delta \log(N)$ = -2.9. The comparison of the two trajectories shows the effectiveness of the plug. The plug beam used here has a power of 1.55 W and a beam waist of 35 μm. 158

11.4 The trajectories of MW evaporative cooling of a Na and Rb mixture gas in the plug trap. The Na atoms (red) are sympathetically cooled by Rb atoms (black). The high plug potential for Na atoms prevent any loss of Na atoms during the cooling. The largest PSD achieved is one and two orders away from the quantum degeneracy for Na and Rb respectively. The sympathetic cooling becomes inefficient when the Rb atom number is comparable with the Na. The plug beam used here has a power of 1.55 W and a beam waist of 35 μm. 159

11.5 Optical layouts for optical lattice and ODT. (A) The layout of the optics for the optical lattice on the optical table before the fibers. (B) The layout of the optics for the ODT on the optical table before the fibers. (C) The layout of the optics for the horizontal optical lattice and the ODT after the fibers. (D) The layout of the optics for the vertical optical lattice after the fibers. 161

11.6 Schematic setup of Gaussian beam propagation for optical lattice. (A) shows the horizontal beam shaping and (B) shows the vertical beam shaping. 163

11.7 Schematic setup of Gaussian beam propagation for ODT. (A) shows the horizontal beam shaping and (B) shows the vertical beam shaping. 164

11.8 RIN of optical lattice beam. The RIN of the Nufern amplifier working at current = 23 A in a open-loop configuration (red) and in a closed-loop configuration (blue) and the thermal background noise (grey) are shown. The RIN the about on the lower frequency side is suppressed by the servo. The average RIN is about -100 dBc/Hz. 167

11.9 Band structure of a cubic lattice in one dimension given by solutions to the Mathieu's differential equation. The lowest seven bands of different lattice depths are shown: (A) $V_0 = 1E_r$, (B) $V_0 = 10E_r$, (C) $V_0 = 20E_r$, (D) $V_0 = 40E_r$. 170

11.10 Kapitza-Dirac scattering of Rb atoms in 1D lattice. (A) The diffraction pattern with different evolution times. (B) Extracted population fraction evolutions from the experimental data and the theoretical fittings. The fitted lattice depth is 7.6 μK 173

11.11 Visualize phase correlation among 1D lattice sits. (A) Interference pattern of the BEC after TOF from the vertical optical lattice of different depths. (B) Visibility decay of interference pattern. the visibility is defined by Eq. 11.25. The lattice depth is obtained according to the calibration from the Kapitza-Dirac scattering measurement in Fig. 11.10. 175

11.12 Scheme of producing a lattice gas of ultracold NaRb polar molecules (A) Double first-lobe Mott insulator of degenerate gas of Na and Rb atoms. (B) One Feshbach molecule per lattice site after magnetoassociation (C) One ground-state molecule per lattice site after STIRAP. 177

List of Tables

6.1 The binding energies of ground-state dimers and trimers of Na and Rb system 64

8.1 Coupling constants of molecular Hamiltonian for ground vibrational state NaRb molecule 103

9.1 Van der Waals interaction in atom-molecule collision and loss rate constant from the universal model. 121

Chapter 1

Introduction

Atomic, molecular and optical (AMO) physics experiments provide a clean environment for studies of quantum systems with precise quantum controls. Since the development in the cooling of alkaline atoms in the last two decades of the 20th century and the great milestone of the realization of the long-predicted Bose-Einstein condensation (BEC)[2, 3], experiments with ultracold ensembles of atoms have enjoyed great success in research fields such as precision measurement, many-body physics, few-body physics and quantum optics. On the other hand, the production of ultracold ensembles of molecules is difficult compared with atoms mainly due to their complex internal structures. Difficult as it is, however, the production of ultracold molecules has drawn more and more interests because of the new application potentials that are also given by their complexity.

There are essentially two routes to pursue the ultracold molecules. One way is to directly cool the molecules via cooling techniques such as buffer gas cooling[4], Stark deceleration[5, 6] and laser cooling[7, 8, 9]. Another way is to assemble molecules from an ultracold mixture of atoms. So far, the second way is more successful and has yielded ultracold polar molecules

(UPM) of KRb[10], RbCs[11, 12], NaK[13], NaRb[14], LiNa[15]. Upon the production of UPMs, researches in the uncharted fields such as collisional properties[16, 17, 18, 19], coherence properties[20, 21, 22] and many-body dynamics[23] of UPMs are followed immediately. In this thesis, we focus on the studies of collisional properties of ultracold NaRb polar molecules.

1.1 Ultracold polar molecule: dipole-dipole interaction (DDI)

UPM is now an exciting research direction for experiments. This is mainly due to the electric dipole-dipole interaction (DDI) offered by the permanent electric dipoles of UPMs. The DDI goes the following way,

$$V_{dd} \propto \frac{1}{r^3}\Big[\vec{d_1}\cdot\vec{d_2} - \frac{3(\vec{d_1}\cdot\vec{r})(\vec{d_2}\cdot\vec{r})}{r^2}\Big], \tag{1.1}$$

where $\vec{r}$ is the separation of the two dipoles, $\vec{d_1}$ and $\vec{d_2}$.

The electric DDI has essentially the following four important attributes.

First, the interaction is long-range. By long-range, we mean comparing it with the van der Waals interaction which commonly exists between neutral particles. The van der Waals interaction, originating between an instantaneous dipole and another dipole that induced by it, is short-range and decays fast with $1/r^6$. In many cases, the van der Waals interaction can be effectively described by a delta-function pseudo-potential with matched scattering length. An important consequence is that if simulating spin models with neutral atoms loaded in optical lattices, one can only obtain effective spin-spin interaction between nearest neighbors mediated from tunneling[24, 25]. On the contrary, the DDI can go beyond nearest neighbors, offering long-range interaction in a lattice system.

Second, the interaction is quite strong. The electric DDI is usually more intense than its magnetic counterpart. Typical electric dipole a UPM possesses is of order of 1 Debye, while the magnetic dipole moment that a magnetic atom, like Dy and Er, possesses is several Bohr magnetons. Under similar density conditions, the electric DDI energy is usually two orders above the magnetic one.

Third, the DDI is anisotropic. From Eq. 1.1, we see that the strength and the sign of the interaction depends strongly on the orientations of the two dipoles. For example, as shown in Fig. 1.1, in a parallel configuration, the interaction is repulsive while the head-to-tail configuration is attractive. As a result of the angular dependency, a physical system with DDI has much richer quantum phases.

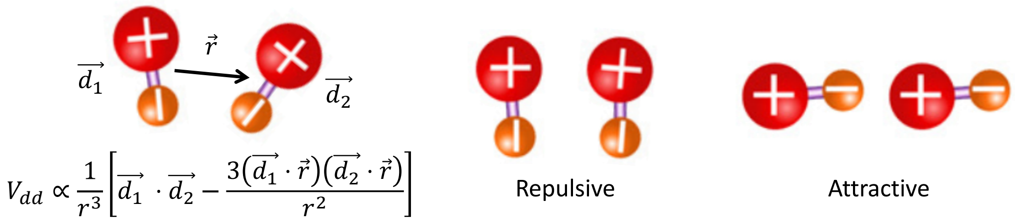
$\vec{d_1}$
$\vec{r}$
$\vec{d_2}$
$V_{dd} \propto \frac{1}{r^3}\left[\vec{d_1} \cdot \vec{d_2} - \frac{3(\vec{d_1}\cdot\vec{r})(\vec{d_2}\cdot\vec{r})}{r^2}\right]$
Repulsive
Attractive

Figure 1.1: The DDI depends on the orientation of the two dipoles. The interaction is positive (repulsive) with a parallel configuration and negative (attractive) with a head-to-tail configuration.

Lastly, the electric dipole-dipole is highly tunable. Through the E-field's direction control and the trapping geometry control, one can align dipoles with different configurations, which in turns controls the interaction of the system, as mentioned above. Also, because the electric dipole is an extrinsic property (contrary to the magnetic dipole which is an intrinsic property of a particle), one can control the magnitude of dipoles by controlling the magnitude of the E-field and obtain a wide range of interaction strengths.

1.2 Ultracold polar molecule: applications

The DDI together with attributes like rich internal structures make the UPMs good candidates for a variety of research directions. I list some of the directions below, but the applications of UPMs are not limited to those directions.

1.2.1 Ultracold chemistry

It has been a long-term challenge to investigate, understand and even control the chemical reactions with a resolution down to a single quantum state. UPMs together with the precise control of all degree of freedom of a UPM including electronic, vibration, rotation, electron and nuclear spin, spatial orientation etc., provide exciting perspectives on the ultracold chemistry[26]. The works with KRb fermionic molecules in the few hundred nK regime [16, 18] set up a paradigm for ultracold chemistry experimental research with UPMs. With techniques to detect reaction products, such as a two-color resonance-enhanced multiphoton ionization, it is promising to observe state-to-state chemical reactions in UPM system. Such reactions are already observed with atoms and non-polar molecules[27, 28]. With optical tweezers, building one molecule from two individual atoms in a bottom-up fashion is recently realized[29].

1.2.2 Quantum simulation

Simulating quantum mechanics is a very challenging problem because of the large amount of computer memory needed to store the quantum state of a large physical system. The number of parameters grows exponentially with the system size[30]. One way to circumvent this difficulty is to map the problem, i.e. the quantum state and the Hamiltonian, to another physical system which is more controllable and easier to conduct measurements.

UPMs in optical lattice is considered a great platform for simulating large physical systems. Such a system combines the advantages of optical lattice, such as the flawless nature, controllable defect and geometry, and the advantages of UPMs, such as DDI, long lifetime (compared with Rydberg atoms) and the controllability via external dc and ac fields.

There are now a large number of proposals dedicated to the Hamiltonian engineering of UPM in optical lattices[31, 32, 33, 34, 35, 36, 37, 38]. The proposals show the possibilities of simulating and understanding the behaviors of quantum magnetism, high-T_c superconductivity and other novel quantum phases. On the experimental side, JILA Jin and Ye's group make the initial exploration of the behaviour of many-body spin models with direct, long-range spin interactions and lays the groundwork for future studies of many-body dynamics in spin lattices[23].

1.2.3 Quantum computation

Since its inception in 1982 by Feynman[39], the idea of a universal quantum computer has been pursued in many fields of physics. The UPMs are considered as potential candidates for the physical implementation of quantum computation for their potentials on both scalability and fidelity. UPM realization of logic gates such as Hadamard gate, CNOT gate and iSWAP gate are proposed and are considered of high-fidelity based on simulations[40, 41, 42, 43, 44, 45].

1.2.4 Precision measurements

The UPMs is an ideal system for high-resolution spectroscopy and hence precision tests of fundamental laws of nature[46]. Measurements of physical constants are usually cast to measurements of the energy shift between two sublevels in a cold polar molecule. For instance, OH molecules allow a high sensitivity measurement of the fine structure constant variation[47]. The huge internal electric fields of heavy polar molecules[48, 49] offer a great sensitivity to the permanent electric dipole moment of an electron and help to test the violation of discrete symmetries[50].

1.3 Thesis outline

This thesis mainly focuses on the investigation of the collisional properties of the ultracold NaRb polar molecule. To realize the collision experiments, necessary steps will be included and described also, such as the creation of the ultracold NaRb polar molecule, the internal state manipulation of the ultracold NaRb polar molecule as well as the investigations on the coherence of the ultracold NaRb polar molecule. In addition, recent progress towards the ultracold NaRb polar molecules in the 3D optical lattice will also be covered. The detailed organization of this thesis is as follows.

In chapter 2, the basic theories of quantum scattering and ultracold collisions of molecules are presented.

In chapter 3, the setups of our experimental system are briefly introduced. Meanwhile, the production of ultracold Na and Rb atomic mixture is also introduced.

In chapter 4, the production of the ultracold NaRb molecules in the absolute ground state and the internal-state control are described.

In chapter 5. several technical issues are discussed. These issues, such as the number calibration and the temperature calibration, commonly exist and matter the accuracy of loss rate constant measurements in collision experiments.

In chapter 6, the study of ultracold collisions of NaRb molecules with controlled chemical reactivities is presented in detail. We observe similar loss behavior for molecules with or without available reaction channels, and our result semi-quantitatively agrees with the loss model based on transition complex formation.

In chapter 7, the study of dipolar collisions of NaRb molecules in the exposure of an external dc E-field is presented. The existence of E-field modifies the collision properties between molecules and the loss rate constant shows a step-wise enhancement as the E-field strength increases.

In chapter 8, the study of ultracold collisions of molecular mixture is presented, the collisional properties of molecular mixture shows obvious dependence on the state-dependent DDI.

In chapter 9, the collisions of ground-state NaRb molecules with atoms are presented.

In chapter 10, the investigations on the coherence properties of NaRb molecules in a bulk sample is presented.

In chapter 11, the most recent progress of the 3D optical lattice in our lab is presented.

Finally, the conclusions are given in chapter 12.

□ End of Chapter.

Chapter 2

Theoretical backgrounds

2.1 Quantum scattering theory

Collisional study is a primary way to understand the structure and the interaction between particles; for example, much of today's knowledge on chemical reaction dynamics can be attributed to pioneering studies on elementary reaction processes with crossed molecular beam experiments[51]. To understand the underlying physics of a collision experiment, quantum scattering theory is introduced. Not only in the studies of ultracold atoms and molecules, quantum scattering theory is also an important tool in a variety areas of research. The most well-known example should be Rutherford's discovery of the nucleus.

According to the result of the collisions, they can be roughly divided into three groups: elastic, with the outgoing state the same as the incoming state; inelastic, with the outgoing state different with the incoming state while the particle species unchanged; and reactive, the particle species changed after collision. The last two kinds of collisions are usually accompanied by additional kinetic energy transferred from internal degree of freedoms.

2.1.1 Basics

The simplest case considers the elastic collision of a pair of structureless particles with isotropic interaction. In such a case, the particle number and the kinetic energy are conserved. Since, the center-of-mass motion is irrelevant to the collision problem, we can drop out the center-of-mass part after the variable separation. Therefore, the problem is reduced to a structureless particle being scattered by an isotropic potential $V(\vec{r})$.

For simplicity, here we consider that the incoming flux is always on and solve a time-independent Schrodinger equation Eq. 2.1 subject to the boundary condition, $\psi(\vec{r}) \sim e^{i\vec{k}\cdot\vec{r}}$ when $\vec{r} \to \infty$. Here, $\vec{k}$ is the momentum of the particle.

$$E\psi(\vec{r}) = \big[-\frac{\hbar}{2m}\nabla^2 + V(\vec{r}) \big] \psi(\vec{r}). \tag{2.1}$$

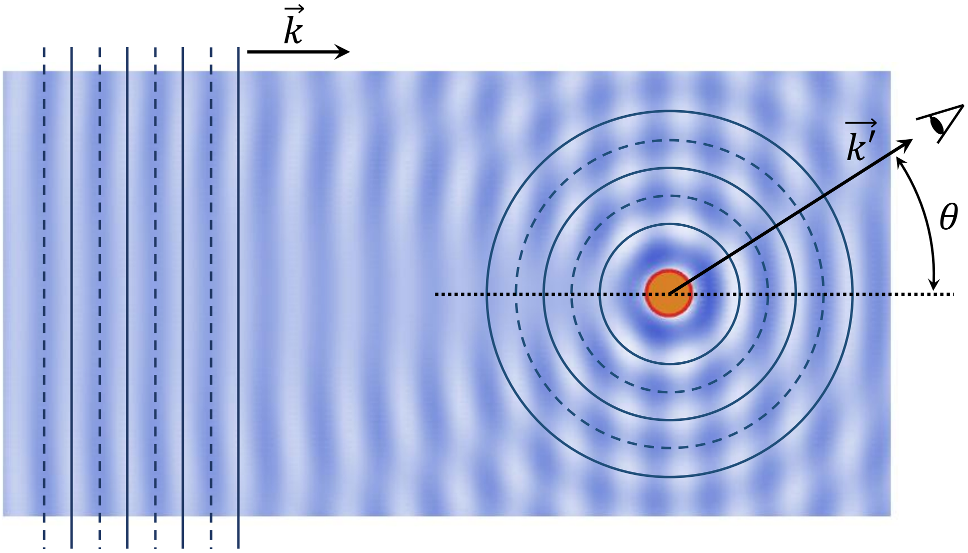

Figure 2.1: An illustration of the quantum scattering. The incoming wave is a plane wave with momentum $\vec{k}$. The orange target scatters the incoming wave, generating outgoing waves with momentum $\vec{k'}$. The outgoing flux is measured at an angle of θ.

As illustrated in Fig. 2.1, the incoming wave is propagating along the $+x$

direction coming from $-\infty$. The interaction potential $V(\vec{r})$ is represented by an orange target. The incoming wave hits on the target and get scattered all around with momentum $\vec{k'}$ and angle θ. For elastic collisions, $k = k'$.

To quantify the scattering process, the differential cross section $\mathrm{d}\sigma/\mathrm{d}\Omega$ is introduced, which is defined as,

$$\frac{\mathrm{d}\sigma}{\mathrm{d}\Omega} = \frac{N}{j_i}. \tag{2.2}$$

The differential cross section describes the number of particles N per unit time received by a detector which has a detection solid angle of $\mathrm{d}\Omega$, given the incoming particle flux j_i. The particle flux j can be obtained from wave function with,

$$\vec{j} = -i\frac{\hbar}{m}(\psi^*\nabla\psi + \psi\nabla\psi^*), \tag{2.3}$$

where m is the particle mass which takes the value of the reduced mass here.

The wave function ψ is naturally divided into two parts,

$$\psi = e^{ikx} + \psi_{sc}(r,\theta). \tag{2.4}$$

Put Eq. 2.4 back to Eq. 2.1, we can find scattered wave ψ_{sc} is purely spherical. Thus, the wave function ψ when $r \to \infty$ can be formally expressed as,

$$\psi \simeq e^{ikx} + f(\theta)\frac{e^{ikr}}{r}, \tag{2.5}$$

where f is called the scattering amplitude. Then, with Eq. 2.2 and 2.3, we establish the relation between the scattering amplitude and the differential cross section,

$$\frac{\mathrm{d}\sigma}{\mathrm{d}\Omega} = |f(\theta)|^2. \tag{2.6}$$

Integrating the differential cross section over all directions, one get the total cross section,

$$\sigma_{tot} = \int \frac{\mathrm{d}\sigma}{\mathrm{d}\Omega}\mathrm{d}\Omega = \int |f(\theta)|^2 \mathrm{d}\Omega. \tag{2.7}$$

2.1.2 Partial wave expansion

The cylindrical symmetry of the system implies us to expand the wave function Eq. 2.5 with the Legendre polynomials $P_l(\cos\theta)$,

$$\psi(\vec{r}) \simeq \frac{i}{2k}\sum_{l=0}^{\infty} i^l(2l+1)\left[\frac{e^{-i(kr-l\pi/2)}}{r} - e^{2i\delta_l(k)}\frac{e^{i(kr-l\pi/2)}}{r}\right]P_l(\cos\theta), \tag{2.8}$$

Or equivalently,

$$f(\theta) = \sum_{l=0}^{\infty}(2l+1)f_l(k)P_l(\cos\theta). \tag{2.9}$$

with

$$f_l(k) = \frac{e^{2i\delta_l(k)}-1}{2ik}. \tag{2.10}$$

Such a decomposition is called the partial wave expansion, with l denoting the index of the partial waves. By convention, we name $l = 0$, $l = 1$, $l = 2$ ... as s-wave, p-wave, d-wave ... respectively. Under the partial wave expansion, the total cross section becomes,

$$\sigma_{tot} = 4\pi\sum_{l=0}^{\infty}(2l+1)|f_l(k)|^2 = \frac{4\pi}{k^2}\sum_{l=0}^{\infty}(2l+1)\sin^2\delta_l(k). \tag{2.11}$$

Here, the phase shift δ_l is an important quantity in the context of quantum scattering and is closely related to the scattering length and the unitarity limit as we will see later.

2.1.3 Scattering length

For a convenient description of ultracold collisions, the concept of scattering length is introduced. The scattering length a is defined as,

$$a = -\lim_{k \to 0} \frac{1}{k} \tan \delta_0(k). \tag{2.12}$$

The scattering length has the same dimensionality as a length and it describes the effective size of the collisional target in the low-energy limit. This can be shown from the relation between the scattering length and the cross section,

$$\sigma_{tot} = \frac{4\pi}{k^2} \sin^2 \delta_0(k) \overset{k \to 0}{\simeq} \frac{4\pi}{k^2} \frac{(ka)^2}{1 + (ka)^2} \simeq 4\pi a^2. \tag{2.13}$$

2.1.4 Unitarity limit

In Eq. 2.11, because the phase shift appears in sinusoidal functions, there exists a maximum cross section for each partial wave. This maximum value is called the unitarity limit because it is obtained when the sinusoidal function takes the unity value. The scattering rates in all situations will be bounded by this limit. The unitarity discussed above defines the maximum cross section for a pair of particles. However, when we turn to an ensemble where the particles are distributed in a Boltzmann distribution, unitarity limit of the ensemble is obtained via the integration. For identical bosons in low-energy limit when there is only s-wave scattering, the maximum scattering rate constant is[52],

$$\beta_{s-limit} = \frac{4\pi\hbar}{m} \langle 1/k \rangle_T, \tag{2.14}$$

where $\langle 1/k \rangle$ is the thermal average of $1/k$ and is calculated by,

$$\langle 1/k \rangle_T = \int_0^\infty 4\pi v^2 (\frac{m}{4\pi k_B T})^{3/2} \exp\left(-\frac{mv^2}{4k_B T}\right) \times \frac{2\hbar}{mv} \mathrm{d}v, \tag{2.15}$$

where m is the mass of the molecule.

2.1.5 Wigner threshold law

The scattering of particles at ultralow energies exhibits a series of universal behaviors. Those universal behaviors follows the so-called Wigner threshold law[53, 54], which contains a set of relations between the cross-section (or rate constant) and the collision energy. Here I list those relations without proof[55, 56, 57, 58].

Given the interaction potential $V(r) = \pm C_s/r^s$, with $s > 2$. For partial waves $l < (s-3)/2$, the threshold behavior of elastic collisions is given by,

$$\begin{aligned} \sigma_l^{el} &\propto k^{4l} \propto E_c^{2l} \\ \beta_l^{el} &\propto k^{4l+1} \propto E_c^{2l+1/2}. \end{aligned} \tag{2.16}$$

For partial waves $l > (s-3)/2$, the threshold behavior of elastic collision is given by,

$$\begin{aligned} \sigma_l^{el} &\propto k^{2s-6} \propto E_c^{s-3} \\ \beta_l^{el} &\propto k^{2s-5} \propto E_c^{s-5/2} \end{aligned} \tag{2.17}$$

For the description of partial waves $l = (s-3)/2$, the contribution from the above two relations should be taken.

For inelastic or reactive collisions, the behavior is given by,

$$\begin{aligned} \sigma_l^{in/re} &\propto k^{2l-1} \propto E_c^{l-1/2} \\ \beta_l^{in/re} &\propto k^{2l} \propto E_c^{l} \end{aligned} \tag{2.18}$$

2.2 Ultracold collisions of molecules

2.2.1 Scattering in highly resonant regime

A molecule has a larger number of degree of freedom than an atom, such as the vibration and the rotational degree of freedom. Therefore, considering the collision of a pair of molecules, the number of collisional channels is exponentially larger. For UPMs, the van der Waals interaction coefficient C_6 is generally large. For ground-state NaRb molecules, C_6 reaches the order of 10^6 atomic unit(a.u.)[59, 60, 61] and results in deep inter-molecular potentials. Four-body bound states are supported in the inter-molecular potentials. Therefore, as depicted in Fig. 2.2, due to the large number of possible channels and the depth of each channel, there is a high density of four-body bound states at the short range at the level of collisional threshold. The density of four-body bound states can be estimated with the method described in Ref. [62]. For NaRb case, the density of states is at least 10^3 per μK. Since, the typical temperature of our molecular sample is of order 100 nK, it is impossible to resolve the resonances in the experiment. The existence of the four-body bound state allows a pair of molecules to form one big molecule during the process of the collision, therefore, we say the molecules are scattering in a highly resonant regime. Under the poor energy resolution assumption, one can analytically obtain the bound-state formation rate constant in the Wigner regime[62],

$$\beta_{mm}^{(l,m_l)} = \Delta \frac{2^{-3l+2}\pi^{5/2} R_{\mathrm{vdW}}^{2l+1}}{\Gamma(l/2+1/4)^2\Gamma(l+3/2)} \frac{m_r^{l-1}}{\hbar^{2l-1}} (k_B T)^l, \tag{2.19}$$

where van der Waals length $R_{\mathrm{vdW}} = (2m_r C_6/\hbar)^{1/4}$, m_r is the reduced mass, $\Gamma(\cdot)$ is the Gamma function and $\Delta = 2$ for indistinguishable particles and equals to 1 otherwise. Interestingly, Eq. 2.19 gives the same result as the rate constant for bimolecular reactions within the framework of the universal model[63, 64, 65].

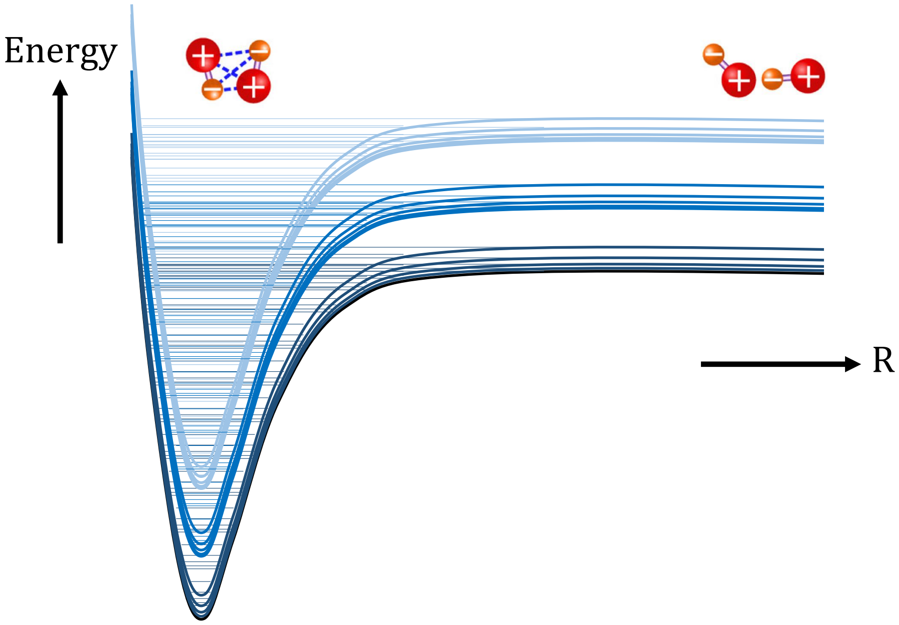

Figure 2.2: Origin of high density of four-body bound states. The number of collision channels is large due to the rich internal structures of a molecule. Channels in different colors corresponds to different vibrational quantum numbers. Within each bunch of states of the same color, the splitting is due to rotational structures and hyperfine structures. Each potential curve is deep due to the large C_6 between a pair of UPMs. Molecular collisions take place in a highly resonant regime with the large density of four-body bound states at the short range.

2.2.2 Universal model for bimolecular reaction

For heteronuclear molecules, there is a possibility of having a bimolecular chemical reaction,

$$\mathrm{AB} + \mathrm{AB} \rightarrow \mathrm{A}_2 + \mathrm{B}_2. \tag{2.20}$$

To get the reaction rate, one need to solve the quantum scattering problem. However, in a real calculation of a bimolecular chemical reaction, the potential energy surface (PES) at the short range is difficult to accurately model. The universal model for bimolecular reaction is a simplified model that introduces a boundary between the short range and the long range with a unity absorption coefficient. It assumes that the "bad" things will always happen at the short range when the chemical reaction is energetically allowed. So, whenever the wave function touches this boundary, its amplitude becomes zero. The introduction of the absorptive boundary masks out the complicated short range physics that is hard to tackle with. Mathematically, the model can be analytically solved in the framework of generalized multichannel quantum defect theory[66, 67], or numerically solved with close-coupling calculation[68, 69, 70, 71].

2.2.3 Coupled equations

Before we get to the close-coupling calculation, we first derive the coupled equations from the Schrodinger equation.

For a given partial wave l, m_l, the Schrodinger equation is,

$$H\psi_{\alpha l m_l}^{E_{tot}} = E_{tot}\psi_{\alpha l m_l}^{E_{tot}}, \tag{2.21}$$

where

$$\psi_{\alpha l m_l}^{E_{tot}}(\vec{\rho}_1, \vec{\rho}_2, \vec{r}) = \sum_{\alpha'}\sum_{l'=0}^{\infty}\sum_{m_l'=-l'}^{l'} \frac{f_{\alpha' l' m_l', \alpha l m_l}(r)}{r} Y_{l'}^{m_l'}(\hat{r})\phi_{\alpha'}(\vec{\rho}_1, \vec{\rho}_2). \tag{2.22}$$

Here, the quantum number $(\alpha l m_l)$ and $(\alpha' l' m_l')$ defines the incoming and outgoing channels. ρ_1 and ρ_2 stand for the internal coordinates of the two molecules and r stands for the separation. The functions $f_{\alpha' l' m_l', \alpha l m_l}$ describes the strength of the transition from the $(\alpha l m_l)$ state to the $(\alpha' l' m_l')$ state.

Here, we use the uncoupled representation of the wave function[72, 73] and only the channels asymptotically lay below the total energy E_{tot} are included in this problem.

The Schrodinger equations thus gives a series of coupled equations of $f_{\alpha' l' m_l', \alpha l m_l}$. One can arrange $f_{\alpha' l' m_l', \alpha l m_l}$ in a matrix $\mathbf{F}$, with $F_{i',i} = f_{i',i}^{E_{tot}}(r)$, where i' and i are the row and the column index of the matrix, and the index i one-to-one maps to the quantum number $(\alpha l m_l)$. The coupled equations can then be expressed in a compact matrix form[68, 69, 70],

$$(\mathbf{D}^2 + \mathbf{W})\mathbf{F} = \mathbf{0}, \tag{2.23}$$

where

$$\mathbf{D}^2 = \mathbf{I}\frac{d^2}{dr^2}, \tag{2.24}$$

$$W_{i',i} = -\frac{2m_r}{\hbar^2}[U_{i',i}^{cent}(r) + U_{i',i}^{int}(r) + (\epsilon_{\alpha'} - E_{tot})\delta_{i',i}]. \tag{2.25}$$

Here, m_r is the reduced mass, $\epsilon_{\alpha'}$ is the asymptotic energy of channel α', $U_{i',i}^{cent}$(r) is the centrifugal barrier introduced by partial waves,

$$U_{i',i}^{cent}(r) = \frac{\hbar^2 l'(l'+1)}{2m_r r^2}\delta_{i',i}. \tag{2.26}$$

$U_{i',i}^{int}$(r) is the inter-molecular interaction and can be generally described by an electrostatic multipole-multipole expansion[74]. Because the DDI dominates for UPMs, given rotational quantum numbers (J,m_J), the inter-molecular interaction is expressed as,

$$\begin{aligned}
&\langle J_1, m_{J_1}, J_2, m_{J_2}, l, m_l | \, U^{int} \, | J_1', m_{J_1}', J_2', m_{J_2}', l', m_l' \rangle = \\
&-\sqrt{30}\frac{d^2}{4\pi\epsilon_0 r^3} \sum_{m_{\lambda_1}, m_{\lambda_2}} (-1)^{m_{J_1}+m_{J_2}+m_l} \begin{pmatrix} 1 & 1 & 2 \\ m_{\lambda_1} & m_{\lambda_2} & -(m_{\lambda_1}+m_{\lambda_2}) \end{pmatrix} \\
&\times\sqrt{(2J_1+1)(2J_1'+1)} \begin{pmatrix} J_1 & 1 & J_1' \\ 0 & 0 & 0 \end{pmatrix} \begin{pmatrix} J_1 & 1 & J_1' \\ -m_{J_1} & m_{\lambda_1} & m_{J_1}' \end{pmatrix} \\
&\times\sqrt{(2J_2+1)(2J_2'+1)} \begin{pmatrix} J_2 & 1 & J_2' \\ 0 & 0 & 0 \end{pmatrix} \begin{pmatrix} J_2 & 1 & J_2' \\ -m_{J_2} & m_{\lambda_2} & m_{J_2}' \end{pmatrix} \\
&\times\sqrt{(2l+1)(2l'+1)} \begin{pmatrix} l & 2 & l' \\ 0 & 0 & 0 \end{pmatrix} \begin{pmatrix} l & 2 & l' \\ -m_l & -(m_{\lambda_1}+m_{\lambda_2}) & m_l' \end{pmatrix}
\end{aligned} \tag{2.27}$$

where d is the permanent dipole of the molecule and $\begin{pmatrix} \cdots \\ \cdots \end{pmatrix}$ is the Wigner 3j symbol which doesn't vanish unless the first-row elements fulfill the triangle inequality and the second-row elements sum up to zero.

2.2.4 Close-coupling calculation

For the convenience of close-coupling calculation, the log-derivative of the matrix **F**(r) is usually calculated, instead of **F**(r) itself. The log-derivative matrix **Z**(r) is defined as,

$$\mathbf{Z}(r) = \left[\frac{d}{dr}\mathbf{F}(r)\right]\left[\mathbf{F}(r)\right]^{-1} \tag{2.28}$$

In a close-coupling quantum calculation, the range of the radial coordinate r is divided into small sectors with width Δr from $r_{min} \simeq 0$ to $r_{max} \simeq \infty$. The log-derivative matrix **Z** are propagated according to the coupled equations sector by sector starting from r_{min}. If unity loss condition is assumed at the short range boundary, the boundary condition of $\mathbf{Z}$ is[75],

$$Z_{i,i}(r_{min}) = -i\sqrt{W_{i,i}(r = r_{min})}. \tag{2.29}$$

The generalized boundary condition of $\mathbf{Z}$ for non-unity loss can be found in Ref. [75]. Once the $\mathbf{Z}$ matrix is calculated, one can find the scattering matrix $\mathbf{S}$ via its relation to the $\mathbf{Z}$ matrix[71]. Finally we find the cross sections starting in a certain entrance channel i from the facts that,

$$\begin{aligned} \sigma^{el} &\propto |S_{i,i}|^2 \\ \sigma^{in} &\propto \sum_{i',i'\neq i} |S_{i',i}|^2 \\ \sigma^{re} &\propto 1 - \sum_{i'} |S_{i',i}|^2, \end{aligned} \tag{2.30}$$

where el, in and re stands for elastic, inelastic and reactive respectively.

□ End of Chapter.

Chapter 3

Experimental setups

This chapter briefly introduces the experimental apparatus and meanwhile the production of an ultracold atomic Na and Rb mixture. An ultracold mixture is the starting point of all molecule experiments mentioned in this thesis. For more details about the experimental apparatus, see Ref. [76] and [77].

3.1 Overview

Our experimental system adopts a two-chamber design. Each chamber is a glass cell. Considering the wide range of laser wavelengths we will use, the cells are without any particular anti-reflection coating. We name the two glass cells as the MOT (magneto-optical trap) cell and the science cell. The dimensions of the MOT cell is 100 mm × 40 mm × 40 mm. The sources of Na and Rb atoms are commercial dispensers (Alvatec) installed inside the MOT cell and are activated by applying electric current though them. The dimensions of the science cell is 100 mm × 20 mm × 20 mm. The smaller size of the science cell help to obtain stronger dc B-field or E-field with available current and voltage in our experiments. The centers of the cells separate by about half a meter. The holders (G11 Glass Epoxy Composite Laminate Material - Polymer Plastics) of the MOT coils are mounted on a motored translational stage (Parker). The atoms are mechanically transported between cells by utilizing the translational stage. On the science cell side, there is another pair of large coils installed in fixed coil holders. The atoms or the molecules in the science cell can be manipulated with a variety of external fields. Standard absorption imaging are provided on the two directions of the horizontal plane for both Rb and Na atoms.

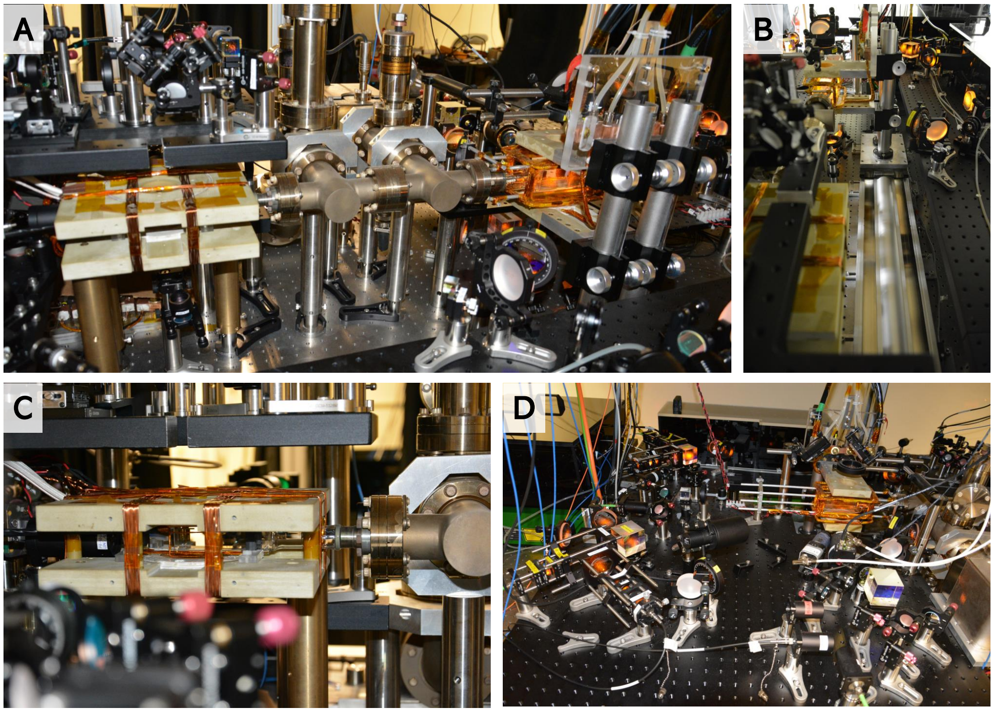

Figure 3.1: The experimemtal system. (A) An overview of the system. (B) The translation stage for magnetic transport of atoms. (C) Science cell and coils. (D) MOT cell and MOT optics.

Photos of the experimental apparatus are shown in Fig 3.1. (A) shows an overview of the whole system. The MOT cell and the science cell locate on the right-hand side and the left-hand side respectively. (B) shows the translational stage and the coil holders mounted upon it. (C) gives a closer look at the science cell. The shim coils are winded outside the coil holders. Near the cell, we can see the large coil sealed in white epoxy and several square-shaped antennas. There is also a pair of ITO (Indium-Tin-Oxide) coated glass plates for dc E-field generation, which can hardly be seen in this figure, locating at the top/down sides of the cell. (D) shows the MOT cell and the MOT optics surround it.

3.2 Vacuum

The two-chamber design help to circumvent the contradictory demands on background vapor pressure at MOT stage (high pressure) and the evporative cooling stage (low pressure). A differential tube between the two cells maintains the pressure difference between the two cells. From the ion pump gauges, the vacuum in the MOT cell is lower than 3×10^{-10} Torr. The reading for the science cell is 1×10^{-11} Torr, which is the lowest reading the gauge can give. The actual vacuum of the science cell should be better than this. The pressure difference manifests as different magnetic trap lifetimes in the MOT cell and the science cell. In the MOT cell, the lifetime is only 4 s, while the lifetime in the science cell can extend to even more than 3 minutes as shown in Fig. 3.2.

3.3 Stages in MOT cell

The MOT cell is in charge of the stages before the microwave (MW) evaporative cooling. Those include a MOT stage, a CMOT (compressed MOT) stage, a molasses stage and a optical pumping stage. We collect Na atoms and Rb atoms simultaneously in the MOT stage. Light induced atomic desorption

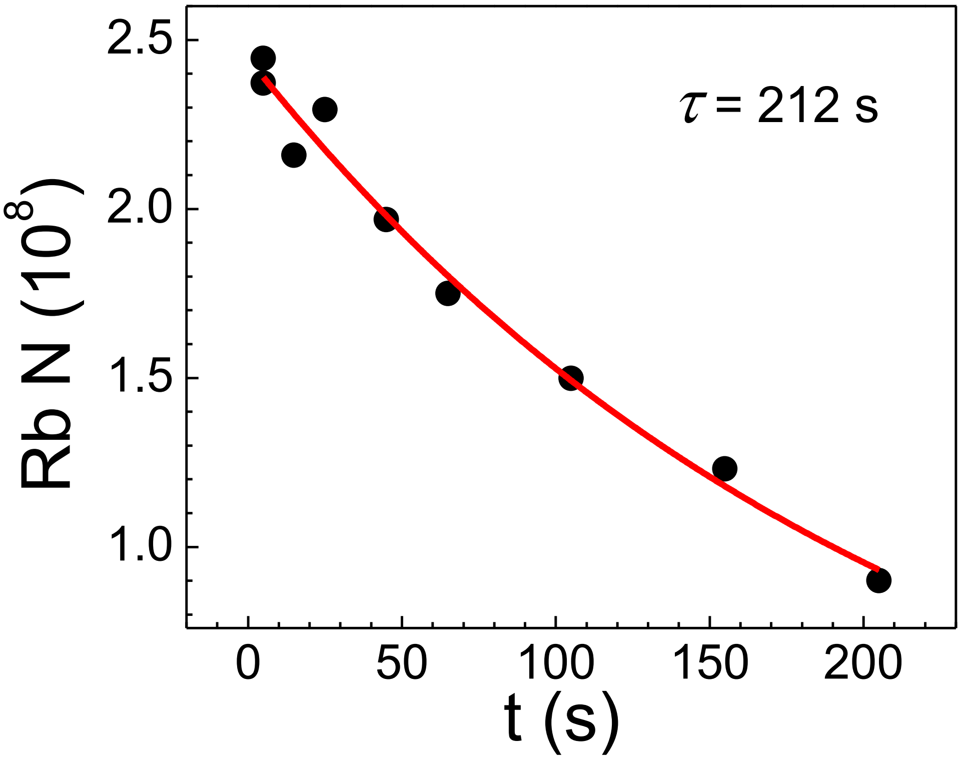

Figure 3.2: Trap lifetime in the science cell. The remaining Rb atom number is measurement with different holding times in the magnetic trap. The first-order exponential decay fitting gives $\tau = 212$ s.

technique is used to enhance the MOT loading with UV LEDs (Thorlabs M375L3). A near-resonance Rb push beam is applied to push the cold Rb atoms away from the cold Na atoms. This mitigates the light-assisted inelastic collisions between Na and Rb and increases the MOT numbers. The MOT loading takes 20 s. Afterwards, the CMOT and the molasses stage further cool the atomic cloud and increase its phase space density (PSD). The optical pumping stage prepares both Na and Rb atoms in Zeeman sublevel $|F, m_F\rangle = |1, -1\rangle$ and the atoms are then loaded into a magnetic trap with a gradient of 147 G/cm on the vertical direction in 300 ms and wait for the transport.

3.4 Magnetic transport

The magnetic transport of the atoms from the MOT cell to the science cell takes about 4 s. The displacement of the transport is 612.06 mm with a maximum velocity of 600 mm/s, a maximum acceleration of 400 mm/s^2, a maximum deceleration of 200 mm/s^2, a jerk of 2000 mm/s^3 and a jerkdecel of 200 mm/s^3. The short trap lifetime in MOT cell kills the atoms while a fast transport excites the atoms. The chosen trajectory is thus a result of the trade-off between the atom number and the temperature of the atomic cloud, and preserves the PSD as much as possible.

Measured from the fluorescence of a pure Rb cloud with MOT recapture method, the recapture after loading into the magnetic trap is 75(3)% and the recapture after a round-trip of magnetic transport is 32(2)%. Therefore, by calculation, the one-way transport efficiency is 49(3)% starting from the MOT stage.

As the atoms arrive in the science cell, the magnetic trap at the science cell side takes over the atoms. The take-over process takes 950 ms by linearly ramping the currents in the two pairs of coils at the same time.

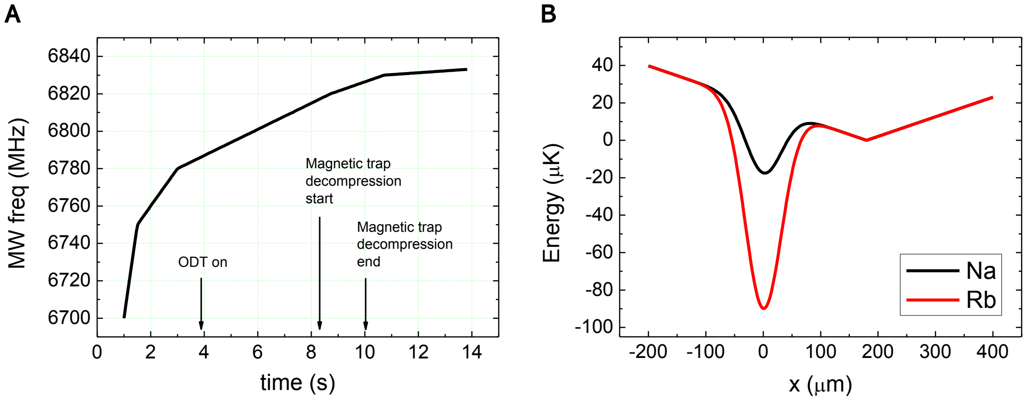

Figure 3.3: MW evaporative cooling in a hybrid trap. (A) Typical MW sweeps for the evaporation. (B) Hybrid trap potential after the magnetic trap decompression for Na (black) and Rb (red).

3.5 MW evaporative cooling in hybrid trap

In the science cell, we perform the MW evaporative cooling of the Rb atoms. The background inter-species scattering length $a_{bg} = 75.91\ a_0$ between Rb $|1, -1\rangle$ state and Na $|1, -1\rangle$ state[78]. Benefiting from this good collisional property, Na atoms can be sympathetically cooled in this stage efficiently.

The initial B-field gradient of the magnetic trap in the science cell is 178 G/cm in the vertical direction. During the MW evaporative cooling from 6820 MHz to 6830 MHz, the magnetic gradient is gradually decompressed down to 62 G/cm. An 1064 nm optical dipole trap (ODT) beam is also turned on to horizontally shift the potential minimum away from the zero B-field point in order to mitigate the Majorana loss and maintain the efficiency of the cooling. The ac-Stark shift introduced by far-detuned lasers can be approximated with the following formula[79],

$$V(\vec{r}) = -\frac{3\pi c^2}{2\omega_0^3}(\frac{\Gamma}{\omega_0 - \omega} + \frac{\Gamma}{\omega_0 + \omega})I(\vec{r}), \tag{3.1}$$

where ω_0 and Γ are the frequency and the line width of the transition respectively, ω_0 and $I(\vec{r})$ are the frequency and the intensity of the optical field respectively. The displacement of the optical potential center from the magnetic potential center is 183 μm. By convention, we call the trap formed of the magnetic potential and the optical potential as a hybrid trap[80]. The typical MW evaporation sequence ending at 6833.1 MHz and the hybrid trap potential after the decompression of the magnetic trap are shown in Fig. 3.3.

3.6 Crossed ODT

There are about 3×10^6 Na atoms and about 3×10^5 Rb atoms left at the end of the MW evaporative cooling. The PSD of the atomic cloud is 1 to

2 orders away from the quantum degeneracy. To further increase the PSD, we load the atoms into a crossed ODT formed of two 1064 nm beams. Since the majority of the atoms already sit at the bottom of the single-beam ODT potential at the end of the MW evaporative cooling in the hybrid trap. The atoms are naturally loaded into the crossed ODT with high efficiency with the second beam turns up and the magnetic trap turns down in 400 ms. The angle of the two beam is about 21°. The resulting geometry is a short cigar shape. We perform further evaporative cooling, which usually takes 2 s, in the crossed ODT by gradually lowering the ODT power. According to Eq. 3.1, the trap depth for Na is about 3 times shallower than that for Rb. Hence, in the crossed ODT, Rb is sympathetically cooled. Because with background inter-species scattering lengths, the Na BEC and Rb BEC are immiscible[81], therefore, a Na BEC with a thermal Rb cloud near quantum degeneracy as shown in Fig. 3.4 is a good starting point for molecule experiments.

3.7 B-field

Quite a number of experiments in our lab that demand a large bias B-field. The large bias B-field is generated by the same pair of coils that generate the magnetic trap in the science cell. The transform from a Helmholtz configuration to an anti-Helmholtz configuration is achieved by an H-bridge, which consists of four relays (LEV200, Tyco Electronics), that can direct the flow of the current in either way.

We calibrate the B-field and measure its stability with Rb atomic transition from the $|F, m_F\rangle = |1, -1\rangle$ state to the $|2, 0\rangle$ state. A MW pulse drives some Rb population to the $|2, 0\rangle$ state and the spin components are separated with a magnetic gradient pulse. We get the resonance frequency from the $|2, 0\rangle$ fraction and obtain the B-field from the frequency. Once we find the resonance frequency, we can set the frequency half way on the slope and repeat the experiment several times. The $|2, 0\rangle$ fraction fluctuation gives a measure of the stability of the B-field. Fig. 3.5 (A) shows an example of such a measurement. The stability of the B-field is 30 ppm. Interestingly, when we plot the red dots with respect to time, we find an oscillation with a period of 10.3 min. This may be due to the working cycle of the chiller or the aliasing of some higher frequency noise.

3.8 LabVIEW control

The time sequence of the experiment is controlled by a LabVIEW program. It is developed based on a simpler program from JILA KRb group. The hardware for the digital outputs is PXI-7811R (Virtex-II 1M Gate FPGA) and the hardware for the analog outputs are PXI-6713 and PXI-6733 from National Instruments. The overall architecture of the experimental control is shown in Fig. 3.6 (A).

The logic of the user interface follows the hierarchy of ”module list → module → command”. The logic of the underlying program is a ”state machine”. Fig. 3.6 (B) and (C) shows the state flow of the state machines. The modular programming style makes it easy to maintain and add on new functions.

The program provides a flexible ”programmable data acquisition” function where one has the access to control almost all degrees of freedom of an experiment and allows the experimental system to operate following programmed instructions.

□ End of Chapter.

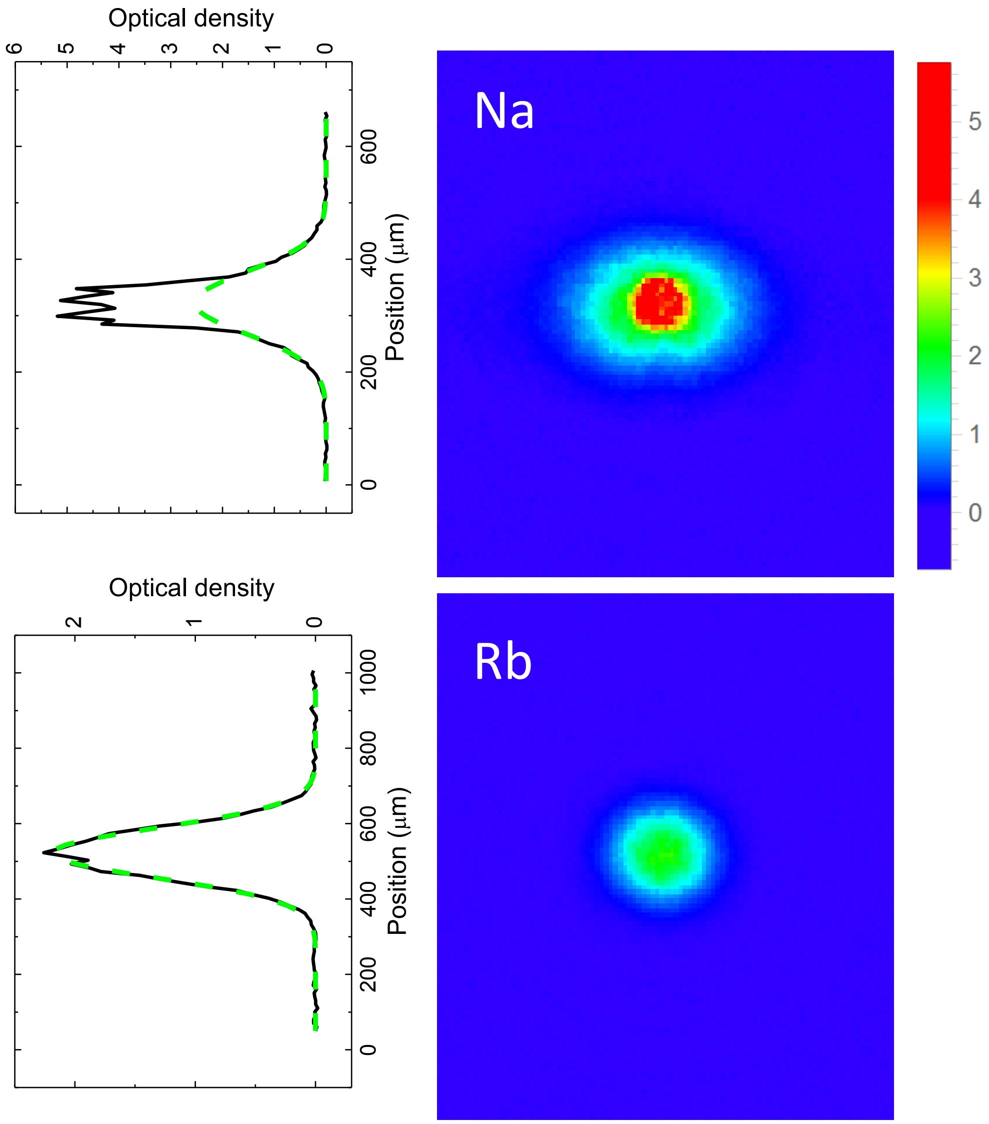

Figure 3.4: The ultracold mixture of Na and Rb atoms. Pictures are taken after a time-of-flight of 5 ms for Na and 10 ms for Rb. On the left-hand side plot the optical density distributions along vertical lines slicing through the centers of the clouds. The Na atoms are partially in BEC state shown clearly by the bimodal distribution. The Rb atoms are thermal gas but close to the quantum degeneracy.

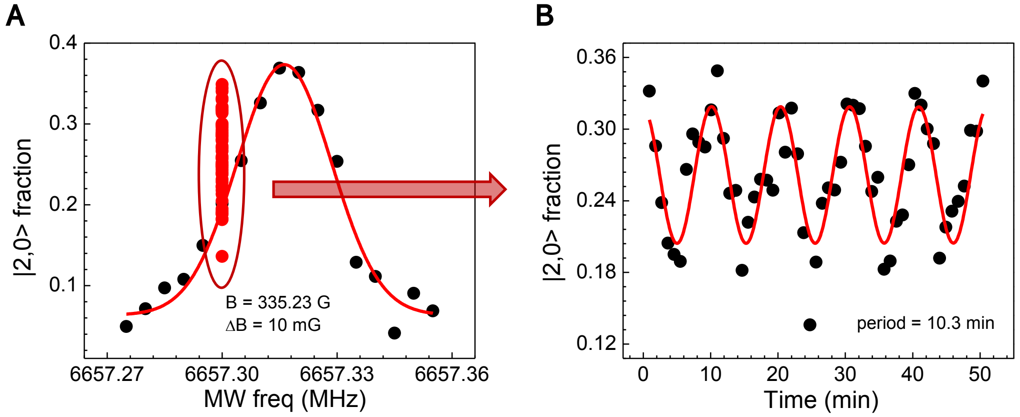

Figure 3.5: Measure the B-field magnitude and the stability. Rb atom transition from the $|F, m_F\rangle = |1, -1\rangle$ state to the $|2, 0\rangle$ state is used. (A) Measured B field = 335.23 G with a standard deviation of 10 mG. (B) Plot the red points with respect to time. The data show an oscillation with a period of 10.3 min.

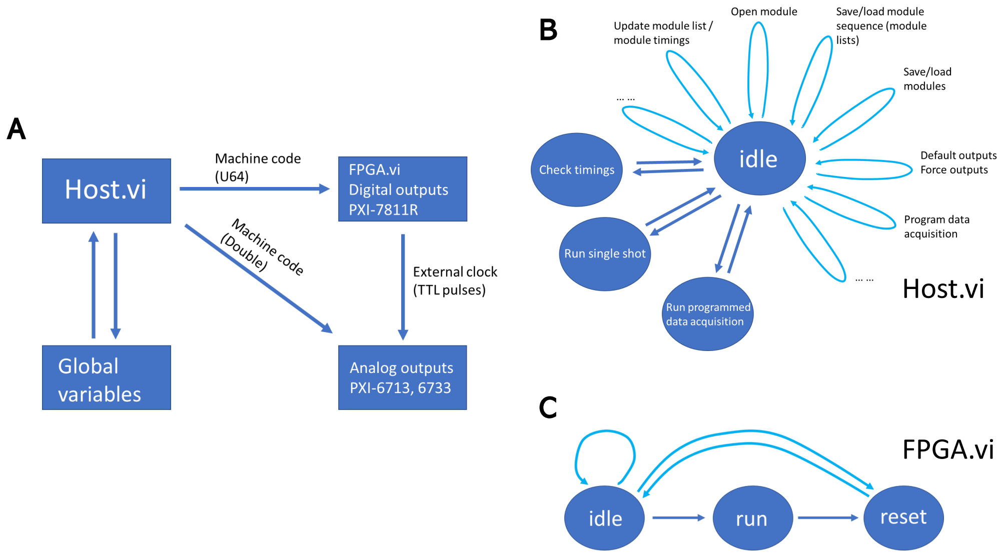
A
Host.vi
Machine code (U64)
FPGA.vi Digital outputs PXI-7811R
Machine code (Double)
External clock (TTL pulses)
Global variables
Analog outputs PXI-6713, 6733
B
Update module list / module timings
Open module
Save/load module sequence (module lists)
Save/load modules
… …
Check timings
idle
Default outputs Force outputs
Program data acquisition
Run single shot
Run programmed data acquisition
… …
Host.vi
C
FPGA.vi
idle
run
reset

Figure 3.6: (A) The overall architecture of the LabVIEW control. (B) The state flow of Host.vi. (C) The state flow of FPGA.vi.

Chapter 4

Production of ground-state NaRb molecule and its internal state control

4.1 Feshbach resonance

The Feshbach resonance is an essential tool to control the interaction between particles in ultracold quantum gases. It has found numerous experimental applications and becomes the key of many great breakthroughs in physics[82].

Because of the difficulties in the direct cooling of molecules, the magnetoassociation of ultracold atoms near Feshbach resonances is so far the most successful scheme for producing ultracold molecules[83] since 2002, when the coherent oscillations between atom pairs and Feshbach molecules was observed for the first time[84].

4.1.1 Basics

The Feshbach resonance can be understood in a simple physical picture. Let us consider a collision problem with two channels as illustrated in Fig. 4.1(A). One of the channels is the ”entrance channel” where a pair of free atoms enter. The other one is the ”closed channel” with its asymptotic energy higher than the collisional threshold. When one of the bound states in the closed channel is energetically close to the collisional threshold, the free atom pair state could couple to the molecular bound state and the Feshbach resonance happens.

Collision channels can have different magnetic dipole moments due to the different coupling schemes of the angular momentums of the collisional partners. Therefore the energy difference between channels can be tuned by an external magnetic field and that leads to the so-called magnetically tuned Feshbach resonances. Because of the coupling, near the Feshbach resonance, the eigenstates become superpositions of the atom pair state and the molecule state and the avoided crossing emerges as depicted in Fig 4.1(B). Adiabatically tuning the B-field across the Feshbach resonance allows the atom pair to follow one of the branches and become a molecule.

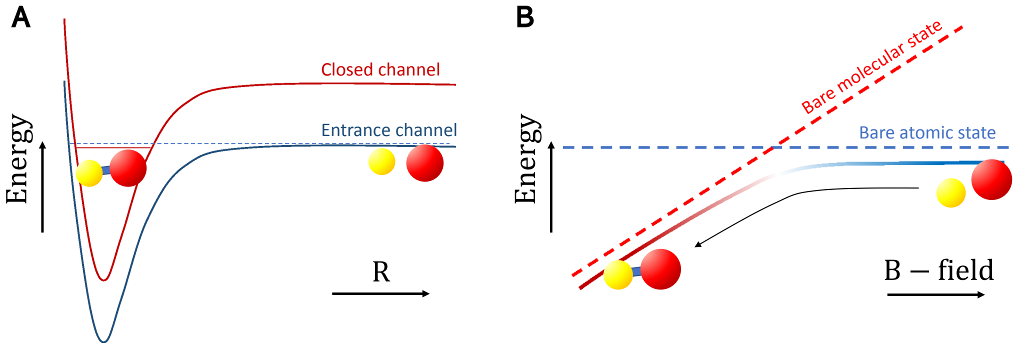

Figure 4.1: Basic two-channel picture of a Feshbach resonance. (A) Feshbach resonance happens when one bound state in the closed channel gets energetically close to the collisional threshold. (B) Avoided crossing of a magnetically tuned Feshbach resonance and adiabatic B-field ramping for molecule association.

4.1.2 Production of NaRb Feshbach molecule

In our previous study, we identified a series of Feshbach resonances between Na and Rb atoms[78]. The resonance that we use in experiment for molecule association is locating at 347.64(3) G with a width of 5.20(27) G between Na $|F, m_F\rangle = |1, 1\rangle$ state and Rb $|1, 1\rangle$ state. The magnetic dipole moment difference $\delta\mu$ between the entrance and the closed channel is 2.66(29) μ_B, where μ_B is the Bohr magneton[85]. The Feshbach resonance have a dominant fraction of the closed channel quantum state $a^3\Sigma^+ |v = 21, J = 1\rangle$. The coupling strength of this resonance is in the intermediate regime with the dimensionless resonance strength parameter s_{res}[86] of 0.72.

To utilize the resonance, atoms are transferred from the $|1, -1\rangle$ state to the $|1, 1\rangle$ state with an adiabatic rapid passage (ARP) pulse. At low field, the Zeeman sublevel structures are quite similar for Na and Rb, and the transition frequencies from the $|1, -1\rangle$ state to the $|1, 0\rangle$ state are slightly higher than that from the $|1, 0\rangle$ state to the $|1, 1\rangle$ state. Benefited from the above two facts, the population transfer can be achieved with one single radio-frequency pulse with the frequency chirped from 2.985 MHz to 1.985 MHz in 10 ms with a quantization field of 3.4 G. For Na, the ARP performance is always good and no population in other states can be observed. For Rb, there are sometimes 1% to 2% of the atoms left in the $|1, 0\rangle$ state. Those atom can be removed from the trap by holding the atoms several hundreds of milliseconds near the Feshbach resonance between Rb $|1, 0\rangle$ state and Na $|1, 1\rangle$ state at 388 G.

To produce the molecules, we first turn on the bias B-field with a value above the resonance point, and then ramp the B-field across the resonance with ramping rate of -2.2 G/s. The conversion efficiency is below 10% and we observe that the produced molecular sample has a temperature higher than the atomic sample. While the downward B-field ramp associates the molecule, a reversed one dissociates the molecule. So far, we don't have the imaging of the molecule, so the creation of molecules is confirmed by the atomic signal revival after the dissociation as shown in Fig. 4.2(A).

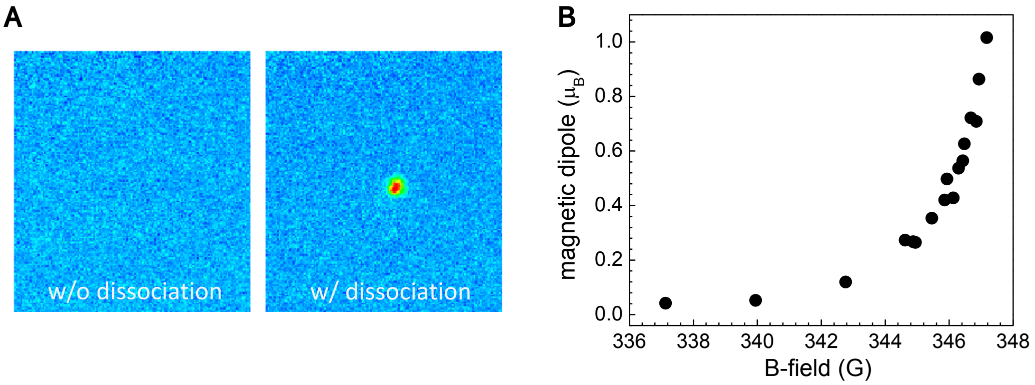

Figure 4.2: The NaRb Feshbach molecule near the 347.6 G Feshbach resonance. (A) Creation of NaRb Feshbach molecule confirmed by the atomic signal revival after the dissociation. (B) The B-field dependent magnetic dipole of the Feshbach molecule extracted from measurements of the binding energy.

4.1.3 Residual atom removal

The relatively low conversion efficiency of magnetoassociation means that there are still plenty of atoms left in trap after the molecules being formed. To obtain a pure molecular sample, one needs to selectively remove those atoms while leave the molecules unaffected. The residual atoms also limit the molecule number obtainable because of the inelastic collisions between the atoms and the molecules. Hence, one needs the atom removal, and also to make it happen as soon as possible.

Remove with magnetic gradient pulse

The old method we use is using a magnetic gradient pulse. The Na and Rb atom in the state $|F, m_F\rangle = |1, 1\rangle$ have magnetic dipole moments, and feel a force pushing them out of trap in an inhomogeneous B-field. On the other hand, the Feshbach molecule's magnetic dipole moment is a function of the B-field. At B-fields close to the Feshbach resonance, the magnetic dipole moment is close to the total magnetic dipole moment of the free atom pair. The dipole gradually transits to the dipole of the deeply bound molecular state as the B-field gets away from the resonance. Fig.4.2(B) shows the molecule's dipole extracted from binding energy measurements. We see that below 340 G, the dipole of the molecule is no larger than 0.05 μ_B. We perform the removal at 335.2 G B-field and we indeed see that the magnetic gradient pulse exert only slight effect on the molecules. The pulse length is typically 2 to 3 ms and the maximum gradient can be generated is 168 G/cm by calculation. The major shortage of this method is that the removal is not fast enough since the B-field value need to be shifted to the desired 335.2 G and the pulse can only be applied after the B-field settles down. This process usually takes several ms because of the finite bandwidth of the B-field servo.

Remove with MWs and lasers

To overcome the shortages, we switch to a removal scheme using MWs and lasers. The idea is to remove the atoms by photon recoils when the atoms are consistently driven in a cycling transition. Starting from the $|1, 1\rangle$ state, there is no cycling transition. We therefore apply extra MW pulses first to transfer the population to the $|2, 2\rangle$ state, which has a cycling transition with the $|3, 3\rangle$ state. There are basically two approaches for the population transfer, either perform a π-pulse or an ARP. Considering the stability of our B-field of about 10 mG, using π-pulse is not a good idea, so we choose the more robust ARP method.

To get the best population transfer efficiency, we demand large Rabi frequencies for the MW transitions that suppress the Landau-Zener tunneling during the ARP. Fig. 4.3(A) and (B) show the MW Rabi oscillations of Na and Rb atoms with a Rabi frequency of $2\pi\times45$ kHz and $2\pi\times39$ kHz respectively. For Rb, the MW circuit is the exact circuit for the MW evaporative cooling. The emission end uses a WR-137 waveguide. For Na, we use an one-loop square-shaped Q-section antenna[87] and a 16W amplifier (Mini Circuits ZHL-16W-43+).

Using the MWs and lasers at first glance may still be troubled by the slow settlement of the B-field, since usually the ARP is done with a fixed field and a driving MW with a varying frequency. However, we can exchange the role of the field and the MW. We can slow vary the B-field while keeping the MW at a fixed frequency. Naturally, the ramp for the ARP follows immediately the ramp for the magnetoassociation but with a reduced ramping rate from -2.2 G/s to -1.7 G/s. A single MW transfer takes 65 μs with an efficiency of about 80% to 90%. After the MW transfer, a 15 μs laser pulse resonant with the high-field $|2,2\rangle$ to $|3,3\rangle$ transition can completely remove the population on the $|2,2\rangle$ state.

Usually, we repeat the MW and the laser pulse for 5 times for a thorough removal. For each time, the B-field value is different, so we also dynamically change the MW frequency with the signal generator in frequency modulation mode and an external step-wise voltage control. The frequency shift is -360 kHz and -380 kHz per pulse for Na and Rb respectively. The optical transition line widths are fairly large, so we don't need to fine tune the frequency of the lasers.

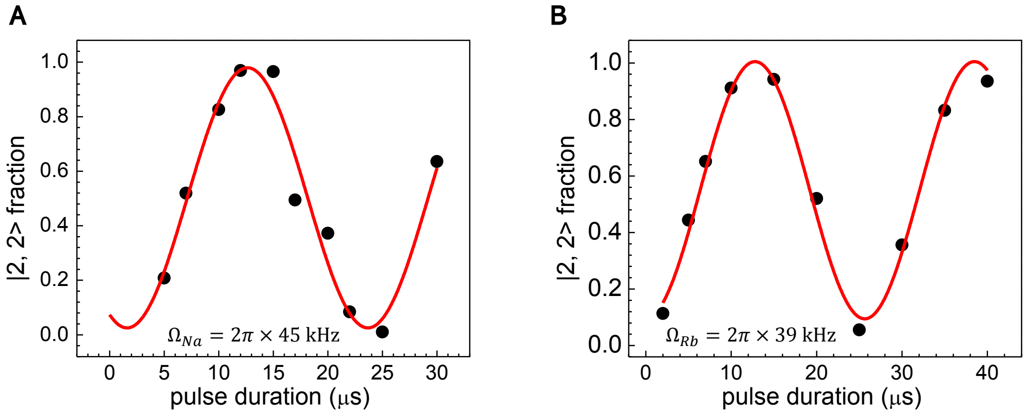

Figure 4.3: MW Rabi frequencies for the residual atom removal. MW transition from $|1,1\rangle$ to $|2,2\rangle$. (A) The Rabi frequency for Na is $\Omega = 2\pi\times45$ kHz. (B) The Rabi frequency for Rb is $\Omega = 2\pi\times39$ kHz

4.2 Stimulated Raman Adiabatic Passage (STIRAP)

The Stimulated Raman Adiabatic Passage (STIRAP) is right now the most successful way of creating ground-state molecules start from a gas of weakly-bound Feshbach molecules. The STIRAP solves the problems that usually occurs in a single-photon process, such as the bad Franck-Condon factor (FCF), or that the transition is forbidden by the selection rules[88]. The Raman process is a coherent process that removes the huge binding energy difference between the molecular states without heating the molecular sample and thus preserves the PSD. The method has been proved to be rubust and efficient in systems either homonuclear or heteronuclear.

4.2.1 Basics

In the production of ground-state molecule, the STIRAP is usually implemented in a three-level system with a Λ configuration as depicted in

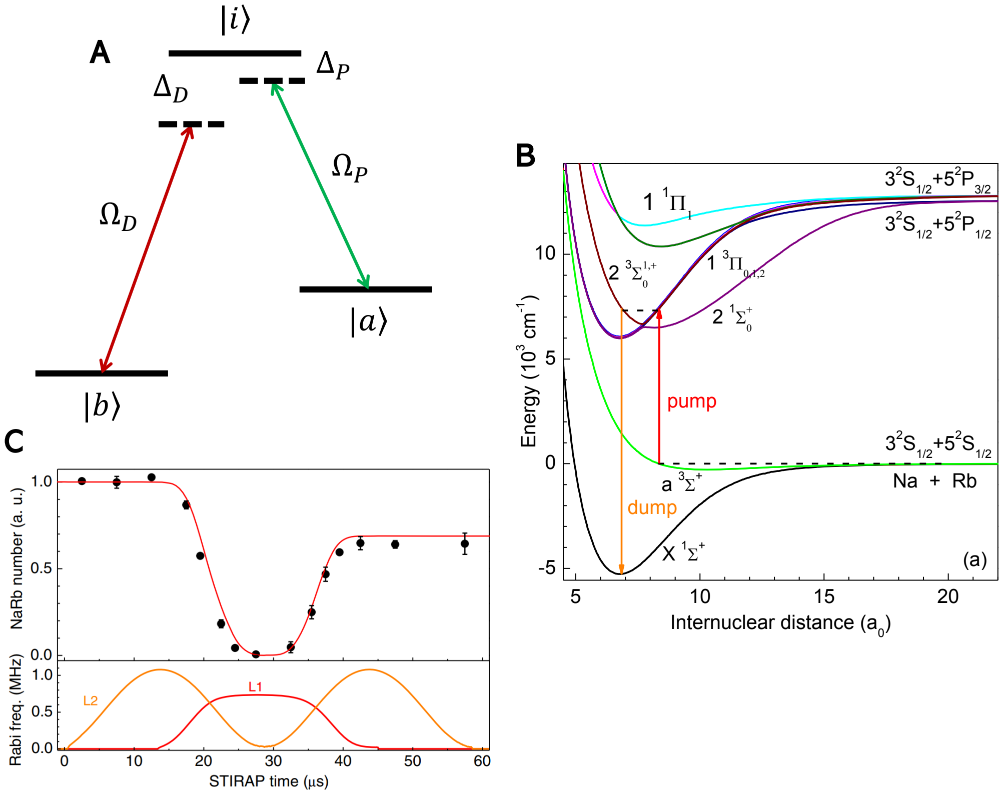

Figure 4.4: (A) A sketch of a three level system. (B) The STIRAP scheme for ground-state NaRb molecule production. The initial state is $a^3\Sigma^+\,|v=21, J=1\rangle$, the intermediate state is the coupled $2^1\Sigma^+/1^3\Pi\,|v'=55, J'=1\rangle$. The target state is $X^1\Sigma^+\,|v=0, J=0\rangle$. (C) Feshbach molecule number evolution during a double STIRAP process together with the STIRAP pulse shape.

Fig. 4.4(A). Here, we label the three states as $|a\rangle$, $|b\rangle$ and $|i\rangle$, where $|a\rangle$ is the Feshbach state (initial state), $|b\rangle$ is the ground state (target state) and $|i\rangle$ is the intermediate state in this context. Two Raman beams with phase coherence couples the three-level system. Conventoionally, we name the beam that couples $|a\rangle$ and $|i\rangle$ as the pump beam, and the beam that couples $|i\rangle$ and $|b\rangle$ as the dump beam. Under the rotating wave approximation, the Hamiltonian is described by a three-by-three matrix.

$$\hat{H} = \frac{\hbar}{2}\begin{pmatrix} 0 & \Omega_P(t) & 0 \\ \Omega_P(t) & -2\Delta & \Omega_D(t) \\ 0 & \Omega_D(t) & -2\delta \end{pmatrix} \tag{4.1}$$

Here, Ω_P and Ω_D are the Rabi frequencies that correspond to the pump beam and the dump beam respectively. Δ is called the one-photon detuning and is equal to Δ_P. δ is called the two-photon detuning defined as Δ_P - Δ_D. Δ_P and Δ_D are defined in Fig 4.4(A) with negative values correspond to red-detunings.

When the system is on the two-photon resonance, namely $\delta = 0$, the Hamiltonian yields three eigenstates.

$$\left|a^+\right\rangle = \sin\theta\sin\phi\left|a\right\rangle + \cos\phi\left|i\right\rangle + \cos\theta\sin\phi\left|b\right\rangle \tag{4.2}$$

$$\left|a^0\right\rangle = \cos\theta\left|a\right\rangle - \sin\theta\left|b\right\rangle \tag{4.3}$$

$$\left|a^-\right\rangle = \sin\theta\cos\phi\left|a\right\rangle - \cos\phi\left|i\right\rangle + \cos\theta\cos\phi\left|b\right\rangle \tag{4.4}$$

where θ and ϕ are mixing angles defined as,

$$\tan\theta = \frac{\Omega_P}{\Omega_D} \tag{4.5}$$

$$\tan 2\phi = \frac{\sqrt{\Omega_P^2 + \Omega_D^2}}{\Delta} \tag{4.6}$$

What makes STIRAP possible here is $|a_0\rangle$ which emerges as only a superposition of $|b\rangle$ and $|a\rangle$. We name this state as the dark state because the intermediate is usually lossy and short-lived. Another important point here is two components of this eigenstate completely depends on the Rabi frequency ratio of the two Raman beams. Therefore, if the powers of the two beams are tuned adiabatically, we can achieve the population transfer by making use of, but not really occupying the intermediate state. In order to initially project $|a\rangle$ to $|a^0\rangle$, we need $\theta = 0$, that is $\Omega_D >> \Omega_P$. To have the final $|a^0\rangle$ overlap with $|b\rangle$. we need $\theta = \pi/2$ which means $\Omega_P >> \Omega_D$.

4.2.2 Ground-state NaRb molecule production and internal state control via STIRAP

Fig. 4.4(B) shows the scheme for the ground-state NaRb molecule production. The STIRAP is usually implemented at 335.2 G B-field. The intermediate state is the coupled $2^1\Sigma^+/1^3\Pi\,|v' = 55, J' = 1\rangle$, which has 95% $1^3\Pi_0$ and 5% $2^1\Sigma^+$ character[89]. With the help of the intermediate state, the molecules start at the triplet Feshbach state $a^3\Sigma^+\,|v = 21, J = 1\rangle$ and end up in the singlet ground state $X^1\Sigma^+\,|v = 0, J = 0\rangle$. The pump beam has a frequency of 8012.7 cm^{-1} and a π polarization while the dump beam has a frequency of 12989.8 cm^{-1} and a σ^+/σ^- polarization.

Fig. 4.4(C) shows an example of the pulse sequence of the Raman beams. Here, a double-STIRAP sequence is shown with the STIRAP and the reversed STIRAP directly connected. The disappearance and the revival of the Feshbach state population indicates the population is transferred to the target ground state. In most experiments that will be mentioned afterwards, the parameters used for the STIRAP is as follows. The Rabi frequencies of pump beam and dump beam are about $2\pi\times1.2$ MHz and $2\pi\times1.3$ MHz respectively. The two beams have a 50 μs overlap in the time domain. The single STIRAP transfer efficiency is calculated by taking the square root of the recover rate after the double-STIRAP pulse. With the above settings, single STIRAP transfer efficiency can readily reach around 93 %.

Several factors limit the STIRAP efficiency. Those factors are: the lifetime of the intermediate state, the one-photon detuning, the two-photon detuning, the Rabi frequency, the phase coherence between Raman lasers, etc. Although the intermediate state is not really occupied in an idealistic STIRAP process, its lifetime sets a charateristic energy (or time) scale of the parameters needed for an efficient transfer. The one-photon detuning can effect the efficiency but very weakly. In practice, we use about 1 MHz one-photon detuning, but the performance is basically the same as the on-resonance case. The two-photon detuning has a strong influence on the transfer efficiency and we always tune it on-resonance. We perform the STIRAP in trap, so the spatial-dependent or time-dependent ac-Stark shift from the trapping beams will cause two-photon detuning. However, the energy shift should be small compared with the STIRAP transition linewidth of about 80 kHz. Therefore, so far, the major factors limit the efficiency are the phase coherence between the lasers and the Rabi frequencies. The relative laser linewidth estimated from current efficiency is about $2\pi\times1$ kHz. The efficiency can be further increased with narrower linewidths. On the other hand, numerical calculations show that with Rabi frequencies up to $2\pi\times2$ MHz and 7 MHz, the efficiency can go to 97% and 99%.

As long as the selection rules permits, a bunch of states at the bottom of the $X^1\Sigma^+$ potential can be accessed via STIRAP owing to the similar FCFs. Thus, STIRAP itself provides us a simple way to control on internal degrees of freedom. Fig.4.5 shows the successful control of the internal degrees of freedom directly via STIRAP. Here, v stands for the vibrational quanta and J stands for the rotational quanta.

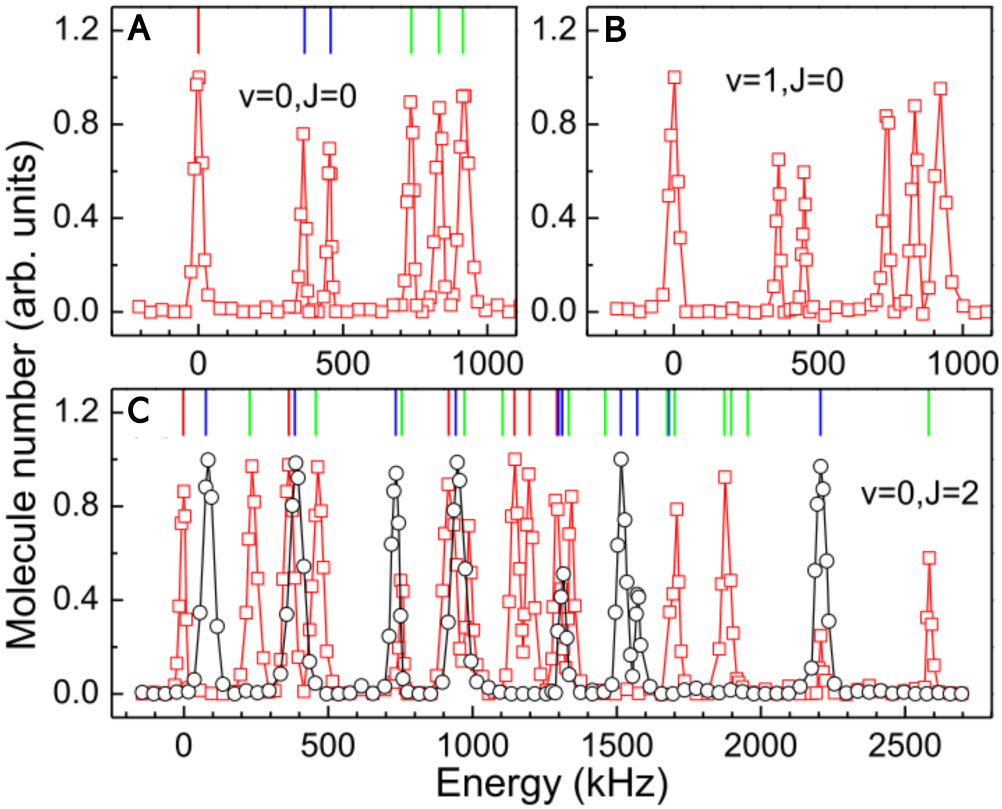

Figure 4.5: Internal state control via STIRAP. (A), (B) STIRAP spectra of the ($v = 0$,$J = 0$), ($v = 1$,$J = 0$) with dump beam of mixed polarization. (C) STIRAP spectra of ($v = 0$,$J = 2$) with dump beam of π polarization (black) and σ^+/σ^- polarization (red). Spectra are obtained by tuning the wavelength of the dump beam. The vertical colored bars indicate the quantum number M_F with $M_F = 3$ in red, $M_F = 2$ in blue, and $M_F = 1$ in green

4.3 One-photon MW transition

Because the selection rules for Hund's case (a)[90] forbid the transitions with $\Delta J = 0$ and $\Omega = 0 \rightarrow \Omega = 0$, the ground states with $J = 1$ can hardly be accessed directly via STIRAP. To access $J = 1$ states, we can first prepare the molecules in the $J = 0$ states and then drive them with a MW pulse. The MW couples to the permanent dipole of the molecule and results in strong E1 transition with moderate MW power. The nuclear spins essentially don't flip during such transitions.

Fig. 4.6(A) shows the MW transitions starting from the absolute ground state with $m_{Na} = 3/2$ and $m_{Rb} = 3/2$. The six dips here correspond to six $J = 1$ states with considerable components of $m_{Na} = 3/2$ and $m_{Rb} = 3/2$.

With the molecules already in $J = 1$ states, one can further apply a MW pulse to get to other hyperfine states in the $J = 0$ manifold. The mixing between different nuclear spins is critical for such population transfers. The mixing in $J = 1$ states is mainly a physical consequence of the rotation-nuclear spin coupling.

Fig. 4.6(B) shows a "upward" one-photon transition as well as two "downward" one-photon transitions to two other hyperfine states. The Rabi oscillations here indicate the coherence of such transitions. The coherent MW transfer here provides a simple way to either prepare a pure molecular sample in a certain state or a molecular mixture of two states with an arbitrary ratio. In principle, one could also get to $J = 2$ states with successive MW pulses.

4.4 Two-photon MW transition

Prepare a hyperfine mixture with two successive MW pulses doesn't guarantee the coherence between the two states. This is because an excited state with $J = 1$ is really occupied via this route and during this occupation, dephasing or relaxation may kill the coherence. To better preserve the coherence, one can resort to the two-photon process.

The molecule population can be coherently transfered between hyperfine states in the $J = 0$ manifold. Recall Eq. 4.1, we have the Schrodinger equation in the matrix form,

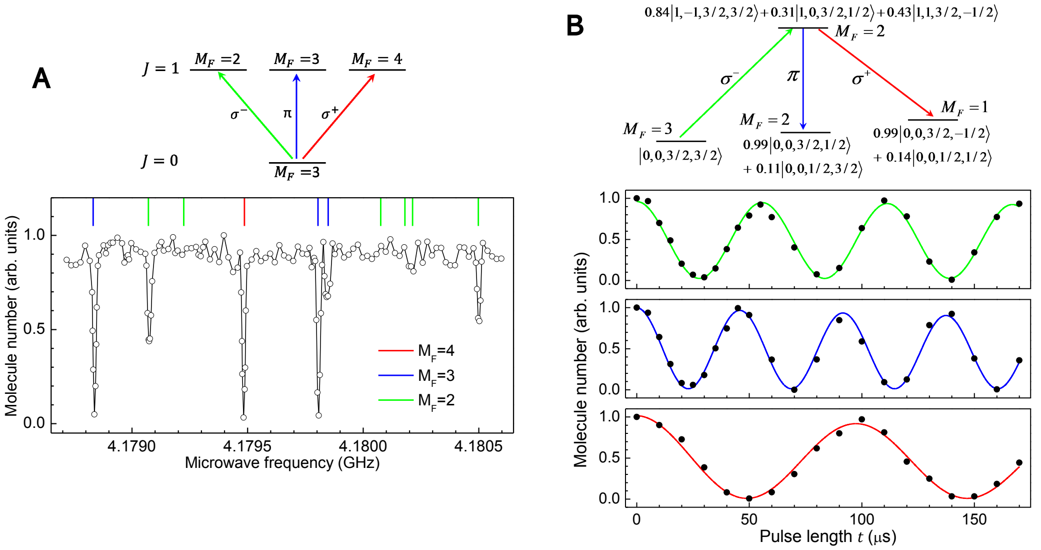

Figure 4.6: Internal state control via one-photon MW transition. (A) MW transitions to the $J = 1$ rotational state from the absolute ground state. The colored vertical bars indicate the calculated positions of the relevant hyperfine levels of $J = 1$. Note some transitions are not observable due to the weak transition dipole. (B) Coherent population transfer between the hyperfine levels of the $J = 0$ and $J = 1$ states with MW pulses. $J = 1$ states possess considerable mixing between different nuclear spins due to the rotation-nuclear coupling

$$i\frac{d}{dt}\begin{pmatrix} c_a \\ c_i \\ c_b \end{pmatrix} = \frac{1}{2}\begin{pmatrix} 0 & \Omega_a & 0 \\ \Omega_a & -2\Delta & \Omega_b \\ 0 & \Omega_b & -2\delta \end{pmatrix}\begin{pmatrix} c_a \\ c_i \\ c_b \end{pmatrix}. \tag{4.7}$$

The solution of the coefficient $c_i(t)$ has the following integral form,

$$c_i(t) = -i\int_0^t e^{i\Delta(t-t')} \times \frac{\Omega_a c_a(t') + \Omega_b c_b(t')}{2} dt'. \tag{4.8}$$

When one-photon detuning Δ is much larger than the two-photon detuning δ and Rabi frequencies $\Omega_{a,b}$, the dynamics of c_i has a shorter time scale (defined by the large Δ). Hence, we can regard $c_a(t')$ and $c_b(t')$ as constants in the

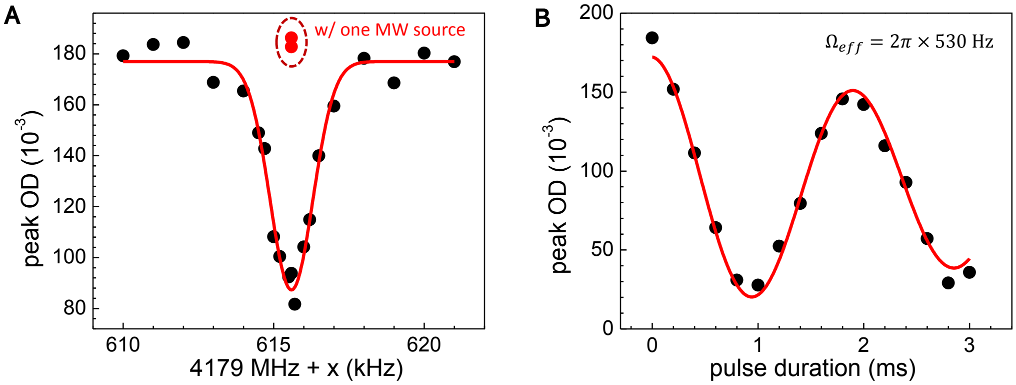

Figure 4.7: Internal state control via two-photon MW transition. The two-photon transition starts from the absolute ground state $|J, m_J, m_{Na}, m_{Rb}\rangle$ $= |0, 0, 3/2, 3/2\rangle$ to the third lowest state $|0, 0, 3/2, 1/2\rangle$. The intermediate state is the lowest state in the $J = 1$ manifold. The one-photon detuning Δ is -$2\pi\times200$ kHz, the Rabi frequency of the two MWs are $2\pi\times12$ kHz and $2\pi\times19$ kHz. The pulse duration is 500 μs in (A). The two red point are only with either one MW source and confirm the observed transition is a two-photon transition. (B). The two-photon Rabi oscillation, the measured effective two-photon Rabi frequency is 530 Hz

above integral and $c_i(t)$ can be approximated as,

$$c_i(t) \approx \frac{1 - e^{i\Delta t}}{2\Delta}[\Omega_a c_a(t') + \Omega_b c_b(t')]. \tag{4.9}$$

We can see that the magnitude of c_i is always little. Drop the oscillating term $e^{i\Delta t}$ in Eq. 4.9 and substitute it into Eq. 4.7, the three-level system can be effectively reduced to a two-level system,

$$i\frac{d}{dt}\begin{pmatrix} c_a \\ c_b \end{pmatrix} = \frac{1}{4\Delta}\begin{pmatrix} \Omega_a^2 & \Omega_a\Omega_b \\ \Omega_a\Omega_b & \Omega_b^2 - 4\Delta\delta \end{pmatrix}\begin{pmatrix} c_a \\ c_b \end{pmatrix}. \tag{4.10}$$

An intermediate from the $J = 1$ manifold need to be chosen for the coherent two-photon transfer. The choice of the intermediate state depends on the target hyperfine state. A good choice of the intermediate state is the lowest state of $J = 1$ that has 82% $|1, 0, 3/2, 3/2\rangle$ component and 18% $|1, 1, 3/2, 1/2\rangle$

component and therefore can be used to connect the $|0,0,3/2,3/2\rangle$ state and the $|0,0,3/2,1/2\rangle$ state. Since it is the lowest one, we can get rid of unexpected couplings between other undesired states when large red-detuned MWs are used. The situation might be tricky if some other state is used, considering the complex internal structures of the molecule.

Fig. 4.7 shows the result of the two-photon coherent transfer. We get two outputs from two signal generators and combine them with a splitter used in a reversed way. Each output is controlled by an individual MW switch. Here, Δ = -$2\pi\times200$ kHz, $\Omega_a = 2\pi\times12$ kHz and $\Omega_b = 2\pi\times19$ kHz. The calculated effective Rabi frequency $\Omega_{eff} = \Omega_a\Omega_b/4\Delta$ is 570 kHz. In Fig 4.7(A), we fix the frequency of one generator and scan the other one. The pulse duration is 500 μs. The two red points show the result with only either one of the MW source and confirm that the signal observed due to a two-photon process. Extending the MW pulse at the two-photon resonance, we observe the two-photon Rabi oscillation and extract an effective Rabi frequency of 530 Hz.

□ End of Chapter.

Chapter 5

Technical issues

Before moving forward to collision experiments, several technical issues should be taken care of. One of the central tasks of a collision experiment is the determination of the collision rate constants, in particular, the inelastic or the reactive collision rate constants in the context of this thesis. One typical way of extracting these rate constants is measuring the trap loss, i.e. the number evolution inside a trap with a variable holding time. This is because traps like ODT are usually extremely shallow compared to the kinetic energy released during an inelastic or a reactive collision process. Since the collision products are too kinetic to be trapped anymore, the decrease of the in-trap particle number faithfully reflects the number of the collision events. In light of this, an accurate determination of the number is demanded. This leads to the number calibration as well as the image denoising when dealing with low optical density images.

Generally, the number evolution can be modeled with the following expression,

$$\frac{\mathrm{d}n}{\mathrm{d}t} = -\sum_{i} \beta_i n^i, \tag{5.1}$$

where summation index i iterates over positive integers. The index i labels the i-body process. For example, $i = 1$ term is a one-body process which usually means the collisions of the particles from the ensemble with the particles from the background or the reservoir. On the other hand, $i = 2$ term describes a process happens between a pair of particles from the ensemble. Note that although macroscopically we measure the total particle number N, microscopically the rate constants β_i are naturally defined with the particle density n. Hence, only an accurate determination of the number is no enough. We also need the ability to extract the accurate in-trap density. Given a total particle number, the in-trap density depends on the temperature of the ensemble as well as the geometry of the trapping potential. This leads to the temperature calibration as well as the trap frequency measurement. For a simple determination of the in-trap density, an implicit prerequisite is the thermal equilibrium assumption. Although we are not always guaranteed to have the thermal equilibrium, we should manage not to induce undesired out-of-equilibrium dynamics. This leads to the suppression of the in-trap motions of the molecules.

5.1 Number calibration

In our experiment, we measure the atom number with the standard absorption imaging technique. Probe laser beams resonant with certain atomic transitions are shined onto the ultracold atomic cloud and the shadows are cast and imaged onto the CCD chip. The attenuation of the beam intensity after passing through reveals the column density of the atomic cloud. Integrating over the column density distribution and knowing the photon scattering cross section of the atomic species, one can get the total atom number of the cloud.

Ideally, the photon scattering cross section σ_0 for a certain probe beam polarization and a certain atomic transition can be found from existing data. In practice, however, we always face different sorts of imperfections. For instance, the slight misalignment of the quantization field and the impurity in probe beam polarization components will effectively make the cross section smaller than that in the ideal case and lead to the underestimation of the atom number. The errors in the determination of atom number directly affect the accuracy of the extracted rate constants in Eq. 5.1 with $i > 1$.

We follow the method described in Ref.[91] to calibrate our absorption imaging. Optical depth defined as

$$od_0(x,y) \equiv \sigma_0 \int n(x,y,z)\mathrm{d}z = -\alpha \times \ln\left(\frac{I_f(x,y)}{I_i(x,y)}\right) + \frac{I_i(x,y) - I_f(x,y)}{I_0^{sat}} \tag{5.2}$$

is a quantity that only depends on the atomic density distribution while independent on the intensity of the probe beam. Here, α is the parameter we need to figure out, I_{sat} stands for the saturation intensity of the transition, I_i and I_f denote the probe intensity before and after the cloud respectively. According to this optical depth definition, as long as the ensemble is the same, we should get the same values according to Eq. 5.2 even if profoundly different probe intensities are used. This lays the foundation for extracting the value of α. In practice, we take a series of images with different probe intensities ranging from 0.136 to 5.29 times saturation factor. Then, we tweak the value of α and try to best balance all the optical depths calculated according to Eq.5.2. Fig. 5.1 shows the result for the number calibration. In panel (A), optical depths calculated with different choices of α are shown. In each set, there are six points. Panel (B) shows the standard deviation of each set with respect to the α value. A minimum fit for Fig. 5.1(B) gives α equal to 1.21 in our experiments.

Once we obtain the value of α, together with the saturation factor $s =$

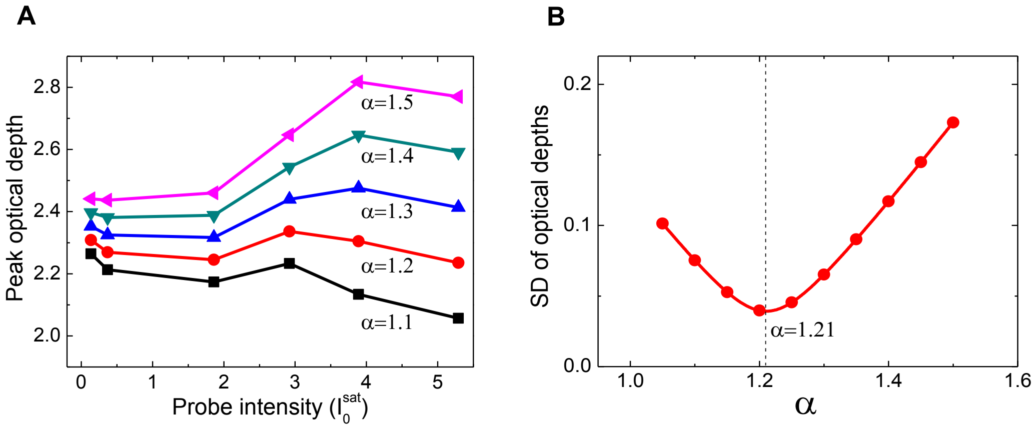

Figure 5.1: Number calibration, extraction of number correction parameter α (A) The calculated peak optical depth of absorption images according to Eq. 5.2 with different given value of α under different probe intensities ranging from 0.136 to 5.29 times saturation intensity (B) The standard deviation of the six optical depths with respect to α value. A minimum fit to the standard deviations gives the optimal $\alpha = 1.21$.

$I_i(x,y)/I_0^{sat}$ and the appeared optical depth $\delta(x,y) = -\ln(I_f(x,y)/I_i(x,y))$, the ratio between the appeared optical depth and the actual optical depth is expressed as,

$$\frac{od_0(x,y)}{\delta(x,y)} = \alpha + s\frac{1-e^{-\delta(x,y)}}{\delta(x,y)}. \tag{5.3}$$

Because the intensity I_i almost doesn't vary within a region of an atomic cloud size, we can take s as a constant. Finally, we can obtain the correction factor by numerically integrating $od_0(x,y)/\delta(x,y)$ over the Gaussian distribution of $\delta(x,y)$,

$$N \text{ correction } \# = \iint \frac{od_0(x,y)}{\delta(x,y)} \mathrm{d}x\mathrm{d}y. \tag{5.4}$$

Within the optical depth range we normally obtain, the correction factor can be well approximated with the below formula,

$$N \text{ correction } \# = A + B \times \delta(0,0), \tag{5.5}$$

where $A = 1.191 + 0.972s$ and $B = -0.165s$.

5.2 Temperature calibration

The most standard way to measure the temperature of a atomic cloud in trap is to measure the expansion of it after an abrupt switch-off of the trapping potential. Usually, the temperature is extracted from a plot of cloud size with respect to different TOFs. The model of the size expansion during the TOF is,

$$\sigma(t) = \sqrt{\sigma_0^2 + \frac{k_B T}{m} t^2} \tag{5.6}$$

where σ_0 is the initial cloud size in trap, k_B is the Boltzmann constant, T is the temperature, m is the mass of the particle and t is the total TOF.

However, in a collision experiment where the temperature need to measured for lots of times, this method is time-consuming. In practice, one can only measure the size of it after one specific TOF, and determine the temperature from such a single-shot measurement. Such measurements need a calibration.

Another reason to have a calibration arises from the difficulty of performing measurements on molecules. The rich internal structures of molecules make it difficult to find a cycling or near-cycling transition for the direct absorption imaging. Since we so far haven't developed the direct absorption imaging for the molecule yet, molecules always need to be dissociated back to atoms first before the imaging. Therefore, the scheme of measuring the molecular temperature becomes, first let the molecular cloud expands during a TOF, then manage to dissociate them back to atoms and finally image the size of the atomic cloud.

Then, another problem comes into play. After dissociation, we need in fact one more millisecond for the settlement of the B-field that switched off from about 350 G (because the dissociation is done near the 347.6 G Feshbach resonance). Consequently, if we take the image of Rb in the end, the size we see is actually from t ms of molecular TOF plus 1 ms of Rb TOF. Such a situation will introduce a systematic error in the temperature determination especially when total TOF is short.

In practice, the total TOF chosen for the single-shot temperature determination is 3 ms. The temperature T_i in i-dimension can be calculated from the following expression,

$$T_i = \alpha' \frac{m\sigma_i^2}{k_B(1/\omega_i^2 + t^2)}. \tag{5.7}$$

Here, σ_i is the size of the cloud in i-dimension, ω_i is the trap frequency in i-dimension, and α' is the correction factor to find out. Excluding factor α', Eq. 5.7 is the exact formula of the normal single-shot temperature extraction for atoms.

The calibration is done over temperatures ranging from 350 nK to 1.3 μK. We compare the temperatures from Eq. 5.7 with the single-shot measurements and that from the standard TOF method with total TOF from 2 ms up to 7 ms. In the standard TOF method, to some extent, the effect of the common 1 ms Rb TOF of all data points is "absorbed" by the free parameter initial size σ_0 in Eq. 5.6. The temperature fitted then is very close to the real temperature. By simulation, with the given TOFs, the fitted temperature is systematically higher than the real temperature with a percentage less than 3%. With all above things, we find factor α' is nearly constant over the whole range as shown in Fig. 5.2(A). The weighted mean gives $\alpha' = 0.90(1)$.

We have also cosidered another easier way of temperature determination besides the above mentioned method. The idea is that we only measure the temperature of the Rb atoms from the dissociation. Assuming the dissociation process is adiabatic, the Rb temperature should equal to the molecular temperature. Or, the dissociation process is not adiabatic, some linear relation is still expected. In addition to its easiness, another benefit of using this method is that it is possible to determine the number and temperature together in one single shot. We check the relation of the two temperatures experimentally. The result is shown in Fig. 5.2(B). Indeed, we see that the mean molecular temperature and the mean atomic temperature more or less the same, showing our dissociation process is nearly adiabatic. However, we also see large fluctuations in each of the three sets of data (labeled by color) with different ODT conditions. Such fluctuation hinders a reliable measurement of the temperature evolution shown in later chapters. Therefore, we adopt the first method but not this method.

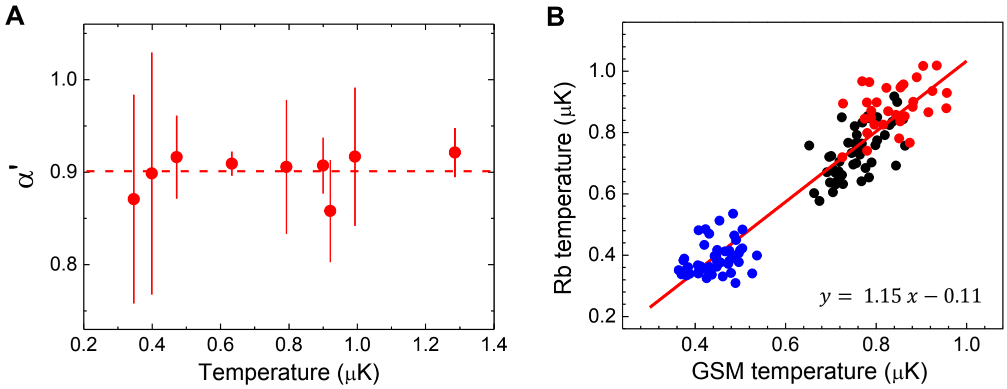

Figure 5.2: Temperature calibration. (A)The extracted temperature correction parameter α' within a range from 350 nK to 1.3 μK by comparing the results from the single-shot measurement and the standard TOF method. (B)Relation between the temperature of the ground-state molecule and the temperature of the product Rb atoms from dissociation. Dots with different colors are with different ODT depths. The x coordinate and y coordinate of each point are from successive two experimental shots. A linear fit gives a slope of 1.15 and an intercept of -0.11.

5.3 Suppression of molecular motion

How well can one control the motion of the molecules in trap really affect the accuracy of the loss rate constant determination. In the fitting model, we always assume that the system is in thermal equilibrium and the density distributes in some Gaussian profile. However, if molecular sample has a motion in trap, especially the breathing motion, the model would fail to faithfully describe the experimental reality. The breathing motion means that the molecular density suffers a considerable modulation during the holding time and that makes the data analysis more complicated.

The motion, i.e. a kind of excitation, can be induced by all kinds sources. In our case, the motion is essentially induced after the STIRAP process. The source of it is the polarizability difference at 1064 nm between the Feshbach state and the ground state. When the transfer has been done, the density profile, which is originally in thermal equilibrium, is no longer in and the breathing motion will arise.

To get rid of this issue, we need to make the potential experienced by the ground-state molecules be the same as what Feshbach molecules experience at the beginning. What we do here is to change the ODT power according to the polarizability ratio abruptly and immediately after ($<$10 μs) after the completion of the STIRAP. At 1064 nm, the polarizability of the Feshbach state is 909 a.u. while the polarizability of the ground state is 674 a.u.[92]. With the starting ODT power control voltage at 0.3 V, Fig. 5.3 shows the resulting amplitude of both the slosh motion and the breathing motion with different final ODT power control voltages. We see indeed a significant suppression of motions at a final control voltage equals to 0.409 V, which is close to the prediction (0.3V×909 a.u./674 a.u.= 0.405 V).

In another set of measurement, we delay the rise of the ODT power, investigating the time scale that significant breathing motions emerge. The result is shown in Fig. 5.4. We find that the delay time is not that critical. No amplification of the breathing motion is observed with the delay time shorter than 500 μs. However, if delay time is more than 1 ms, the breathing motion amplitude is significantly larger.

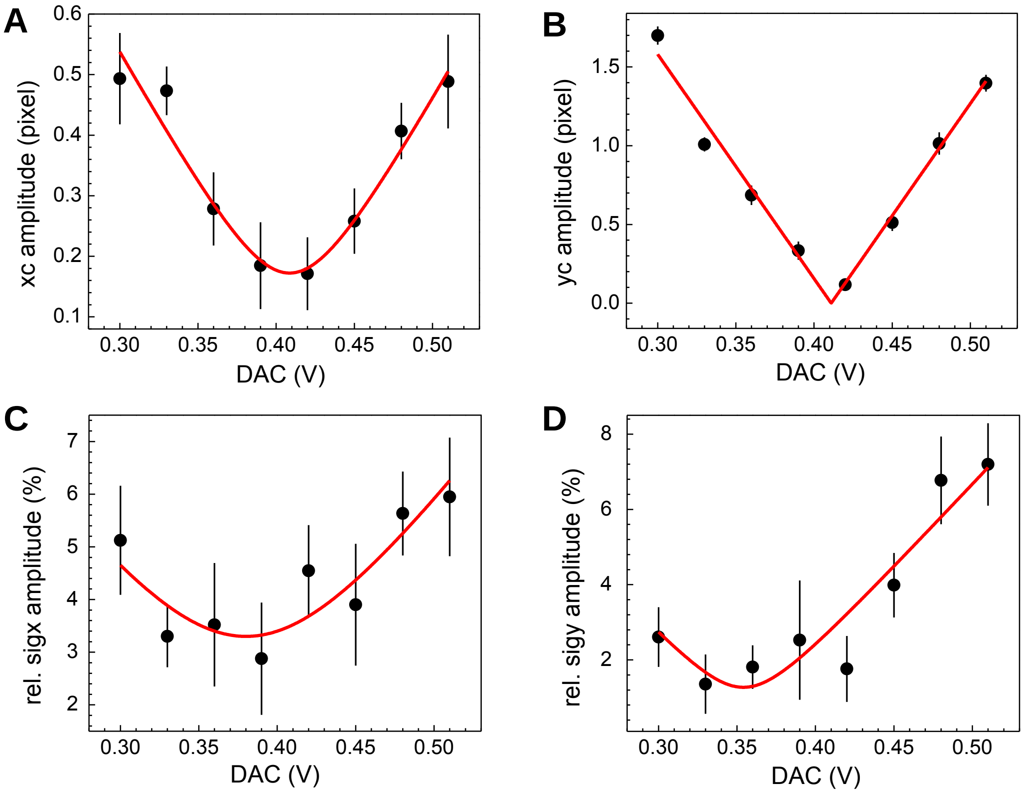

Figure 5.3: Suppress the molecular motion by tuning the ODT control DAC voltage immediately after STIRAP. The Feshbach state is initially in an ODT with DAC voltage = 0.3V. When the final DAC to initial DAC ratio is close to the polarizability ratio of the Feshbach state and the ground state, both the slosh and the breathing motion can be greatly suppressed. The weighted average of the minimum fit results of the four figures gives a target DAC of 0.409 V for an initial DAC = 0.3 V.

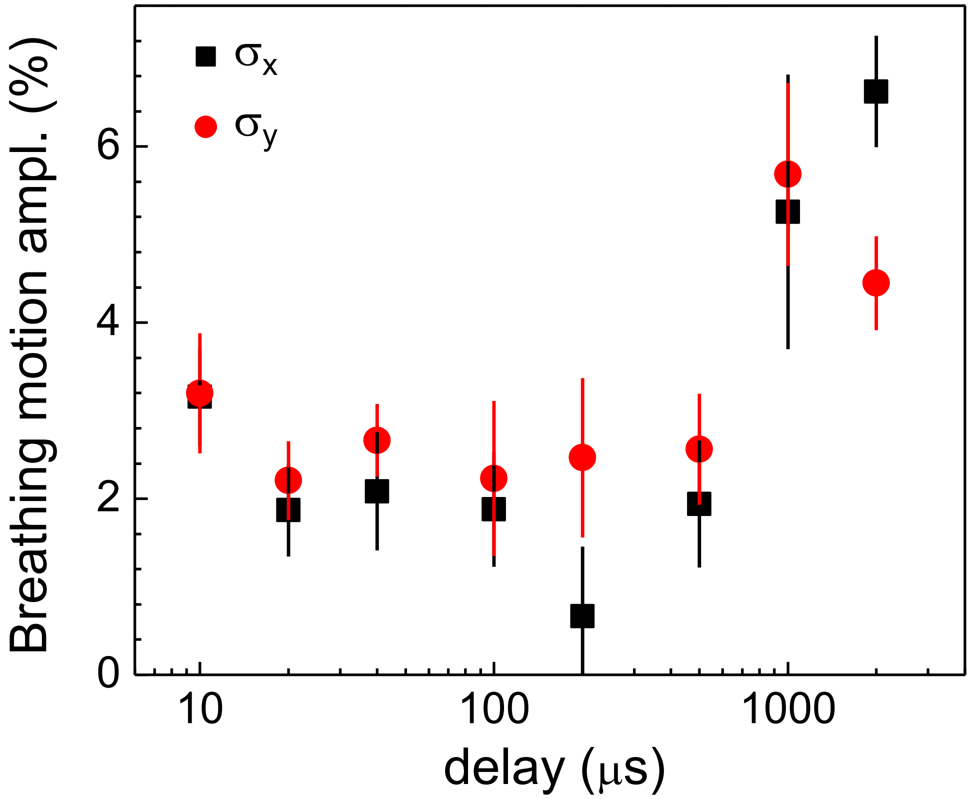

Figure 5.4: Time scale of the emergence of significant breathing motions. The resultant amplitude of the breathing motion is measured with respect to the delay time of the rise of the ODT power after STIRAP. There is no recognizable difference for delays shorter than 500 μs while for delay times larger than 1 ms, the amplitudes of the breathing motion are significantly larger.

5.4 Trap frequency

Because of its ultracold temperature, the ensemble only explores the bottom region of the ODT. As the ODT potential is neither a linear potential nor a box potential, locally the potential at the bottom can be approximated by a quadratic function as,

$$V = \sum_i \frac{1}{2} m\omega_i^2 x_i^2 \tag{5.8}$$

A thermal gas in such a quadratic trap obeys the following density distribution,

$$n(\vec{r}) = \frac{N}{\pi^{3/2}} \prod_i e^{-\frac{x_i^2}{R_i^2}}/R_i, \tag{5.9}$$

where $R_i^2 = 2k_BT/m\omega_i^2$. Here, the parameter ω_i is called the trap frequency. With the number N and the temperature T in hand, one knows the ensemble's density once the trap frequencies are obtained. We measure the trap frequencies by measuring the period of the slosh motions of the molecules in trap. We deliberately delay the ODT power increase after STIRAP for about 1 ms to amplify the in-trap motion. We measure the oscillating position of the cloud after typically a 2 ms TOF. Usually, we also observe a slow damping aside of the oscillation. An Underdamped oscillator oscillates as,

$$x \propto e^{-\gamma t} \sin(\omega' t - \phi). \tag{5.10}$$

Fit the oscillation with the above simple model, and then we get the trap frequencies from,

$$\omega_i = \sqrt{\omega_i'^2 + \gamma_i^2}. \tag{5.11}$$

5.5 Image denoising

The background fringes of images, which comes from the interference of several reflected beams from different interfaces along the optical path, is a common issue of the absorption imaging. The existence of the fringes lowers the signal-to-noise ratio and hinders the correct extraction of number and size from the image especially when the optical depth is low. Therefore, when dealing with those low signal images, one needs to find a way to safely remove the fringes and make the real signals to stand out, if necessary.

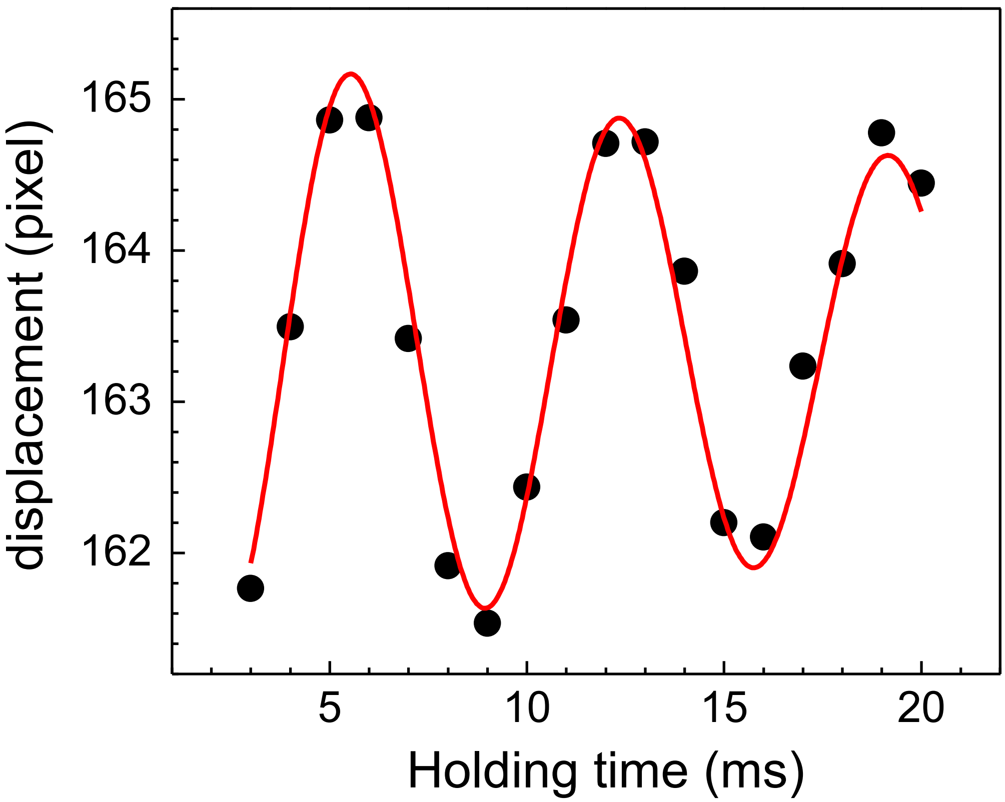

Figure 5.5: Determination of trap frequency of molecules in ODT. The ODT power rise after STIRAP is deliberately delayed to induce motions. The molecules are held in trap with various holding times, dissociated into Rb atoms and immediately released from the trap. The position of the Rb atom cloud is measured after typical TOF of 2 ms. The oscillation of the position is fit with a damped oscillator model.

Mathematically speaking, an image is a point in a linear space with extremely high dimensions. For example, a 100×100 image is a 100×100 matrix or 10,000-component vector if flattened, which lays in a 10,000-dimension linear space. One could notice that the background fringes are not exactly the same from shot to shot, but are more or less similar. There are several specific kinds of pattern repeatedly appear. This phenomenon indicates that the images containing only the background fringes live in a subspace and the size of the subspace is considerably smaller than the size of the whole space.

The key point of doing denoising is then to reconstruct the basis that can span the fringe subspace.

To reconstruct the basis, we first take n_{max} images without the atoms, only capturing the background fringes. Then, we flatten the images into vectors and perform the Gram-Schmidt process[93] to obtain n_{max} orthonormal basis of the spanned space by the n_{max} vectors.

The Gram-Schmidt process is as follows. First we define the projection operator as,

$$\mathrm{proj}_{\vec{u}}(\vec{v}) = \frac{\langle \vec{u}, \vec{v} \rangle}{\langle \vec{u}, \vec{u} \rangle} \vec{u} \tag{5.12}$$

Now, with n_{max} vectors $\vec{v}_1$, $\vec{v}_2$, $\vec{v}_3$,...,$\vec{v}_{n_{max}}$, we can construct n_{max} orthogonal vectors with the following process,

$$\begin{gathered}
\vec{u}_1 = \vec{v}_1 \\
\vec{u}_2 = \vec{v}_2 - \mathrm{proj}_{\vec{u}_1}(\vec{v}_2) \\
\vec{u}_3 = \vec{v}_3 - \mathrm{proj}_{\vec{u}_1}(\vec{v}_3) - \mathrm{proj}_{\vec{u}_2}(\vec{v}_3) \\
\cdots \\
\vec{u}_{n_{max}} = \vec{v}_{n_{max}} - \sum_{n=1}^{n_{max}} \mathrm{proj}_{\vec{u}_n}(\vec{v}_{n_{max}})
\end{gathered} \tag{5.13}$$

Then, to have an orthonormal set, we just normalize the vector $\vec{u}$'s.

$$\vec{e}_n = \frac{\vec{u}_n}{||\vec{u}_n||} \tag{5.14}$$

By reshaping the orthonormal vector back to the shape of the image, a set of basis images are constructed. With the basis images, we can now denoise the images. We first mask the region where the atom signal appears in an image. Then, we find out the image's components in the fringe subspace by taking the inner products,

$$\alpha_j = \langle \mathrm{IMG}_{masked}, \mathrm{IMG}_{basis,j} \rangle. \tag{5.15}$$

Subtracting all those components that fall into the fringe subspace, we get the denoised image.

$$\mathrm{IMG}_{denoised} = \mathrm{IMG}_{unmasked} - \sum_{j=1}^{n_{max}} \alpha_j \cdot \mathrm{IMG}_{basis,j} \tag{5.16}$$

Fig. 5.6 sketches the aforementioned procedures. An example image is denoised with 59 constructed basis. Indeed, the background fringe is reduced and the image quality is improved. With a higher number of basis, one could expect a better performance.

□ End of Chapter.

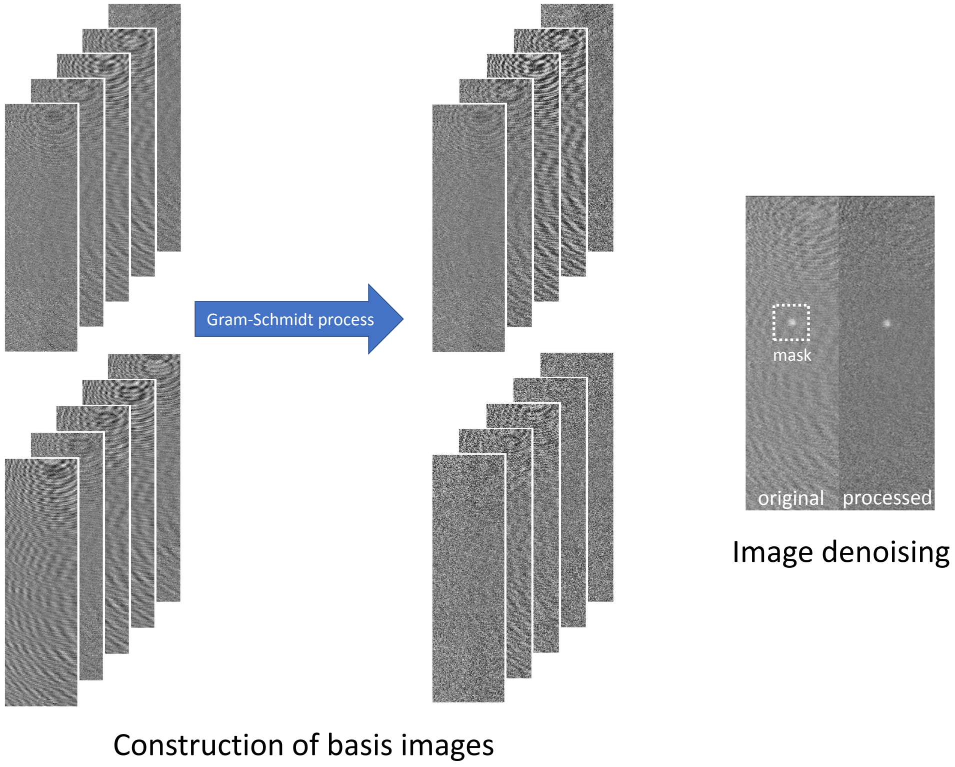
Gram-Schmidt process
mask
original
processed
Image denoising
Construction of basis images

Figure 5.6: A sketch of the image denoising process. A bunch of basis images are constructed from a same number of raw images with only the background fringe via the Gram-Schmidt process. To denoise a image with the atom signal, the region contains the atom signal is masked and the rest of the image takes the inner products with the basis images. The inner products give the components of the image that fall into the fringe subspace. Subtracting these components, the image gets denoised. The image on the right hand side is denoised with 59 basis images.

Chapter 6

Collisions with controlled chemical reactivities

6.1 Overview

The UPMs can be roughly divided into two groups according to their chemical reactivity in the absolute ground state. The reactive species include KRb, LiNa, LiK, LiRb etc., while the nonreactive species include NaK, NaRb, RbCs etc. Such a classification makes sense because, on one hand the reactive ones are ideal candidates for ultracold chemistry researches, while on the other hand nonreactive ones are expected to possess extremely long trap lifetime for other research purposes. However, the extremely long trap lifetime doesn't show up along with the advent of several nonreactive UPM species in the recent years[11, 12, 13, 14].

The nonreactive UPMs can be easily tuned to be reactive by the method of vibrational excitation, which has already been established as an efficient way to control both the chemical reaction rate and the outcome since the 1970s[94, 95, 96, 97]. In most cases, one or two quanta of vibrational excitation are enough to switch on the chemical reactivity for UPMs. One can easily prepare molecules with those excitations by simply tuning the wavelength of the dump beam of STIRAP. Such ability is already demonstrated in the previous chapter.

Equipped with the control ability of the vibrational degree of freedom and driven by the mysterious trap loss for nonreactive UPMs, we describe in this chapter our investigation on the collisions of ultracold NaRb polar molecules with controlled chemical reactivities. The reactive collision is considered to be a simpler scenario as described in the universal model, which has already been mentioned in chapter 2. A comparison between the reactive collision and the nonreactive collision should give insights to the physics of the nonreactive collision and check the validity of proposed models such as the highly resonant scattering picture of molecules mentioned in chapter 2.

6.2 Chemical reactivity of Na and Rb system

The main feature of the Na and Rb diatomic molecules that enables our investigation is illustrated schematically in Fig. 6.1. For NaRb molecules in the absolute ground state, the reaction

$$\begin{aligned} &\mathrm{NaRb}(v=0,J=0)+\mathrm{NaRb}(v=0,J=0)\\ &\rightarrow \mathrm{Na}_2(v=0,J=0)+\mathrm{Rb}_2(v=0,J=0) \end{aligned} \tag{6.1}$$

is endothermic by 47 cm^{-1}[98, 99, 100, 101]. Here, v and J are the vibrational and rotational quantum numbers, respectively. The situation is starkly different for NaRb in the first excited vibrational level because the reaction

$$\begin{aligned} &\mathrm{NaRb}(v=1,J=0)+\mathrm{NaRb}(v=1,J=0)\\ &\rightarrow \mathrm{Na_2}(v=0,J=0)+\mathrm{Rb_2}(v=0,J=0) \end{aligned} \tag{6.2}$$

is exothermic by 164 cm^{-1}[98, 99, 100, 101]. This large amount of energy released can be disposed into many vibrational and rotation levels of the Na_2 and Rb_2 product molecules as well as the relative translational motions (partial waves) between them when two ($v = 1$, $J = 0$) NaRb molecules react. This reaction, as well as all other bimolecular reactions between alkali molecules[98, 102], should be barrierless with the Na_2Rb_2 potential well lying thousands of wave numbers below both the NaRb + NaRb and the Na_2 + Rb_2 asymptotic limits.

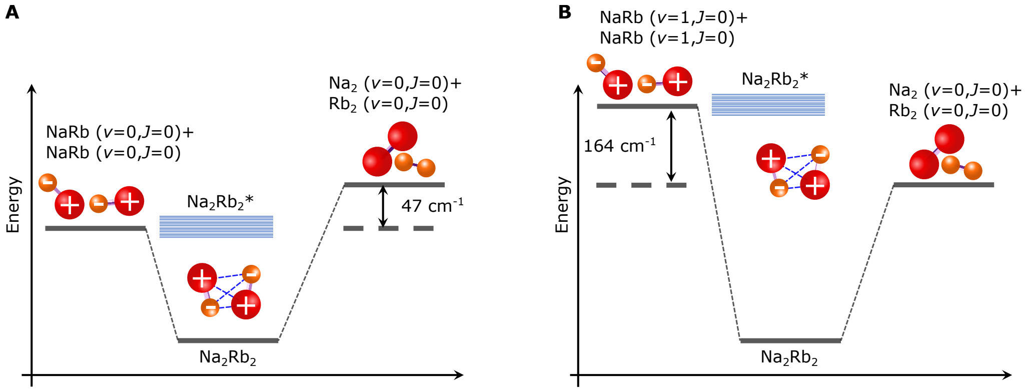

Figure 6.1: The schematic reaction coordinates for the NaRb + NaRb → Na_2 + Rb_2 process are shown. (A) In the lowest rovibrational level (v = 0, J = 0), the reaction is endothermic by 47 cm^{-1} and thus forbidden at ultracold temperatures. (B) In the first excited rovibrational level (v = 1, J = 0), the same reaction is already exothermic by 164 cm^{-1} and thus allowed. Molecules can also relax from v = 1 to v = 0 following the collision, but experimentally, this cannot be distinguished from chemical reactions. The ground Na_2Rb_2 tetramer level, which has much lower energy than both the reactant and product molecule pairs, is also shown. Near the NaRb + NaRb collision threshold, the density of Na_2Rb_2* states is estimated to be too large to be resolved. As a result, the collision is in the highly resonant regime.

Besides the above dimer + dimer to dimer + dimer reaction, several other types of reactions including atoms or trimers can happen in such a Na and Rb system. To facilitate the discussion not only in this chapter, but also later chapters. I list here all relevant energy levels in Table. 6.1.

Table 6.1: The binding energies of ground-state dimers and trimers of Na and Rb system

Species	Binding energy (cm^{-1})	Ref.
Na_2	5942.688(5)	[99]
Rb_2	3965.8(4)	[103]
NaRb	4977.308(3)	[89]
Na_2Rb	7649	[98]
$NaRb_2$	6783	[98]

6.3 Procedures

The starting point of the experiment is an ultracold mixture contains about 2×10^5 atoms prepared in $|F, m_F\rangle = |1, 1\rangle$ state for both species at the high B-field condition, with Na partially in the BEC state and thermal Rb near the BEC critical point. The acquisition of the ultracold mixture has already been described in chapter 3. Here F stands for the total angular momentum of the atom and m_F is its projection on the quantization axis.

The typical experimental time sequence is plotted in Fig. 6.2. Before the magneto-association of the Feshbach molecules, the B-field is at 349.5 G which is above the interspecies Feshbach resonance locating at 347.64 G. The B-field ramps across the resonance with a rate of -2.2 G/s and the Feshbach molecules are produced. Immediately after the association, the ramping rate is reduced to -1.7 G/s for the removal of the residual atoms with MWs and lasers. Once we get a pure sample of Feshbach molecules, the B-field quickly ramps to 335.2 G at which the Feshbach molecules are transferred to the ground states via the STIRAP. The ODT power is immediately increased with the production of the ground-state molecules to suppress the molecular motion. Then, a 2 ms long magnetic gradient field pulse is applied to ensure the purity of the sample as atoms are pushed away while the ground-state molecules are left unperturbed due to the negligible magnetic dipole moment. The molecules are then held in the ODT for variable holding times. After the holding, the ODT power returns to its lower value and the STIRAP transfers the molecules back to the Feshbach state. For the measurement of number N evolution (as shown in Fig. 6.2), the B-field is quickly raised to 348 G to dissociates the molecules and then cut off. The atoms are further held in ODT for 20 ms to let the B-field settle down. The atomic loss during the low-field holding is verified to be negligible. The atoms (usually Rb) are imaged after an 2-ms TOF. For the measurement of temperature T evolution, the ODT is cut off immediately after the backward STIRAP while the dissociation is delayed for a 2-ms molecule TOF. The temperature is determined via the single-shot method with a total TOF of 3 ms.

6.4 Exclusion of dependencies on several factors

Although the ensemble in an AMO experiment in many sense is a clean and isolated system, the ensemble still inevitably interacts with external dc or ac fields. Since the trap loss of nonreactive NaRb molecules can not be trivially understood in terms of chemical reaction or relaxation of internal degree of freedoms, one should be suspicious about that the loss may be some "catastrophic" consequence of some factors from the technical aspect. In our case, those factors includes the non-100% STIRAP efficiency, the choice of

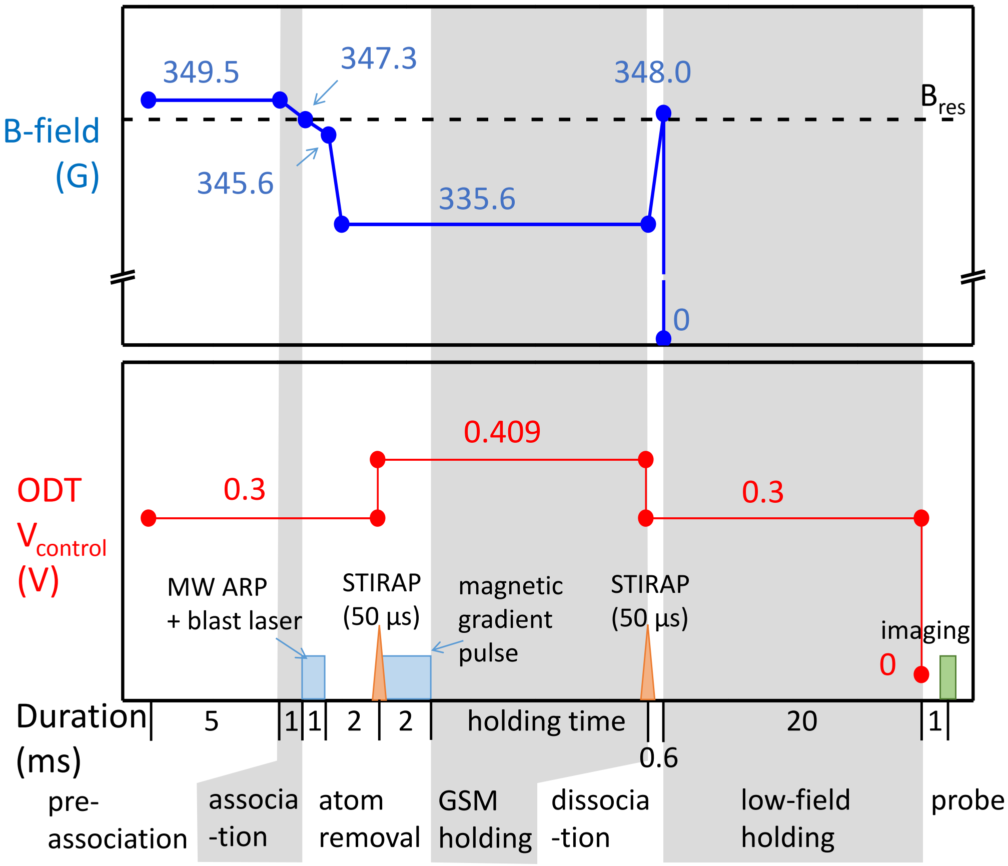
B-field
(G)
349.5
347.3
348.0
B_{res}
345.6
335.6
0
ODT
$V_{control}$
(V)
0.3
0.409
0.3
MW ARP
+ blast laser
STIRAP
(50 μs)
magnetic
gradient
pulse
STIRAP
(50 μs)
imaging
0
Duration
(ms)
5
1
1
2
2
holding time
0.6
20
1
pre-
association
associa
-tion
atom
removal
GSM
holding
dissocia
-tion
low-field
holding
probe

Figure 6.2: The experimental time sequence for collision experiments. The sequence is mainly divided into seven phases, i.e. the pre-association, the association, the atom removal, the ground-state molecule (GSM) holding, the dissociation, the low-field holding and the probe. B-field, ODT power control voltage and other relevant pulses that involves molecular state transfer and residual atom removal are shown.

the ODT wavelength and the choice of the B-field value. Logically, to perform a rigid investigation on collisions with controlled chemical reactivities, one need to first identify the roles and evaluate their effects of these factors.

6.4.1 Exclusion of dependency on STIRAP efficiency

Since the STIRAP efficiency is never 100% in reality, there is always a small portion of the Feshbach molecules that leave the Feshbach state but does not reach the target state. These molecules may occupy a series of rovibrational levels of the $X^1\Sigma^+$ and $a^3\Sigma^+$ potentials. It is always a concern that these populations in the “dark” states can cause unexpected and unaware losses for the ground-state molecules via collisions. In order to evaluate this effect, we measure the two-body loss rate constant β of the ground-state molecule at STIRAP efficiencies from 63% to 91%. The reduction of the STIRAP efficiency is achieved by reducing the STIRAP power delivered. With the same 50 μs overlap of the pump and the dump beam, the maximum transfer efficiency is achieved with a pump/dump Rabi frequency of $2\pi\times1.2$ MHz while the lowest corresponds to $2\pi\times0.3$ MHz. As can be seen from Fig.6.3, β only has a very weak dependence on the STIRAP efficiency. A linear fit gives an increase of 1.8% in β per 10% decrease of the STIRAP efficiency. The result indicates the molecule population not in the ground state is not the major cause of the loss. And, under a typical STIRAP efficiency of more than 90%, the influence of the molecules not in the target level can be neglected.

6.4.2 Exclusion of dependency on ODT wavelength

Because the molecular ground state is a singlet state with no electronic magnetic dipole, we lack of the ability of magnetically trapping of those molecules. Therefore, the optical trapping potential is inevitably involved in the exper-

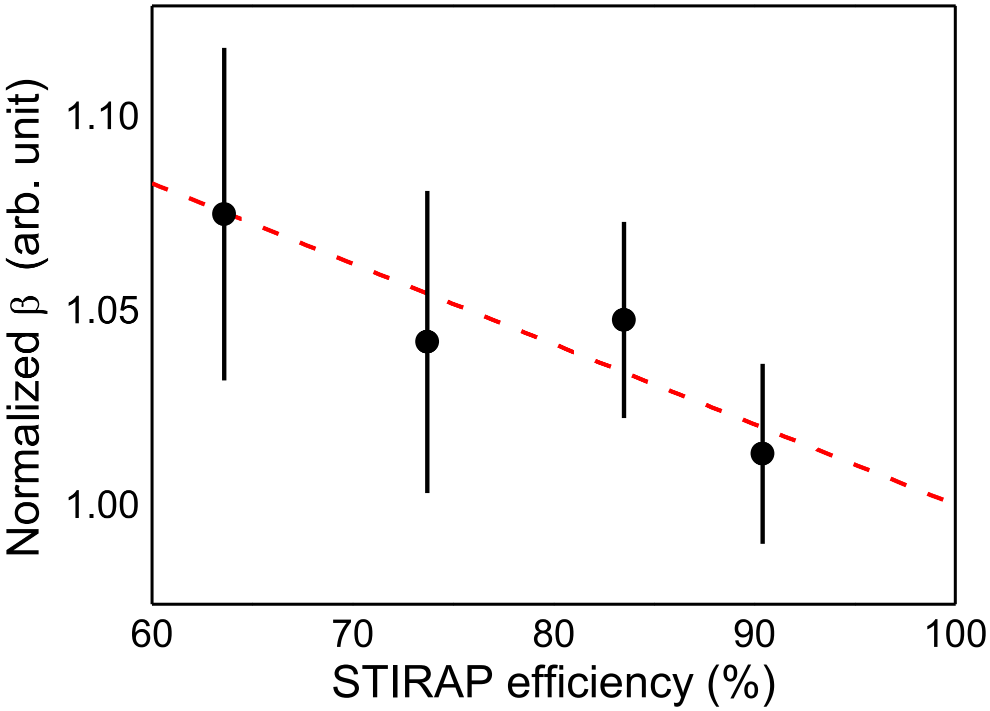

Figure 6.3: The effect of STIRAP efficiency on the resulting loss rate constant β. STIRAP efficiency are controlled by varying the power of the Raman beams. STIRAP efficiencies from 63% to 91% is achieved with pump/dump Rabi frequencies from $2\pi\times0.3$ MHz to $2\pi\times1.2$ MHz. A linear fit shows an 1.8% increase of β per 10% decrease of STIRAP efficiency. The result indicates the molecule population not in the ground state is not the major cause of the loss of the ground-state molecules. Besides, the result shows we can neglect the effect from the non-100% STIRAP efficiency given our STIRAP efficiency higher than 90%

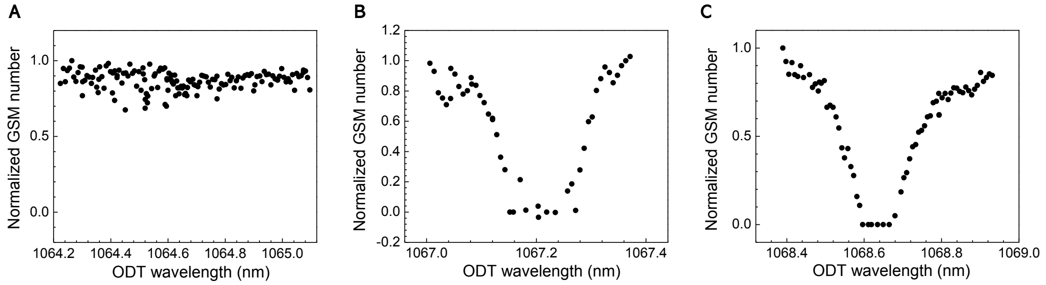

Figure 6.4: The effect of ODT wavelength on the ground-state NaRb molecule's loss. The number of remaining molecules in trap after a certain holding time is measured under different ODT wavelengths. (A) No loss resonance is observed at the vicinity of 1064.4 nm, which is the ODT wavelength used in collision experiments. (B and C)Two of the broad loss features due to resonances of the Feshbach molecule but not the ground-state molecule.

iment. Clearly from the NaRb potentials, there is no state available for a one-photon process to happen starting from the ground state. However, considering the large intensity involved in the optical trapping, there is, in principle, a possibility to have a two-photon process or a photoassociation process of two molecules.

We investigate the dependence of molecule's trap lifetime on the wavelength of the ODT beams. In this set of measurement, we tune the wavelength of the seeding diode laser of the ODT beams, and measure the number of remaining molecules in trap after a certain holding time. We scan the wavelength from 1064 nm to 1069 nm. Here, in Fig. 6.4 show some parts of the result. We do see some resonances as shown in panel (B) and (C). The resonances are quite wide because of the large intensity of the ODT beams (>10 kW/cm^2) and the long interaction time (~10 ms). We double check the existence of those resonances without the STIRAP and find all resonances still exist. This indicates that the signals are all due to the transitions of the Feshbach molecule but not the ground-state molecule. Panel (A) shows the situation at the vicinity of 1064.4 nm, the wavelength which we eventually choose for all of the collision experiments. No resonance and no wavelength dependent loss behavior are observed here.

6.4.3 Exclusion of dependency on B-field

Also because the ground-state molecule doesn't have electronic magnetic dipole, it seems that the choice of the background bias B-field is arbitrary. However, the B-field somehow may matter. In Innsbruck's paper on the production of ground-state RbCs molecule, a B-field dependent loss behavior is observed. When the B-field is lower than a critical value, the molecule's loss greatly enhanced. It is conjectured that the enhanced loss is due to the hyperfine-changing collision as the "ground state" is no longer the ground one below that critical B-field[11]. In our experiment, we also investigate the B-field's role in the collision experiments. The number of remaining molecules in trap is measured after the molecules being held at different B-fields. Fig 6.5 shows a large scale scan from 5.6 G to 339.2 G. The "ground state" is no longer the ground one below 16 G here. We see no obvious B-field dependent loss behavior from the result. Besides the possible loss enhancement from the hyperfine relaxation, we also scan the B-field at the vicinity of 335.2 G where we perform the experiments and exclude the existence of loss resonances in smaller B-field scales.

6.5 Loss comparison and loss model

To best compare the collisions of different chemical reactivities, and also to best understand the underlying mechanism of the loss of the nonreactive case, the evolution of N and T are measured with the most holding times.

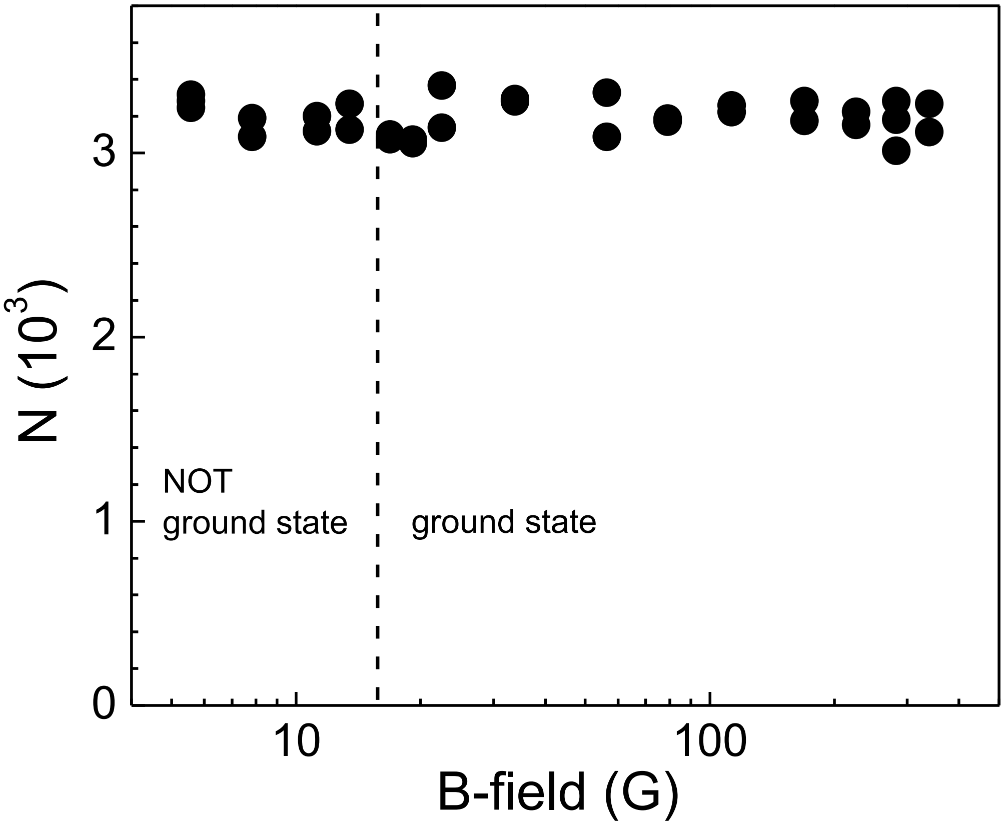

Figure 6.5: The effect of B-field on the ground-state NaRb molecule's loss. The remaining molecule number are measured after a certain fixed holding time under different B-field. Below 16 G, the "ground state" is no longer the ground one. The loss of the ground-state molecule show no dependence on the B-field from 5.6 G to 339.2 G.

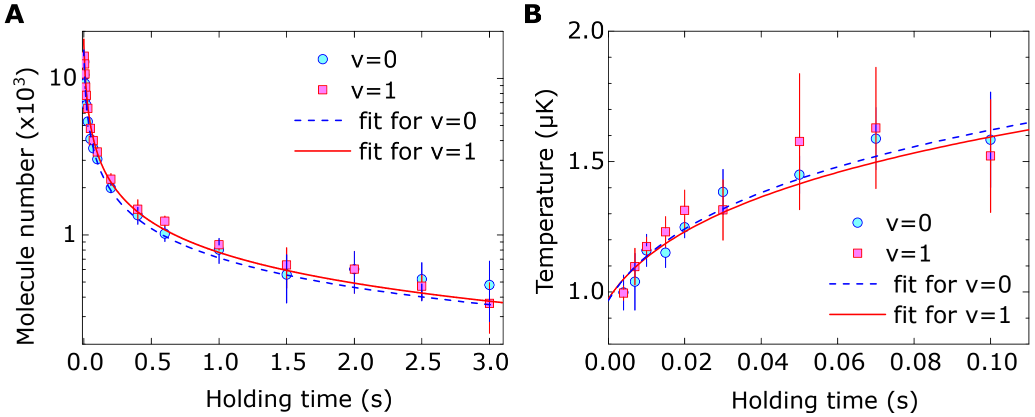

Figure 6.6: Inelastic collisions with different chemical reactivities. (A and B) Time evolutions of (A) molecule numbers and (B) temperatures for both nonreactive ($v = 0$, $J = 0$) (filled circles) and reactive ($v = 1$, $J = 0$) (filled squares) samples. The temperature measurement, which stops at 0.1 s because of reduced signal-to-noise ratio following the time-of-flight expansion, is obtained separately from the number evolution with samples of essentially identical conditions. Error bars represent 1 standard deviation. The blue dashed and red solid curves are fitting results using Eq. 6.3 with temperature-dependent loss rate constants obtained from Fig. 6.8. The measured trap oscillation frequencies are $[\omega_x, \omega_y, \omega_z] = 2\pi \times [217(3), 208(3), 38(2)]$ Hz for the ($v = 0$, $J = 0$) molecules and $2\pi \times [219(3), 205(2), 40(2)]$ Hz for the ($v = 1$, $J = 0$) molecules. The calculated initial peak densities can reach 6×10^{11} cm^{-3}.

Imaging along the long axis of the trap enables the N evolution as long as 3 s as shown in Fig. 6.6. The dynamical range of N is then nearly 40 times. The temperature evolution however, because of its longer TOF, has the largest holding time of 0.1 s. A very striking feature in Fig. 6.6 is the number loss and the heating of the two cases being nearly identical, despite their distinctly different chemical reactivities and the very large range of number variations. Both the nonlinear appearance of N evolution in the log-linear plot and the increase in the T evolution indicate the loss is not one-body process. On the other hand, if we attribute the loss to a three-body process, we find the loss rate constant is way beyond the unitarity limit. Hence, to obtain a more quantitative picture, we simultaneously fit the number and temperature evolutions for each case to the two-body loss model[104]

$$\begin{aligned} \frac{\mathrm{d}N(t)}{\mathrm{d}t} &= -\beta A \frac{N(t)^2}{T(t)^{3/2}} \\ \frac{\mathrm{d}T(t)}{\mathrm{d}t} &= -\beta A N(t) \frac{1/4 + h_0}{T(t)^{1/2}} \end{aligned} \tag{6.3}$$

to extract the loss rate constant β. Here, $A = (\overline{\omega}^2 m/4\pi k_B)^{3/2}$ is a constant, where m is the mass of the molecule and $\overline{\omega}$ is the geometric mean of the trap frequencies, which is measured to be $2\pi\times119.9(1.5)$ Hz for ($v = 0$, $J = 0$) molecules and $2\pi\times122.0(1.5)$ Hz for ($v = 1$, $J = 0$) molecules.

The heating phenomena here is called the "anti-evaporation effect". It is due to the fact that the average energy of lost particles is lower than the ensemble average. The 1/4 term on the right-hand side of the T evolution is from the trapping potential part. For a two-body process, whose chance of occurrence is proportional to the square of the local density, one can easily find that the average potential energy of lost particles is merely $3/4 \times k_BT$ instead of the ensemble average of $3/2 \times k_BT$ in a 3-dimensional harmonic trap. The h_0 term deals with the momentum dependence of β as well as any other possible heating contributions. Assuming $\beta(T) = \beta_0(T/T_0)^b$, where β_0 is the rate constant at a selected sample temperature T_0, one can find $h_0 =$ -$b/6$[104]. Note that although the number loss and heating in Fig. 6.6 appear identical for the two cases, the β values are actually slightly different because of slight difference of the trap frequencies and the initial molecule numbers.

6.6 Segment fit

There is an annoying loop in the data analysis of the collision experiments. We know that the sample temperature evolves during the holding. Hence, a correct modelling needs the correct $\beta(T)$ function. However, on the other hand, it is exactly this function that we want to find out through the model fitting. Therefore, we need to find a way to break the loop.

Fig. 6.7 shows the way we break the loop. To extract the T dependence of β, we first pick four segments from a whole measurement based on the criteria that the change of T is less than 20% during each segment. The segments partially overlap with each other. The segments here are 4 ms $\sim$ 21 ms, 12 ms $\sim$ 33 ms, 27 ms $\sim$ 60 ms and 41 ms $\sim$ 100 ms. Given the relative small variation of T, we assume the change of β is also small and take it as a constant in each of these segments. Here, only data from the first 100 ms are used since we cannot measure the temperature reliably for holding times beyond that.

For each segment, the evolutions of N and T are fitted simultaneously with the two-body loss model Eq. 6.3 by minimizing the total dimensionless χ^2, defined as

$$\chi^2 \equiv \sum_{i;\ y=N,T} \frac{(y_i - \overline{y}_i)^2}{\Delta y_i^2}. \tag{6.4}$$

Here, y_i is the fitted value, $\overline{y}_i$ and Δy_i are the mean and the standard deviation of the measurements respectively. The free parameters of the fit are the initial number $N(0)$, the initial temperature $T(0)$, β and h_0. In Fig. 6.7, the fitting results of each segments are color coded.

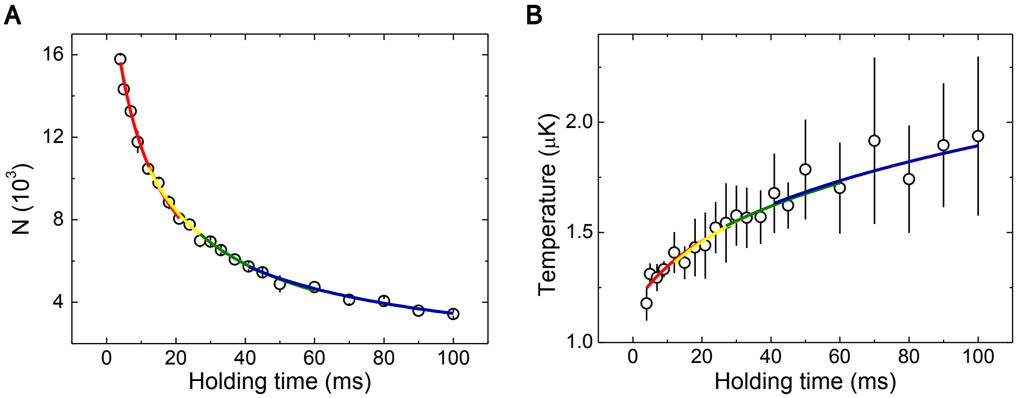

Figure 6.7: Extraction of β with segment fit. The number evolution (A) and the temperature evolution (B) are measured from holding time = 4 ms to holding time = 100 ms. The each whole curve, it is divided into four segments, coded with different color. In each segment, the temperature evolution doesn't exceed 20%, so that we can neglect the temperature dependence of β and treat β as a constant parameter in the fitting model Eq. 6.3. The number and the temperature in each segment are fitted together by minimizing a joint χ^2.

6.7 Temperature dependence

The segment fitting procedure is repeated for several data sets with initial temperatures ranging from 370 nK to 1.4 μK. The different temperature of the molecules are inherited from the temperature of the ultracold mixtures prepared in ODTs of different trap depths. Following the temperature increase, this has allowed us to sample β from 390 nK to 1.85 μK for the nonreactive molecules and from 500 nK to 1.85 μK for the reactive molecules. Fig. 6.8 shows the results with the mean temperature of each corresponding segment as the horizontal axis. Within the temperature range covered, the lowest and the highest β values only differ by a factor of 2. This small dynamical range and the relatively large error bars prevented us from confirming any structures in β, although an overall decrease toward higher temperatures is obvious for both cases. In addition, the measured β values for nonreactive samples are all larger than those for the reactive ones within the same temperature range. In the log-log scale, forcing linear fits to the data points in Fig. 6.8, slopes of b = -0.38(4) and b = -0.27(8) can be obtained for nonreactive and reactive samples, respectively. Thus, approximately, during each set of measurements, the loss rate constant follow a power-law function $\beta(T) = \beta_0(T/T_0)^b$. Substituting b in Eq. 6.3 with this function and h_0 with -b/6, the number and temperature evolutions in Fig. 6.6 can be fitted again to obtain the β_0 values. The solid and dashed curves in Fig. 6.6 shows this fitting result. For the data set of nonreactive molecules, this kind of modeling gives $\beta_0 = 3.4(2)\times10^{-10}$ cm^3 s^{-1} at $T_0 = 0.97(9)$ μK. For the reactive molecules, $\beta_0 = 2.7(2)\times10^{-10}$ cm^3 s^{-1} at $T_0 = 0.97(2)$ μK is obtained. Within the mutual error bars, the two β_0 values obtained this way agree with the corresponding data points around 0.97 μK in Fig. 6.6. This agreement verifies self-consistently that the β values obtained by the segment fitting method are reasonable.

A temperature-dependent β signifies the collisions are not in the Wigner threshold regime in which $\beta \propto T^l$ should be a constant for s-wave (l = 0) collisions. This non-Wigner behavior can be understood by the much smaller characteristic temperature of the van der Waals potential $T_{\mathrm{vdW}} = (\hbar^2/mr_6^2)(1/k_B)$ for NaRb[64], which is only 2.8 μK because of the very large long-range C_6 coefficients[59, 60, 61]. Here, $r_6 = (mC_6/\hbar^2)^{1/4}$ is the characteristic length. The Wigner threshold regime which requires that $T << T_{\mathrm{vdW}}$, is thus not reached with the current sample temperature.

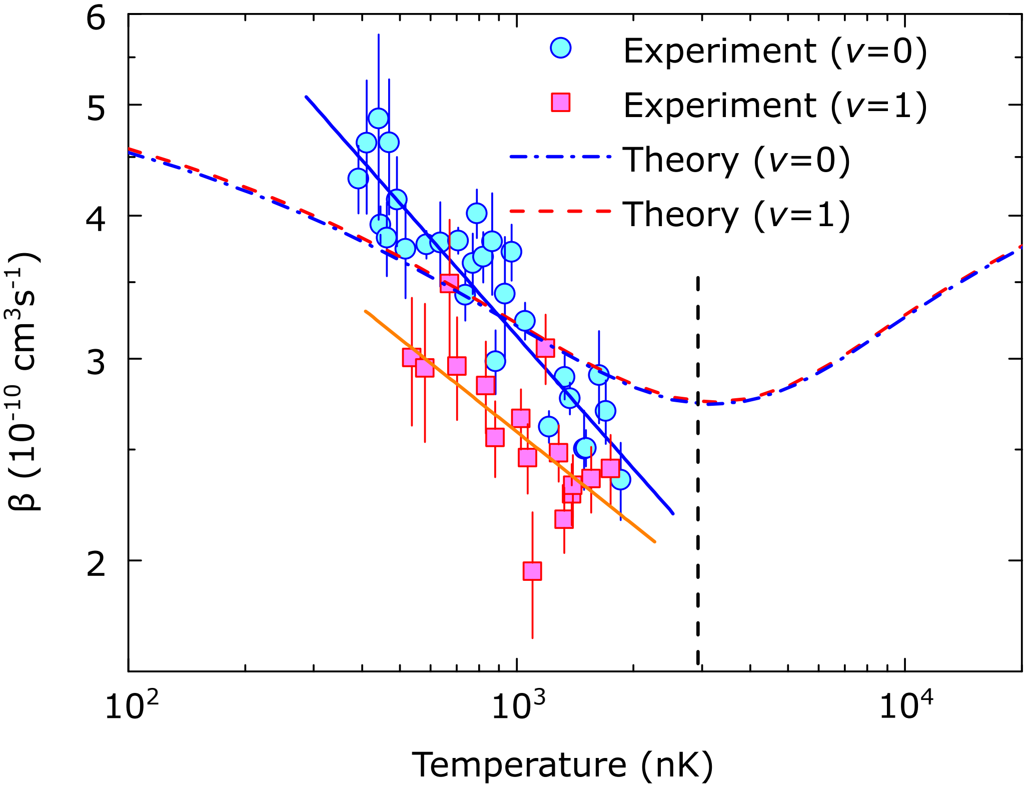

Figure 6.8: Temperature dependence of β for different chemical reactivities. Each β is obtained from a fit to Eq. 6.3 to a segment of one full loss and heating measurement. The solid lines are from fits of β to power-law functions of T. Theoretical results based on the CC calculation are also shown. The dashed vertical line marks the position of T_{vdW}. The error bars represent 1 standard deviation.

6.8 Comparison with close-coupling quantum calculations

For the reactive case, the loss can be well understood with the universal model with the rate constant and its temperature dependence determined by the long-range collision dynamics[16, 64, 105, 106, 107]. For the nonreactive case, in the framework of the highly resonant scattering picture of UPMs[62], the loss of the dimer molecules is think of as a result of the formation of tetramers. If a unity probability is assumed for the formation of the tetramers at the short range, we reach the same universal model as already be pointed out in chapter 2. On the basis of this model, we performed close-coupling (CC) quantum calculations for both ($v = 0$, $J = 0$) and ($v = 1$, $J = 0$) NaRb molecules using a time-independent quantum formalism, including the rotational structure of the molecules and a partial wave expansion[75]. As shown in Fig. 6.8, semi-quantitative agreements between the calculations and the data can already be obtained without any free parameters in terms of the absolute value of β. However, from the calculation, because the C_6 coefficient between two ($v = 0$, $J = 0$) NaRb molecules is nearly identical to that between two ($v = 1$, $J = 0$) NaRb molecules[59, 60, 61], the complex formation rate constant for nonreactive molecules (blue dashed-dotted curve) is essentially the same as the loss rate constant for reactive molecules (red dashed curve). This actually cannot explain the apparently larger β measured for nonreactive molecules. This discrepancy could reflect the idea that the short-range physics for chemical reaction and complex formation are not exactly identical. It is possible to modify the rate constants for better agreements if more elaborate short-range models, including a non-unity reaction probability and the phase of the reflected scattering wave, were considered[75].

6.9 Post-complex formation dynamics

6.9.1 Rice-Ramsperger-Kassel-Marcus (RRKM) theory

The Rice-Ramsperger-Kassel-Marcus (RRKM) theory is theory of chemical reactivity[51][108][109], developed by Rice and Ramsperger[110] and Kassel[111] and generalized in by Marcus[112]. In chemistry, RRKM successfully explains the long lifetime before dissociation for a energy-rich polymer. The RRKM theory is a transition state theory and in the context of ultracold bimolecular collision, the transition complex is the tetramer and its lifetime is predicted as,

$$\tau_{\mathrm{RRKM}} = \frac{2\pi\hbar\rho}{N_{\mathrm{o}}}. \tag{6.5}$$

Here, ρ is the density of transition complex states at the collisional threshold, N_{o} is the open channel number. The lifetime can be viewed as a result of the competition of the internal and external degrees of freedom. In an intuitive picture, the extra energy randomly flows among different degrees of freedom and the complex only dissociate when the external degree of freedom gains enough energy. More density of states here means more ways to distribute the energy internally, while less open channel number means less way to dissociate the complex.

Although the theory yields quite simple results, one need to remember that it is only an approximation whose core assumptions are the thermal equilibrium assumption and the no return assumption. That is, the molecules' configurations are in equilibrium until they cross a reaction surface, and once the crossover has been, the molecules never cross back again[51].

6.9.2 The complex-mediated collision model

To investigate the post-complex formation dynamics, one needs to develop a more complete loss model instead of the simple two-body loss model. The existence of the complexes in the trap provides two additional physical processes, the molecule-complex collision and the complex dissociation,

$$\begin{aligned} \mathrm{NaRb} + \mathrm{Na_2Rb_2} &\rightarrow \text{"}lost\text{"} \\ \mathrm{Na_2Rb_2} &\rightarrow 2\mathrm{NaRb} \end{aligned} \tag{6.6}$$

The molecule-complex collision kills one more molecule in trap and in total kills three molecules, while the complex dissociation returns back two molecules. The dissociation is the reverse process of the complex formation, so there is no additional energy released and the product molecules can be further trapped. Ref.[62] gives a model that include the post-complex formation dynamics, consisting of two coupled rate equations of the number densities of the molecule n and the four-atom complex n_c

$$\frac{\mathrm{d}n}{\mathrm{d}t} = -\beta_{mm} n^2 + 2\gamma_c n_c - \beta_{cm} n_c n \tag{6.7}$$

$$\frac{\mathrm{d}n_c}{\mathrm{d}t} = \frac{1}{2}\beta_{mm} n^2 - \gamma_c n_c - \beta_{cm} n_c n, \tag{6.8}$$

with β_{mm} and β_{cm} the complex formation and complex-molecule collision rate constants respectively, and $\gamma_c = 1/\tau$ the complex dissociation rate. In principle, the model is correct, but it is inconvenient to use because the differential equations are written in terms of densities instead of the numbers that we measure in the experiment. Thus, we develop a full model in terms of molecule numbers as well as the evolution of the temperature.

If we think of trappable complexes, basically we assume that the complexes are loosely-bound. A loosely-bound molecule's polarizability can be approximated by the sum of the polarizabilities of its constituents. So the first assumption we take in the derivation is, the polarizability of a complex is twice than that of a molecule. Then, since we know that the mass of a complex is also twice than that of a molecule, we can conclude that the trapping frequencies of a complex are exactly the same as that of a molecule.

$$\begin{aligned} \alpha_c &= 2 \times \alpha_m \\ f_{c,i} &= f_{m,i} \end{aligned} \tag{6.9}$$

We still assume that the sample is always in thermal equilibrium. And moreover, the complexes and molecules share the same temperature. Therefore, the distribution of particles all obeys the Boltzmann distribution. For the convenience of the following derivations, we separate the spatial part and the momentum part of the Boltzmann distribution, and define them as two functions, F and G,

$$\begin{aligned} F(x, y, z, m, T, f_i) :=& \, 2\sqrt{2}\pi^{3/2} f_x f_y f_z (\frac{m}{k_B T})^{3/2} \\ & \times \exp\left[-\frac{2\pi^2 m (f_x^2 x^2 + f_y^2 y^2 + f_z^2 z^2)}{k_B T} \right] \end{aligned} \tag{6.10}$$

$$G(p, m, T) := C \times \exp\left[-\frac{p^2}{2mk_B T} \right] \tag{6.11}$$

The β's are defined with the density. Switching to number evolutions, we use $\tilde{\beta}$. Let $\tilde{\beta}_{mm} = A_{mm} \times \beta_{mm}/T^{3/2}$, $\tilde{\beta}_{cm} = A_{cm} \times \beta_{mm}/T^{3/2}$, we find,

$$\begin{aligned} A_{mm} = T^{3/2} & \iiint F(x, t, z, m, T, f_i) F(x, y, z, m, T, f_i) \mathrm{d}x\mathrm{d}y\mathrm{d}z \\ &= \frac{f_x f_y f_z \pi^{3/2} m^{3/2}}{k_B^{3/2}} \end{aligned} \tag{6.12}$$

$$\begin{aligned} A_{cm} = T^{3/2} \iiint & F(x,t,z,2m,T,f_i)F(x,y,z,m,T,f_i)\mathrm{d}x\mathrm{d}y\mathrm{d}z \\ &= \frac{8f_xf_yf_z\pi^{3/2}m^{3/2}}{3\sqrt{3}k_B^{3/2}} \end{aligned} \tag{6.13}$$

The derivation of the temperature evolution is based on the conservation of energy. From

$$\begin{aligned} \frac{\mathrm{d}N_m}{\mathrm{d}t} &= -\tilde{\beta}_{mm} \times N_m^2 + 2\gamma \times N_c - \tilde{\beta}_{cm} \times N_mN_c \\ \frac{\mathrm{d}N_c}{\mathrm{d}t} &= -\frac{1}{2}\tilde{\beta}_{mm} \times N_m^2 - \gamma \times N_c - \tilde{\beta}_{cm} \times N_mN_c \end{aligned} \tag{6.14}$$

we have,

$$\begin{aligned} &(N_m + N_c)T - \frac{3}{4}\mathrm{d}N_{m,1}T + \frac{3}{4}\mathrm{d}N_{m,2}T - \frac{2}{3}\mathrm{d}N_{m,3}T + \mathrm{d}N_{c,1}T \\ &-\mathrm{d}N_{c,2}T - \frac{5}{6}\mathrm{d}N_{c,3}T = (N_m + \mathrm{d}N_m + N_c + \mathrm{d}N_c)(T + \mathrm{d}T) \end{aligned} \tag{6.15}$$

where $\mathrm{d}N_{m,1} = \tilde{\beta}_{mm}N_m^2\mathrm{d}t$, and the rest terms are defined in a similar way according to the order of their appearance in Eq. 6.14. $\mathrm{d}N_m = \mathrm{d}N_{m,1} + \mathrm{d}N_{m,2} + \mathrm{d}N_{m,3}$, and $\mathrm{d}N_c = \mathrm{d}N_{c,1} + \mathrm{d}N_{c,2} + \mathrm{d}N_{c,3}$.

Eq. 6.15 describes the energy flow in and out of the ensemble in a small time interval $\mathrm{d}t$ without an overall constant $3k_B$. The sign of each terms marks the direction of particle flow and the factor is the fraction of the average energy of the particles compared to $3k_BT$. For example, the 3/4 factor before $\mathrm{d}N_{m,1}T$ terms is a sum of $\frac{1}{4}(3k_BT)$ from the spatial potential energy and $\frac{1}{2}(3k_BT)$ from the kinetic energy. The spatial potential energy is calculated from

$$\frac{\iiint V(x,y,z,m,T)F(x,y,z,m,T,f_i)^2\mathrm{d}x\mathrm{d}y\mathrm{d}z}{\iiint F(x,y,z,m,T,f_i)^2\mathrm{d}x\mathrm{d}y\mathrm{d}z}. \tag{6.16}$$

One can then expand the expression, discard the second order small quantities,

$$\begin{aligned}-\frac{3}{4}\mathrm{d}N_{m,1}T+\frac{3}{4}\mathrm{d}N_{m,2}T-\frac{2}{3}\mathrm{d}N_{m,3}T+\mathrm{d}N_{c,1}T-\mathrm{d}N_{c,2}T-\frac{5}{6}\mathrm{d}N_{c,3}T\\=N_m\mathrm{d}T+\mathrm{d}N_mT+N_c\mathrm{d}T+\mathrm{d}N_cT\end{aligned}\tag{6.17}$$

After some substitutions, rearrangements and a division on both sides with dt,

$$\frac{1}{4}\tilde{\beta}_{mm}N_m^2T-\frac{1}{2}\gamma N_cT+\frac{1}{2}\tilde{\beta}_{cm}N_cN_mT=\frac{N_m\mathrm{d}T}{\mathrm{d}t}+\frac{N_c\mathrm{d}T}{\mathrm{d}t}\tag{6.18}$$

Finally we obtain the full model that include the molecule-complex collision and complex dissociation,

$$\begin{aligned}\frac{\mathrm{d}N}{\mathrm{d}t}&=-A_{mm}\beta_{mm}\frac{N^2}{T^{3/2}}+2\gamma_cN_c-A_{cm}\beta_{cm}\frac{N_cN}{T^{3/2}}\\\frac{\mathrm{d}N_c}{\mathrm{d}t}&=\frac{1}{2}A_{mm}\beta_{mm}\frac{N^2}{T^{3/2}}-\gamma_cN_c-A_{cm}\beta_{cm}\frac{N_cN}{T^{3/2}}\\\frac{\mathrm{d}T}{\mathrm{d}t}&=\frac{1}{4}\frac{A_{mm}\beta_{mm}N^2+2A_{cm}\beta_{cm}N_cN-2\gamma N_c}{(N+N_c)T^{1/2}}\end{aligned}\tag{6.19}$$

The best fit of the nonreactive loss and heating data is shown in Fig. 6.9. The fitting results in a complex lifetime of $\tau=1/\gamma=0.038(6)$ s, which is shorter than the lower bound of our estimation from the RRKM theory, and a complex-molecule loss rate constant of $4.4(6)\times10^{-9}$ cm^3 s^{-1}, which is more than one order of magnitude larger than the s-wave unitary limit and is thus nonphysical. Although this seems to support the absence of the complex-mediated collisions, we think that it is still not conclusive because of the crudeness of the approximations made in the model.

Why no post-complex formation dynamics observed? Here, we provide two plausible explanations. Considering the large density of states of tetramer almost everywhere, one thing very likely to happen is that the photons from

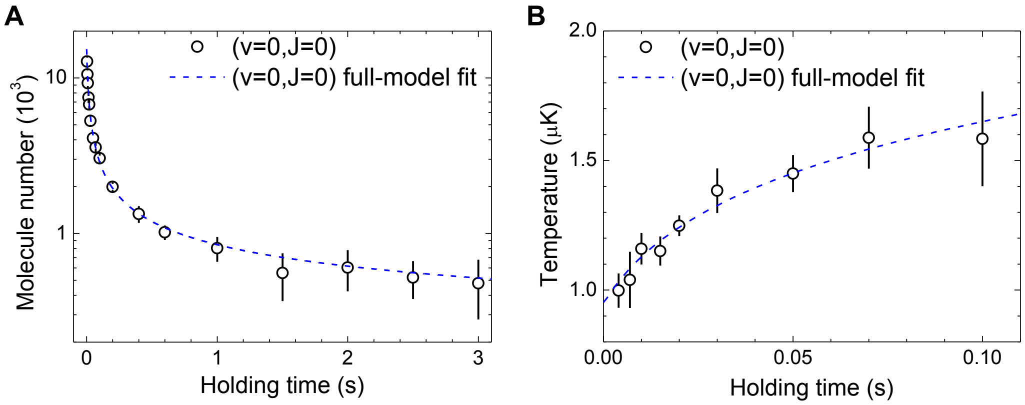

Figure 6.9: Fit the nonreactive collisions with the full loss model including the post-complex formation dynamics. (A)The N evolution and (B)the T evolution are fitted simultaneously with Eq. 6.19. The fitting extracts a complex lifetime $\tau = 1/\gamma = 0.038(6)$ s and a non-physical complex-molecule loss rate constant $\beta_{cm} = 4.4(6)\times10^{-9}$ cm^{3}s^{-1}

the trapping beams can interact with (for example, excite) the complexes and somehow make them no longer in trap quickly. Another possibility is that the complexes are not trappable at 1064.4 nm because of unfavorable polarizabilities. The naive assumption that the complex has twice the polarizability than a molecule is actually questionable here.

6.10 Conclusion

We report in this chapter a detailed study on the inelastic loss with and without the NaRb + NaRb $\rightarrow$ Na_2 + Rb_2 chemical reaction. Contrary to intuitive expectations, we observe very similar loss and heating, regardless of the chemical reactivities. In addition, as evidenced by the reducing loss rate constants with increasing temperatures, we find that these collisions are already outside the Wigner region although the sample temperatures are sub-microkelvin. Our measurement agrees semi-quantitatively with models of the resonant scattering picture based on long-range interactions, but calls for a deeper understanding on the short-range physics for a more complete interpretation.

□ End of Chapter.

Chapter 7

Collisions with induced electric dipoles in E-fields

7.1 Overview

The dipolar collisions, or collisions with DDI of UPMs are basically uncharted so far. On the other hand, it is critical to investigate such collisions. For example, measuring collision rate constants in dc E-fields can provide us a more comprehensive understanding of the underlying mechanisms of the nonreactive UPM losses. In Ref. [65], it is pointed out that the short-range physics can manifest as peaks and valleys in rate constants as the E-field rises. Based on the understandings of the dipolar collisions, one can harness the elastic and the inelastic collisions and enable the evaporative cooling of UPMs[113, 114, 115, 116, 117] just like that for the atoms. The evaporative cooling of UPMs can then lead to the BEC of polar molecules with strong DDI. Even a dipolar BEC of molecules in bulk is going to bring lots of fascinating observations, let alone the Hamiltonian engineering in an optical lattice. In the recent years, the fast developing field of dipolar BEC of magnetic atoms has already made some important observations, such as the *d*-wave patterned collapse[118], the droplet stabilization[119, 120, 121] and the roton quasiparticles[122].

In this chapter, we describe our investigation on the collisions of ultracold nonreactive NaRb polar molecules in a dc E-field. The induced electric dipole reaches as large as 0.7 D. The DDI modifies the collisional behavior and a step-wise enhancement of loss is observed.

7.2 Induction of electric dipole moment

There exists a permanent electric dipole moment for a NaRb molecule due to the asymmetric distribution of the electron cloud in the molecular frame of a NaRb molecule. However, when there is no external E-field, the orientation of the molecular axis has no preference when we project the system from the molecular frame to the lab frame. Therefore, in the lab frame, the molecules are not polarized and don't have electric dipoles. To induce the electric dipole, one needs to exert an E-field.

The E-field in our experiment is generated by a pair of high voltage amplifiers (Matsusada AMT-5B20). The amplifier amplifies an external control voltage by 500 times. The output voltage's range is -5 kV to 5 kV. Although so far, we've only used dc outputs, the amplifiers have a slew rate of 360 V/μs and accept modulated signals up to 40 kHz. The control voltages are given by RIGOL DG1022 aribitrary waveform generators and calibrated by an Agilent Technologies U3402A multimeter. The output cables of the amplifiers are connected to a pair of ITO-coated glass plates with conductive silver adhesive. The plates are 80 mm×23 mm×0.7 mm large and separated by about 25 mm.

Quantum mechanically, the induction of the electric dipole in an E-field can be understood in terms of symmetry. Since the ground state NaRb molecules are in a $^1\Sigma$ potential, they have no total electronic orbital angular momentum or electronic spin. Neglecting the hyperfine structures, we can describe the molecular state with only the rotation angular momentum J and its projection onto the quantization axis m_J. We define the bare states $|J, m_J\rangle$ under the zero E-field condition and those states are the eigenstates of the parity operator. This means that each $|J, m_J\rangle$ state has a certain parity, either odd or even. The dipole operator $\hat{d}$ is a rank-1 tensor operator and inverts the parity symmetry of a state, thus the observable of $\hat{d}$, $\langle J, m_J|\, \hat{d}\, |J, m_J\rangle$, becomes an inner product of two states with different parities and results in a zero value. When there is an E-field, the new eigenstates are no longer the eigenstates of the parity operator, but superpositions of the bare states with different parities and that leads to non-zero dipoles.

To be specific, one can show that the Hamiltonian can be expressed as,

$$\begin{aligned} \langle J, m_J|\, \hat{H}\, |J', m_J'\rangle &= B_v \cdot J(J+1)\delta_{JJ', m_J m_J'} \\ -d \cdot \mathcal{E} \cdot \sqrt{(2J+1)(2J'+1)}(-1)^{m_J} & \begin{pmatrix} J & 1 & J' \\ -m_J & 0 & m_J' \end{pmatrix} \begin{pmatrix} J & 1 & J' \\ 0 & 0 & 0 \end{pmatrix}, \end{aligned} \tag{7.1}$$

where B_v is the rotational constant, d is the permanent dipole, $\mathcal{E}$ is the E-field magnitude. $\begin{pmatrix} \cdots \\ \cdots \end{pmatrix}$ is the Wigner 3j symbol which doesn't vanish unless the first row fulfill the triangle inequality and the second row sum up to zero. Therefore, the E-field couples directly the two states that gives $\Delta m_J = 0$ and $\Delta J = \pm 1$, and indirectly couples all the states with the same m_J.

Diagonalizing Eq. 7.1, we get the dc Stark shift for NaRb ground states with J truncated at $J_{\max} = 9$. Fig. 7.1 shows the calculation result for the lowest three rotational levels of NaRb molecule with $B_v = h \times 2.0896628$

GHz[123] and $d = 3.2$ D[14].

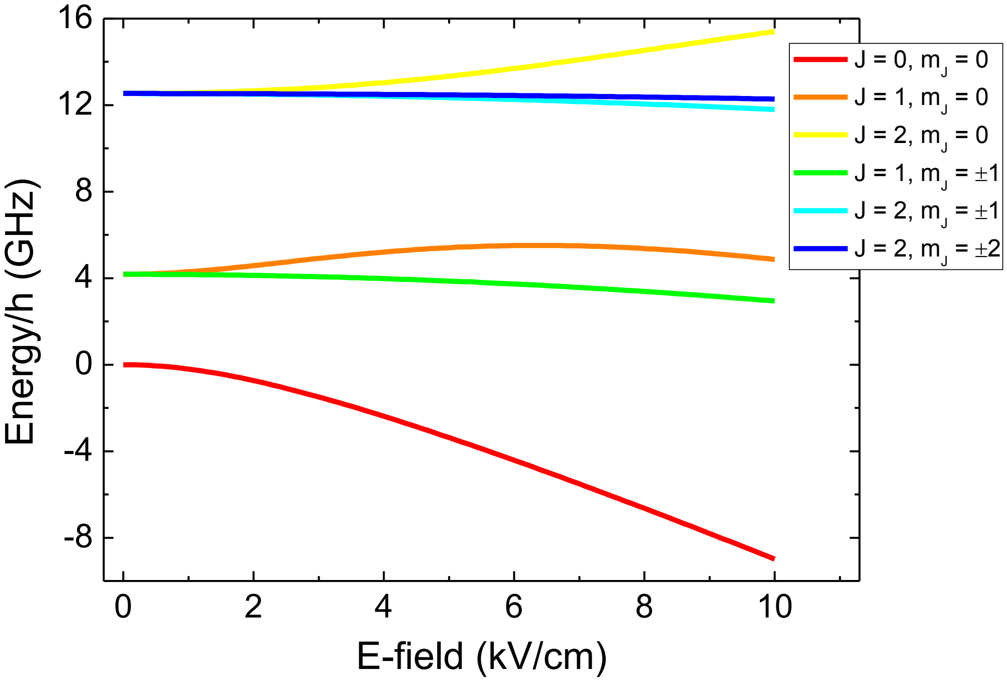

Figure 7.1: dc Stark shift of NaRb molecules in the lowest three rotational levels ($J = 0$, 1, 2). Energy levels are calculated by solving the eigenvalues of Eq. 7.1 with J truncated at $J_{\max} = 9$.

From the dc Stark shift, we can obtain the induced dipole moment from

$$\mu_{\text{ind}} = -\frac{\partial E}{\partial \mathcal{E}}. \tag{7.2}$$

Note that there is a clear distinction between an electric dipole and a magnetic dipole. The electric dipole moment as an extrinsic property, its magnitude can be readily tuned by the strength of the external field as shown in Fig 7.2, while the magnetic dipole moment as an intrinsic property always takes a fixed value.

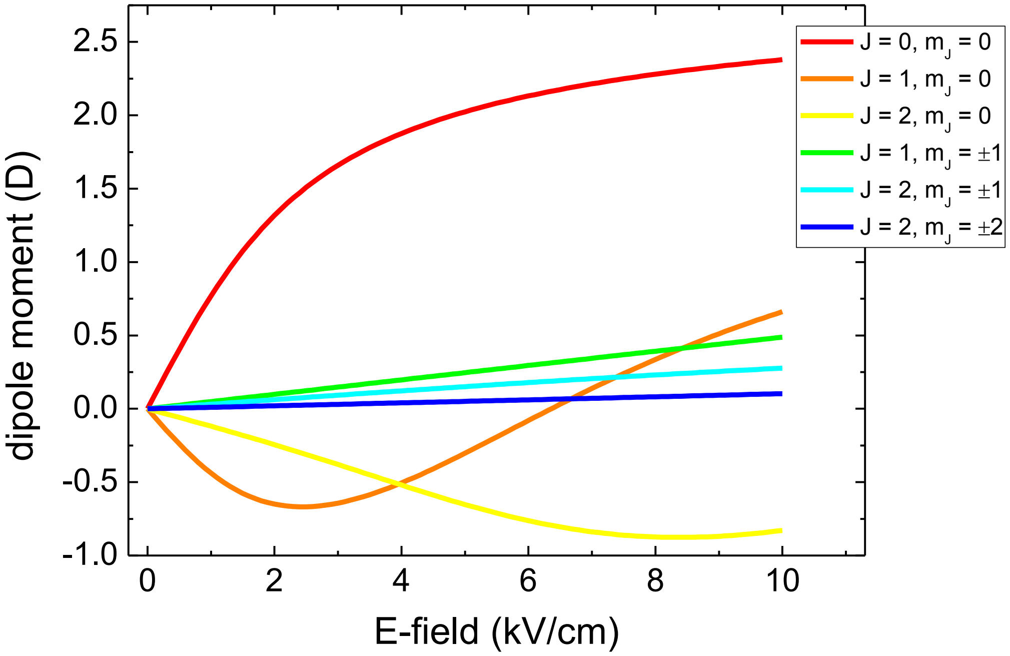

Figure 7.2: Induced electric dipole of NaRb molecule in the lowest three rotational levels ($J = 0, 1, 2$). Dipoles are calculated according to Eq. 7.2 based on the results in Fig. 7.1.

7.3 Modification to molecule-molecule interaction potentials

The E-field modifies the molecule-molecule interaction potential by introducing the DDI term. The effective potential for molecules in the absolute ground state can be written as[106, 63]

$$\langle LM_L|\, V(R)\, |L'M'_L\rangle = \left[\frac{\hbar^2 L(L+1)}{mR^2} - \frac{C_6}{R^6}\right]\delta_{LL',M_LM'_L} - \frac{C_3(L,L';M_L)}{R^3}\delta_{M_LM'_L}. \tag{7.3}$$

Here the first term is the centrifugal potential which will take non-zero value for non-zero L. The second term is the van der Waals interaction characterized by the C_6 coefficient. The first two terms are diagonal terms. The third term is the DDI which is off-diagonal and is characterized by C_3. The C_3 coefficient can be expressed as

$$\begin{aligned} C_3(L, L'; M_L) = {} & \frac{\mu^2}{4\pi\epsilon_0} 2(-1)^{M_L}\sqrt{2L+1}\sqrt{2L'+1} \\ & \times \begin{pmatrix} L & 2 & L' \\ 0 & 0 & 0 \end{pmatrix} \begin{pmatrix} L & 2 & L' \\ -M_L & 0 & M_L \end{pmatrix}. \end{aligned} \tag{7.4}$$

From the Wigner 3j symbol in the expression of C_3, we find that the DDI introduces coupling between different partial waves. Channels with $\Delta L = \pm 1$ and ± 2, and $\Delta M_L = 0$ are directly coupled. Since the NaRb molecules are identical bosons, there are only even partial waves, so ΔL can only take ± 2. The same M_L components from all even partial waves are then mixed either directly or indirectly. Due to the coupling, the partial wave L doesn't remain a good quantum number. However, for the convenience of the discussion, we still label them as what they should be at the infinity far away.

To map out the interaction potentials, we have to diagonalize the system defined by Eq. 7.3 for each value of R. The van der Waals coefficient C_6 can be divided into two parts, one from electronic structures and one from rotational structures. For the electronic one, we take the value from Ref. [61], $C_6^{el} = 9018$ a.u., and for the rotational one, we calculate it with $C_6^{rot} = d^4/(96\pi^2\epsilon_0^2 B_v) = 1.3184 \times 10^6$ a.u. based on our experimental measurement of permanent dipole $d = 3.2(1)$ D [14] and rotational constant $B_v = h \times$ 2.0896628(4) GHz[123]. The total C_6 is then 1.3274×10^6 a.u.

We visualize the E-field's modification to the molecule-molecule interaction potentials. Fig. 7.3 compares the potentials with zero induced dipole and 0.5 D induced dipole. Panel (A) shows the case of $L = 0$. We see with the DDI, and the potential clearly becomes more attractive with considerable decline of $\sim \mu$K start to take place at larger $R \sim 2000 a_0$. Panel (B) shows the case of $L = 2$. When there is no dipole, we see that the five M_L components are degenerate with a barrier of 17.2 μK locating at $R = 600\ a_0$. When there is a dipole, the different coupling schemes introduced by the DDI breaks the degeneracy. We see a suppression of the barrier for $|M_L| = 1$ and also an enhancement of the barrier for $|M_L| = 2$. The modification of the potential shape reflects the strong mixing of different partial waves. To better understand it, we look into the eigenstates of those channels. For instance, at $R = 630\ a_0$, the so-called $M_L = -2$ channel is actually 0.752$\times\ |2, -2\rangle$+0.633$\times\ |4, -2\rangle$+0.180$\times\ |6, -2\rangle$, the so-called $M_L = -1$ channel is 0.859$\times\ |2, -1\rangle$+0.497$\times\ |4, -1\rangle$+0.119$\times\ |6, -1\rangle$, and the so-called $M_L = 0$ channel is 0.703$\times\ |0, 0\rangle$-0.337$\times\ |2, 0\rangle$-0.596$\times\ |4, 0\rangle$-0.191$\times\ |6, 0\rangle$. The enhancement of the barrier of the $M_L = -2$ state is mainly due to the strong coupling to the centrifugal barrier of the $|4, -2\rangle$ state and the repulsive DDI for the $|2, -2\rangle$ state. On the other hand, the suppression of the barrier for $M_L = -1$ is due to the strong attractive DDI between all its components. The $M_L = 0$ lays in between and has strong mixing to the $|0, 0\rangle$ state and the $|4, 0\rangle$ state. Even the $|2, 0\rangle$ state itself is not the largest component. The large repulsive DDI between the $|2, 0\rangle$ state and the $|0, 0\rangle$ state cancels much of the other attractive DDI contributions and left this channel less modified.

7.4 E-field dependence and temperature dependence of dipolar collision

We measure the loss rate constant β with respect to the induced dipole. The experimental procedure is similar as what we discussed in the previous chapter. We turn on the E-field in 15 to 40 μs after the molecules are prepared in the ground state. As shown in Fig. 7.2, with less than 1 kV/cm of E-field,

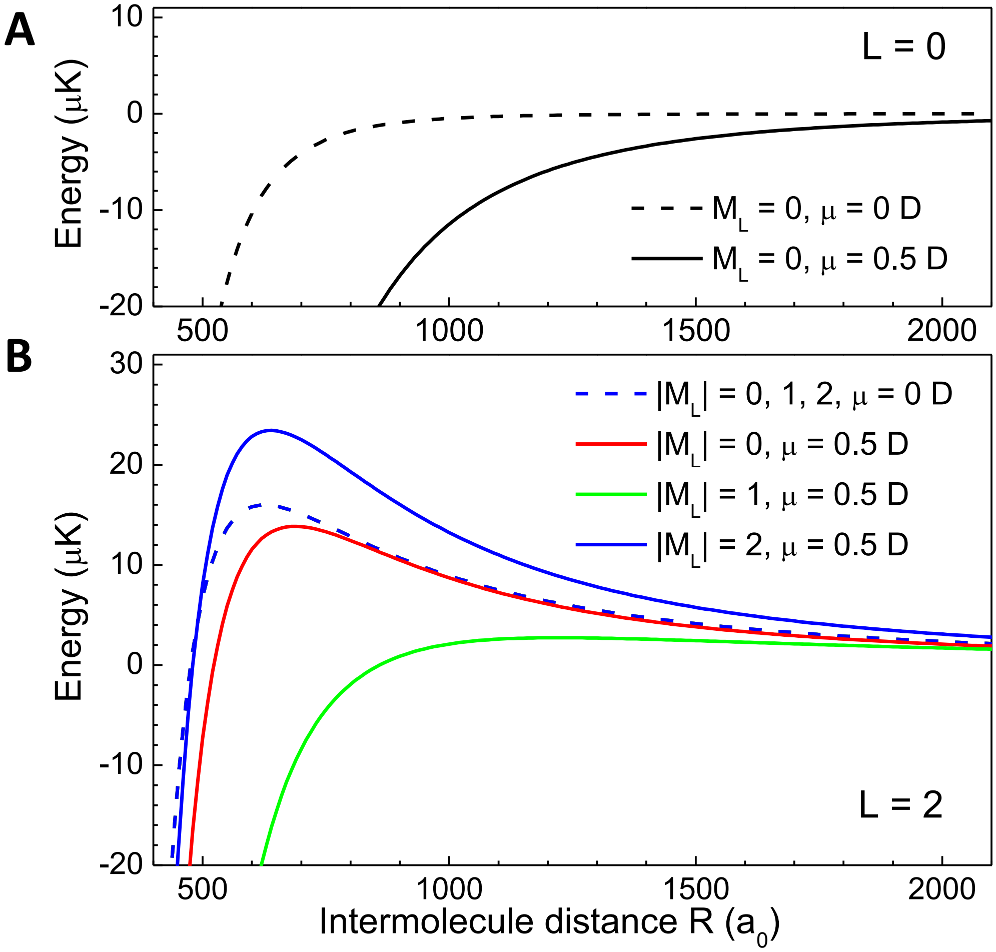

Figure 7.3: DDI's modification to molecule-molecular interaction potentials. (A)The modification of the *s*-wave potential. The dashed curve is for $\mu = 0$ D and the solid curve is for $\mu = 0.5$ D. The potential becomes more attractive with the DDI. (B)The modification of the *d*-wave potentials. The blue dashed curve is for $\mu = 0$ D. Without the induced dipole, the different M_L channels are degenerate. The *d*-wave barrier with a height of 17.2 μK is located at 600 a_0. For $\mu = 0.5$ D, the DDI breaks the degeneracy of different $|M_L|$ and results in substantially modified heights and locations of the barriers.

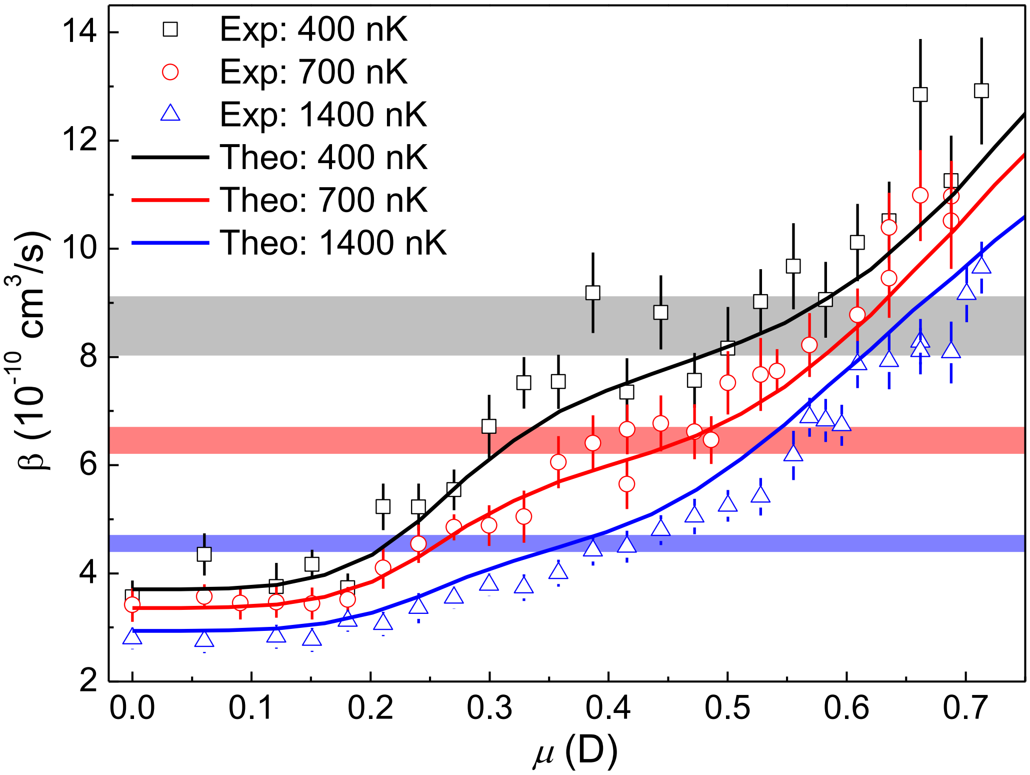

Figure 7.4: β's dependence on induced dipole moment under different temperatures. The induce dipole moment ranges from 0 to 0.7 D with E-field less than 1 kV/cm. The data points in black squares, red circles, and blue triangles are measured with sample temperatures of about 400 nK, 700 nK and 1400 nK, respectively. The solid curves of the same colors are close-coupling calculations with the corresponding sample temperatures. The horizontal belts indicate the unitarity limit of the *s*-wave scattering with temperature ranges of 400 ± 50 nK, 700 ± 50 nK and 1400 ± 100 nK. β increases stepwisely with a plateau occurs at the unitarity limit of the *s*-wave scattering. The overall magnitude of β is smaller and the plateau is vaguer for higher sample temperature.

we can already polarize the ground-state molecule up to 0.7 D. The molecules are held in the ODT for 20 ms. During the holding, the N evolution and the T evolution are measured. Because of the short holding time, the increase in T is less than 30%. For instance, the black set of data in Fig. 7.4, the initial molecule T is about 350 nK, while the average T during the course of holding is about 400 nK. We do observe for larger β cases, the average T tend to be slightly larger, which agrees with the anti-evaporation model. For the black set of data, the average T ranges from 360 nK to 440 nK. From each pair of evolutions, we fit β according to the two-body loss model.

We see an overall increase of β with the increase of the induced dipole. An interesting feature is that the enhancement is step-wise. There is a plateau between 0.4 D to 0.55 D where β cease to increase. The grey belt presents the s-wave unitarity limit for 400 nK ± 50 nK. The position of the plateau agrees well with the unitarity limit. Therefore, we attribute the loss before the second rise to the s-wave and the loss start from the plateau to the d-wave. For dipolar collisions in the Wigner regime, there is a universal relation between β and μ, $\beta \propto \mu^{4(L+1/2)}$[63, 106]. For identical bosons, $\beta_{s-wave} \propto \mu^2$ and $\beta_{d-wave} \propto \mu^{10}$. Fitting the 400 nK data set, we find $\beta_{s-wave} \propto \mu^{1.3(0.6)}$ and $\beta_{d-wave} \propto \mu^{5.4(2.1)}$, giving another clue that our system is outside the Wigner regime.

Knowing that our system is outside the Wigner regime, we also investigate the temperature effect. Molecular sample of different temperatures up to 1400 nK are prepared in ODTs with different trap depths and similar data acquisition and analysis are performed. The results are shown in red circle and blue triangle in Fig. 7.4. With the increasing temperature, the overall magnitude of β decreases which agrees with the observation in the previous chapter. Meanwhile, the plateau feature becomes vaguer. The s-wave unitarity limits defined by the two other temperature are also shown in colored belts in Fig. 7.4, with the red belt for 700 nK ± 50 nK and the blue belt for 1400 nK ± 100 nK.

7.5 Characteristic energy scales

To quantitatively describe and understand the observations, we introduce the generalized characteristic length for power-law potentials -C_α/R^α,

$$r_\alpha = \left(\frac{mC_\alpha}{\hbar^2}\right)^{1/(\alpha-2)}, \tag{7.5}$$

and its corresponding characteristic energy[124]

$$E_\alpha = \frac{\hbar^2}{mr_\alpha^2}. \tag{7.6}$$

When the s-wave potentials are modified with the DDI, the potential doesn't strictly follow $1/R^6$ or $1/R^3$. An effective α can be extracted by fitting the potential to -C_α/R^α. The fitting result is not unique and it depends on the range of potential that you put in your fitting. While the outer bound show negligible effect in the fitting, we do observe that the inner bound have some effect. In practice, we consistently take the range from $R = 400\ a_0$ to $2000\ a_0$ and fit the s-wave potentials calculated with μ up to 0.7 D. The inner bound $400\ a_0$ is smaller than r_6 so that the contribution of the van der Waals interaction can be effectively taken into account. Fig. 7.5(A) shows how this characteristic energy changes as the molecules become more polarized. The whole figure as shown is divided into three regimes with two vertical dashed lines at $\mu = 0.21$ D and $\mu = 0.44$ D. Start from the left, in the first regime, the van der Waals interaction dominates. The weak DDI can hardly make significant modifications to the nature of the potential, and α is nearly 6. In the third regime, the DDI dominates, α is nearly 3 and the van der Waals interaction is no longer important. The energy values are approximately constant in both regimes. In between is a transition regime, where the two interactions are comparable and the value quickly drops to nearly 0 μK from 3 μK. Meanwhile in Fig. 7.5(B), we see β changes almost in a same pace with the characteristic energy. In the first regime, β show no significant increase until about 0.21 D, then it quickly increases and saturates at about 0.44 D. The solid curve gives the s-wave contribution from the close-coupling calculation.

For higher partial wave potentials with barriers, the most proper characteristic energy is the height of the barrier. When the barrier height is much larger than the thermal energy, the molecules are prevented from entering the short range and there is little chance for inelastic processes via those channels. When the barrier height is comparable to the thermal energy, the inelastic processes become available through quantum tunneling to the short range. Fig. 7.6(A) shows the potential heights of channels of different $|M_L|$ with respect to μ. In Fig. 7.6(B), β's are shown with the s-wave unitarity limit subtracted. At about $\mu = 0.54$ D where β start to rise again. The barrier of the $|M_L| = 1$ channels is lowered down to $5T$. Thus, the loss is mainly due to collisions via $|L = 1, M_L = 1\rangle$ and $|1, -1\rangle$ channels. The solid curve in Fig. 7.6(B) shows the d-wave contribution from the close-coupling calculation. More than 99% of the predicted contribution is from channels of $|M_L| = 1$.

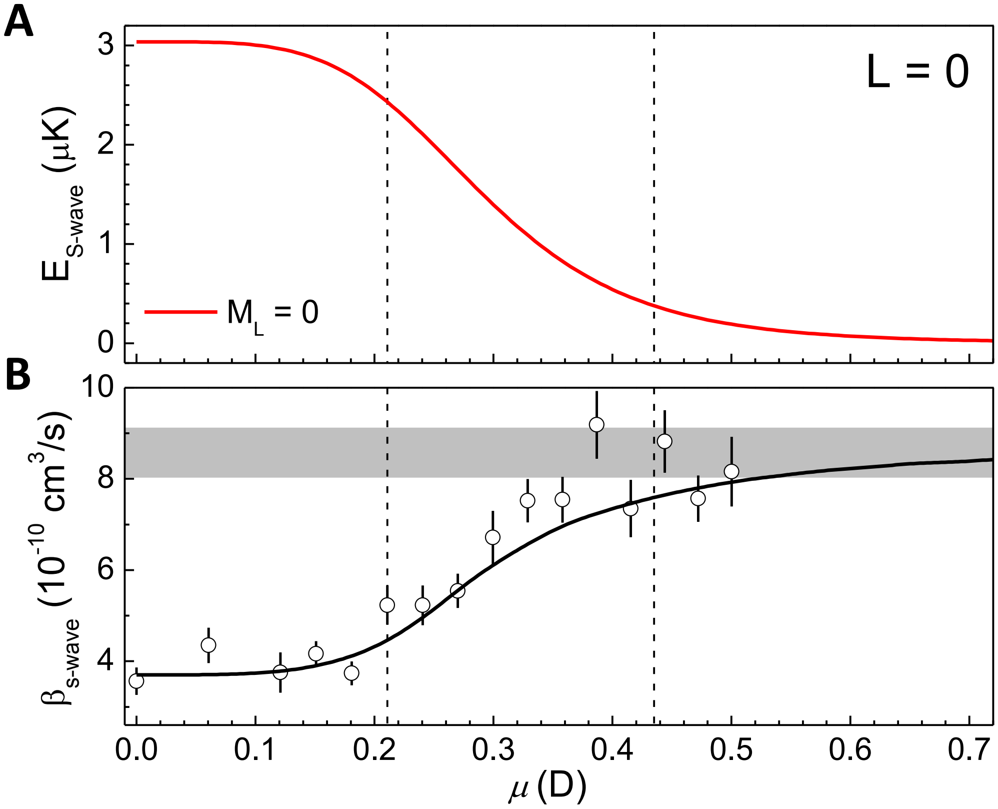

Figure 7.5: (A)The generalized characteristic energy E_α for s-wave potential, E_{s-wave} with respect to μ. (B)β attributed to the s-wave scattering with respect to μ. The data points are from the black squares in Fig. 7.4 with μ ¡ 0.5 D. The vertical line at $\mu = 0.21$ D marks the position where the DDI starts to be comparable with the van der Waals interaction. The vertical line at $\mu = 0.44$ D represents the point when E_α is lowered to about T. The grey horizontal belt represents the inelastic s-wave unitarity limit for $T = 400 \pm 50$ nK. The black solid curve gives the prediction of the s-wave contribution of β from the close-coupling calculation.

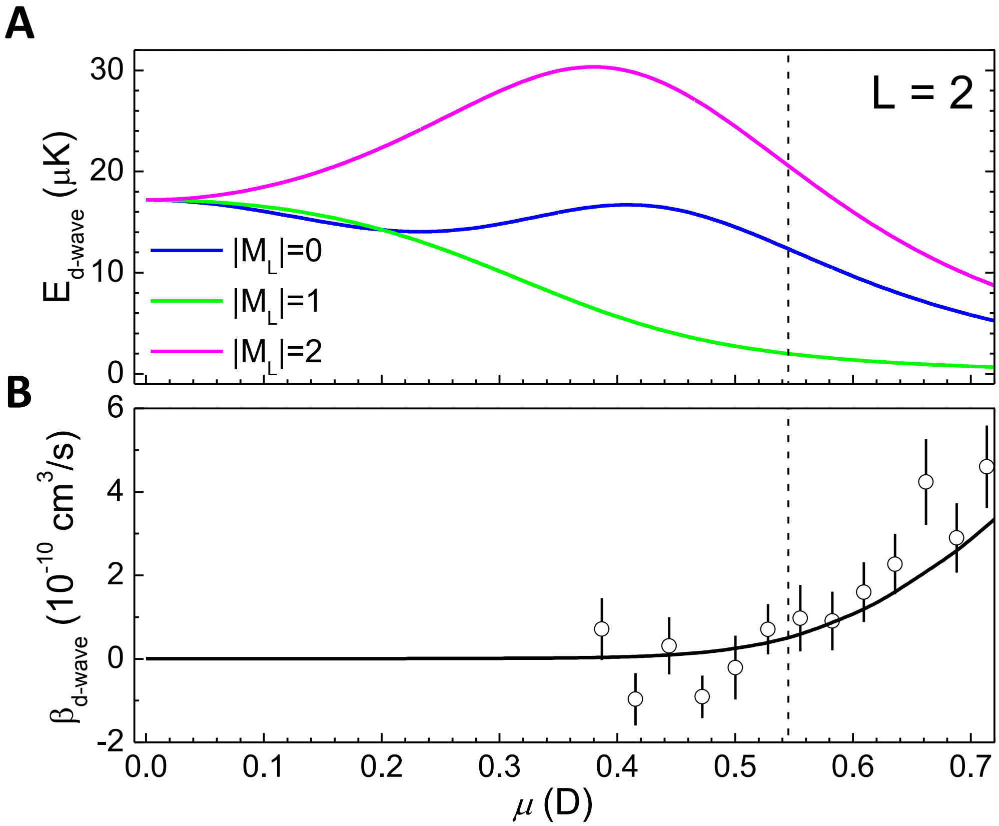

Figure 7.6: (A)The *d*-wave barrier heights E_{d-wave} for different $|M_L|$ channels. (B)β_{d-wave} attributed to all five different M_L channels. The $|M_L| = 1$ channels with the lowest barriers dominate the contribution. The vertical line at 0.55 D marks the position where $E_{d-wave} = 5T$ for $|M_L| = 1$. The black solid curve gives the prediction of the *d*-wave contribution of β from the close-coupling calculation, in which more than 99% is attributed to the $|M_L| = 1$ channels.

7.6 Conclusion

We report in this chapter the investigation of collisions between ultracold ground-state NaRb molecules in electric fields with induced electric dipole moments as large as 0.7 D. We observe a stepwise enhancement of losses due to the coupling between different partial waves induced by the increasingly stronger anisotropic dipolar interactions. Varying the temperature of our sample, we find good agreement with theoretical loss rates assuming complex formation as the main loss process. The results shed light on the understanding of complex molecular collisions in the presence of strong dipolar interactions and also demonstrate the versatility of modifying molecular interactions with electric fields.

□ End of Chapter.

Chapter 8

Collisions in molecular mixtures

8.1 Overview

While the E-field mixes the molecular states of different parities to induce DDI, DDI naturally arises in a mixture ensemble consisting of two rotational states of different parities in the absence of an E-field. Such DDI is also called the resonant dipole interaction as a result of two molecules sharing the rotational excitation back and forth, similar to the origin of the $1/r^3$ potentials of homonuclear dimers. The mixture ensemble can be initialized and controlled with MWs. Comparing with using E-field, such a system has several advantages. For example, the DDI can be switched on or off in a very short time scale. Combining the use optical potentials, it is possible to induce DDI locally by addressing single molecule or a single layer of molecules in optical lattices. Moreover, the DDI is state-dependent, one can tune the strength by preparing molecules in different states simply utilizing MWs of different frequencies. In this chapter, we present our investigation on collisions in molecular mixtures. We find that the state-dependent DDI directly reflects in the measured loss rate constants.

8.2 Molecular Hamiltonian

Since a number of molecular states are involved in this chapter, it is necessary to take a closer look at the molecular Hamiltonian first. The more degrees of freedom of a molecule than an atom make the molecular Hamiltonian more complicated than the atomic ones. Consider a diatomic molecule exposed in a homogeneous B-field, the Hamiltonian can be written as[125, 90, 126, 127, 128]

$$\begin{aligned} H &= H_{rot} + H_{hf} + H_Z \\ H_{rot} &= B_v \vec{J}^2 \\ H_{hf} &= \sum_i \vec{V}_i \cdot \vec{Q}_i + \sum_i c_i \vec{J} \cdot \vec{I}_i + c_3 \vec{I}_1 \cdot \vec{T} \cdot \vec{I}_2 + c_4 \vec{I}_1 \cdot \vec{I}_2 \\ H_Z &= -g_r \mu_N \vec{J} \cdot \vec{B} - \sum_i g_i (1-\sigma_i) \mu_N \vec{I}_i \cdot \vec{B}. \end{aligned} \tag{8.1}$$

The Hamiltonian are divided into three parts, the rotational part H_{rot}, the hyperfine part H_{hf} and the Zeeman part H_Z. In the rotational part, B_v is the rotational constant, $\vec{J}$ is the rotational angular momentum operator. The rotational part simply treats the diatomic molecule as a rigid rotor. In the hyperfine part, the first term is the electric quadrupole interaction, this energy is between an E-field gradient at the nucleus i and the nuclear quadrupole dipole of nucleus i. The coupling constants are $(eqQ)_1$ and $(eqQ)_2$. This term dominates for excited rotational states but vanishes for $J = 0$. The second term is the direct coupling between the rotation and the nuclear spins with spin-rotation coupling constants c_1 and c_2. The rotational motion of a molecule generates a B-field at the nucleus i. The third and fourth term describes the tensor and the scalar coupling between the two nuclei. In the Zeeman part, the rotational Zeeman shift and the nuclear Zeeman shift are included. Here g's are the Landé g factors, μ_N is the nuclear magneton. σ_i is the isotropic part of the nuclear shielding tensor $\vec{\sigma}_i$. In our NaRb case, the dummy index i iterates through Na(1) and Rb(2). Table 8.1 shows the relevant coupling constants for the ground vibrational state NaRb molecule.

Table 8.1: Coupling constants of molecular Hamiltonian for ground vibrational state NaRb molecule

Constant	Value	Ref.
B_v	2.0896628(4) GHz	[123]
$(eqQ)_1$	-0.139(40) MHz	[123]
$(eqQ)_2$	-3.048(13) MHz	[123]
c_1	60.7 Hz	[129]
c_2	983.8 Hz	[129]
c_3	259.3 Hz	[129]
c_4	6.56(23) kHz	[123]
$g_1(1-\sigma_1)$	1.484(1)	[123]
$g_2(1-\sigma_2)$	1.832(1)	[123]
g_r	0.001(6)	[123]

With the coupling constants in Table 8.1, we can solve the molecular Hamiltonian and obtain all the molecular states. Fig. 8.1 and Fig. 8.2 show all the molecular states in the $v = 0$ level, with $J = 0$ and $J = 1$ respectively up to 350 G. In Fig. 8.1, the two red dots at 335.2 G mark the two states that are used in the following mixture experiments. The lower one is $|J = 0, m_J = 0, m_{I,\mathrm{Na}} = 3/2, m_{I,\mathrm{Rb}} = 3/2\rangle$ and the upper one is $|0, 0, 3/2, 1/2\rangle$. In Fig. 8.2, the two red dots at 335.2 G mark the two states that are used in the following mixture experiments. The other four black dots in Fig. 8.2 mark the other states that are available via MW transition start from the $|0, 0, 3/2, 3/2\rangle$ state.

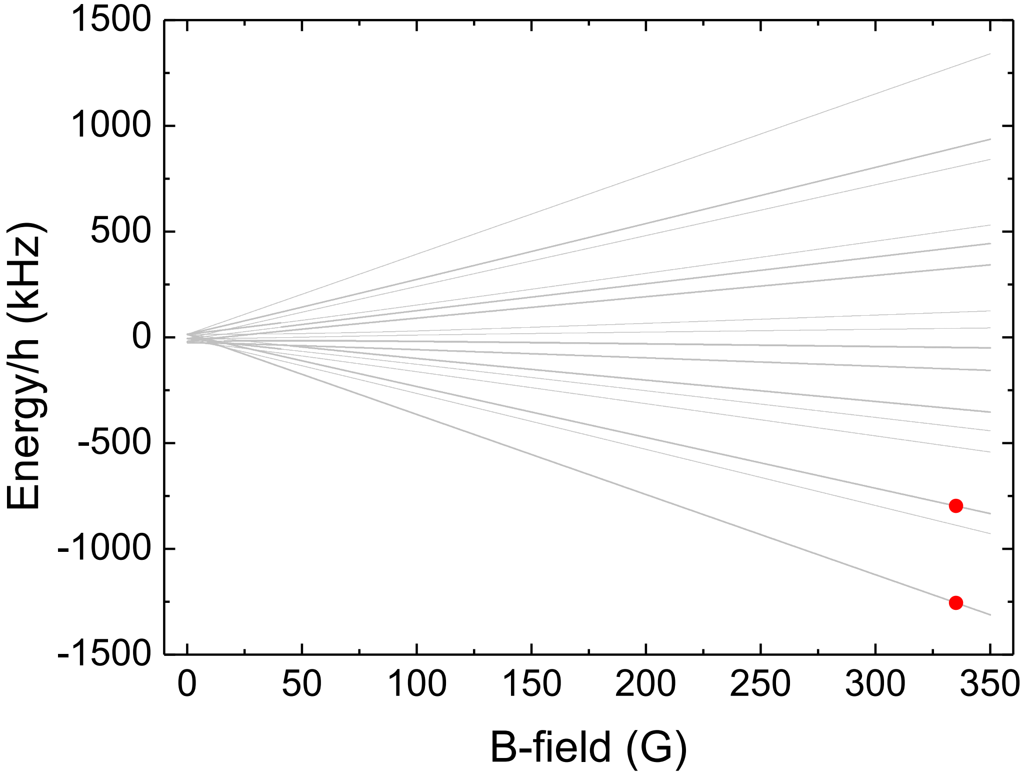

Figure 8.1: $J = 0$ molecular levels with respect to B-field. The red dots mark the states we use in the mixture collision experiments at B = 335.2 G.

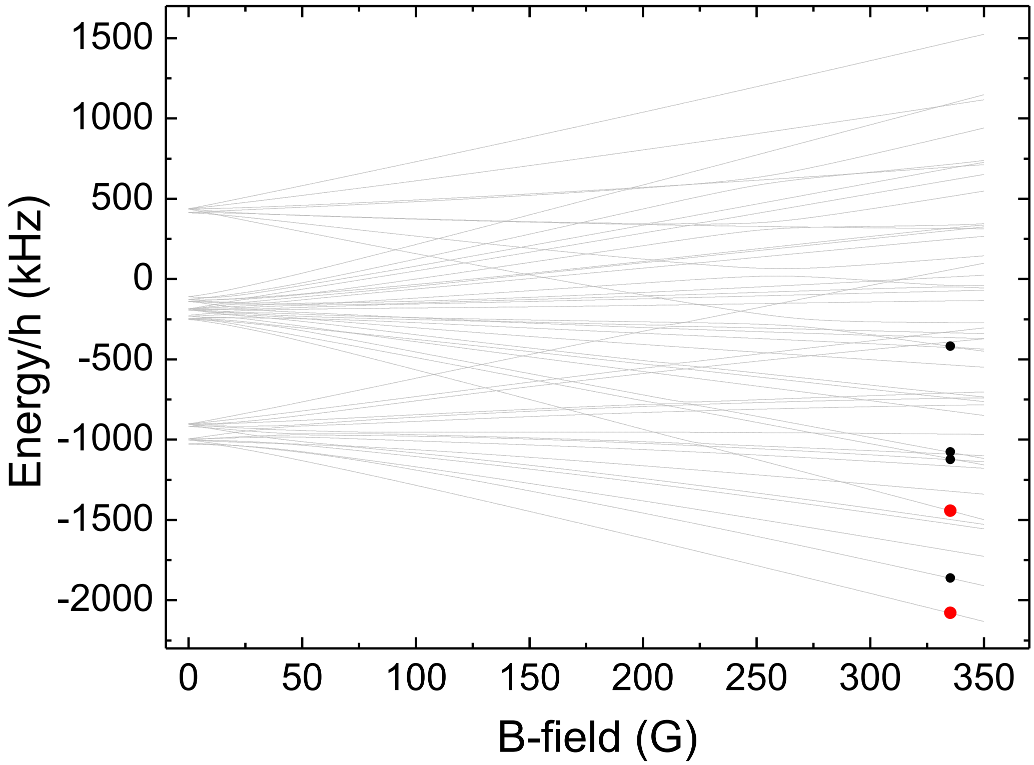

Figure 8.2: $J = 1$ molecular levels with respect to B-field. The red dots mark the states we use in the mixture collision experiments at B = 335.2 G. The other four black dots mark the other states that are available via MW transition from the absolute ground state $|0, 0, 3/2, 3/2\rangle$.

8.3 State-dependent DDI

The collisions between a molecule without rotational excitation and a molecule with one quantum of rotational excitation is highly dipolar.

We take the molecular state without the excitation here as the absolute ground state $|0, 0, 3/2, 3/2\rangle$. For simplicity, it will also be referred to as $|0, 0\rangle$ hereafter in this chapter. And among the six accessible $J = 1$ states start from the $|0, 0\rangle$ state, two states are picked for the collision experiment. The lower one, also the lowest state with $J = 1$, is $0.91 \times |1, 0, 3/2, 3/2\rangle - 0.42 \times |1, 1, 3/2, 1/2\rangle$. Because it has the most component of $m_J = 0$, it is referred to as $|1, 0\rangle$ for simplicity. The upper one is $|1, 1, 3/2, 3/2\rangle$. which is a fully-stretched state with all angular momentum projection taking the largest value. It can not get mixed with other state, and it is referred to as $|1, 1\rangle$.

To describe the mixture collision and reveal the state-dependent DDI, we need to first symmetrize the internal wave functions because the particles are identical. Assuming the quantum numbers $\alpha_1 \neq \alpha_2$, the internal wave function $\phi_\alpha(\vec{\rho}_1, \vec{\rho}_2) = \phi_{\alpha_1}(\vec{\rho}_1)\phi_{\alpha_2}(\vec{\rho}_2)$ should be symmetrized as

$$\phi_{\alpha\eta}(\vec{\rho}_1, \vec{\rho}_2) = \frac{1}{\sqrt{2}}\big[\phi_{\alpha_1}(\vec{\rho}_1)\phi_{\alpha_2}(\vec{\rho}_2) + \eta\phi_{\alpha_2}(\vec{\rho}_1)\phi_{\alpha_1}(\vec{\rho}_2)\big]. \tag{8.2}$$

Combining the partial wave (l, m_l), the basis function $\Phi_{\alpha l m_l \eta}(\vec{\rho}_1, \vec{\rho}_2, \hat{r}) = \phi_{\alpha\eta}(\vec{\rho}_1, \vec{\rho}_2)Y_l^{m_l}(\hat{r})$ is formed. The introduced parameter η takes value from ± 1. The basis is a symmetrized basis with $\eta = 1$ and an anti-symmetrized basis with $\eta = -1$. Considering the permutation symmetry of the basis. Because the molecules are identical bosons, the basis is unchanged under the permutation operation, $\hat{P}\Phi_{\alpha l m_l \eta} = +\Phi_{\alpha l m_l \eta}$. On the other hand, from the expression of the basis, one can find $\hat{P}\Phi_{\alpha l m_l \eta} = \eta(-1)^l\Phi_{\alpha l m_l \eta}$. Here, η comes from the symmetrization scheme of the internal wave function and (-1)^l comes from the spherical harmonics of the partial wave. Therefore, $\eta(-1)^l = +1$. This indicates that only even partial waves are available for symmetrized basis and only odd partial waves are available for anti-symmetrized basis.

Substituting the symmetrized or anti-symmetrized basis into the multipole-multipole expansion of Eq. 2.27, one can find the strong DDI between the molecules and its dependence on the choice of the states. Comparing the interaction between molecules in an E-field, one can find that for collisions between $|0,0\rangle$ and $|1,1\rangle$, the effective dipole is $d/\sqrt{6}$. For collisions between $|0,0\rangle$ and $|1,0\rangle$, the effective dipole is about 0.55 d. Here, d is the permanent dipole of the molecule and the DDI in the symmetrized basis and the anti-symmetrized basis will have the opposite sign. Note how strong the effective dipole is. Take $d = 3.2$ D, 0.55 $d = 1.76$ D and $d/\sqrt{6} = 1.31$ D, easily surpassing the maximum induced dipole of 1 D so far reached in our experimental system with E-field.

8.4 Procedures

Now we introduce the procedures of the mixture collision experiments. We initialize the 50/50 molecular mixture with a $\pi/2$-pulse applying on the pure $|0,0\rangle$ sample. The mixture sample is then held in trap for a variable holding time. The number of remaining molecules in both states are measured. However, so far, we can not do it in a single shot. The populations in the two states are measured in two successive shots. A final π-pulse can exchange the population between the two states, and only the population finally in the $|0,0\rangle$ state actually is measured. Besides the molecule number, the temperature is also measured.

In practice, we use large MW power. The MW transition Rabi frequency is $\Omega = 2\pi\times 83$ kHz. Accordingly, the pulse durations are 6 μs and 12 μs for a $\pi/2$- and a π-pulse respectively. The short pulse duration time is crucial in this experiment. With longer pulses, the collisional loss during the course of the pulses can not be negligible, and that makes $\pi/2$- and π-pulses not act like what they should do and complicates all the data analysis hereafter. One thing need to pay attention to is that the short pulse duration and large Rabi frequency broadens the line width of the transition, we need to check that the pulse will not drive the population to undesired states. The line width defined by the power is $\sqrt{2}\Omega = 2\pi \times 117$ kHz. In our case, we check that the nearest available excited states at 335.2 G is 247 kHz away for the $|1, 0\rangle$ state and 320 kHz away for the $|1, 1\rangle$ state. Therefore, the population in undesired states is negligible.

Initially, for N evolution, five different holding times are taken in a duration of 4 ms. To simplify the measurement, we switch to only measuring holding time = 0 ms and 4 ms afterwards. Meanwhile, to ensure the accuracy of the measurement, we double the number of shots for each holding time. We find the two method gives the same β within the mutual uncertainties. In experiments involving MW pulses, we find the number fluctuation somehow becomes larger. The second method with more points for each holding time reduces the variation in number and actually results in a smaller uncertainty of β. Fig. 8.3 shows an example measurement. In the temperature determination, the measurement starts from 0 ms all the way to 4 ms with a time interval of 0.5 ms. We are not really measuring the temperature evolution here. For such a short measurement with the maximum holding time of 4 ms, we can safely assume the temperature is a constant value. However, there is a residual breathing motion, so we need to measure multiple points to get the mean size instead of a single point.

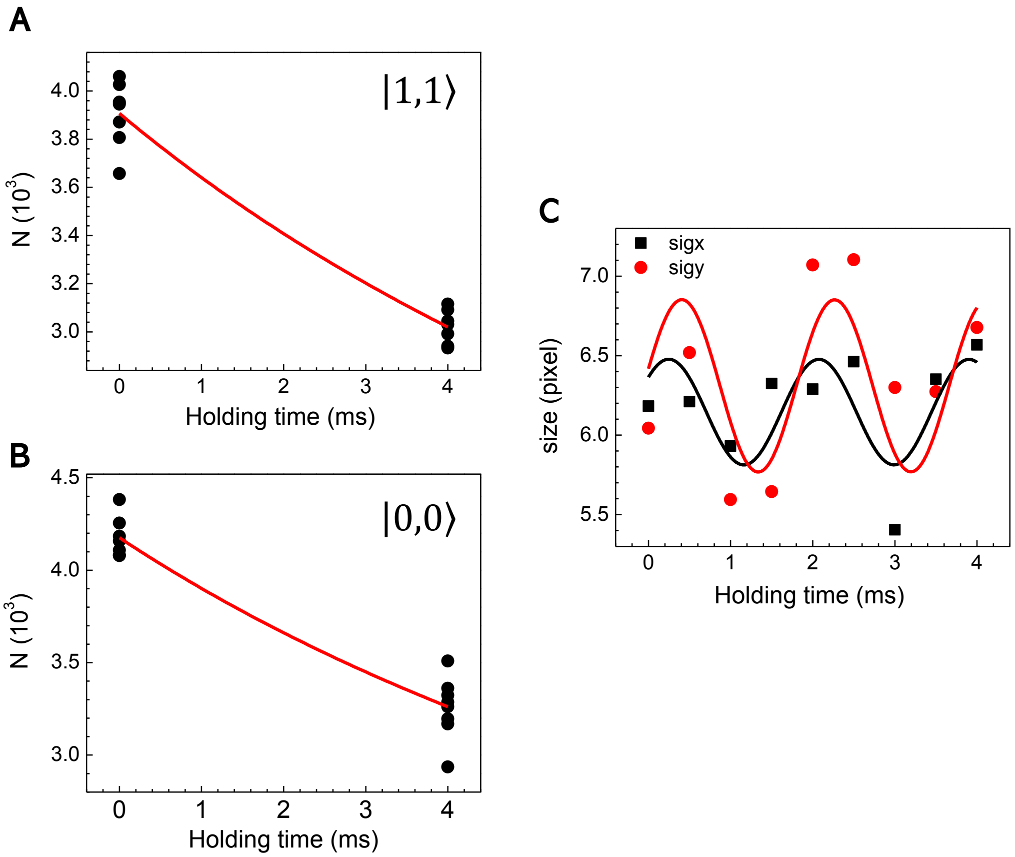

Figure 8.3: An example of measuring the mixture collision. The 50/50 mixture of the ground state and the rotational excited state is initialized with a 6-μs $\pi/2$ MW pulse. The starting point of the measurement is 3 ms after the initialization for the coherence to die out. Population in the rotational excited state (A) and the ground state (B) is measured at holding time = 0 ms and 4 ms. The solid curves are the fitting results according to Eq. 8.3. (C)The temperature is determined by measuring the cloud size after TOF for holding times start from 0 ms to 4 ms with an interval of 0.5 ms. The size is oscillating because of the breathing motion of molecules and the sinusoidal function is used to fit out the mean size.

β strongly depends on the coherence of the ensemble. For an ensemble with full coherence, β would be twice as that of an ensemble without any coherence. And, β of an ensemble with partial coherence would lie in between these two values. The coherence of our molecular mixture here decays as the holding proceeds. For simplicity, we only measure β when no coherence exists. To this end, the starting point of the holding time here is not the immediate instance after the $\pi/2$-pulse initialization, but 3 ms after it. We confirm this by measuring the decay of the Rabi oscillations as shown in Fig.8.4. In either case, we see that the coherence dies out at holding time = 3 ms. For a 50/50 molecular mixture held in trap, the actual coherence time should be much shorter than that appeared in the Rabi oscillation.

In this experiment, the polarizations of the two ODT beams are perpendicular to each other with the angle with respect to the quantization B-field in the vertical direction being 0° and 90°. Under such circumstances, we check the trap frequencies with our slosh motion measurement in all three directions for molecules in different rotational states. We find they are basically the same within the mutual uncertainties. Evaluate the product of the three trap frequencies $f^3 = f_x f_y f_z$, $f^3_{|0,0\rangle}/f^3_{|1,0\rangle} = 0.98(7)$ and $f^3_{|0,0\rangle}/f^3_{|1,0\rangle} = 1.01(8)$. So as a good approximation, we assume the trap frequencies don't depend on the internal state and the molecules in different states share the same density profile.

With the above considerations, we arrives at the following fitting model for the N evolution,

$$\begin{aligned}\frac{\mathrm{d}N_g(t)}{\mathrm{d}t} &= -A\beta_{gg}\frac{N_g(t)^2}{T^{3/2}} - A\beta_{eg}\frac{N_g(t)N_e(t)}{T^{3/2}},\\ \frac{\mathrm{d}N_e(t)}{\mathrm{d}t} &= -A\beta_{ee}\frac{N_g(t)^2}{T^{3/2}} - A\beta_{eg}\frac{N_g(t)N_e(t)}{T^{3/2}}.\end{aligned} \tag{8.3}$$

Here, $A = (\overline{\omega}^2 m/4\pi k_B)^{3/2}$ is a constant with k_B the Boltzmann constant, m

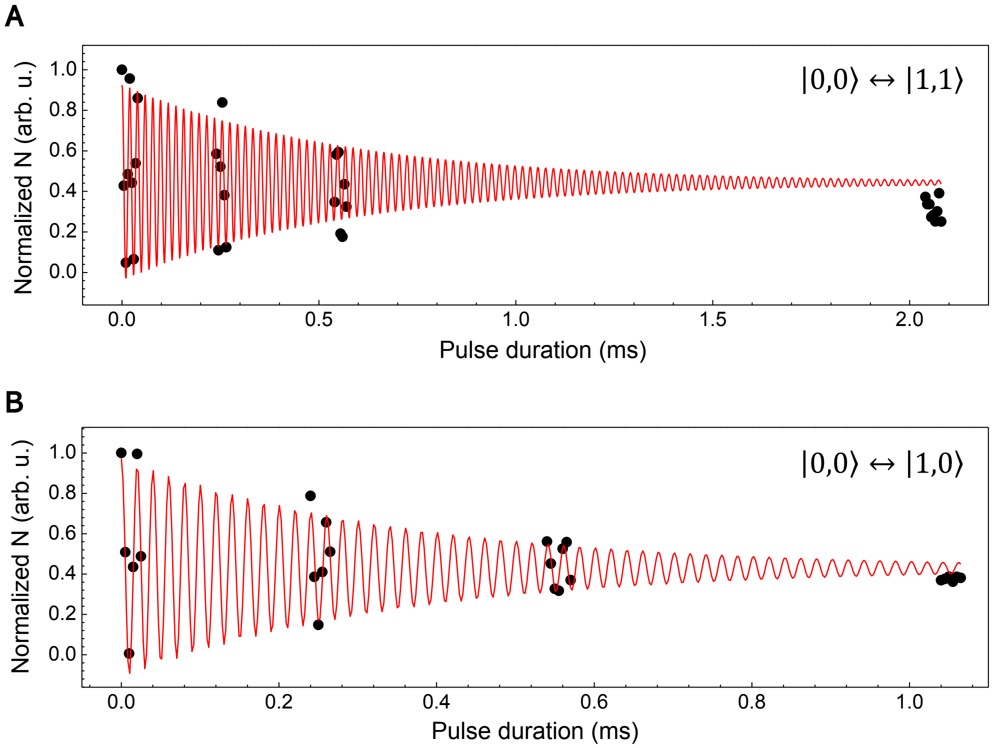

Figure 8.4: Rabi oscillation decay between the rotational excited state $|1,1\rangle$(A), $|1,0\rangle$(B) and the ground state $|0,0\rangle$. The decay time constant is 590 μs for (A) and 360 μs for (B). The decay time constant of the Rabi oscillation sets an upper limit for the decay time constant of the 50/50 molecular mixture. The result confirms that there is no coherence in the ensemble for measurements start from 3 ms after the MW initialization.

the mass of the molecule, and $\overline{\omega}$ the geometric mean of the trap frequencies. The subscript g and e stand for the ground state and the excited state respectively. The temperature T is given by the size measurement as in Fig. 8.3(C). For β_{ee}, we take it the same value as β_{gg} in the fitting. That is, $\beta_{ee} = \beta_{gg} = \beta_0 \times (T/T_0)^b$ where $\beta_0 = 3.4 \times 10^{-10}$ cm^3 s^{-1}, $T_0 = 0.97$ μK and b = -0.38. We confirm that β_{ee}'s are similar to β_{gg} with pure samples of excited-state molecules. Fig. 8.5 shows the comparison. With those quantities given, we fit the N evolutions of the two states simultaneously to extract β_{eg}. The solid curves shown in Fig. 8.3(A) and (B) are the fitting curves to the data.

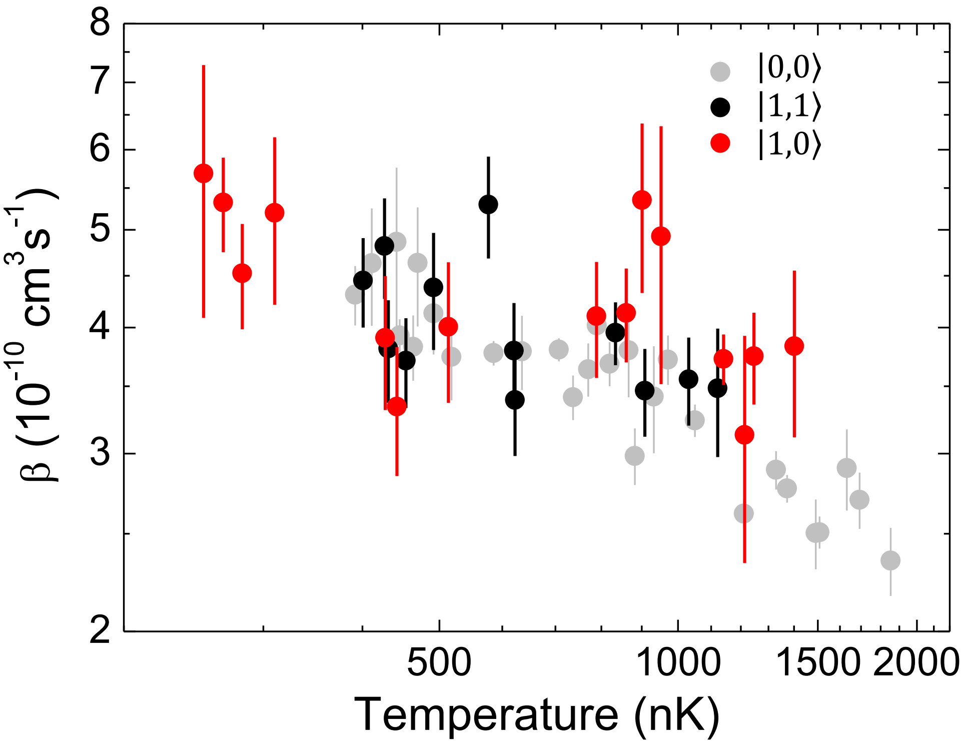

Figure 8.5: Comparison between β_{gg} of a pure $|0,0\rangle$ sample (grey) and β_{ee} of a pure $|1,1\rangle$ sample (black) and a pure $|1,0\rangle$ sample (red). Similar magnitudes and T-dependence are found. It indicates that as a good approximation, we can take β_{ee} the same value as β_{gg} of the ground state in the data analysis of mixture collisions.

8.5 DDI-dependent loss and temperature dependence

We perform the measurement with different sample temperatures in ODTs of different depths. The extracted β_{eg}'s are summarized in Fig. 8.6. Here, points in black are β_{eg}'s between $|0,0\rangle$ and $|1,0\rangle$, and points in red are β_{eg}'s between $|0,0\rangle$ and $|1,1\rangle$. Qualitatively, we observe that the relative comparison of β_{eg} agrees with the underlying DDI strength. Within the temperature range covered, the β_{eg} relates to $|1,0\rangle$ is about 2.3 times larger than the β_{eg} relates to $|1,1\rangle$. Both case show very weak dependence within the temperature range, but there is a qualitative difference that the sign of the dependency is opposite.

The exact calculation for the $J=0$ and $J=1$ mixture collision involves too many molecular states and is almost an intractable problem. Simplifications need to be made to reduced the number of states included. Since the hyperfine quantum number simply acts as spectators in the collisions, therefore we only select those dressed states that contains considerable component (>0.15) of the bare states with $m_{I,\mathrm{Na}}$=3/2, $m_{I,\mathrm{Rb}}$=1/2 and/or $m_{I,\mathrm{Na}}$=3/2, $m_{I,\mathrm{Rb}}$=3/2. To check the validity of this simplification, we calculate the adiabatic collision channels with and without the simplification. We see the approximated calculations only deviate slightly from the exact calculation.

Due to the symmetry constraints, the $J=0+J=1$ collision can not relax to $J=0+J=0$. Therefore, the $|1,0\rangle$+$|0,0\rangle$ channel is the lowest channel and no inelastic process is allowed. All loss is attributed to the complex formation. On the other hand, there are several available channels below $|1,1\rangle$+$|0,0\rangle$, so both complex formation and hyperfine changing collision contribute the loss.

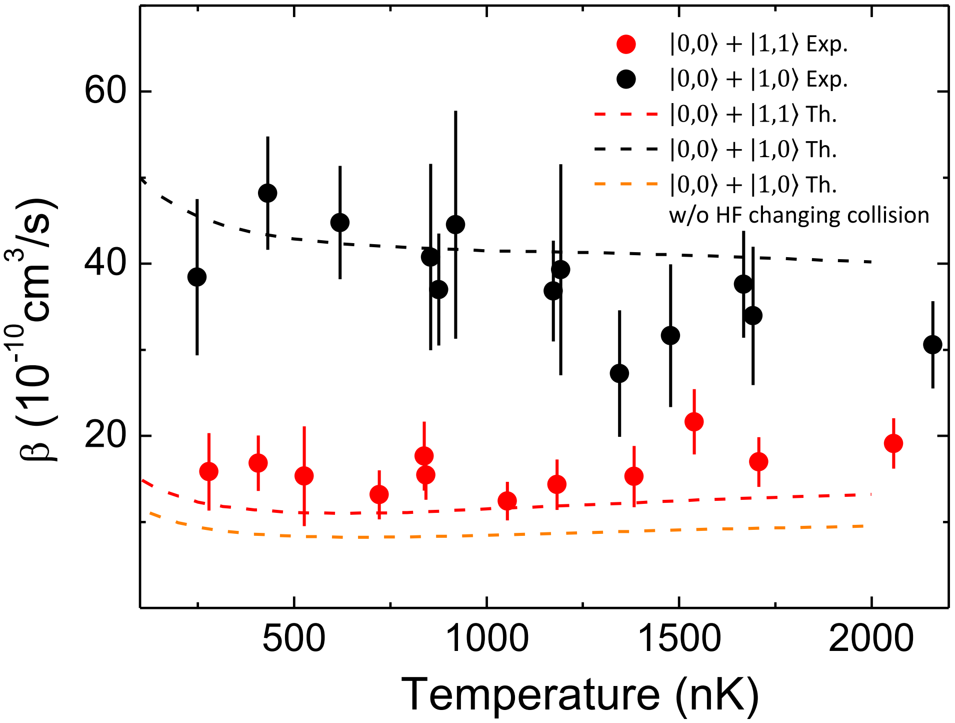

Figure 8.6: Summary of β_{eg} for $|0,0\rangle + |1,0\rangle$ mixture and $|0,0\rangle + |1,1\rangle$ mixture and their temperature dependence. The $|0,0\rangle + |1,0\rangle$ data are shown in black and the $|0,0\rangle + |1,1\rangle$ data are shown in red. The dashed curves are resuls from close-coupling calculation. The orange dashed curve is the calculation for $|0,0\rangle + |1,1\rangle$ with only the complex formation but without the hyperfine changing collision.

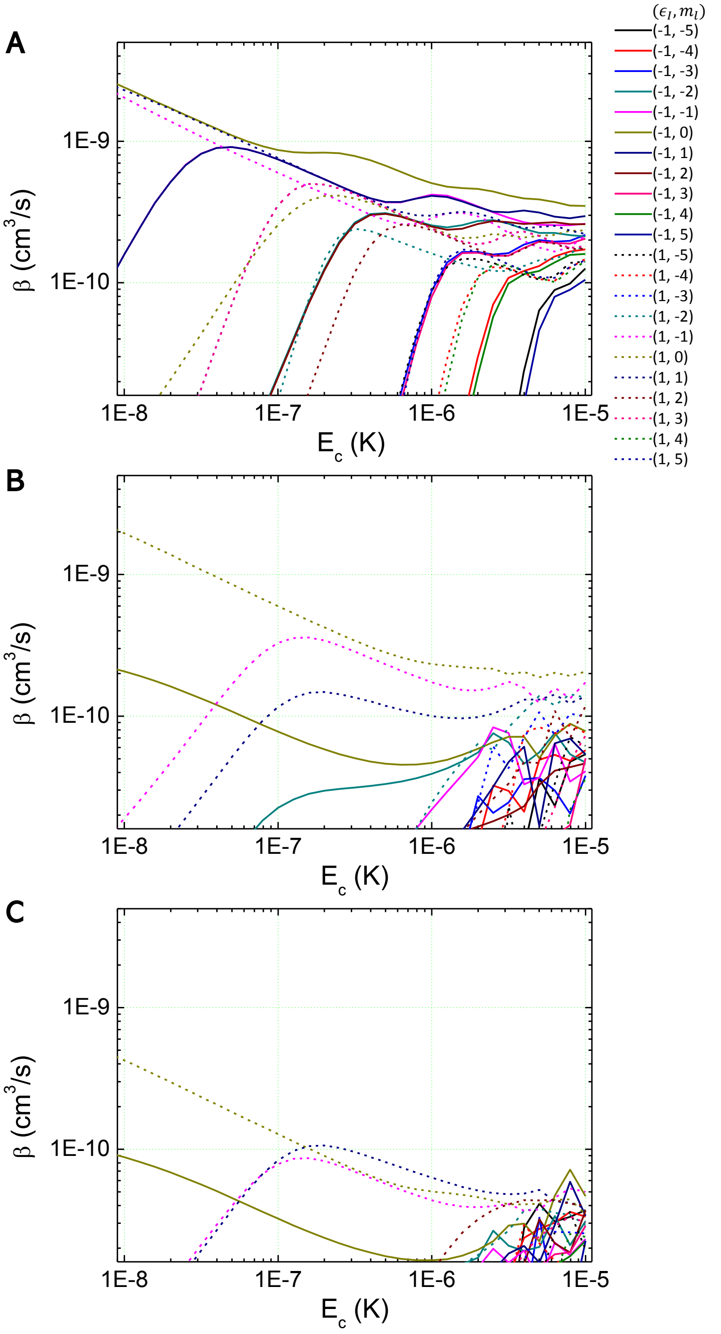

Figure 8.7: Rate constants for the mixture collision grouped by partial wave projection m_l and inversion symmetry ϵ_I. (A) is the complex formation rate constant for $|0,0\rangle+|1,0\rangle$. (B) and (C) are the complex formation and the hyperfine changing collision rate constant for $|0,0\rangle+|1,1\rangle$, respectively.

During the collision, the inversion symmetry $\epsilon_I = \pm 1$ and the total quantum number M are conserved. The loss rate constant are calculated for m_l from -5 to 5 with the $\epsilon_I = 1$ and $\epsilon_I = -1$ symmetries. The maximum partial wave included is $l = 10$. Fig. 8.7 shows the loss rate constants with respect to the collisional energy, grouped according to m_l and ϵ_I. Panel (A) shows the complex-formation rate constant for the $|1, 0\rangle + |0, 0\rangle$ case. Panel (B) and (C) show the complex-formation rate constant and the hyperfine changing collision rate constant for the $|1, 1\rangle + |0, 0\rangle$ case, respectively. We observe here due to the strong DDI, at the sub-μK regime, a number of partial waves already contribute considerably to the loss. With the stronger DDI, the $|1, 0\rangle + |0, 0\rangle$ case also give higher rate constants on average. Due to the different signs of the DDI in the two cases, the channels contribute the most in the two cases have different inversion symmetry. Compare Fig. 8.7(B) and (C), we find in the temperature range of interest, the loss from hyperfine changing collisions are less severe, about one order below the complex formation.

Summing up all the partial waves and averaging it over the Boltzmann distribution, we obtain the theoretical predictions shown in dashed lines in Fig. 8.6. We see a good agreement between the theoretical and the experimental result both in magnitude and temperature dependency without any free parameter. Now, we confirm the rate constants agree with the magnitude of the DDI both theoretically and experimentally. However, the real collision problem has its complexity different from toy models, preventing us from giving the naive inference. The complexity comes from the relative position of the collision channels. The $|1, 0\rangle + |0, 0\rangle$ channel is the lowest one, so couplings to other channels all push this channel downward. On the other hand, the $|1, 1\rangle + |0, 0\rangle$ channel lives amid a bunch of channels, so there are also couplings that raise the channel. In the calculation, we do see the barriers induced from those couplings at an intermolecular distance about 1000 a_0. In Fig. 8.6, the lowest orange line gives only the complex formation rate constant for the $|1,1\rangle$+$|0,0\rangle$ case. Although the data seem suggest the existence of the hyperfine changing collision, the difference is still too small to draw such a conclusion. It would be interesting to observe the products with deeper traps or other techniques, and measure the state-to-state collision rate in the future.

8.6 Mixture collision without DDI

As a complement to collisions with DDI, we finally investigate the mixture collision without DDI. This is achieved by preparing a hyperfine mixture within the $J = 0$ states. The two states as indicated in Fig. 8.1 are the $|m_{\mathrm{Na}} = 3/2, m_{\mathrm{Rb}} = 3/2\rangle$ and the $|3/2, 1/2\rangle$ state. Since we need an ensemble without the coherence, the population flow between the two hyperfine state always transit at the lowest state of $J = 1$, instead of via a two-photon process. Therefore, most parts of the experiment remains the same but some extra MW π-pulses are added if neccessary. For example, to initialize half of the population in the $|3/2, 1/2\rangle$ state, we first drive half of the population to the lowest state of $J = 1$, wait for 2 ms to let the coherence die out, and then apply another π-pulse to make all the population in the excited state down to the $|3/2, 1/2\rangle$ state. The preliminary results of this mixture in shown in Fig. 8.8. The dashed line shows the theoretical prediction from the universal model[64]. Overall, we see that the β here are all lower than those with DDI, which agrees with the intuitive picture that DDI enhances the collision. However, to our surprise, the β here sometimes appears to be quite different in magnitude. Among the five points here, two are high above and three lie below. The ratio between the high values and the low values can be as large as 3. Possible reasons of this phenomena might come from two aspects. First is the technical aspect. Technically, it is more difficult to extract β_{eg} here because β_{ee} and β_{gg} are comparable with β_{eg}. Meanwhile, the introduction of more MW pulses amplifies the fluctuations in population. The extraction of β_{eg} might be less reliable considering those factors. Another reason might be from the science aspect. There might really be some resonances observable between such a hyperfine mixture. Although, we are supposed to perform the experiment under the same B-field of 335.2 G every time, there may be a tiny B-field drifts in a daily time scale. The slight change in B-field may make the system sometimes on resonance and sometimes not, resulting in starkly different β_{eg}. The hyperfine mixture collision is still a topic for future finer investigations.

□ End of Chapter.

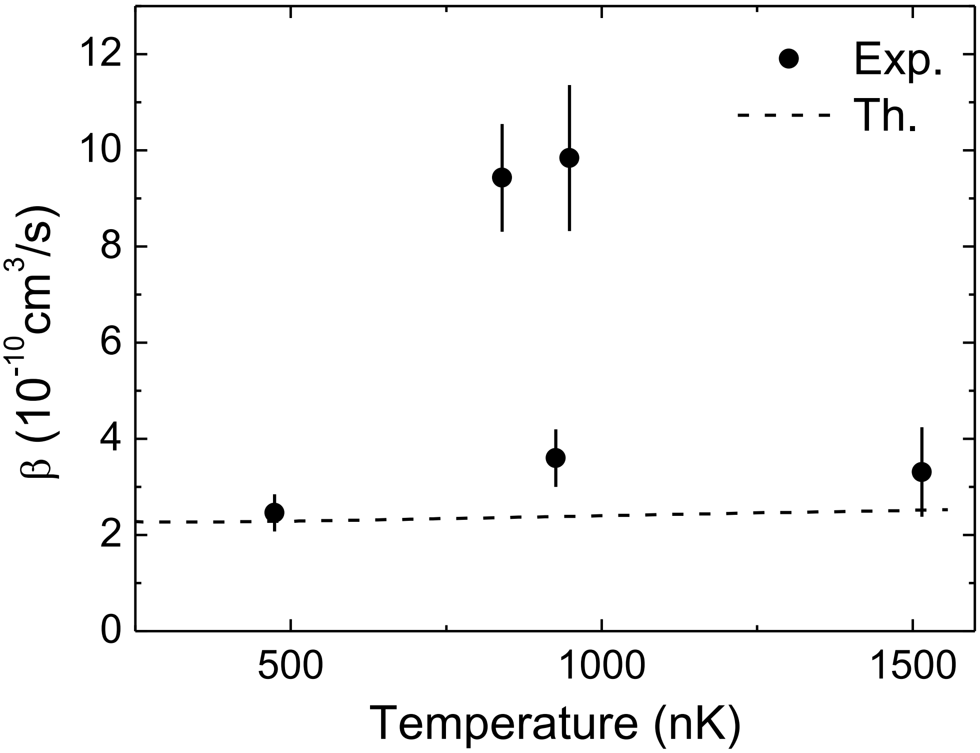

Figure 8.8: β_{eg} for hyperfine mixture of $|m_{\mathrm{Na}} = 3/2, m_{\mathrm{Rb}} = 3/2\rangle$ and $|3/2, 1/2\rangle$. The dashed curve represents the prediction from the universal model.

Chapter 9

Atom-molecule collisions

9.1 Overview

It is believed that for ultracold NaRb molecules, the density of resonances induced by the existence of transition complex states is too high to resolve. Therefore, what we observe is always a smoothened, average effect from a large number of resonances under current experimental conditions. The case of the atom-molecule collision, however, the resonances should be much sparser. In the context of atom-molecule collision, the transition complex is a trimer. Compared with the molecule-molecule collision, the reduction in degree of freedom as well as the weaker van der Waals interaction result in a fewer transition complex states. See Table 9.1 for the strength of the van der Waals interaction.

One important benefit that the atom bring along is the controllability on the collisional threshold level. The ground-state molecule don't possess a magnetic dipole whereas the atoms do have. The Zeeman shift, which is a function of B-field, serves as a control knob to tune the threshold level. Hence, there is a possibility to scan and to resolve individual resonances with the atom-molecule collision. Once we can scan out a spectrum of resonances, the statistics of the resonance position, resonance width etc. can be extracted and provide evidence about whether the underlying scattering is chaotic. The chaotic behavior has been discovered and studied in systems such as complex atoms and ions[130], solid-state systems[131, 132], nuclear systems[133, 134] and recently in magnetic atoms[135, 136, 137, 138].

Considering the atom-molecule collision with NaRb molecule, there are two possible species combinations. One is Na+NaRb and the other is Rb+NaRb. For all those particles in their own ground state, the two combinations have the distinct chemical reactivity according to Table 6.1. The chemical reaction channel Na + NaRb → Na_2 + Rb is open while the channel Rb + NaRb → Na + Rb_2 is closed. Therefore, we are also capable of investigating collisions with controlled chemical reactivities on the atom-molecule platform.

Table 9.1: Van der Waals interaction in atom-molecule collision and loss rate constant from the universal model.

Species	C_6(a.u.)	Ref.	$T_{\rm vdW}(\mu\text{K})$	$E_{\rm vdW}$(MHz)	$\beta_{\rm u}(10^{-10}\ \text{cm}^3/\text{s})$
Na+NaRb	3948	[59]	275.4	5.7	1.36
Rb+NaRb	6896	[59]	51.1	1.1	0.78

9.2 Tuning collisional threshold

Generally, the Zeeman shift should be calculated by numerically diagonalizing the full Hamiltonian of a system that exposed in a B-field. However, for the ground-state manifold of the D transition of Na and Rb, there exists an analytical formula for it. That is the Breit-Rabi formula[139, 140],

$$E = -\frac{\Delta E_{\rm hfs}}{2(2I+1)} + g_I \mu_B m B \pm \frac{\Delta E_{\rm hfs}}{2}\left(1 + \frac{4mx}{2I+1} + x^2\right)^{1/2} \tag{9.1}$$

where I is the nuclear spin, g_J is the fine structure Landé g-factor, g_I is the nuclear Landé g-factor, $\Delta E_{\text{hfs}} = A_{\text{hfs}}(I + 1/2)$ is the hyperfine splitting, $m = m_I \pm 1/2$ and $x = (g_J - g_I)\mu_B B/\Delta E_{\text{hfs}}$. Fig. 9.1 shows the Zeeman splitting for the ground states of Na and Rb, with respect to B-field. We perform the experiment under B-field = 335.2 G, therefore one quantity we care about is the derivative of the energy with respect to the B-field at 335.2 G. In Fig 9.1, this derivative for the three states of total atomic angular momentum $F = 1$ for both atom are displayed.

Another aspect of the tunability comes from the fact that different atomic state can be chosen. This tunes the threshold in a larger energy scale and changes the number of the open channel. For the Rb+NaRb case, considering only the s-wave scattering, the open channel number is 1, 3, 6 for the Rb atom in the $|F, m_F\rangle$=$|1, 1\rangle$, $|1, 0\rangle$, $|1, -1\rangle$ state respectively. This open channel number can be simply counted based on the magnetic quantum number conservation. For instance, when the Rb atom is in the $|1, 0\rangle$ state, the total magnetic quantum number is $M = 0 + (3/2 + 3/2) = 3$, where the two numbers in the bracket represent the nuclear magnetic quantum numbers of the two constituent atoms of the molecule. Then there are three combinations that has a energy no higher than the entrance channel, they are $0 + (3/2 + 3/2)$, $1 + (1/2 + 3/2)$, $1 + (3/2 + 1/2)$.

9.3 Density of trimer states

Ref. [141] estimates the density of trimer states for a series of atom-molecule combination. In their method, short-range interaction potential is approximated by a Lennard-Jones potential

$$V_{sr}^{(L)}(R) = \frac{C_{12}}{R^{12}} - \frac{C_6}{R^6} + \frac{L(L+1)}{2m_r R^2}. \tag{9.2}$$

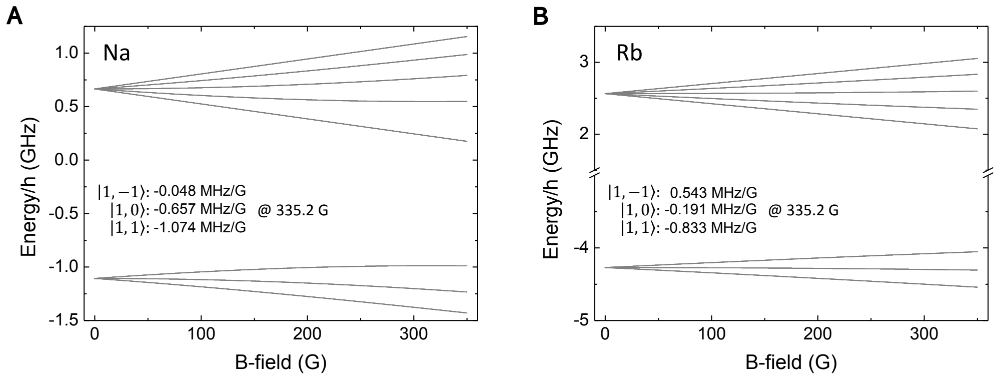

Figure 9.1: (A) ^{23}Na $3^2S_{1/2}$ (ground) level hyperfine structure in an external B-field. The Zeeman shift at B-field = 335.2 G is -0.048, -0.657 and 1.074 MHz per Gauss for $|F, m_F\rangle = |1, -1\rangle$, $|1, 0\rangle$ and $|1, 1\rangle$ respectively. (B) ^{87}Rb $5^2S_{1/2}$ (ground) level hyperfine structure in an external B-field. The Zeeman shift at B-field = 335.2 G is 0.543, -0.191 and 0.833 MHz per Gauss for $|F, m_F\rangle = |1, -1\rangle$, $|1, 0\rangle$ and $|1, 1\rangle$ respectively.

Knowing the C_6 coefficient, the C_{12} coefficient can be approximated by $C_{12} = C_6/4D_e$, where D_e the dissociation energy of the ground trimer state AB_2 into $AB + B$. After formulating the potentials, the bound state energies are calculated. The available states are counted according to the conservation laws. During a collision, the total angular momentum of the partial wave and the molecular rotation is assumed to be conserved, meanwhile, the total magnetic quantum number M is conserved.

For Rb + NaRb collision, based on the calculation result in Ref. [141], the density of trimer states is 0.14 states per E_{vdW}. Namely, 2.73 states per mK and 0.13 states per MHz. The above density of states is only considers the rotational and the vibrational degree of freedom. If the nuclear spin can flip during the collision time, the available density of states should multiply by a factor of 4. Therefore, the density of $NaRb_2$ states is between 0.13 and 0.52 states per MHz. For Rb in the $|1, 1\rangle$ state, the energy shift is -0.833 MHz/G. Therefore, converting the density of trimer states with respect to B-field is 0.16 to 0.63 states per G.

9.4 Measuring atom-molecule loss

The time sequence for measuring the atom-molecule collision is similar to other collision experiments. The low conversion of the magnetoassociation leaves a large number of residual atoms. By selectively removing one of the species with the MW and the laser, we can successfully obtain a atom-molecule mixture. The number of the atom is usually one order above the number of the molecule. The large ratio makes the molecule-molecule collision insignificant and benefits the extraction of the atom-molecule collision rate constant. We measure the temperature with the single-shot TOF method. We find the atomic cloud and the molecular cloud is not in thermal equilibrium. The typical atomic temperature is 400 nK and the typical molecular temperature is 700 nK.

Fig. 9.2 and Fig. 9.3 show the number evolutions for the atoms and the molecules. We see a rapid decay in molecule number and the atom number essentially remains the same. For the data analysis, we always take the data within the first 20 ms. We find that within the first 20 ms, the temperature doesn't increase as much as the case of molecule-molecule collision. This may be partially due to the fact the atom-molecule collision is more like a one-body process for the molecules, and partially due to the possible thermalization in the cold atomic reservoir.

We fit the experimental data with the following model,

$$\frac{\mathrm{d}n}{\mathrm{d}t} = -\beta_{mm} n^2 - \beta_{am} n_a n. \tag{9.3}$$

Here β_{mm} is the loss rate constant between the molecules and β_{am} is the loss rate constant between the atom and the molecule. n_a is the density of the atom and n is the density of the molecule without the subscript m

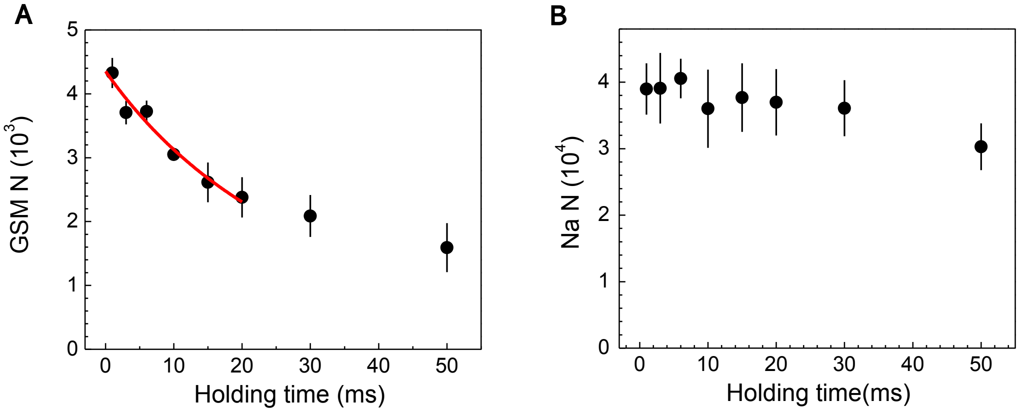

Figure 9.2: Ground-state NaRb molecule loss with Na atoms in $|1,1\rangle$ state. (A) shows the number evolution of the molecules and (B) shows the number evolution of Na atoms.

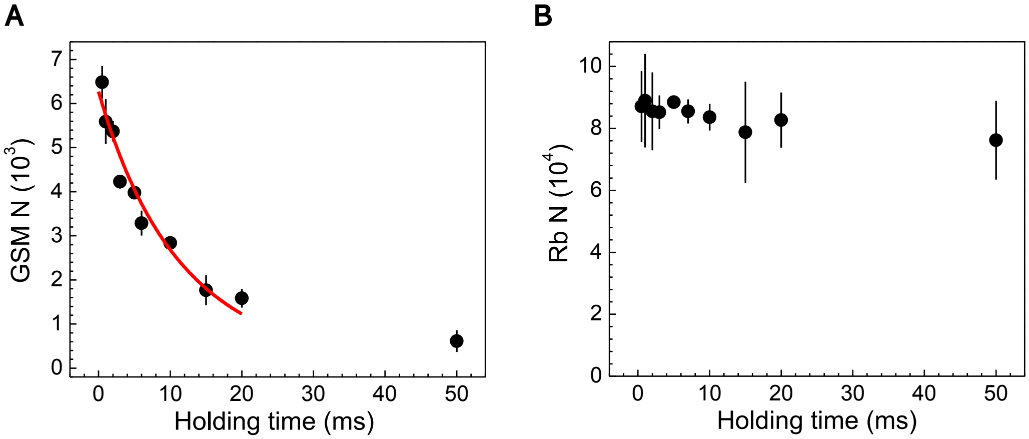

Figure 9.3: Ground-state NaRb molecule loss with Rb atoms in $|1,1\rangle$ state. (A) shows the number evolution of the molecules and (B) shows the number evolution of Rb atoms.

for simplicity. Written it in terms of the total number we measure in the experiment,

$$\frac{\mathrm{d}N}{\mathrm{d}t} = -\tilde{\beta}_{mm}N^2 - \tilde{\beta}_{am}N_aN, \tag{9.4}$$

where

$$\tilde{\beta}_{mm} = \beta_{mm}\iiint \alpha_m^2 \mathrm{d}x\mathrm{d}y\mathrm{d}z = \beta_{mm} \times (\overline{\omega}_m^2 m_m/4\pi k_B T_m)^{3/2} \tag{9.5}$$

and

$$\begin{aligned}\tilde{\beta}_{am} = \iiint \alpha_m\alpha_a \mathrm{d}x\mathrm{d}y\mathrm{d}z = \beta_{am} \times \overline{\omega}_m^3\overline{\omega}_a^3(\frac{m_m m_a}{2\pi k_B})^{3/2} \\ \times e^{-\frac{\Delta^2 m_m m_a \omega_{m,y}^2\omega_{a,y}^2}{2k_B(m_m T_a\omega_{m,y}^2 + m_a T_m \omega_{a,y}^2)}} \times \frac{1}{\sqrt{m_m T_a \omega_{m,x}^2 + m_a T_m \omega_{a,x}^2}} \\ \times \frac{1}{\sqrt{m_m T_a \omega_{m,y}^2 + m_a T_m \omega_{a,y}^2}} \times \frac{1}{\sqrt{m_m T_a \omega_{m,z}^2 + m_a T_m \omega_{a,z}^2}}.\end{aligned} \tag{9.6}$$

Here, m, ω and T represent mass, trap frequency and temperature respectively with subscript a for the atom and m for the molecule. α is the normalized density distribution with the total number factored out,

$$\alpha_i(x, y, z; f_x, f_y, f_z, T) = \frac{n_i(x, y, z)}{N_i}. \tag{9.7}$$

Note how complex the expression for $\tilde{\beta}_{am}$ is. This is because the atomic cloud and the molecular cloud are partially overlapped due to the different trap frequencies and the different gravity sag. For a harmonic trap, the gravity sag is g/ω_y^2, where g is the gravitational acceleration and ω_y is the trap frequency along the vertical direction. The Δ parameter in Eq. 9.6 represent the difference between the gravity sags. If we assume the temperatures and the atom number can be regarded as constants during the course of the measurement, Eq. 9.4 can give analytical result

$$N(t) = \frac{N_0 N_a \tilde{\beta}_{am}}{e^{N_a \tilde{\beta}_{am} t} N_a \tilde{\beta}_{am} + (e^{N_a \tilde{\beta}_{am} t} - 1) N_0 \tilde{\beta}_{mm}}, \tag{9.8}$$

where N_0 is another free parameter besides β_{am}, meaning the initial value for N.

An important difference between the atom-molecule collision and the molecule-molecule collision is, the atom-molecule collision is in the Wigner regime. This is because the van der Waals interaction is much weaker between a molecule and an atom. The corresponding van der Waals temperature, as shown in Table 9.1, tend to be much larger than the atomic or the molecular temperature. The collision rate in the framework of the universal model can therefore be calculated easily according to Eq. 2.19 without resorting to numerical methods.

We take five sets of data, two for Rb+NaRb and three for Na+NaRb. The results are summarized in Fig. 9.4. The horizontal axis here is $m_r^{-3/4} C_6^{1/4}$ in the atomic unit. Under this scale, the loss rate constant of the universal model shows up in a straight line. The dashed black line shows this prediction from the universal model. The two grey dashed lines in the vertical direction at $m_r^{-3/4} C_6^{1/4} = 0.496$ and $m_r^{-3/4} C_6^{1/4} = 0.871$ mark the positions for the two cases. The temperature uncertainties dominate the error bars. We see the good agreement between the measured value and the theoretical prediction. The relative ratio of the β magnitude between the two cases also agree with the universal model. However, the Rb+NaRb case is nonreactive, and the density of trimer states is supposed to be low, it ought not to fall on the same line. On possible reason is that we get this value only by accident at the B-field of 335.2 G. Therefore, if we tune the B-field, we ought to see some variations in the loss.

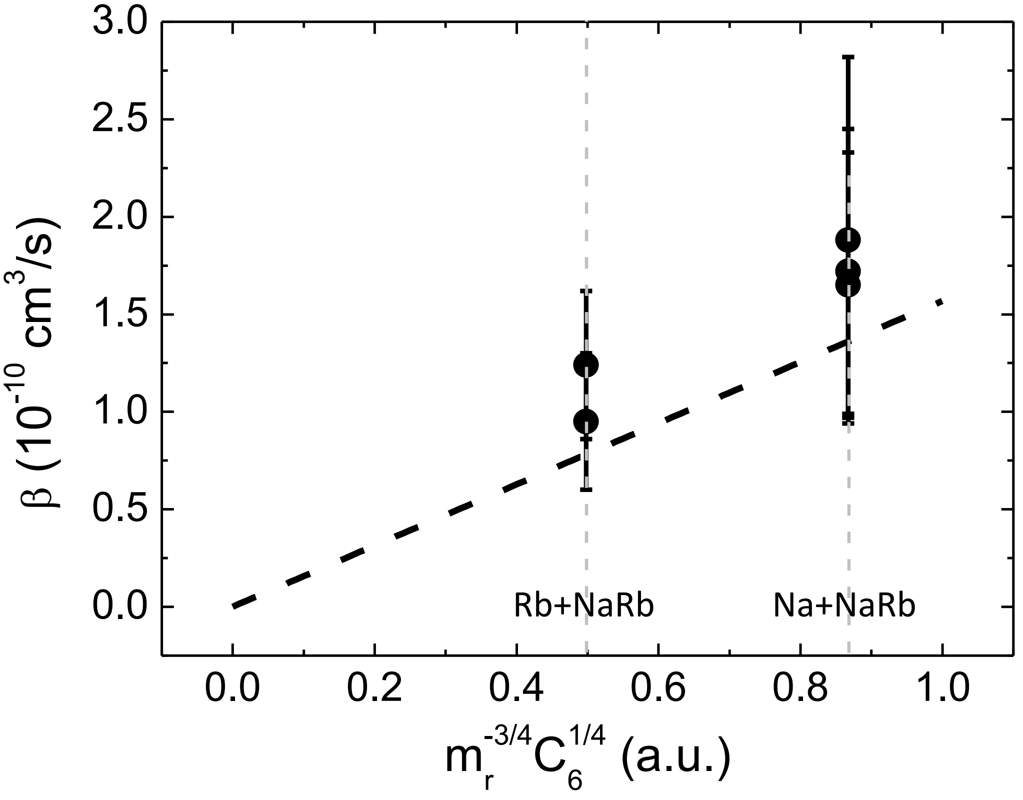

Figure 9.4: Summary of atom-molecule collisions at 335.2 G. The black dashed line represent the universal model prediction. The two vertical grey dashed lines mark the case for Rb+NaRb and Na+NaRb at $m_r^{-3/4}C_6^{1/4} = 0.496$ and $m_r^{-3/4}C_6^{1/4} = 0.871$. Within the uncertainties, the two cases both agree with the universal model.

9.5 B-field dependence

To investigate the B-field dependence of the Rb-molecule collision, we hold the mixture at each desired B-field for 4 ms and measure the remaining molecule number. The Rb atom number is 3.5×10^4. Since the STIRAP need to be performed at 335.2 G, we first reach 335.2 G and ramp to the desired B-field in 0.5 ms after the STIRAP. The time sequence is symmetric for the backward STIRAP. Fig. 9.5 shows the result from 325 G to 339 G. In a total range of 14 G, according to the estimation, 2 to 9 resonances should be seen. However, the experimental result only shows a overall decline due to the condition drift and no structure is seen within the number fluctuation. This may indicates that the available trimer states may be much larger than the predicted number, or the widths of the resonances with the trimer states are so large that still make the resonances overlapping. This may also due to some other factors we are unaware of. The reason why the Rb+NaRb collision agrees with the universal model is still unknown, and it is one thing that need to be figured out in the future.

□ End of Chapter.

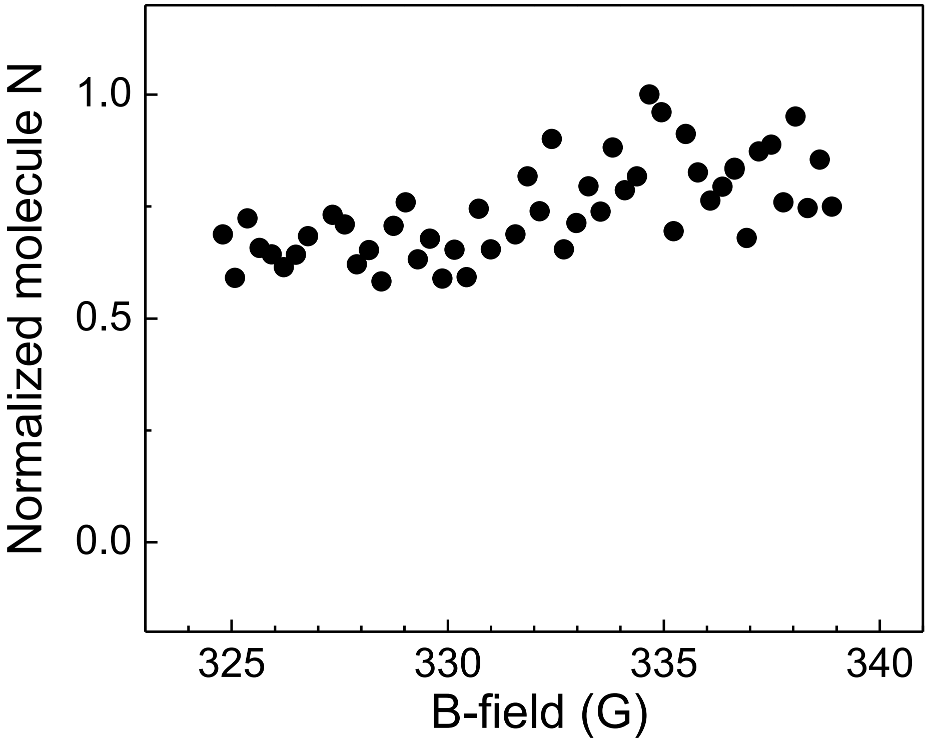

Figure 9.5: The B-field dependence of the ground-state molecule loss with Rb atoms in $|1,1\rangle$ state. The remaining molecule number is measured after a fixed holding time of 4 ms after the target B-field is reached with a ramp in 0.5 ms from 335.2 G. The Rb atom number is 3.5×10^4. Despite an overall decline due to the condition drift and no structure is observed.

Chapter 10

Molecular coherence

10.1 Overview

Coherence is one of the central concepts in quantum mechanics. A robust coherence, or a long coherence time, is the prerequisite of many physical applications, such as the precision measurement and the quantum computation. Since the experimental realizations of the UPM production, understanding and extending the coherence time of the UPM sample has been one of the major research topic[21, 142]. Regarding the importance of it, an exploration on the coherence of the ground-state NaRb molecule is still necessary, though this thesis is mainly about the collisions. There is no doubt the investigation on the molecular coherence will be the foundation for many of the future works.

In fact, the coherence and the collision are also closely linked. This can be understood in the following three aspects. First, the coherence can affect the collisional properties. For example, in an ensemble of identical bosonic molecules, the collision rate is larger if more coherence is preserved. Second, the collisional properties can affect the coherence, the collisional dephasing is one of the terms that can cause the decoherence. Third, both the coherence and the collisional properties can be greatly depend on the inter-particle interaction such as the DDI, and they provide two different aspects to reveal the underlying interactions.

In this chapter, we present our investigation on the coherence evolution of superposition states of NaRb molecule in a bulk sample.

10.2 Anisotropic polarizability

The ground-state molecule's polarizability depends on the angle between the quantization field and the linear polarization of the trapping beam. Meanwhile, the molecule's rotational quantum number and its projection onto the quantization axis effect this angular dependence[143]. Pictorially, this can be understood by the angular distribution of the wave function of rotational state $|J, m_J\rangle$.

Fig. 10.1 shows several examples of wave functions of different rotational states. The figures are plotted in 3D spherical coordinates. The radial distance represents the probability amplitude and the color represents the phase. For the simple model of rigid rotor, the eigen wave functions are the spherical harmonics. The different spherical harmonics possess different angular distributions. For example, the $|0, 0\rangle$ state's wave function distribution is isotropic, so is its polarizability. On the other hand, the $|1, 0\rangle$ state or the $|1, 1\rangle$ state possesses an obvious anisotropic characteristic and that agrees with their polarizabilities.

To solve the exact ac-Stark shift for each state, we need to incorporate the ac-Stark term, which describes the molecule-light interaction, into the molecular Hamiltonian. The matrix elements of the ac-Stark term for $J = 1$

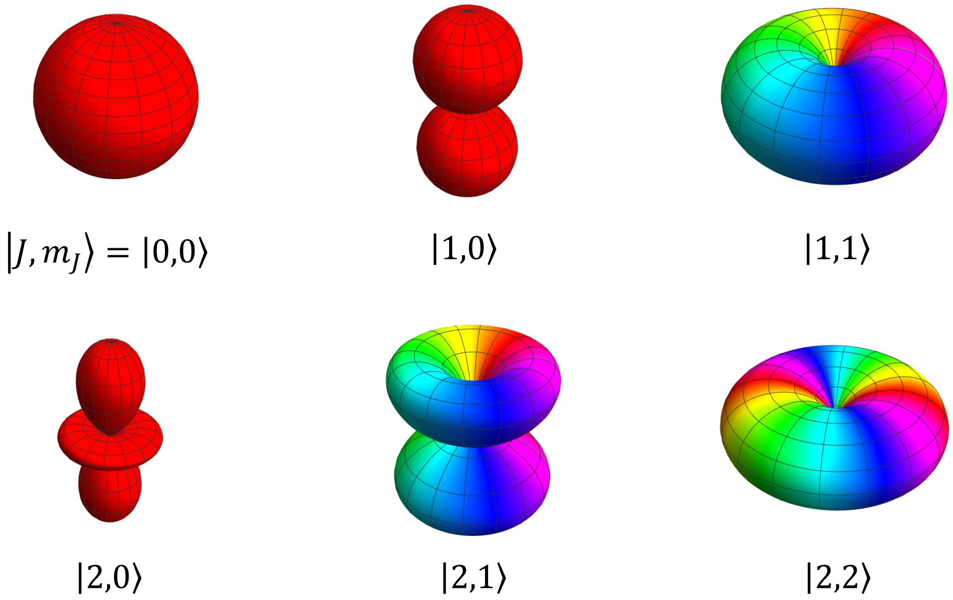

Figure 10.1: Spherical harmonic wave functions of different rotational states. Plotted in the 3D spherical coordinates, the radial distance represents the probability amplitude and the color represents the phase of the wave function.

states are as follows,

$$\begin{aligned} H &= -\alpha_{3\times 3} I \\ \alpha_{11} &= \frac{\alpha_\parallel + 4\alpha_\perp}{5}\sin^2\theta + \frac{3\alpha_\parallel + 2\alpha_\perp}{5}\cos^2\theta \\ \alpha_{22} = \alpha_{33} &= \frac{2\alpha_\parallel + 3\alpha_\perp}{5}\sin^2\theta + \frac{\alpha_\parallel + 4\alpha_\perp}{5}\cos^2\theta \\ \alpha_{12} = -\alpha_{13} &= \sqrt{2}\frac{\alpha_\parallel - 3\alpha_\perp}{5}\sin\theta\cos\theta \\ \alpha_{23} &= -\frac{\alpha_\parallel - \alpha_\perp}{5}\sin^2\theta. \end{aligned} \tag{10.1}$$

Here, I is the trapping beam intensity and α is a 3 by 3 matrix with the index 1 to 3 represent the rotational state $|1,-1\rangle$ to $|1,1\rangle$. The $\alpha_\parallel$ and $\alpha_\perp$ are the reduced polarizabilities describing the averaged contributions from excited rovibrational states on the parallel and perpendicular direction with respect to the inter-molecular axis[144, 20]. For ground-state NaRb molecules, $\alpha_\parallel =$

5.89554×10^{-2} MHz cm^2/kW and $\alpha_\perp = 1.90617\times10^{-2}$ MHz cm^2/kW[92].

10.3 Magic angle

Generally, due to the angular-dependent polarizability, the polarizabilities of two rotational states are not the same if the linear polarization direction of the trapping beams is not fine tuned. The ac-Stark shifts of two rotational states then gives a spatial-dependent energy difference between the two states and introduces decoherence into the two-level system[145]. For most times, this single-particle decoherence is the major source that limits the coherence time for UPMs[146]. Fortunately, for a certain choice of state pair, there may exist a specific angle under which there is no differential ac-Stark shift and the coherence decay rate can be greatly suppressed. We call this angle the magic angle[143, 20]. At the magic angle, the polarizability defined locally as $\tilde{\alpha} = -\partial E/\partial I$ are the same for the two states. Note that $-\partial E/\partial I$ does not necessarily equal to $\alpha = -E/I$. In other words, when the shapes of the trap bottom are the same for the two states, the trap depths are not generally the same. This is because the energy does not only linearly depend on I but also some higher order correction terms of I. The defined $\tilde{\alpha}$ is therefore also a function of I.

To find out the magic angle condition, we first need to figure out the intensity of the trapping beams. In Fig. 10.2(A), we show that we tune the ODT beam linear polarization direction and observe the frequency shift of the transition from $|0,0\rangle$ to $|1,0\rangle$ (all states discussed in this chapter have the most component of $m_{\mathrm{Na}} = m_{\mathrm{Rb}} = 3/2$). By fitting the molecular Hamiltonian to the energy shift of Fig. 10.2(A), we get the total intensity of ODT beams being 10.5 kW/cm^2. Later, we check this fitted intensity with the transition from $|0,0\rangle$ to $|1,1\rangle$ as shown Fig. 10.2(B).

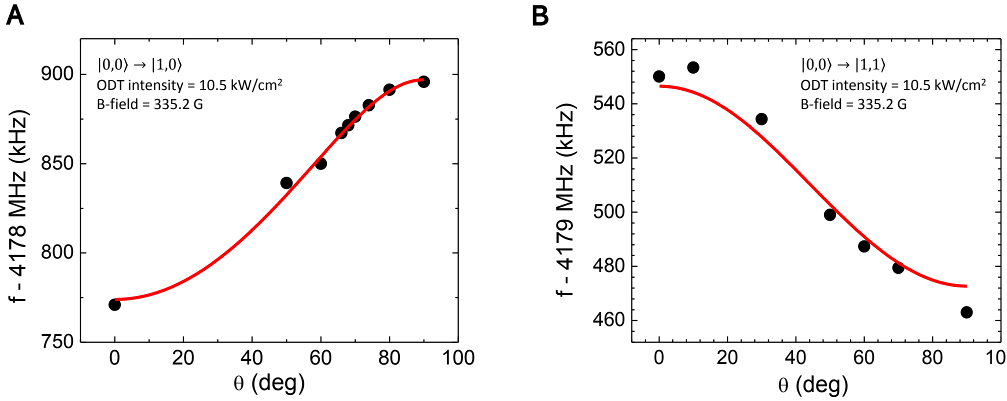

Figure 10.2: The transition frequency of from $|0,0\rangle$ to $|1,0\rangle$ (A) and from $|0,0\rangle$ to $|1,1\rangle$ (B) with respect to the angle θ between the quantization axis and the linear polarization of the trapping beams at B-field = 335.2 G. The red curve in (A) is a fitting result from the molecular Hamiltonian with the trapping beam intensity set as a free parameter. The fitted trapping beam intensity is 10.5 kW/cm^2. (B) shows the comparison of the transition frequency from the theoretical calculation with 10.5 kW/cm^2 trapping beam intensity and the experimental result.

Once the intensity is obtained, we can calculate the magic angle. Shown in Fig. 10.3 is the polarizability difference of the three states of $J = 1$ compared to the $|0,0\rangle$ state, with the intensity being 10.5 kW/cm^2. The constant polarizability of the $|0,0\rangle$ state is named as α_{00}, where

$$\alpha_{00} = \frac{\alpha_{\parallel} + 2\alpha_{\perp}}{3}. \tag{10.2}$$

The y-axis of Fig. 10.3 is rescaled to $(\tilde{\alpha} - \alpha_{00})/\alpha_{00} = \Delta\alpha/\alpha_{00}$, so the magic angle condition is where the curve crosses $y = 0$. We see that for the $|1,1\rangle$ state and the $|1,0\rangle$ state, the magic angle coincidentally appears together at about 68°.

Experimentally, we have one $\lambda/2$ waveplate to change the direction of the linear polarization for each ODT beam. We tune the angle and measure the remaining coherence at a fixed evolution time with the spin echo method

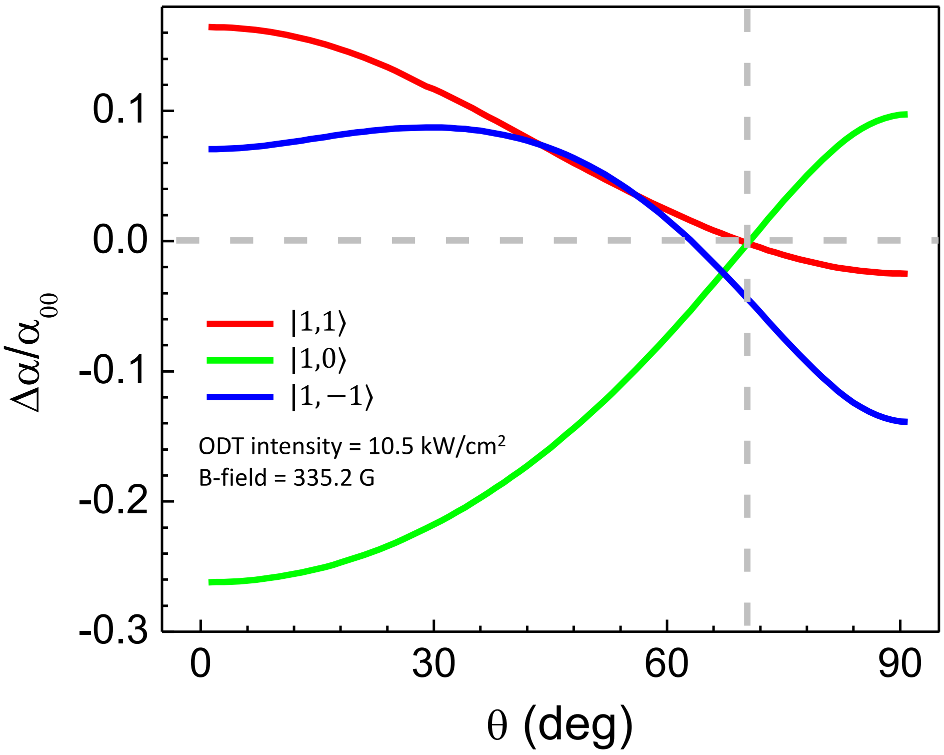

Figure 10.3: Calculated relative polarizability difference between the the $|1,-1\rangle/|1,0\rangle/|1,1\rangle$ state and the $|0,0\rangle$ state. The polarizability $\tilde{\alpha}$ is defined as $-\partial E/\partial I$. The vertical axis is $(\tilde{\alpha}-\alpha_{00})/\alpha_{00}$ where α_{00} is the polarizability of the $|0,0\rangle$ state.

(will be discussed later). As it is shown in Fig. 10.4, pronounced peaks of coherence at the vicinity of the calculated magic angles show up for the two cases. The results agree well with the calculation. The overall coherence of the $|1,0\rangle$ state appears to be less. This is because at that time, the MW switch leaks some tiny MW power. Since the MW transition of the molecule are quite strong so the tiny leakage kills partial coherence of the ensemble. For the $|1,1\rangle$ case, this problem is fixed.

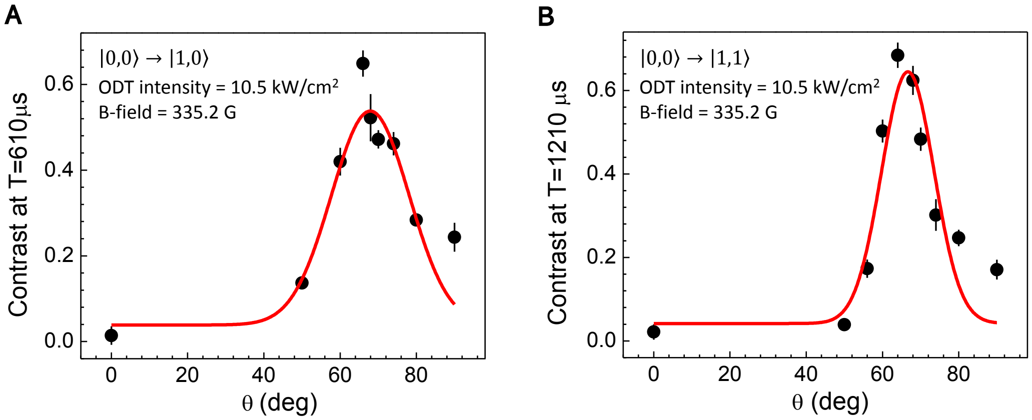

Figure 10.4: The magic angle measurement of the $|1,0\rangle$ state (A) and the $|1,1\rangle$ state (B). The coherence are measured with spin echo method with respect to different linear polarization of the ODT beams. The contrast shows a peak at $\theta = 68°$ for both case, which is consistent with the theoretical calculation. The overall contrast of the $|1,0\rangle$ state appear to be less, because the MW switch leaks some MW power and kills the coherence of the ensemble. For the $|1,1\rangle$ case, this problem is fixed.

10.4 Spin echo method

A two-level system can be mapped to a spin-1/2 system. With the rotating-wave approximation, the system can be described by the Bloch sphere representation[147]. As shown in Fig. 10.5, each point (u, v, w) within the Bloch sphere represents a density matrix of a two-level system with the following mapping relation[148],

$$\begin{aligned} u &= \tilde{\rho}_{eg} + \tilde{\rho}_{ge} \\ v &= -i(\tilde{\rho}_{eg} - \tilde{\rho}_{ge}) \\ w &= \rho_{ee} - \rho_{gg} \end{aligned} \tag{10.3}$$

Equivalently, any point in the Bloch sphere can be replaced by a vector pointing to that point from the origin.

$$\vec{R} = u\hat{x} + v\hat{y} + w\hat{z}. \tag{10.4}$$

Then, the magnitude of the vector indicates the coherence of the system.

If we name the excited state as $|\uparrow\rangle$ and the ground state as $|\downarrow\rangle$, then in our experiment, we investigate the coherence decay of the superposition state $1/\sqrt{2}\,|\uparrow\rangle + 1/\sqrt{2}\,|\downarrow\rangle$ which is initialized by a $\pi/2$-pulse bringing the arrow from pointing to the south pole to the equator of the Bloch sphere. The coherence of the system will then gradually decay due to several factors such as inhomogeneous external fields, interactions between particles, etc.

The simplest way to visualize the process of decoherence is by using the Ramsey method[149]. The Ramsey method consists of two $\pi/2$-pulses separated by a variable evolution time T. One simply measures the population recovered in one of the states after performing the pulse sequence. If one use a pulse with moderate detuning, the recovered population will display a damped oscillation with respect to T. Fitting the damping rate of the oscillation, one obtain the coherence decay rate.

The drawback of using the simple Ramsey method is that one can not distinguish different sources of the decoherence. The demand to filter out or to minimize the single-particle effect and to reveal the effect from two-particle interaction leads us to the spin echo method[150].

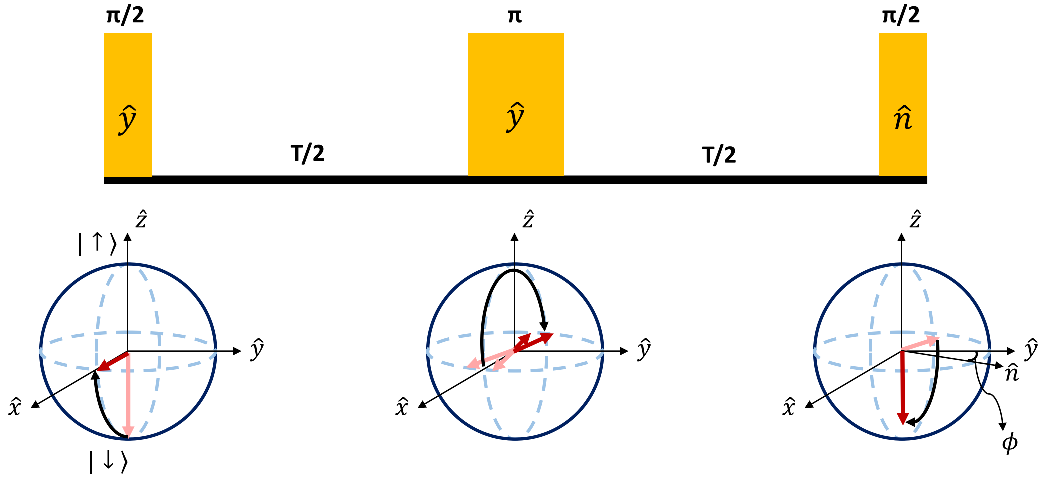

Figure 10.5: A schematics of the spin echo method in the Bloch sphere representation. In a Bloch sphere, the south pole represent the $|\downarrow\rangle$ state, the north pole represent the $|\uparrow\rangle$ state, and other points represent the superposition states of $|\downarrow\rangle$ and $|\uparrow\rangle$. The system is initialized by a $\pi/2$-pulse, the red arrows rotate 90 degrees with respect to $\hat{y}$ axis from the $|\downarrow\rangle$ state. During the first $T/2$ evolution time, the single-particle dephasing introduces different angular displacements of the red arrows. A π-pulse flips the red arrows. During the second $T/2$ evolution time, the accumulated angular displacements are the same but has an opposite sign than the previous ones. The angular displacements cancel out each other during the two $T/2$ evolution times. A third $\pi/2$-pulse further rotates the arrows and the population projects back to $|\downarrow\rangle$ will be measured. A phase shift ϕ can be introduced in the third MW pulse to change the rotation angle to $\hat{n}$ other than $\hat{y}$ axis.

Based on the Ramsey method, the spin echo method further inserts a π-pulse at the midpoint of the pulse sequence as in Fig. 10.5. The additional π-pulse flips the states on the equator plane of the Bloch sphere, and makes the phase accumulations from the inhomogeneous external fields between the two $T/2$ evolution times have the opposite sign and cancel each other.

A MW pulse is a rotation with respect to certain axis in the Bloch sphere representation. In Fig. 10.5, the first two rotations have the same axis $\hat{y}$. By adding a phase shift ϕ to the third pulse, the rotation axis becomes $\hat{n}$ other than $\hat{y}$. Therefore, to visualize the coherence with the spin echo method, one can tune ϕ while keeping the evolution time T fixed. A sinusoidal variation of the recovered number in one of the states with respect to ϕ can then be seen. The contrast of the curve, $(N_{max} + N_{min})/(N_{max} - N_{min})$, directly reflects the system's remaining coherence after T evolution.

If we assume that the molecules don't move, but are pinned to their local positions, the spin echo method can in principle completely filter out the external fields' contribution. In reality, this is not the case. However, we can still make considerable improvement within times shorter than the characteristic time scale defined by the trap frequencies.

10.5 Moving average cluster expansion (MACE) calculation

The DDI between molecules are long-range. This makes the large number of molecules get entangled no matter in a bulk sample or a lattice sample. Therefore, it is really hard, or even impossible to numerically solve the dynamics of a UPM system with usual algorithms.

Moving average cluster expansion (MACE) is an easy-to-operate algo-

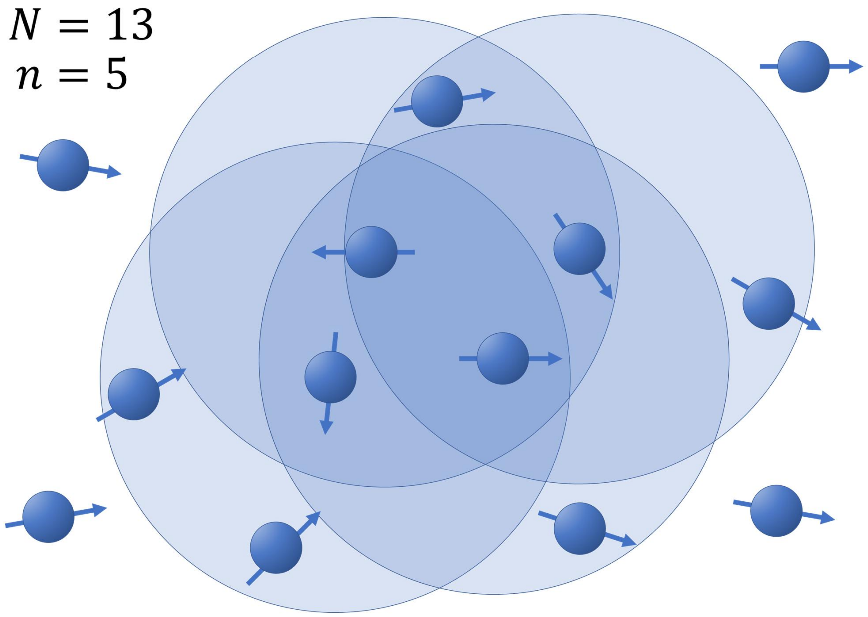

Figure 10.6: A schematics of the MACE calculation. Solving an ensemble of N molecules are broken down to solving N independent clusters of size n. A cluster is constructed with a central molecule and its $n-1$ neighbors with the most interaction strengths. The dynamics of the central molecule of each cluster are picked and added up for the ensemble dynamics.

rithm proposed in Ref. [1] by Kaden Hazzard et al. which can give an approximate solution to the problem. Within the framework of this algorithm, the whole system is broken into independent clusters which are tackled separately. As shown in Fig. 10.6, in an ensemble of N molecules, there are N clusters, each contains only n molecules. Among the molecules of one cluster, one is the central molecule and the other $n-1$ are the neighbors of the central molecule with the most interaction strengths. When solve the system, the dynamics within each cluster is exactly solved. However, only the observable of the central molecule is picked. Adding up all the observable of the central molecules, one obtains the observable for the ensemble.

Neglecting the single-particle decoherence and the losses, the Hamiltonian that governs the spin dynamics is as follows[151, 33, 152],

$$H = \sum_{i \neq j} \frac{V_{ij}}{2} \Big[\frac{J_\perp}{2} (S_i^+ S_j^- + \text{h.c.}) \Big]. \tag{10.5}$$

Here, $V_{ij} = (1 - 3\cos^2 \Theta_{ij})/|\vec{r}_i - \vec{r}_j|^3$, where Θ_{ij} is the angle between the quantization axis and $\vec{r}_i - \vec{r}_j$. $S_i^\pm$ and S_i^z are the spin-1/2 operators. The term $\frac{J_\perp}{2}(S_i^+ S_j^- + \text{h.c.})$ is called the exchange term because it swaps the two spin i and j with the coupling constant $J_\perp$. Neglecting the hyperfine mixing of $J = 1$ states, $J_\perp = d^2/6\pi\epsilon_0$ for $|0,0\rangle$ and $|1,0\rangle$, and $-d^2/12\pi\epsilon_0$ for $|0,0\rangle$ and $|1,1\rangle$, where d is the permanent dipole. For NaRb, considering the hyperfine mixing, $J_\perp = d^2/6.6\pi\epsilon_0$ for $|0,0\rangle$ and $|1,0\rangle$, and $-d^2/12\pi\epsilon_0$ for $|0,0\rangle$ and $|1,1\rangle$.

Before we perform the MACE calculation for our NaRb system. We first check the convergence of the algorithm. In Fig. 10.7, we show the coherence evolution results within 50 ms with a lattice sample of 2.8% uniform filling with other conditions similar to those in Ref. [1]. In panel (A), we tune n

with $N = 1000$ and in panel (B), we tune N with $n = 5$. We find that, under such realistic experimental conditions, $n = 5$ and $N = 1000$ can already give fairly good convergence. The calculations agree very well semi-quantitatively. Calculations with n and N larger than those values only differ by some details.

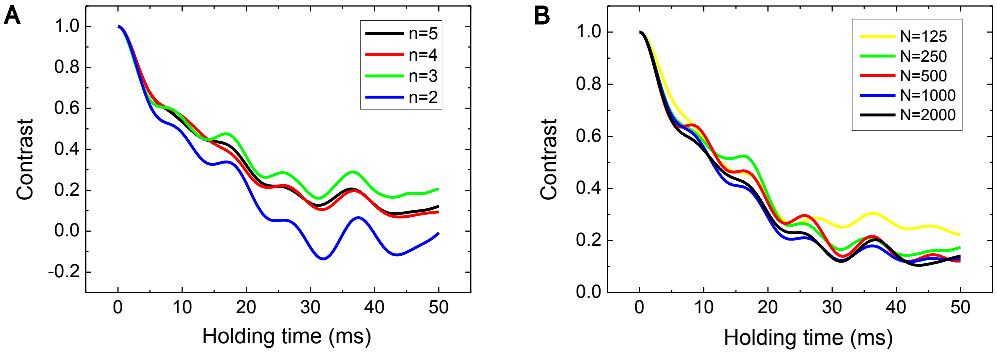

Figure 10.7: Convergence of the MACE calculation. (A) The cluster size n is tuned with molecule number $N = 1000$. (B) N is tuned with $n = 5$. Other conditions are, $|\downarrow\rangle = |0,0\rangle$, $|\uparrow\rangle = |1,0\rangle$, lattice constant = 0.532 nm, uniform lattice filling = 2.8%, molecular mass = 127 a.u., permanent dipole = 0.57 D, quantization axis direction = (1,1,0). Apart from some detailed differences, the MACE calculation converges well with $n \sim 5$ and $N \sim 1000$ and gives very reliable calculation result semi-quantitatively.

Then, we check the validity of our own developed program by reproducing the results reported in Ref. [1]. For simplicity, the conditions in the calculations here are slightly different. We take uniform filling and take the pure $|1,0\rangle$ state without hyperfine mixing. We tune the filling fraction to 2.8% and reach a consistent coherence decay curve as shown in Fig. 10.8(A). By discrete Fourier transforming the coherence decay data, we see peaks in the frequency domain at 56 Hz, 78 Hz, 114 Hz. The peaks agree with the three DDIs between the strong or the weak neighbors with the most interaction strengths and also agree with the relative ratio of the strengths of $\nu/2$, $\nu/\sqrt{2}$ and ν[23].

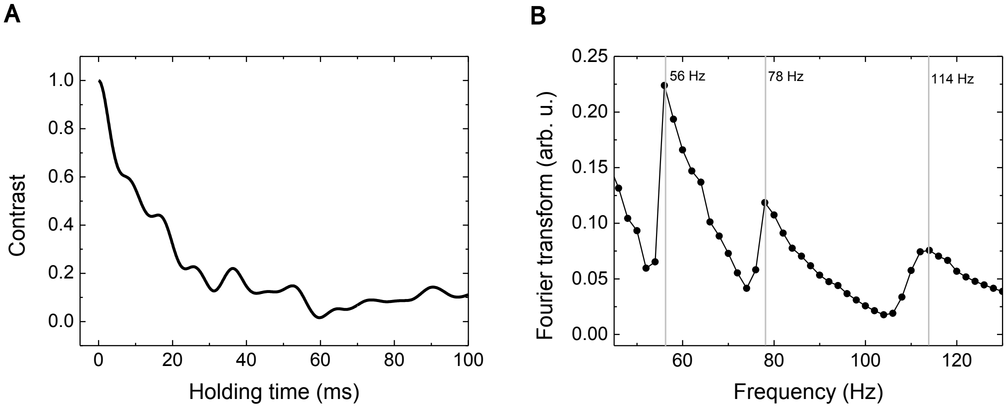

Figure 10.8: MACE calculation of the coherence evolution and its Fourier transform. (A) The evolution in Ref. [1] is reproduced up to 500 ms with a time interval of 0.1 ms. Only the dynamics of the first 100 ms is shown. (B) The discrete Fourier transform of the calculated coherence evolution. Peaks appear at 56 Hz, 78 Hz and 114 Hz with a relative ratio about $1 : \sqrt{2} : 2$, indicating the underlying DDI between the weak and the strong neighbors.

Having confirmed the correctness of the program, we then numerically investigate the NaRb bulk sample with the program. We first generate a molecular clouds with ∼1000 molecules according to the given temperature and the given trap frequencies. A typical molecular cloud distribution is shown in Fig. 10.9(A). Then we perform MACE to calculate the coherence decay. Since in a bulk sample, the spacings between molecules no longer take fixed values, the spin dynamics of all frequencies are superposed. As a result, the decay appears like a first-order exponential decay. In Fig. 10.9(B), the black points are the simulation result and the red curve gives the exponential fit to the data. Though very similar, we can still see the difference between the coherence decay and an exact exponential decay. To extract a time constant for the curve, we choose the point where the contrast reaches 37%. We calculate under various total molecule numbers and temperatures, and find the time constant only depends on the sample density. In Fig. 10.9(C), the black points correspond to $|\uparrow\rangle = |1, 0\rangle$. The coherence decay rate linearly depends on the peak density, indicating that the inter-molecular DDI is the source of decoherence. The two red points correspond to the $|1,1\rangle$ state, whose DDI is only 0.55 times than that of the $|1,0\rangle$ state. Therefore, we rescale the peak densities to 0.55 times the value and find the red points fall perfectly on the same line of the black points.

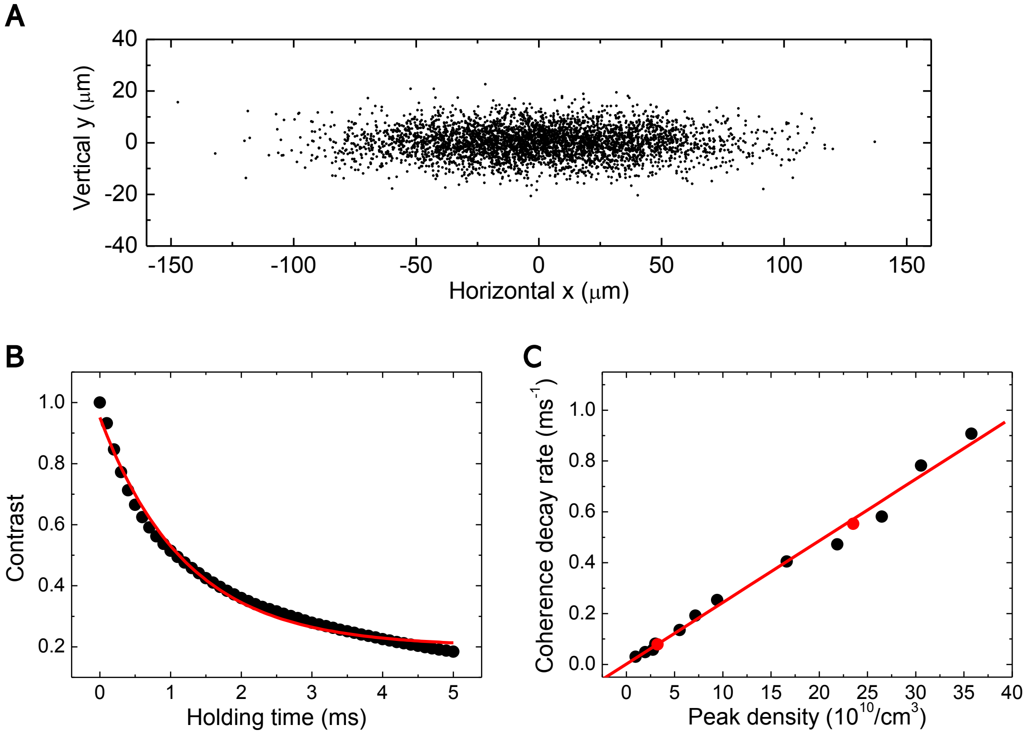

Figure 10.9: Simulating the coherence decay for a bulk sample of NaRb molecules. (A) A realization of 4000 molecules distribution under the typical experimental condition of 700 nK, (200,190,30) Hz trap frequencies and the quantization axis on the vertical direction. (B) An example coherence decay of the bulk sample with the first-order exponential fitting in red curve. (C) The density dependence of the coherence decay rate. The decay rate is extracted from the time when the coherence decays down to 37%. The decay rate shows linear dependency on the peak density with a slope of $0.024(1)\times10^{-10}$ cm^3/ms. The red points are for $|\uparrow\rangle = |1,1\rangle$ with the density rescaled to 0.55 times. The scaled red points fall on the same line with the black points.

10.6 Density dependence and state dependence of decoherence

After the numerical calculation, we turn to experimentally measuring the coherence decay in our system. The coherence is extracted with the spin echo method. An example set of data is shown in Fig. 10.10. The vertical axis is the number of molecules recovered in the $|\downarrow\rangle$ state $|0,0\rangle$ after the pulse sequence. The horizontal axis ϕ is the phase shift of the third MW pulse. We realize this phase shift by turning the signal generator to the phase modulation mode and controlling it with an external voltage. The signal generator is always on during the pulse sequence and the actual pulses going to the experiment are tailored by the MW switches. The external voltage takes a step between the second and the third pulse when the MW switches are off. In this experiment, the π-pulse is chosen to be 10 μs. When the MW is on resonance, as shown in Fig. 10.10, N_{max} occurs at $\phi = 0$ or $360°$ and N_{min} occurs at $\phi = 180°$. To extract the contrast, we fit the data with sinusoidal function with the period fixed to 360° and the contrast equals to the ratio between the amplitude and the offset. Fig. 10.10 shows the results of two different evolution times T, we see that for the blue points with the larger T, the coherence is decayed with a smaller contrast.

Measuring the contrast at different T, we can map out the coherence decay. Thanks to the fact that the magic angles for the $|1,1\rangle$ state and the $|1,0\rangle$ state are coincidentally close, we can switch $|\uparrow\rangle$ between the two states without changing the angle of the waveplates and measure the coherence decay for both case. Although, the magic angle configuration and the spin echo method greatly suppress the single-particle decoherence, we still limit the measurement with T below 1.5 ms in order to minimize the single-particle

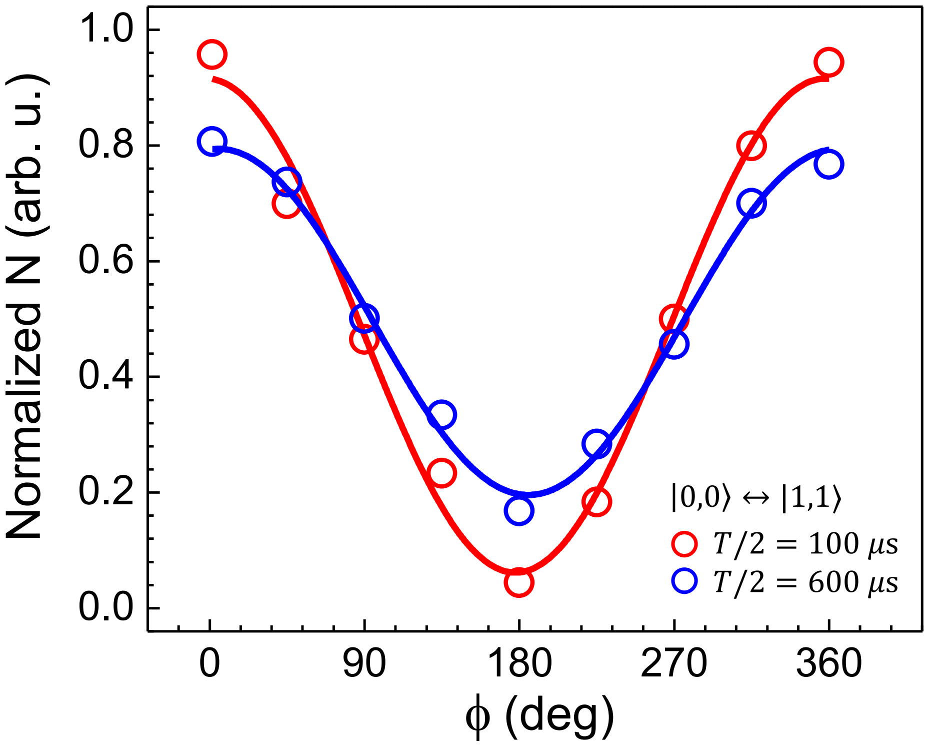

Figure 10.10: Measure the coherence with the spin echo method. The two first pulses of the spin echo method are in phase and the phase of the third pulse is tuned with a shift of ϕ. The molecule population in the $|\downarrow\rangle$ state are measured after the three-pulse sequence. The data are fit with the sinusoidal function with the period fixed to 360°. The contrast of the curve $(N_{max} - N_{min})/(N_{max} + N_{min})$ reflects the coherence of the system. With the longer evolution time, the blue data show less coherence than the red data.

decoherence due to the molecular motion in trap. Fig. 10.11 shows the coherence decay for both cases with a peak density of about 2.9×10^{11} cm^{-3}. We fit first-order exponential decay with a fixed unity contrast at $T = 0$ and get the coherence decay rate.

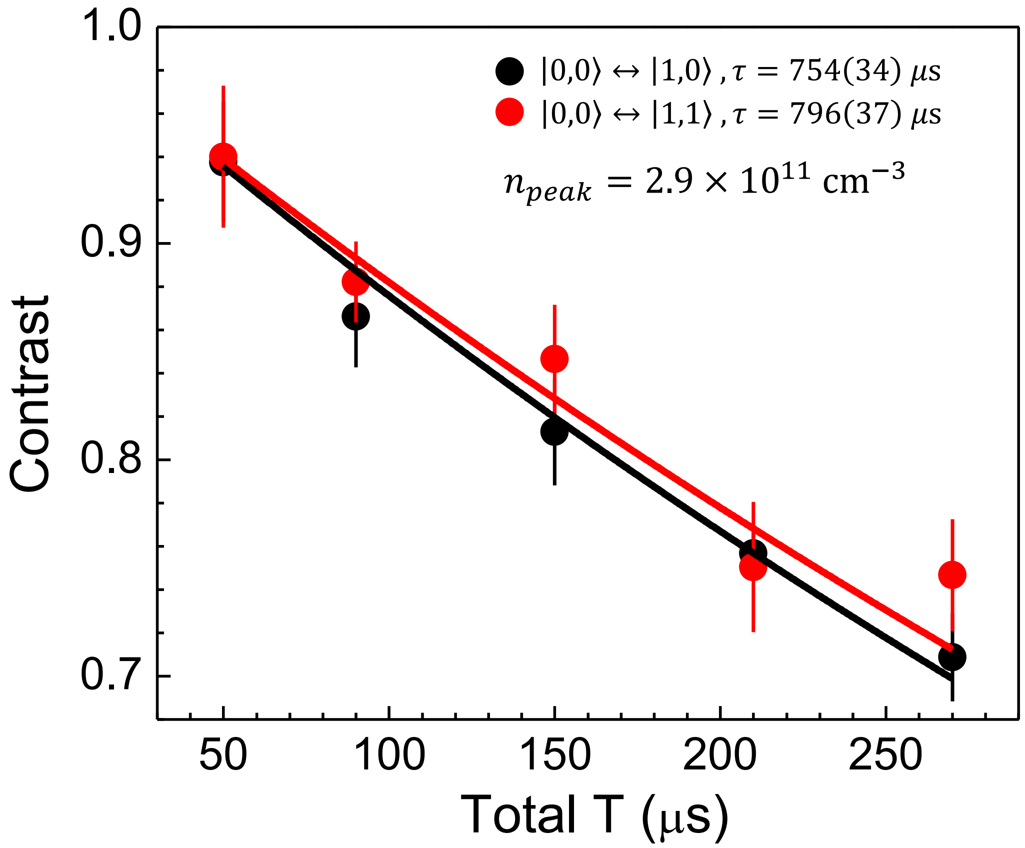

Figure 10.11: The coherence decay of the NaRb bulk sample. The contrast is measured under different total evolution time T by tuning the interval length between the pulses. The red points represent the case with $|\uparrow\rangle = |1, 1\rangle$ and the black points represent the case with $|\uparrow\rangle = |1, 0\rangle$. The contrast decay are fitted with the first-order exponential decay with a fixed unity contrast at zero evolution time. The decay rates appear to be similar for the two cases.

We then investigate the density dependence of the coherence decay rate. We tune the density by adding additional holding times for the ground-state molecules before starting the spin echo pulses. We know that there is two-body loss for the molecules in trap and the two-body loss also introduces the anti-evaporation effect. Hence, the longer holding time means that the total molecule number is fewer and the temperature is higher. Both aspects contribute to a lower density. With this method, we can tune the density for about 10 times from 29×10^{10} cm^{-3} down to 3×10^{10} cm^{-3}. The results are summarized in Fig 10.12. The decoherence for the $|1,0\rangle$ case is shown in black, the decoherence for the $|1,1\rangle$ case is shown in red. The MACE calculation for the $|1,1\rangle$, the result already shown in Fig. 10.9, is also included here in blue. The result shows an approximately linear dependence to the density, with the coherence decay rate being significantly slower for lower density cases. The linear dependence strongly indicates that the underlying process responsible for the decoherence is a two-body process. However, to our surprise, the red points and the black points fall on the same line. This is a strange observation. It disagrees with the DDI picture in which the red points should fall on a different line with 0.55 times the slope. Fit the linear model to all eight red and black points, we get a slope of $0.037(2)\times10^{-10}$ cm^3/ms, the same order but 50% larger than the MACE prediction of $0.024(1)\times10^{-10}$ cm^3/ms. Besides, we see that intercept of the fitted line is not zero, indicating the existence of the residual single-particle decoherence.

So far, we don't have a clear idea why the density dependence of the coherence of the two cases are nearly the same. The problem may have something to do with the severe inelastic collisions, including complex formation and hyperfine-changing collisions, in both cases. In principle, if two molecules leave the ensemble once they take an inelastic collision, such a process won't harm the coherence. But in reality, this assumption may not be fulfilled. The problem may also has something to do also with the ODT beam wavelength or the tiny leakage of MW due to the finite isolation of the

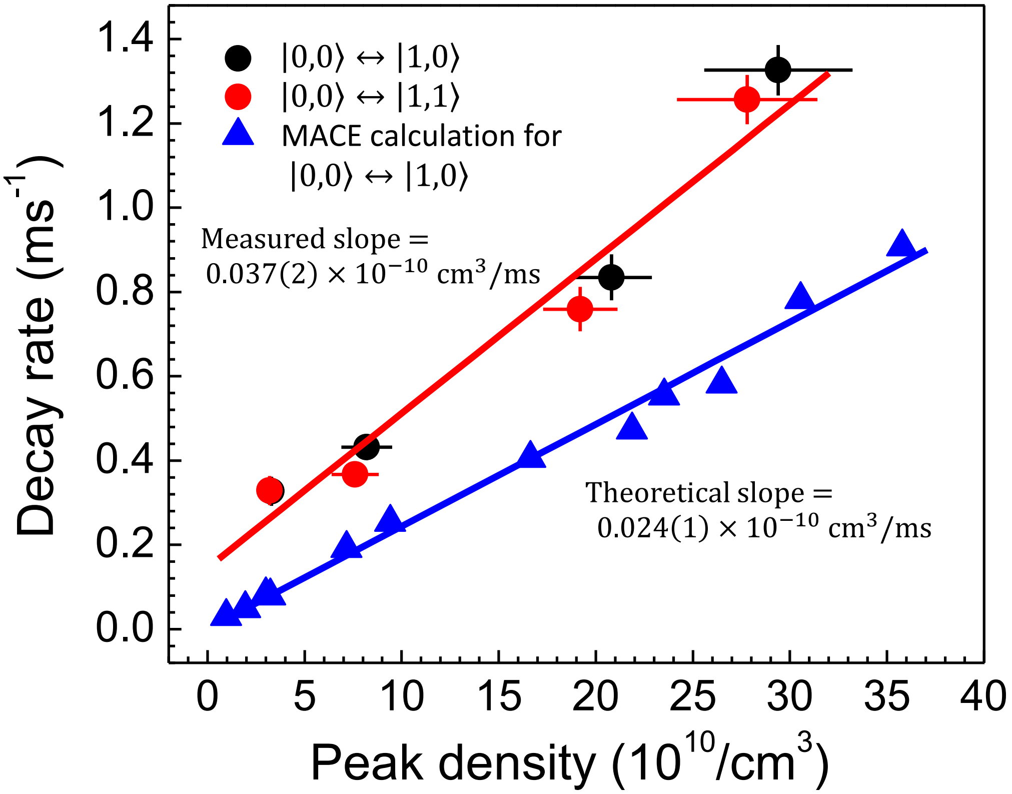

Figure 10.12: The density dependence of the coherence decay rate. The red points represent the case with $|\uparrow\rangle = |1,1\rangle$ and the black points represent the case with $|\uparrow\rangle = |1,0\rangle$. The peak density ranges from 3×10^{10} cm^{-3} to 29×10^{10} cm^{-3}. The coherence decay rate of the two states are similar, depends approximately linearly on the sample density. A linear fit to all eight data points gives a slope of $0.037(2) \times 10^{-10}$ cm^3/ms. The MACE calculation for the $|1,0\rangle$ case is shown in blue triangles which gives a slope of $0.024(1) \times 10^{-10}$ cm^3/ms.

MW switches. These ac fields may somehow interact with two molecules and effect the coherence. The cause behind this strange observation remains to be investigated in the future.

□ End of Chapter.

Chapter 11

Towards molecules in optical lattices

11.1 Overview

The next goal of our lab is producing a sample of ground-state NaRb molecule in a 3D optical lattice with low entropy. Most important applications of UPMs depend on the utilization of the optical lattice. Another advantage of working with optical lattices is that the lattice potential can greatly suppress the inelastic collisions between molecules if there is only one molecule per site.

To achieve this goal, we make several changes to our experimental setups. For instance, we change the ODT beam shape. We try to make the trap pancake-like whose potential is more uniform and holds more dilute samples. we also rearrange the optical paths for the ODT and the optical lattice, and we switch to doing the MW evaporative cooling in a plug trap instead of the original hybrid trap.

In this chapter, we present our recent progress on making the optical lattice.

11.2 Plug trap

Because we modify the shape of the ODT beams in the new setups for producing molecules in the 3D optical lattice, the maximum trap depth provided by ODT beams are much shallower than before. It can no longer be used in the MW evaporative cooling stage for introducing a shifted local potential minimum that mitigate the Majorana loss. To maintain the efficiency of the evaporative cooling, we plug the Majorana hole with a 532 nm laser. The decision on the plug parameters are based on the calculation of the Majorana loss rate[153].

The magnetic trapping is state-sensitive. Due to the motion of the atom, the single particle Hamiltonian may evolve diabatically, resulting in a possibility that the spin flips and the atom gets repelled from the trap. The adiabatic condition fails when the Larmor precession rate is comparable with the changing rate of the Zeeman energy,

$$\omega_L \sim \left| \frac{dB/dt}{B} \right| \tag{11.1}$$

where the Larmor precession rate

$$\omega_L = \frac{\mu_B |g_F m_F| |B|}{\hbar}. \tag{11.2}$$

Relate the B-field changing rate to the motion of the atom,

$$\left| \frac{dB/dt}{B} \right| = \frac{v}{r}. \tag{11.3}$$

The magnetic potential is linear, therefore

$$B = B'r \tag{11.4}$$

where B' is the gradient of the B-field, and for simplicity the B' is assumed to be the same in all three directions.

We can then define the concept of Majorana hole size which is a function of the atom velocity by equalizing the two terms in Eq. 11.1[154],

$$\rho_{hole} = \left| \frac{v\hbar}{\mu_B g_F m_F B'} \right|^{1/2}. \tag{11.5}$$

Once we defined the majorana hole size, we can numerically estimate the Majorana loss rate as a function of the temperature. The majorana loss can be approximately calculated from the following integral,

$$\Gamma_{Majorana} = \int 4\pi^2 v^3 \omega(\rho(v), v) \rho^2(v) dv \tag{11.6}$$

where

$$\omega(\vec{r}, \vec{v}) dr^3 dv^3 = C \exp\left[-\beta\left(\frac{m\vec{v}^2}{2} + V(\vec{r})\right)\right] dr^3 dv^3 \tag{11.7}$$

is the Boltzmann distribution with C being the normalization factor.

The idea here is as follows. We first sample a velocity of the atom from $\omega(\vec{r}, \vec{v})$. Then we find the hole size according to the velocity and we numerically calculate the possibility of finding the atom within the area of the Majorana hole where the atom is supposed to get lost. Finally, the integration is over all possible velocities.

In Fig. 11.1, we show typical plug trap potentials for the two atomic species. The plug beam has a wavelength of 532 nm, a power of 1 W and a beam waist of 35 μm. The magnetic gradient is 62 G/cm, a typical value after the magnetic trap decompression. With the wavelength closer to the Na atomic transition, the plug potential is 69 μK high for Na and 16 μK high for Rb. Under such conditions, we calculate the atom trap lifetime with respect to the temperature with or without the plug potential according to

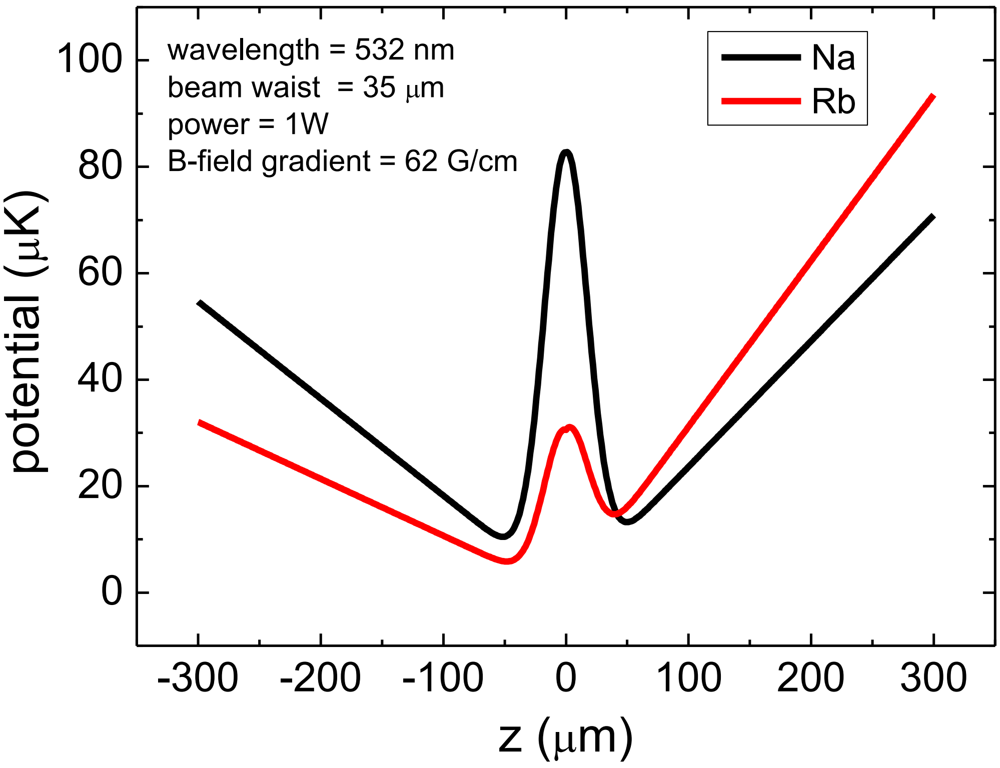

Figure 11.1: The plug trap potentials for Na and Rb atoms generated by a 532 nm laser with a beam waist of 35 μm and a power of 1 W. The B-field gradient is 62 G/cm. The potentials shown are along the vertical direction.

Eq. 11.6. The results are shown in Fig. 11.2. We see with the plug potential, the minimum trap lifetime is several minutes for Rb and even longer for Na. In comparison, without the plug, the lifetimes for both Na and Rb are reduced dramatically with lower temperatures.

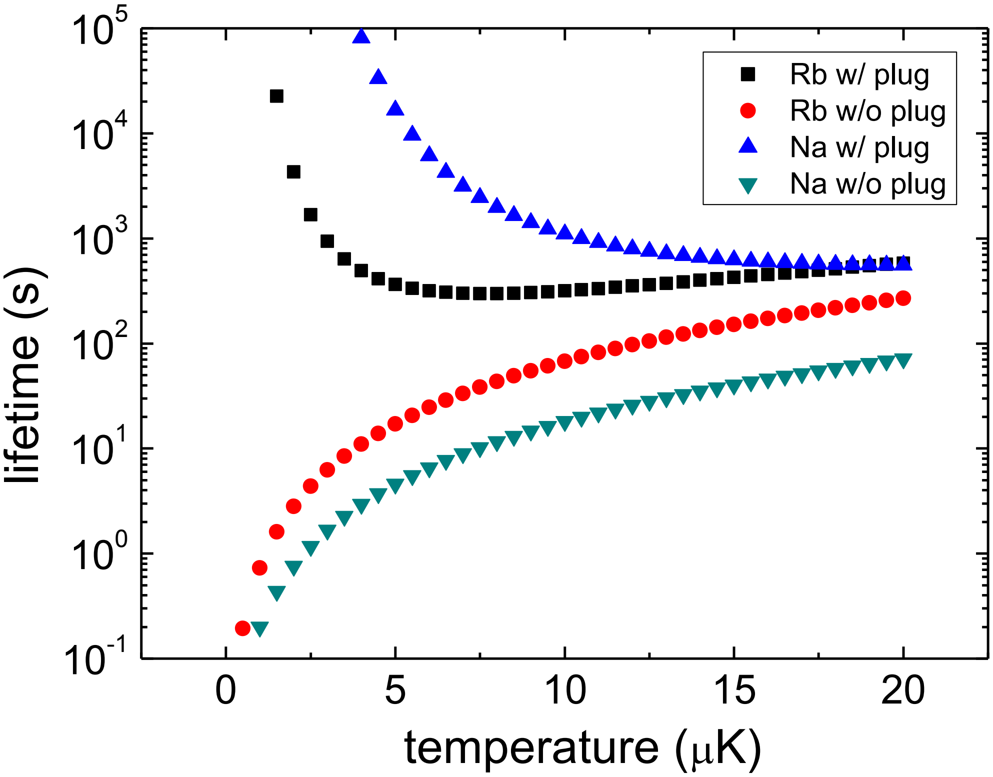

Figure 11.2: The lifetime determined by Majorana loss for Na and Rb, with or without the plug potential. The plug potential is as shown in Fig. 11.1. Without the plug potential, the lifetime drops monotonically as the temperature drops and the lifetime is too short for efficient evaporative cooling under 5 μK. With the plug potential, the lifetime rises again on the low temperature side and gives a minimum lifetime longer than 100 s. The low loss rates promise efficient evaporative cooling.

In practice, we shape the beam with a waist of 35 μm and we use 1.55 W power for the plug so far. We check the evaporative cooling efficiency in such a plug trap. First, we measure the trajectory of the evaporation with the Rb atoms only. We stop the evaporation at different end points and measure the number N and the temperature T of the atomic cloud. From these two quantities, we obtain the PSD by[155, 156]

$$\mathrm{PSD} = \frac{(2\pi\hbar^2/mk_BT)^{3/2}N}{\int \exp[-U(\vec{r})/k_BT]\mathrm{d}^3r} \tag{11.8}$$

where $U(r)$ is the trap potential and m is the mass of the atom. In Fig. 11.3, the evaporative cooling trajectory in the plug trap is shown in red compared with the trajectory in the plain magnetic trap without the plug in black. We see the evaporative cooling maintains good efficiency throughout the cooling process. The fitted slope is $\mathrm{d}\log(\mathrm{PSD})/\mathrm{d}\log(N) = -2.9$.

We then add in the Na atoms, and measure the evaporation trajectory for the mixture. The result is shown in Fig. 11.4 with the Na one shown in red and the Rb one shown in black. We see the trajectory for the Na atoms almost like a vertical line. This is because Na atoms are sympathetically cooled by the Rb atoms and the high plug potential for Na prevent any loss of the Na atoms. Meanwhile, the Rb atoms also gain PSD but with a slightly lower rate $\mathrm{d}\log(\mathrm{PSD})/\mathrm{d}\log(N) = -2.1$ than a pure Rb atomic cloud. We also observe, when the numbers of the two species are comparable, the sympathetic cooling becomes inefficient. The Rb PSD is even lost on the left side of the figure as the evaporation goes on. The best condition is obtained at the top of the bell-shaped curve. At that point, the Na cloud and the Rb cloud are one order and two orders away from the quantum degeneracy respectively. The resulting temperature for the mixture is about 2 μK. The condition is good enough for the further loading into the ODT.

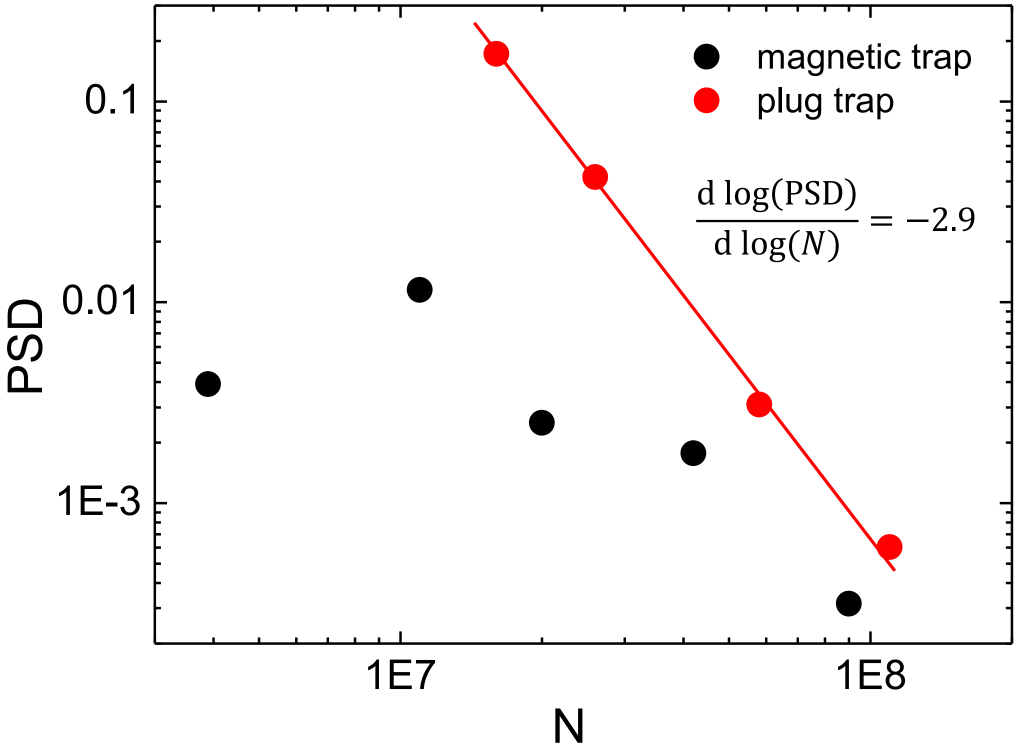

Figure 11.3: The trajectories of MW evaporative cooling with or without the plug. Without the plug (black), the efficiency of cooling gradually decreases as the majorana loss becomes severe with lower temperatures. There is no PSD gain anymore from cooling stages below N = 10^7. With the plug (red), the cooling efficiency maintains the same throughout the stages. The overall efficiency is $\Delta\log(\mathrm{PSD})/\Delta\log(N)$ = -2.9. The comparison of the two trajectories shows the effectiveness of the plug. The plug beam used here has a power of 1.55 W and a beam waist of 35 μm.

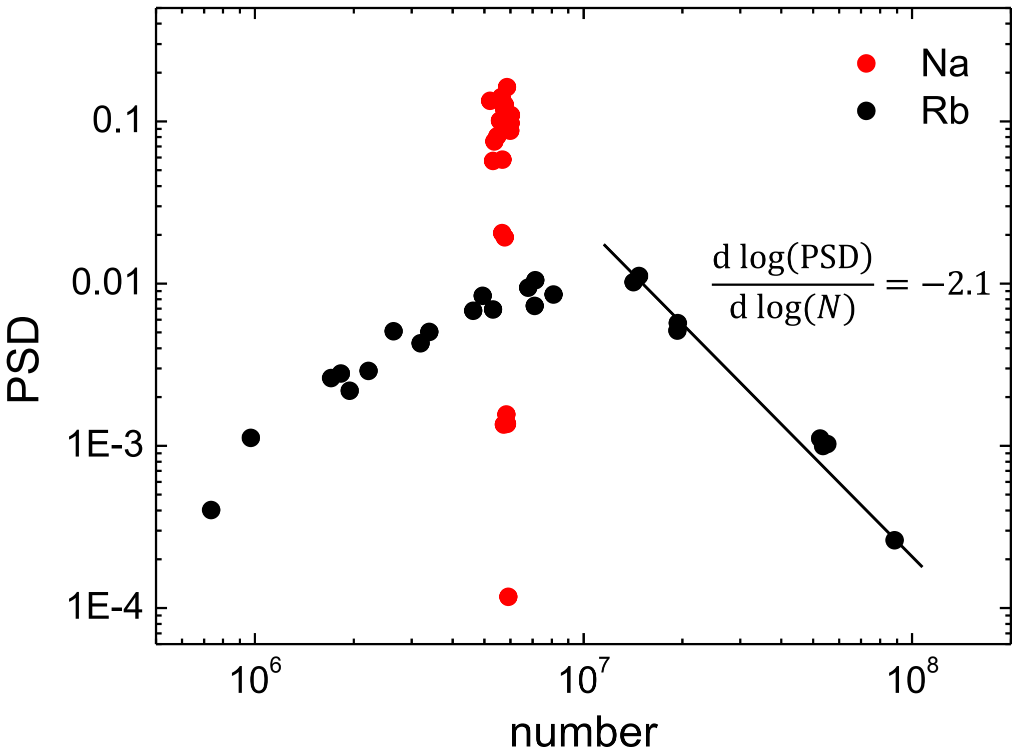

Figure 11.4: The trajectories of MW evaporative cooling of a Na and Rb mixture gas in the plug trap. The Na atoms (red) are sympathetically cooled by Rb atoms (black). The high plug potential for Na atoms prevent any loss of Na atoms during the cooling. The largest PSD achieved is one and two orders away from the quantum degeneracy for Na and Rb respectively. The sympathetic cooling becomes inefficient when the Rb atom number is comparable with the Na. The plug beam used here has a power of 1.55 W and a beam waist of 35 μm.

11.3 Optical lattice optics

Then we introduce the optics for the optical lattice and the ODT. In Fig. 11.6(A), we show the optical layout for the optical lattice before the optical fibers. The beams of the optical lattice are produced by a Nufern amplifier (NUA-1064-PC-0050-D0) which is seeded with a solid state laser from Wavicle Laser. Pairs of a $\lambda/2$ waveplate and a polarized beam splitter (PBS) divide the output beam into three beams with approximately the same power. The beams further pass through AOMs. The diffracted beams by AOMs are coupled into the fibers and the zeroth order beams are picked up by D-shape silver mirrors and directed into beam dumps. To avoid detrimental effects from the interference between lattice beams on different directions, we use one 110 MHz and two 80 MHz AOMs, and the two 80 MHz AOMs are working in different conditions with one of them producing the first order and the other one producing the negative first order diffraction.

The two lattice beams on the horizontal direction are delivered with NKT photonic crystal fibers (LMA-PM-15). The numerical aperture of the NKT fiber we measured is 0.054(2). Due to the hexagonal structure of the photonic crystal inside, the output beam shape also appears to be hexagonal to some extent in highly saturated pictures captured by the CCD. However, with the knife-edge method, we find that the intensity profile actually follows a perfect Gaussian beam quite well.

The layout of the optics for the horizontal optical lattice after the fiber delivering is shown in Fig. 11.5(C). The beam shaping scheme for the horizontal lattice is shown in detail in Fig. 11.6. On the output side, the fiber ports used are from Thorlabs (PAF-X-15-C). We carefully tune the distance between the fiber tip and the aspherical lens in the fiber port so that the horizontal size of the beam at the position of the sample meets our designed dimension, which

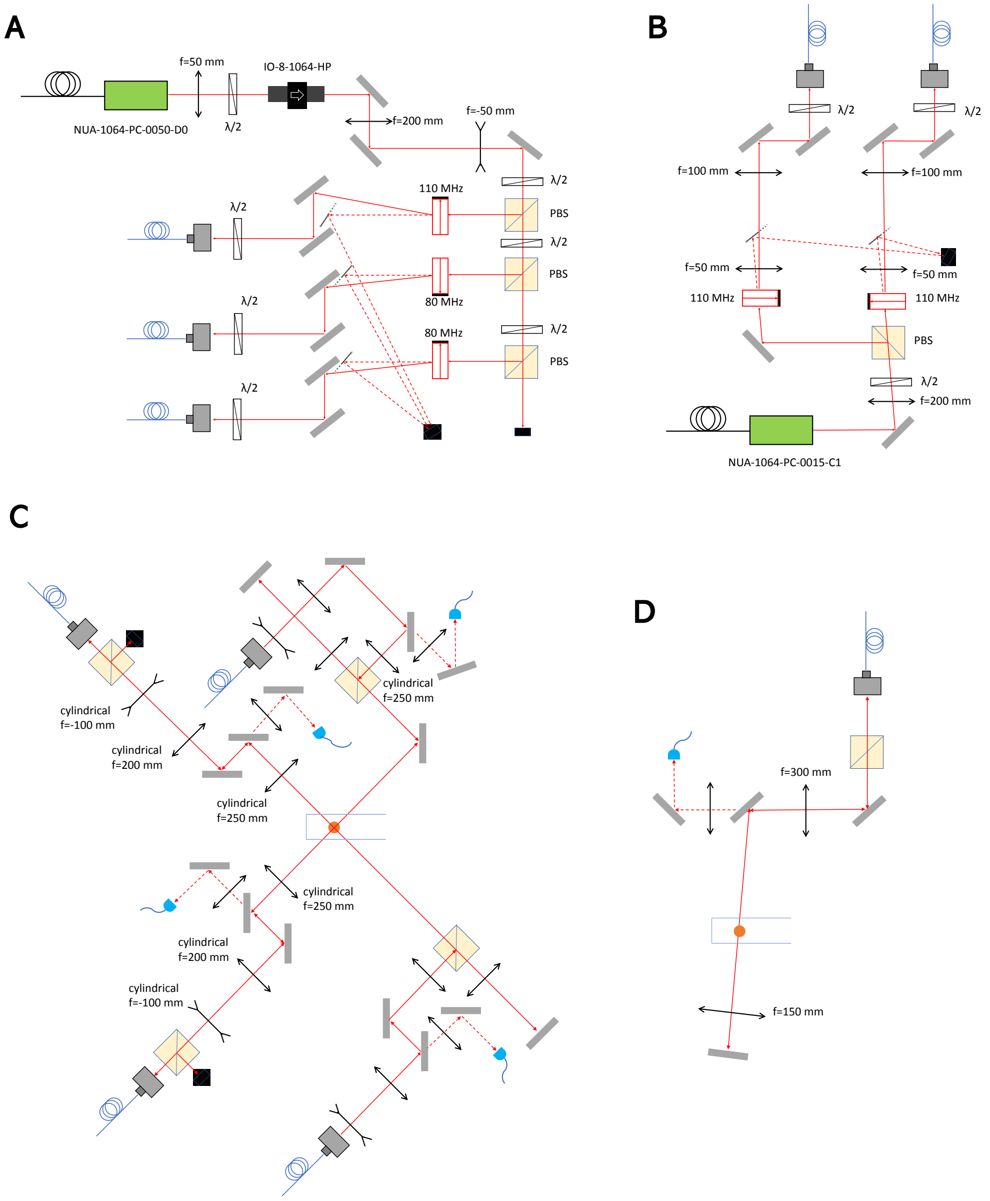
A
f=50 mm
IO-8-1064-HP
NUA-1064-PC-0050-D0
λ/2
f=200 mm
f=-50 mm
λ/2
110 MHz
PBS
λ/2
λ/2
PBS
80 MHz
λ/2
80 MHz
λ/2
PBS
λ/2
λ/2
B
λ/2
λ/2
f=100 mm
f=100 mm
f=50 mm
f=50 mm
110 MHz
110 MHz
PBS
λ/2
f=200 mm
NUA-1064-PC-0015-C1
C
cylindrical
f=250 mm
cylindrical
f=-100 mm
cylindrical
f=200 mm
cylindrical
f=250 mm
cylindrical
f=250 mm
cylindrical
f=200 mm
cylindrical
f=-100 mm
D
f=300 mm
f=150 mm

Figure 11.5: Optical layouts for optical lattice and ODT. (A) The layout of the optics for the optical lattice on the optical table before the fibers. (B) The layout of the optics for the ODT on the optical table before the fibers. (C) The layout of the optics for the horizontal optical lattice and the ODT after the fibers. (D) The layout of the optics for the vertical optical lattice after the fibers.

is 620 μm in diameter. Then, after the fiber port and before the cell, all the lenses are ultraviolet fused silica cylindrical lenses that only responsible for the shaping on the vertical direction. The beam size immediately after the fiber port is 1.7 mm in diameter. The vertical size is first expanded twice with a -100 mm/200 mm lens combination, and then focused by a 250 mm lens before the cell down to a diameter of 116 μm. After the cell, a 500 mm lens is placed to re-collimate the beam in both the horizontal and the vertical dimension. Finally, a mirror retro-reflects the beam and the lattice potential is built up via the interference. The last mirror before the cell is backside polished, and a small portion of power transmits and is picked up by photodiodes for the power feedback. The two lattice beams on the horizontal plane intersect with a right angle. Fig. 11.7(D) shows the optical layout for the vertical lattice. The fiber we use is OZ optics PMJ-A3HPCA3HPC-1064-6/125-3AS-5-1-AR2. The fiber port is Thorlabs PAF-X-7-C. A lens with a focal length of 300 mm is used before the cell, and a lens with focal length of 150 mm is used before the retro-reflecting mirror. The vertical lattice beam is tilted by about 6° to avoid undesired interferences between reflected beams from the multiple interfaces along the optical path. The resulting beam is round at the sample position with a waist of about 150 μm.

11.4 ODT optics

We show the optical layout for the ODT before the optical fibers in Fig. 11.5(B). The beams of the ODT are produced by another Nufern amplifier (NUA-1064-PC-0015-C1). The setup is similar to that of the optical lattice. The two 110 MHz AOMs give the opposite order of diffraction. The ODT beams are delivered by fibers from OZ optics (PMJ-A3HPCA3HPC-1064-6/125-3AS-5-1-AR2). The layout of the optics for the ODT is contained in Fig. 11.5(C).

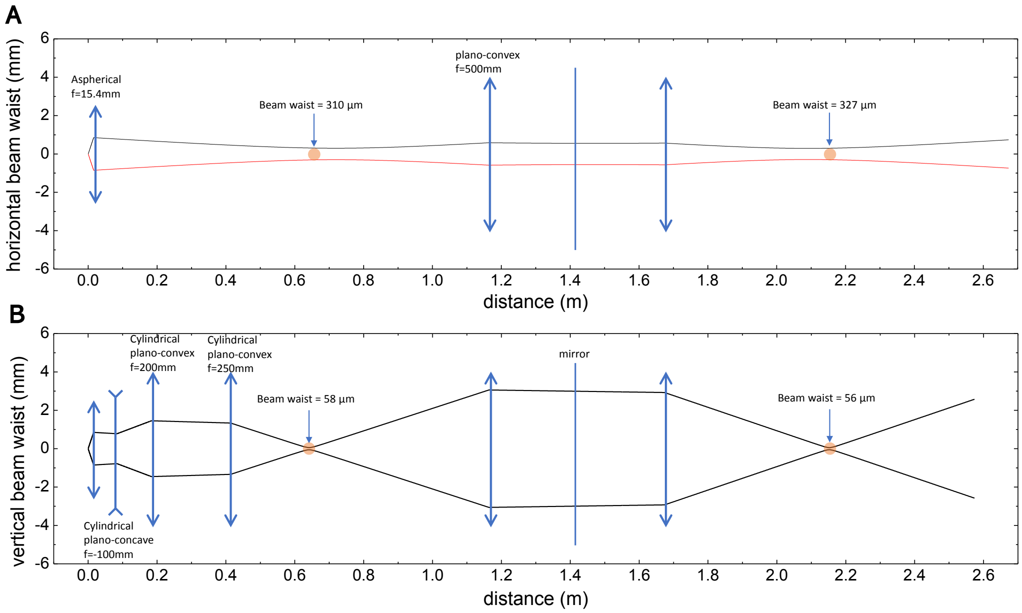

Figure 11.6: Schematic setup of Gaussian beam propagation for optical lattice. (A) shows the horizontal beam shaping and (B) shows the vertical beam shaping.

The beam shaping scheme for the ODT is shown in detail in Fig. 11.7. At the output side, the fiber ports are also from OZ optics (HPUC-2A3-1064-P-11AS-11). Same as the optical lattice case, the horizontal beam size is all taken care by the fiber port, and is 554 μm in diameter at the sample position. The rest lenses reshape the vertical size. The final size in the vertical direction is 98 μm in diameter. The ODT share the same optical path with the optical lattice. On each of the same paths, the polarization of the ODT beam are perpendicular to that of the lattice beam, so that PBS's are used to combine the optical lattice and the ODT beams. At the far end, the PBS after the optical lattice fiber port can avoid the ODT beams pouring into the lattice fiber.

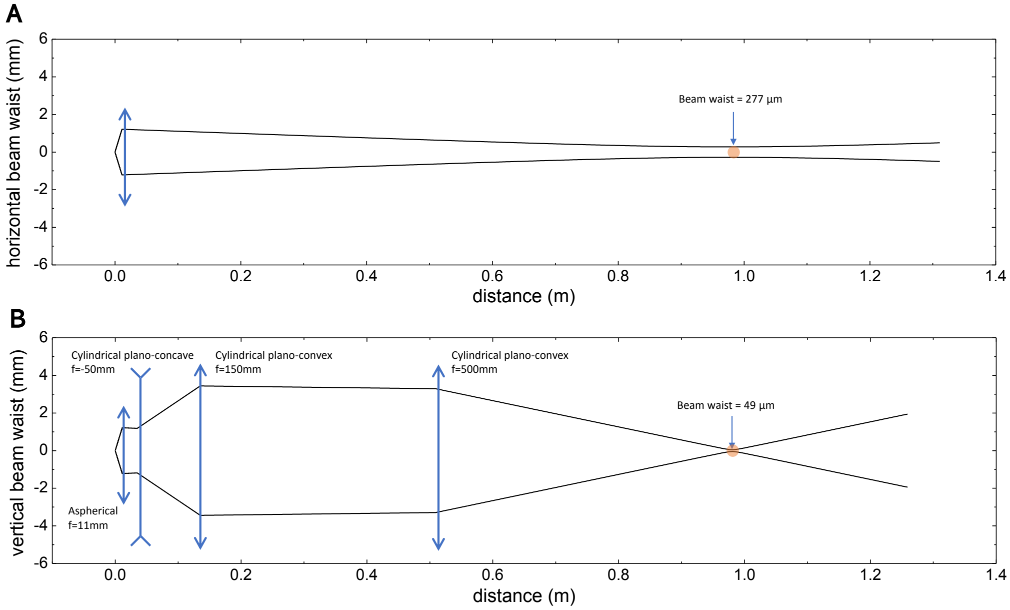

Figure 11.7: Schematic setup of Gaussian beam propagation for ODT. (A) shows the horizontal beam shaping and (B) shows the vertical beam shaping.

11.5 Laser intensity noise

The intensity noise in the lattice beams can induce heating and limit the lifetime of a BEC in the lattice. The instability in intensity can originate from several kinds of sources. For example, the cavity vibration, the intrinsic phase and frequency fluctuations caused by spontaneous emission in laser gain medium, and the intensity noise from a pump source, etc.

The intensity noise is typically proportional to the intensity. Therefore, the relative intensity noise (RIN) characterizes the instability in the power level of a laser[157]. The RIN is defined as

$$\mathrm{RIN} = \frac{\langle \Delta P(t)^2 \rangle}{P_0^2}, \tag{11.9}$$

where $\Delta P(t)$ stands for the fluctuation of the optical power, P_0 is the averaged optical power.

The setup we measure the RIN is simple. The laser beam is measured directly by photodiode for the power feedback, which converts the optical power to a voltage signal. The dc voltage signal is measured with a multimeter. The ac noise on the other hand is analysed by connecting the photodiode output to a spectrum analyzer.

Now, the optical power is converted into electrical signals,

$$P_E \propto i^2 \propto P_{opt}^2, \tag{11.10}$$

where P_E and P_{opt} are the electrical and optical power respectively, and i is the current inside the photodiode. The RIN is rewritten in the terms of electrical powers as below,

$$\mathrm{RIN} = \frac{\Delta P_E}{P_{E0}} \tag{11.11}$$

where ΔP_E is the overall noise, measured in power spectral density per Hz and P_{E0} is the average electrical power.

Because of some technical issues, the electrical RIN is not by itself the optical RIN. During the optical-electrical conversion, two other sources of noise are introduced. They are, the shot noise and the thermal noise in an electrical circuit. The overall noise ΔP_E thus consists of three terms:

$$\Delta P_E = N_L + N_q + N_{th}. \tag{11.12}$$

Here, N_L, N_q and N_{th} are laser noise, shot noise and thermal noise respectively.

To extract the laser noise, one needs to figure out the contributions from the other two sources. The thermal noise is relatively simple to find out. It is a background noise that is always there. So we block the laser beam, and the signal remains in the spectrum analyzer is the thermal noise. The shot noise, which stems from the randomness of the detection, is proportional to the square root of the dc signal. It can be calculated with

$$N_q = 2eI_{dc}R_L. \tag{11.13}$$

Here, e is the elementary charge, I_{dc} is the photo current and the R_L the load resistance inside the photodiode. With considerable amount of laser power of ∼mW, we estimate the relative magnitude of the shot noise is tiny and can be safely ignored.

In Fig. 11.8, we show the result on the RIN measurement. The amplifier is set at 23 A which is a normal current with which the amplifier can deliver enough power to the experiment. In this figure, the data in red are from the Nufern amplifier working in a open-loop configuration, the data in blue are from Nufern amplifier working in a closed-loop configuration, the data in grey are the thermal background. With the servo, the noise below 10 kHz is suppressed by more than 10 dB. Above 100 kHz, the intensity noise is essentially the same because of the finite bandwidth of the servo. On average, the RIN is about -100 dBc/Hz. The noise level is good enough for current purposes.

11.6 Band structure

The band structure calculation of a lattice potential is the starting point of a number of many-body system investigations. The optical lattice potential is generated by retro-reflecting a normal ODT beam with a mirror. The two counter-propagating beams interfere and establish a standing wave in space

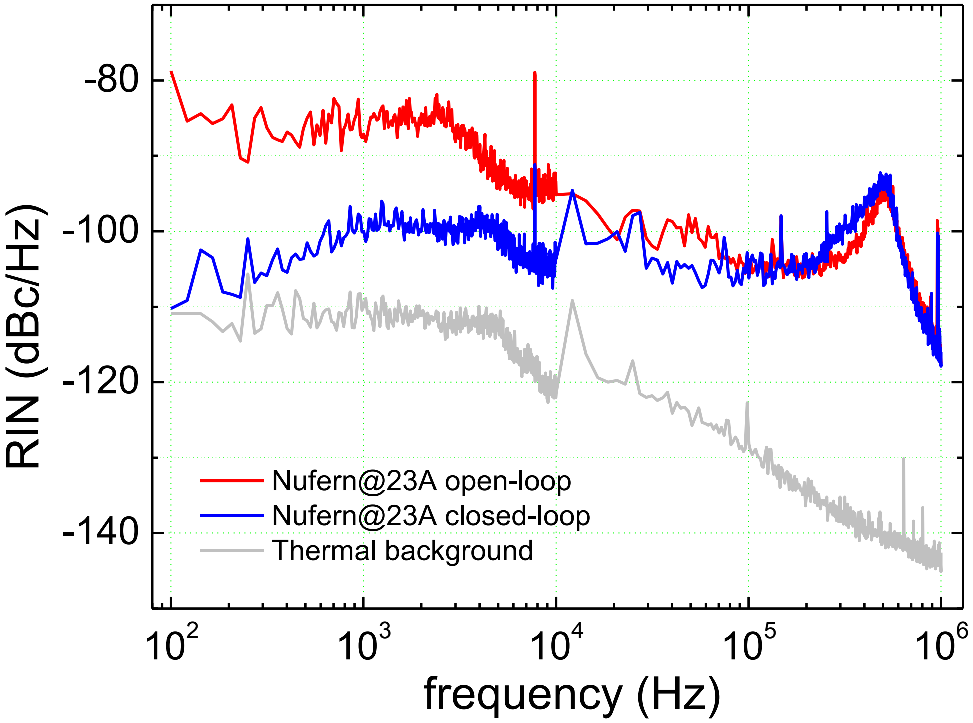

Figure 11.8: RIN of optical lattice beam. The RIN of the Nufern amplifier working at current = 23 A in a open-loop configuration (red) and in a closed-loop configuration (blue) and the thermal background noise (grey) are shown. The RIN the about on the lower frequency side is suppressed by the servo. The average RIN is about -100 dBc/Hz.

if the coherence length[158]

$$L = \sqrt{\frac{2\ln 2}{\pi}}\frac{\lambda^2}{n\Delta\lambda} \tag{11.14}$$

permits. Here, λ is the wavelength and $\Delta\lambda$ is the line width of the beam, n is the diffraction index. Near the center of the beam, the optical potential can be approximated by

$$V(r,z) = -V_0\left(1 - 2\frac{r^2}{\omega_0^2}\right)\sin^2(kz) \tag{11.15}$$

where k and ω_0 are the wave vector and the waist of the beam.

According to the Bloch's theorem[159], the eigenstate of a particle in a periodically repeating potential is a Bloch wave function expressed as

$$\phi_{n,\vec{q}}(\vec{r}) = e^{i\vec{q}\cdot\vec{r}}u_{n,\vec{q}}(\vec{r}). \tag{11.16}$$

Here, q is the quasi-momentum, n is the index for bands and $u(\cdot)$ is a periodic function with the same periodicity of the potential,

$$u_{n,\vec{q}}(\vec{r}+\vec{R}) = u_{n,\vec{q}}(\vec{r}) \tag{11.17}$$

for all $\vec{R}$ in the Bravais lattice.

In a cubic lattice, we can separate the variables of the three dimension. We can solve the band structure for either dimension,

$$\begin{aligned}
H_B u_{n,q}(x) &= E_{n,q}u_{n,q}(x) \\
H_B &= -\frac{1}{2m}(\hat{p}+q)^2 + V(x) \\
V(x) &= -\frac{1}{2}V_0[\cos(kx)+1].
\end{aligned} \tag{11.18}$$

Rearrange the terms in the time-independent Schrodinger equation, we obtain the Mathieu's differential equation,

$$\frac{\mathrm{d}^2 u_{n,q}}{\mathrm{d}x^2} + [a - 2s\cos(2x)]u_{n,q} = 0. \tag{11.19}$$

Here, $s = -V_{latt}/4E_r$. $a = E_{n,q}/E_r - V_0/2E_r$. $E_r = \hbar^2k^2/2m$ is called the recoil energy, which is a natural energy scale for optical lattices. To get the Bloch wave solution from the Mathieu's differential equation, the parameter a must equal to the characteristic value A for even Mathieu functions. The characteristic value A is a function of the quasi momentum q and the parameter s, and can be numerically evaluated. Therefore, to calculate the band structure, we can pick up any q and then find the corresponding A. Let a equal to A, and then solve the eigen-energy $E_{n,q}$ according to the expression of a.

Fig. 11.9 shows the calculated band structures of different lattice depths. With a higher lattice depth, the band gap is larger, the band is flatter and the zero-point energy is also higher.

11.7 Kapitza-Dirac scattering

Once a lattice potential is realized, one have to calibrate the depth of the lattice. One method to calibrate the depth of an optical lattice is the Kapitza-Dirac scattering[160]. In this method, the lattice potential is suddenly turned on and let the system evolve for some time before switching off all trapping potentials and measuring the interference pattern in space after TOF. With the varied evolution time, the final pattern periodically changes. From the evolution of the pattern, we can calibrate the depth of the lattice potential.

To be specific, there are essentially three operations in the Kapitza-Dirac

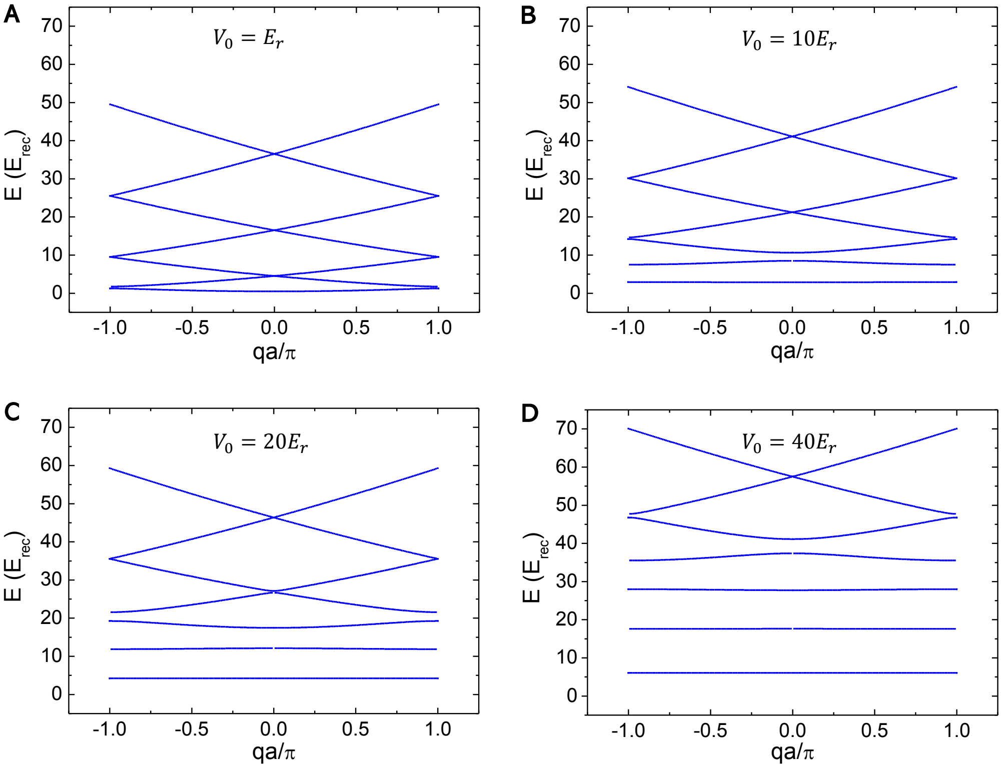

Figure 11.9: Band structure of a cubic lattice in one dimension given by solutions to the Mathieu's differential equation. The lowest seven bands of different lattice depths are shown: (A) $V_0 = 1E_r$, (B) $V_0 = 10E_r$, (C) $V_0 = 20E_r$, (D) $V_0 = 40E_r$.

scattering, two projections and one unitary evolution. At time zero, the initial degenerate Bose gas in bulk is projected onto the eigenstates of the lattice,

$$|\Psi(t=0)\rangle = \sum_{n=0}^{\infty} |n,q\rangle \langle n,q|\phi_q\rangle \,. \tag{11.20}$$

Then during the time interval τ that the lattice potential is on, the system undergoes a unitary evolution. The phase precession of each eigenstate goes in a different pace,

$$|\Psi(t)\rangle = \sum_{n=0}^{\infty} a^*_{n,q}(0)\exp[-iE_n(q)t/\hbar]\,|n,q\rangle \,, \tag{11.21}$$

where $a^*_{n,q}(0) = \langle n,q|\phi_q\rangle$. The third operation is the inverse process of the first projection,

$$b_q(m) = \sum_{n=0}^{\infty} a^*_{n,q}(0)a_{n,q}(m)\exp[-iE_n(q)\tau/\hbar], \tag{11.22}$$

where $b_q(m)$ is the coefficient for the state $|\phi_{q+2m\hbar k}\rangle$ in the lattice frame. Under the so-called Raman-Nath approximation, which is justified if τ is much shorter than the oscillation period of a lattice site[161, 162],

$$|b_q(m)|^2 = J_m^2\Big(\frac{V_0\tau}{2\hbar}\Big) \tag{11.23}$$

where the J_m are Bessel functions of the first kind. In our measurement for Rb atoms with a V_0 about 8 μK, this approximation fails when the measurement extended to several periods of interference pattern oscillation. The exact solution is given by a set of coupled differential equations from the time-dependent Schrodinger equation[163, 164],

$$i\frac{\mathrm{d}b_m}{\mathrm{d}t} = \frac{4m^2E_r}{\hbar}b_m + \frac{V_0}{4\hbar}(b_{m-1} + 2b_m + b_{m+1}). \tag{11.24}$$

Fig. 11.10(A) shows some raw data of the Kapitza-Dirac scattering for the Rb atoms. We see initially the BEC is at the 0th order. Turning on the lattice beam scatters the BEC to higher orders of discrete momentum states. In the CCD frame, diffractions from the -3rd order to the +2nd order are captured. To determine the lattice depth, we segment the figure and extract the population fraction of each order. Since some higher orders are out of frame, the "fraction" we referred to is the fraction only among the orders from the -2nd to the +2nd. The extracted fractions are plotted in Fig 11.10(B), together with fitting results according to Eq. 11.24. With only one free parameter, lattice depth V_0, we see a nice agreement between the theory and the experiment. The fitted V_0 in Fig 11.10(B) is 7.6 μK.

11.8 BEC phase correlation among 1D lattice layers

When a BEC is adiabatically loaded in a shallow optical lattice where particle transport is not prohibited, we can say that the local wave functions in the lattice sites have the same phase (or differ by a constant). Under such circumstances, the BEC released suddenly from the 1D lattice shows an interference pattern like the left figures in Fig. 11.11(A). Knowing the TOF time, one can directly infer the recoil momentum of the lattice from the spacing of the peaks. One the other hand, in the tight-binding limit when the lattice is deep, the condensate is split up into an array of local wave

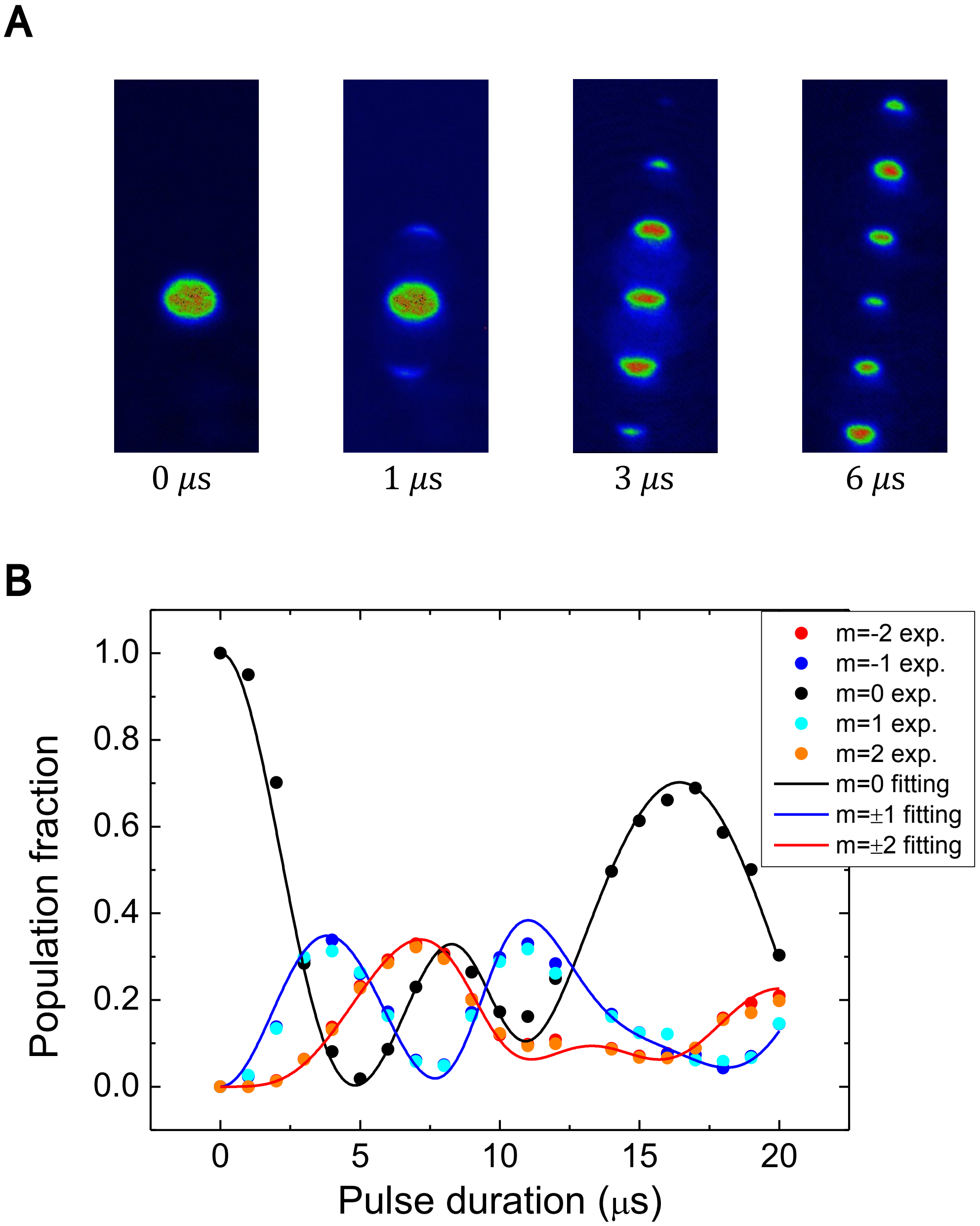

Figure 11.10: Kapitza-Dirac scattering of Rb atoms in 1D lattice. (A) The diffraction pattern with different evolution times. (B) Extracted population fraction evolutions from the experimental data and the theoretical fittings. The fitted lattice depth is 7.6 μK

functions and each posseses a random phase. Therefore, peaks in interference disappear after TOF[165]. Although an array of independent condensates can still interfere after TOF[166], the pattern is not significant due to the large number of layers occupied.

We demonstrate the loss of phase correlation with increasing lattice depth with our vertical lattice beam. Fig. 11.11(A) shows some raw data of the interference of the Rb BEC. The Rb BEC is first produced in the ODT, then while keeping the ODT on, the optical lattice potential is turned on to a certain value with the beam power exponentially increasing with a time constant of 150 ms. We hold the sample in such a potential for some time and then we switch off all potentials to let the sample fly out. The lattice depth is calculated based on the calibration from the Kapitza-Dirac scattering. With low lattice depths, we can see the interference pattern which manifests the phase correlation among the lattice sites. As the lattice gets deeper, the correlation gradually disappears. For a quantitative description, we define

$$\text{Visibility} = \frac{\mathrm{OD}_{\mathrm{max}} - \mathrm{OD}_{\mathrm{min}}}{\mathrm{OD}_{\mathrm{max}} + \mathrm{OD}_{\mathrm{min}}}. \tag{11.25}$$

We fit the first order diffraction to a general 2D Gaussian model in a window of 80×40 pixels, and assign the peak of the Gaussian to $\mathrm{OD}_{\mathrm{max}}$. The $\mathrm{OD}_{\mathrm{min}}$ is obtained by finding the minimum optical depth along the line connecting the centers of the zeroth and the first order diffractions. Fig. 11.11(B) shows the extracted visibility with respect to the lattice depth. The visibility above $30E_r$ becomes not reliable as the first order diffraction can hardly be seen. The visibility drops to 50% at a lattice depth equals to $17E_r$.

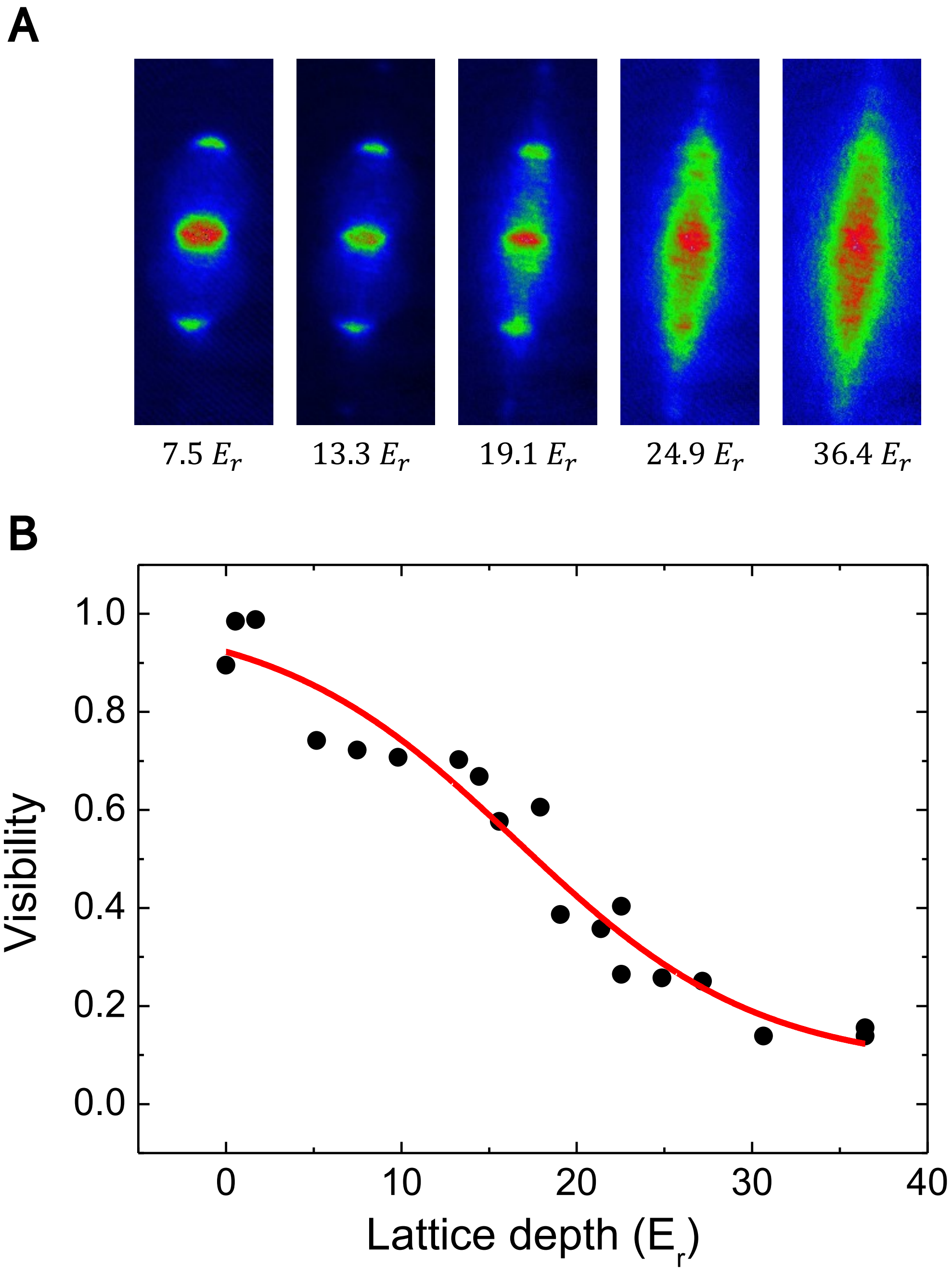

Figure 11.11: Visualize phase correlation among 1D lattice sits. (A) Interference pattern of the BEC after TOF from the vertical optical lattice of different depths. (B) Visibility decay of interference pattern. the visibility is defined by Eq. 11.25. The lattice depth is obtained according to the calibration from the Kapitza-Dirac scattering measurement in Fig. 11.10.

11.9 Outlook

We have already constructed the vertical lattice and the two other horizontal beams are under construction. Once we have all three lattice beams, we will start the endeavor of producing ground-state NaRb molecules in a 3D optical lattice, the scheme of which is illustrated in Fig 11.12. For NaRb, a heteronuclear molecule that made of two bosonic atoms, a natural starting point of producing a lattice molecular gas is a double Mott insulator phase. By tuning the density of BECs, one can obtain Mott insulator phase in the first lobe for both species with one atom per species per site. Under such circumstances, there is only one molecule per site if it is formed, and any inelastic collisions are avoided. One can calculate the density of atoms needed is 6.6×10^{12} cm^{-3}. Normally, the peak density of BECs we achieve now is one to two orders above. Techniques like spilling or tunneling through barrier that could make BEC more dilute are needed. The loading of BECs from ODT to optical lattice is also important. The interspecies interactions can affect the final temperature of the mixture after the adiabatic loading procedure and limit the peak filling[167]. Peak filling f is important because it is closely related to the entropy per particle

$$s \approx -\frac{k_B}{f}[f\ln(f) + (1-f)\ln(1-f)], \tag{11.26}$$

which is a key quantity and some new regimes of many-body systems can only be achieved with sufficiently low entropies[168]. Therefore, during the loading stage, the interspecies scattering length may be elaborately tuned. Once the double Mott insulator is obtained, with a deep lattice potential, the magnetoassociation efficiency of the two atoms is guaranteed to be essentially unity[169, 170]. Start from a lattice sample of Feshbach molecules, the same STIRAP scheme can be followed to produce the ground-state molecules. Although 6.6×10^{12} cm^{-3} is a low density for the atomic BECs, it is a relatively high value for the molecules, whose density is at most 6×10^{11} cm^{-3} in our original ODT. In such a bulk sample, the molecules' PSD are two orders away from the quantum degeneracy. Carefully designed procedures of molecule production in an optical lattice can preserve the PSD to the maximum extent. Therefore, if we then adiabatically turn off the lattice potential, the molecule bulk sample should be very close to the quantum degeneracy. This is already a huge benefit that the lattice can bring, let alone those applications in lattice that we have already discussed a lot throughout this thesis. One may argue that the severe collisional loss in a dense molecular sample may quickly kill the PSD. However, one need also bear in mind that the underlying loss mechanisms are different for reactive and nonreactive molecules. When the nonreactive sample is so cold that single resonances due to the transition complex states are resolvable, then, the loss behavior would deviate from the universal model and stable sample could be obtained with fine tuned external fields.

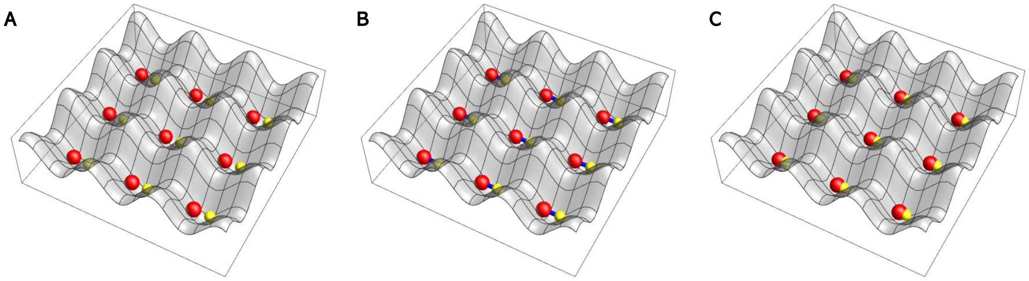

Figure 11.12: Scheme of producing a lattice gas of ultracold NaRb polar molecules (A) Double first-lobe Mott insulator of degenerate gas of Na and Rb atoms. (B) One Feshbach molecule per lattice site after magnetoassociation (C) One ground-state molecule per lattice site after STIRAP.

□ End of Chapter.

Chapter 12

Conclusions

In this thesis, we investigate the ultracold collisions with NaRb ground-state molecules in a series of different scenarios. The foundation of the experiments is the success creation and the precise internal state control of the NaRb molecule. Technical things such as accurate calibration on the molecular number and temperature and the suppression of the molecular motions etc. ensure an accurate and reliable determination of the loss rate constants.

With the control on the vibrational degree of freedom, we compare the collisions with different chemical reactivities. The result agrees with the resonant scattering picture with the complex formation semi-quantitatively. With the utilization of a dc E-field, we further polarize the ultracold ground-state NaRb molecules and investigate the dipolar collisions between them. The result also show agreement with the model and highlights the coupling between DDI and quantized nature of ultracold collisions.

With the population transfer via MWs, we investigate the dipolar collisions in the absence of a dc E-field, in a 50/50 mixture of two different rotational states. We observe different loss rate constants in different combination of states which qualitatively agrees with the relative strength of the

DDIs. As a comparison, we also investigate the collision with two hyperfine states in the ro-vibrational ground state which yields much lower loss rate constants. The result agrees with the close-coupling calculation and reveals the importance of DDI, which modifies the interaction potentials and introduces the hyperfine-changing collisions, in a mixture sample.

With the species-selective removal of residual atoms, we investigate the collision of the NaRb ground-state molecule with the atoms. We explore the collisions of Na+NaRb and Rb+NaRb, which have distinct chemical reactivities. We observe agreement with the universal model in the Wigner regime for both cases. We tune the Rb+NaRb collisional threshold by tuning the Zeeman shift of the Rb atoms and observe no resonance in a scan of 14 G wide. The Rb+NaRb case is supposed to have sparser trimer transition complex states. It should not agree with the universal model and resonances should be observable. The Rb+NaRb result is out of our expectation and future investigations are demanded.

The collisional experiment series deepen our understanding and pave our way towards manipulating interactions between UPMs. It is critical for further experiments of all relevant fields using UPM as a platform. Meanwhile, they also throw out new questions. For example, "how important is the short-range physics in molecular collisions? how can we characterize the short-range physical effects with more reliable experimental methods?", "what really happens to those complexes? can we confirm the existence of complexes with some technique?", "what happens to the nonreactive Rb+NaRb collision? Why no resonance observed?" etc.

To answer those questions, an upgrade on the experimental apparatus is certainly needed. One possible direction is to integrate optical tweezer technique and product detection technique such as REMPI into the system.

With the optical tweezer technique, we can produce a single transition complex and get rid of additional processes like the molecule-complex collision. The complex formed in this way could be detect directly or indirectly by waiting for the molecule revival from the complex dissociation. To capture the complex in trap, a different laser with longer wavelength could be considered. An improvement in B-field stability could also be benefitial for the collisional experiments. With a finer B-field resolution, for instance, the Rb+NaRb resonances in loss rate constants that are originally smoothened out may stand out.

Besides collisions, we also investigate the decoherence between the rovibrational ground state and the first rotational excited states in a bulk sample. Theoretically, we calculate the decoherence rate with the MACE algorithm. Experimentally, we tune the polarization of the ODT beams to the magic angle and use the spin-echo method to eliminate the single-particle decoherence. We then observe a density dependent decoherence rate for two choices of superposition state. The dependence to the density is of the same order as the theoretical calculation. However, the two cases, which have different strengths of DDI, appear to have the same dependence and that disagrees with the spin-exchange picture used in the MACE calculation. Future investigations are demanded for this topic. The key difference between the experimental reality and the simple MACE model is the existence of strong interstate and intrastate lossy molecular collisions in the experiment. It would be interesting to answer questions like “what kind of role does the loss play in the decoherence process in a bulk sample?”.

Finally, we show our recent progress on the 3D optical lattice. We show our design for the optical lattice together with the new ODT. We also switch to the plug trap from the hybrid trap for the MW evaporative cooling. With the vertical lattice, we calibrate the lattice depth with the Kapitza-Dirac scattering and we demonstrate the phase correlation decay between the sites of the 1D lattice by varying the lattice depth and observing the interference pattern after TOF.

□ End of Chapter.

Bibliography

[1] K. R. Hazzard et al., Physical review letters **113**, 195302 (2014).

[2] M. H. Anderson, J. R. Ensher, M. R. Matthews, C. E. Wieman, and E. A. Cornell, science **269**, 198 (1995).

[3] K. B. Davis et al., Physical review letters **75**, 3969 (1995).

[4] J. D. Weinstein et al., Nature **395**, 148 (1998).

[5] H. L. Bethlem, G. Berden, and G. Meijer, Physical Review Letters **83**, 1558 (1999).

[6] J. R. Bochinski, E. R. Hudson, H. J. Lewandowski, G. Meijer, and J. Ye, Physical review letters **91**, 243001 (2003).

[7] J. Barry, D. McCarron, E. Norrgard, M. Steinecker, and D. DeMille, Nature **512**, 286 (2014).

[8] L. Anderegg et al., Physical review letters **119**, 103201 (2017).

[9] L. Anderegg et al., arXiv preprint arXiv:1803.04571 (2018).

[10] K.-K. Ni et al., Science **322**, 231 (2008).

[11] T. Takekoshi et al., Phys. Rev. Lett. **113**, 205301 (2014).

[12] P. K. Molony et al., Phys. Rev. Lett. **113**, 255301 (2014).

[13] J. W. Park, S. A. Will, and M. W. Zwierlein, Phys. Rev. Lett. **114**, 205302 (2015).

[14] M. Guo et al., Phys. Rev. Lett. **116**, 205303 (2016).

[15] T. M. Rvachov et al., Physical review letters **119**, 143001 (2017).

[16] S. Ospelkaus et al., Science **327**, 853 (2010).

[17] K.-K. Ni et al., Nature **464**, 1324 (2010).

[18] M. De Miranda et al., Nature Physics **7**, 502 (2011).

[19] X. Ye, M. Guo, M. L. González-Martínez, G. Quéméner, and D. Wang, Science advances **4**, eaaq0083 (2018).

[20] B. Neyenhuis et al., Physical review letters **109**, 230403 (2012).

[21] J. W. Park, Z. Z. Yan, H. Loh, S. A. Will, and M. W. Zwierlein, Science **357**, 372 (2017).

[22] J. A. Blackmore et al., arXiv preprint arXiv:1804.02372 (2018).

[23] B. Yan et al., Nature **501**, 521 (2013).

[24] S. Trotzky et al., Science **319**, 295 (2008).

[25] D. Greif, T. Uehlinger, G. Jotzu, L. Tarruell, and T. Esslinger, Science , 1236362 (2013).

[26] G. Quemener and P. S. Julienne, Chemical Reviews **112**, 4949 (2012).

[27] J. Wolf et al., Science **358**, 921 (2017).

[28] J. Rui et al., Nature Physics **13**, 699 (2017).

[29] L. Liu et al., Science **360**, 900 (2018).

[30] I. Georgescu, S. Ashhab, and F. Nori, Reviews of Modern Physics **86**, 153 (2014).

[31] A. Micheli, G. Brennen, and P. Zoller, Nature Physics **2**, 341 (2006).

[32] H. P. Büchler et al., Physical Review Letters **98**, 060404 (2007).

[33] A. V. Gorshkov et al., Physical review letters **107**, 115301 (2011).

[34] Y. Zhou, M. Ortner, and P. Rabl, Physical Review A **84**, 052332 (2011).

[35] M. Baranov, M. Dalmonte, G. Pupillo, and P. Zoller, Chem. Rev. **112**, 5012 (2012).

[36] M. Ortner, A. Micheli, G. Pupillo, and P. Zoller, New Journal of Physics **11**, 055045 (2009).

[37] B. Capogrosso-Sansone, C. Trefzger, M. Lewenstein, P. Zoller, and G. Pupillo, Physical review letters **104**, 125301 (2010).

[38] L. Pollet, Phys. Rev. Lett. **104**, 125302 (2010).

[39] R. P. Feynman, International journal of theoretical physics **21**, 467 (1982).

[40] D. DeMille, Phys. Rev. Lett. **88**, 067901 (2002).

[41] S. Yelin, K. Kirby, and R. Côté, Physical Review A **74**, 050301 (2006).

[42] J. Zhu, S. Kais, Q. Wei, D. Herschbach, and B. Friedrich, The Journal of chemical physics **138**, 024104 (2013).

[43] F. Herrera, Y. Cao, S. Kais, and K. B. Whaley, New Journal of Physics **16**, 075001 (2014).

[44] M. Karra, K. Sharma, B. Friedrich, S. Kais, and D. Herschbach, The Journal of Chemical Physics **144**, 094301 (2016).

[45] K.-K. Ni, T. Rosenband, and D. D. Grimes, arXiv preprint arXiv:1805.10930 (2018).

[46] L. Carr, New J. Phys. **11**, 055049 (2009).

[47] E. R. Hudson, H. Lewandowski, B. C. Sawyer, and J. Ye, Physical review letters **96**, 143004 (2006).

[48] J. Baron et al., Science , 1248213 (2013).

[49] J. J. Hudson et al., Nature **473**, 493 (2011).

[50] E. Purcell and N. Ramsey, Physical Review **78**, 807 (1950).

[51] R. D. Levine, *Molecular Reaction Dynamics*, Cambridge University Press, Cambridge, UK, 2009.

[52] P. S. Julienne, T. M. Hanna, and Z. Idziaszek, Physical Chemistry Chemical Physics **13**, 19114 (2011).

[53] H. A. Bethe, Phys. Rev. **47**, 747 (1935).

[54] E. P. Wigner, Phys. Rev. **73**, 1002 (1948).

[55] H. Friedrich and H. Friedrich, *Theoretical atomic physics*, volume 3, Springer, 2006.

[56] M. S. Child, *Molecular collision theory*, Courier Corporation, 1996.

[57] R. V. Krems, Phys. Chem. Chem. Phys. **10**, 4079 (2008).

[58] H. Sadeghpour et al., Journal of Physics B: Atomic, Molecular and Optical Physics **33**, R93 (2000).

[59] P. S. Żuchowski, M. Kosicki, M. Kodrycka, and P. Soldán, Phys. Rev. A **87**, 022706 (2013).

[60] M. Lepers, R. Vexiau, M. Aymar, N. Bouloufa-Maafa, and O. Dulieu, Phys. Rev. A **88**, 032709 (2013).

[61] R. Vexiau, M. Lepers, M. Aymar, N. Bouloufa-Maafa, and O. Dulieu, J. Chem. Phys. **142**, 214303 (2015).

[62] M. Mayle, G. Quéméner, B. P. Ruzic, and J. L. Bohn, Phys. Rev. A **87**, 012709 (2013).

[63] G. Quéméner, J. L. Bohn, A. Petrov, and S. Kotochigova, Phys. Rev. A **84**, 062703 (2011).

[64] B. Gao, Phys. Rev. Lett. **105**, 263203 (2010).

[65] Z. Idziaszek, G. Quéméner, J. L. Bohn, and P. S. Julienne, Phys. Rev. A **82**, 020703 (2010).

[66] M. Seaton, Reports on Progress in Physics **46**, 167 (1983).

[67] C. H. Greene, A. Rau, and U. Fano, Physical Review A **26**, 2441 (1982).

[68] B. R. Johnson, Multichannel log-derivative method for scattering calculations, Technical report, Ohio State Univ., Columbus, 1973.

[69] B. R. Johnson, The Journal of Chemical Physics **69**, 4678 (1978).

[70] D. Manolopoulos, The Journal of chemical physics **85**, 6425 (1986).

[71] G. Quéméner, arXiv preprint arXiv:1703.09174 (2017).

[72] C. Curtiss, The Journal of Chemical Physics **21**, 2045 (1953).

[73] K. Takayanagi, Progress of Theoretical Physics **11**, 557 (1954).

[74] A. Stone, *The theory of intermolecular forces*, OUP Oxford, 2013.

[75] G. Wang and G. Quéméner, New J. Phys. **17**, 035015 (2015).

[76] F. Wang, *Studies of an ultracold Bose-Bose mixture with tunable interspecies interactions*, PhD thesis, The Chinese University of Hong Kong (Hong Kong), 2016.

[77] M. Guo, *An Ultracold Dipolar Gas of Ground-state* $^{23}Na^{87}Rb$ *Molecules*, PhD thesis, The Chinese University of Hong Kong (Hong Kong), 2017.

[78] F. Wang, D. Xiong, X. Li, D. Wang, and E. Tiemann, Phys. Rev. A **87**, 050702 (2013).

[79] R. Grimm, M. Weidemüller, and Y. B. Ovchinnikov, Optical dipole traps for neutral atoms, in *Advances in atomic, molecular, and optical physics*, volume 42, pages 95–170, Elsevier, 2000.

[80] Y.-J. Lin, A. R. Perry, R. L. Compton, I. B. Spielman, and J. V. Porto, Physical Review A **79**, 063631 (2009).

[81] F. Wang, X. Li, D. Xiong, and D. Wang, Journal of Physics B: Atomic, Molecular and Optical Physics **49**, 015302 (2015).

[82] C. Chin, R. Grimm, P. Julienne, and E. Tiesinga, Rev. Mod. Phys. **82**, 1225 (2010).

[83] T. Köhler, K. Góral, and P. S. Julienne, Rev. Mod. Phys. **78**, 1311 (2006).

[84] E. A. Donley, N. R. Claussen, S. T. Thompson, and C. E. Wieman, Nature **417**, 529 (2002).

[85] F. Wang et al., New J. Phys. **17**, 035003 (2015).

[86] C. Chin and P. S. Julienne, Physical Review A **71**, 012713 (2005).

[87] D. E. Miller, *Studying coherence in ultra-cold atomic gases*, PhD thesis, Massachusetts Institute of Technology, Department of Physics, 2007.

[88] G. Herzberg and J. W. T. Spinks, *Molecular Spectra and Molecular Structure: Diatomic Molecules*, volume 1, Van Nostrand, 1950.

[89] M. Guo et al., Physical Review A **96**, 052505 (2017).

[90] J. M. Brown and A. Carrington, *Rotational Spectroscopy of Diatomic Molecules*, Cambridge University Press, Cambridge, UK, 2003.

[91] G. Reinaudi, T. Lahaye, Z. Wang, and D. Guéry-Odelin, Optics letters **32**, 3143 (2007).

[92] R. Vexiau et al., International Reviews in Physical Chemistry **36**, 709 (2017).

[93] W. Cheney and D. Kincaid, The Australian Mathematical Society **110** (2009).

[94] T. J. Odiorne, P. R. Brooks, and J. V. Kasper, The Journal of Chemical Physics **55**, 1980 (1971).

[95] J. C. Polanyi, Acc. Chem. Res. **5**, 161 (1972).

[96] R. N. Zare, science **279**, 1875 (1998).

[97] J. G. Pruett and R. N. Zare, J. Chem. Phys. **64**, 1774 (1976).

[98] P. S. Żuchowski and J. M. Hutson, Phys. Rev. A **81**, 060703 (2010).

[99] K. M. Jones et al., Phys. Rev. A **54**, R1006 (1996).

[100] J. Y. Seto, R. J. L. Roy, J. Vergs, and C. Amiot, J. Chem. Phys. **113**, 3067 (2000).

[101] A. Pashov et al., Phys. Rev. A **72**, 062505 (2005).

[102] J. N. Byrd, J. A. Montgomery Jr, and R. Côté, Phys. Rev. A **82**, 010502 (2010).

[103] C. Amiot, The Journal of Chemical Physics **93**, 8591 (1990).

[104] J. Söding, D. Guéry-Odelin, P. Desbiolles, G. Ferrari, and J. Dalibard, Phys. Rev. Lett. **80**, 1869 (1998).

[105] Z. Idziaszek and P. S. Julienne, Phys. Rev. Lett. **104**, 113202 (2010).

[106] G. Quéméner and J. L. Bohn, Phys. Rev. A **81**, 022702 (2010).

[107] K. Jachymski, M. Krych, P. S. Julienne, and Z. Idziaszek, Phys. Rev. Lett. **110**, 213202 (2013).

[108] W. H. Miller, Accounts of chemical research **26**, 174 (1993).

[109] W. Miller, *Dynamics of molecular collisions*, volume 2, Springer Science & Business Media, 2013.

[110] O. K. Rice and H. C. Ramsperger, Journal of the American Chemical Society **49**, 1617 (1927).

[111] L. S. Kassel, The Journal of Physical Chemistry **32**, 225 (1928).

[112] R. A. Marcus, The Journal of Chemical Physics **20**, 359 (1952).

[113] G. Quéméner and J. L. Bohn, Physical Review A **81**, 060701 (2010).

[114] B. K. Stuhl et al., Nature **492**, 396 (2012).

[115] B. Zhu, G. Quéméner, A. M. Rey, and M. J. Holland, Physical Review A **88**, 063405 (2013).

[116] G. Quéméner and J. L. Bohn, Physical Review A **93**, 012704 (2016).

[117] M. L. González-Martínez, J. L. Bohn, and G. Quéméner, Physical Review A **96**, 032718 (2017).

[118] T. Lahaye et al., Physical review letters **101**, 080401 (2008).

[119] H. Kadau et al., Nature **530**, 194 (2016).

[120] L. Chomaz et al., Physical Review X **6**, 041039 (2016).

[121] M. Schmitt, M. Wenzel, F. Böttcher, I. Ferrier-Barbut, and T. Pfau, Nature **539**, 259 (2016).

[122] L. Chomaz et al., Nature physics **14**, 442 (2018).

[123] M. Guo, X. Ye, J. He, G. Quéméner, and D. Wang, Physical Review A **97**, 020501 (2018).

[124] B. Gao, Phys. Rev. A **78**, 012702 (2008).

[125] N. Ramsey, Phys. Rev. **85**, 60 (1952).

[126] D. L. Bryce and R. E. Wasylishen, Acc. Chem. Res. **36**, 327 (2003).

[127] C. H. Townes and A. L. Schawlow, *Microwave spectroscopy*, Courier Corporation, 2013.

[128] J. Aldegunde, B. A. Rivington, P. S. Żuchowski, and J. M. Hutson, Phys. Rev. A **78**, 033434 (2008).

[129] J. Aldegunde and J. M. Hutson, Physical Review A **96**, 042506 (2017).

[130] V. Flambaum, A. Gribakina, and G. Gribakin, Physical Review A **58**, 230 (1998).

[131] O. Agam, B. L. Altshuler, and A. V. Andreev, Physical review letters **75**, 4389 (1995).

[132] T. Zelevinsky, S. Kotochigova, and J. Ye, Physical Review Letters **100**, 043201 (2008).

[133] H. Liou, H. Camarda, and F. Rahn, Physical Review C **5**, 1002 (1972).

[134] H. Liou et al., Physical Review C **5**, 974 (1972).

[135] K. Aikawa et al., Physical review letters **108**, 210401 (2012).

[136] A. Frisch et al., Nature **507**, 475 (2014).

[137] K. Baumann, N. Q. Burdick, M. Lu, and B. L. Lev, Physical Review A **89**, 020701 (2014).

[138] T. Maier et al., Physical Review X **5**, 041029 (2015).

[139] G. Breit and I. Rabi, Physical Review **38**, 2082 (1931).

[140] A. Corney, *Atomic and laser spectroscopy*, Clarendon Press Oxford, 1978.

[141] M. Mayle, B. P. Ruzic, and J. L. Bohn, Phys. Rev. A **85**, 062712 (2012).

[142] F. Seeßelberg et al., arXiv preprint arXiv:1810.05702 (2018).

[143] S. Kotochigova and D. DeMille, Physical Review A **82**, 063421 (2010).

[144] K. D. Bonin and V. V. Kresin, *Electric-dipole polarizabilities of atoms, molecules, and clusters*, World Scientific, 1997.

[145] J. Ye, H. Kimble, and H. Katori, science **320**, 1734 (2008).

[146] S. Ospelkaus et al., Faraday discussions **142**, 351 (2009).

[147] F. Bloch, Physical review **70**, 460 (1946).

[148] R. P. Feynman, F. L. Vernon Jr, and R. W. Hellwarth, Journal of applied physics **28**, 49 (1957).

[149] N. F. Ramsey, Physical Review **78**, 695 (1950).

[150] E. L. Hahn, Physical review **80**, 580 (1950).

[151] R. Barnett, D. Petrov, M. Lukin, and E. Demler, Physical review letters **96**, 190401 (2006).

[152] S. R. Manmana, E. Stoudenmire, K. R. Hazzard, A. M. Rey, and A. V. Gorshkov, Physical Review B **87**, 081106 (2013).

[153] R. Scelle, Cooling, plugging, trapping: Exploiting optical dipole potentials for polaron experiments, Master's thesis, Universität Heidelberg, 2009.

[154] W. Petrich, M. H. Anderson, J. R. Ensher, and E. A. Cornell, Physical Review Letters **74**, 3352 (1995).

[155] O. Luiten, M. Reynolds, and J. Walraven, Physical Review A **53**, 381 (1996).

[156] W. Ketterle et al., Adv. At. Mol. Opt. Phys **37**, 181 (1996).

[157] E. Eagleyard Photonics, Application note: Relative Intensity Noise of Distributed Feedback Laser .

[158] C. Akcay, P. Parrein, and J. P. Rolland, Applied optics **41**, 5256 (2002).

[159] N. W. Ashcroft and N. D. Mermin, Google Scholar , 461 (2010).

[160] J. H. Denschlag et al., Journal of Physics B: Atomic, Molecular and Optical Physics **35**, 3095 (2002).

[161] Y. B. Ovchinnikov et al., Physical review letters **83**, 284 (1999).

[162] B. Gadway, D. Pertot, R. Reimann, M. G. Cohen, and D. Schneble, Optics express **17**, 19173 (2009).

[163] R. Cook and A. Bernhardt, Physical Review A **18**, 2533 (1978).

[164] H. Batelaan, Reviews of Modern Physics **79**, 929 (2007).

[165] O. Morsch and M. Oberthaler, Reviews of modern physics **78**, 179 (2006).

[166] Z. Hadzibabic, S. Stock, B. Battelier, V. Bretin, and J. Dalibard, Physical review letters **93**, 180403 (2004).

[167] A. Safavi-Naini, M. Wall, and A. M. Rey, Physical Review A **92**, 063416 (2015).

[168] M. Wall, K. Hazzard, and A. M. Rey, Quantum magnetism with ultracold molecules, in *FROM ATOMIC TO MESOSCALE: The Role of Quantum Coherence in Systems of Various Complexities*, pages 3–37, World Scientific, 2015.

[169] F. Deuretzbacher et al., Physical Review A **77**, 032726 (2008).

[170] A. Chotia et al., Physical review letters **108**, 080405 (2012).